

DEPOSITION OF NICKEL COPPER PHOSPHATE THIN FILMS ON CONDUCTING SUBSTRATE FOR SUPERCAPACITOR APPLICATION

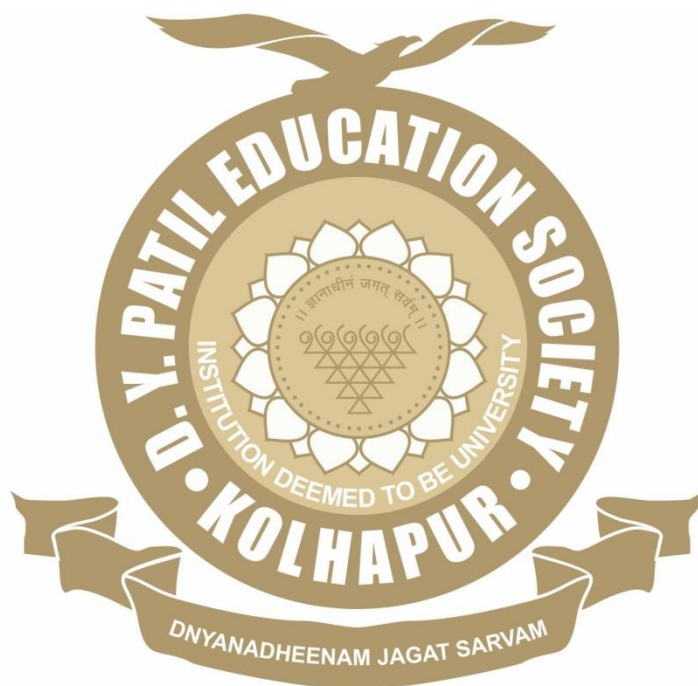
By

Mr. SACHIN S. PUJARI

Under the Supervision of

Dr. UMAKANT M. PATIL

Thesis Submitted to



For the Degree of

Doctor of Philosophy

2021

**DEPOSITION OF NICKEL COPPER PHOSPHATE THIN
FILMS ON CONDUCTING SUBSTRATE FOR
SUPERCAPACITOR APPLICATION**

A THESIS SUBMITTED TO

**D. Y. PATIL EDUCATION SOCIETY (DEEMED TO BE
UNIVERSITY), KOLHAPUR**



FOR THE DEGREE OF

DOCTOR OF PHILOSOPHY

IN

PHYSICS

UNDER THE FACULTY OF

INTERDISCIPLINARY STUDIES

BY

Mr. SACHIN SHIVAJI PUJARI

M.Sc., B.Ed.

UNDER THE SUPERVISION OF

Dr. UMAKANT M. PATIL

M.Sc., Ph.D.

ASSISTANT PROFESSOR, (DST-INSPIRE FACULTY),

CENTRE FOR INTERDISCIPLINARY RESEARCH,

D. Y. PATIL EDUCATION SOCIETY (DEEMED TO BE

UNIVERSITY), KOLHAPUR- 416 006, MAHARASHTRA, (INDIA)

(2021)

DECLARATION

I hereby declare that the thesis entitled **“DEPOSITION OF NICKEL COPPER PHOSPHATE THIN FILMS ON CONDUCTING SUBSTRATE FOR SUPERCAPACITOR APPLICATION”** submitted for the degree of **Doctor of Philosophy (Ph.D.) in Physics** under the faculty of **Centre for Interdisciplinary Research** of D. Y. Patil Education Society (Deemed to be University), Kolhapur is completed and written by me, has not before made the basis for the award of any other higher education institute in India or any other country to the best of my knowledge. Further I declare that I have not violated any of the provisions under Copyright and Piracy/Cyber/IPR Act amended from time to time.

Place: Kolhapur

Research Student



Date: 21 / 10 / 2021

Mr. Sachin Shivaji Pujari

D. Y. Patil Education Society
(Deemed to be University), Kolhapur
Centre for Interdisciplinary Research



CERTIFICATE

This is to certify that the thesis entitled *"Deposition of nickel copper phosphate thin films on conducting substrate for supercapacitor application"* which is being submitted herewith for the award of the Degree of *Doctor of Philosophy (Ph.D.) in Physics* of *D. Y. Patil Education Society (Deemed to be University), Kolhapur*, is the result of the original research work completed by **Mr. Sachin Shivaji Pujari** under my supervision and guidance and to the best of my knowledge and belief the work embodied in this thesis has not formed earlier the basis for the award of any degree or similar title of this or any other University or examining body.

Place: Kolhapur

Research Guide

Date: 21 / 10 / 2021


Dr. Umakant M. Patil


Forwarded through Dean and Research Director

Centre for Interdisciplinary Studies

Prof. C. D. LOKHANDE

Centre For Interdisciplinary Studies
D. Y. Patil Education Society
(Institution Deemed to be University)
869, 'E', Kasaba Bawada
KOLHAPUR- 416006

ACKNOWLEDGEMENT

It was a beautiful journey of expanding the boundaries of knowledge, a journey of finding your strengths and weaknesses, a journey of becoming mentally and emotionally strong. It became more beautiful and exciting because of the people I met along the way. I would like to take this opportunity to acknowledge those fascinating people.

At the completion of my Ph.D. thesis, I would like to express my sincere gratitude towards my advisor, Dr. U. M. Patil [Assist. Professor and DST-INSPIRE Faculty, Centre for Interdisciplinary Research (CIR), D. Y. Patil Education Society (Deemed to be University), Kolhapur] for the continuous support during my PhD study and related research, for his motivation, and immense knowledge. I thank him for the guidance he rendered in the field of research and for enlightening the path of my life with a deep love for science. With his support, I could overcome my scientific problems in writing papers, including this PhD thesis. This work could not have been completed without his inspiring guidance and constant encouragement during research tenure.

I sincerely acknowledge the wholehearted help, valuable discussions, guidelines and suggestions focused by Prof. C. D. Lokhande, Head and Research Director, Centre for Interdisciplinary Research (CIR). He provided a very fruitful discussion and helpful guidance for time management regarding my PhD progress.

I would like to express my sincere thanks to Vice-Chancellor Prof. R. K. Mudgal, Pro-Vice Chancellor Dr. Shimpa Sharma and Registrar Dr. V. V. Bhosale for the inspiration and support. Furthermore, I thank Dr. J. L. Gunjekar, Dr. Vishwajeet Khot and Dr. Arvind Gulbake, who helped me analyze the results with their empathy and cooperative mind. I also thank Dr. S. R. Sabale, Dr. A. C. Lokhande, Mr. S. A. Kadam, Dr. Y. R. Ma, and Dr. V. G. Parale for providing me very important sample characterization data during the entire research work.

I would like to express sincere thanks to my seniors Dr. P. K. Katkar, Dr. S. J. Marje, Dr. T. T. Ghogare and Dr. S. B. Kale, for insightful guidelines, scientific discussions and valuable suggestions on the present work. Good scientific research could not blossom in an alienated desert; it resulted from fruitful discussions and co-operative exercises of many analytical minds.

I am very much thankful to D. Y. Patil Education Society, Kasaba Bawada, Kolhapur, for financial support through the internal research project.

I own a word of thanks to all my friends and research colleague from CIR department viz., Suraj Khalate, Satish Jadhav, Dhanaji Malavekar, Shivaji Ubale, Navnath Padalkar, Rohini Shinde, Shrikant Sadavar, Priti Bagawade, Vikas Mane, Vikas Magdum, Yogesh Chitare, Shirin Kulkarni, Vinod Patil, Akash Patil, Shraddha Bhosale, Sambhaji Kumbhar, Sambhaji Khot and Ranjit Nikam.

I hereby express my most profound appreciation and regards to my beloved parents father Shivaji (Baba), mother Chaya (Aai) and my lovely brother Uday for their continuous support and love.

I would like to confess that even though I try my best, it is not possible for me to acknowledge and thank all those known and unknown faces individually for their direct and indirect contribution to successfully completing this work. I am grateful to all of you for your kind cooperation.

Place: Kolhapur

-Sachin Pujari

SUMMARY OF RESEARCH WORK

Published (Indian) Patents

- 1) Umakant M. Patil, **Sachin S. Pujari**, Chandrakant D. Lokhande, Vishwanath V. Bhosale, “Amorphous nickel phosphate thin film electrode by chemical method for supercapacitor application”, (2020), Application No.- **202021041651**.

Papers Accepted at International Journals

- 1) **Sachin S. Pujari**, Vinod V. Patil, Akash S. Patil, Vinayak G. Parale, Hyung-Ho Park, Jayavant L. Gunjekar, Chandrakant D. Lokhande, Umakant M. Patil, “Amorphous, Hydrous Nickel Phosphate Thin Film Electrode Prepared by SILAR Method as a Highly Stable Cathode for Hybrid Asymmetric Supercapacitor”, Synth. Met., 280, (2021), 116876 (**I. F. 3.26**).
- 2) **Sachin S. Pujari**, Sujit A. Kadam, Yuan R. Ma, Pranav K. Katkar, Supriya J. Marje, Suraj A. Khalate, Umakant M. Patil, “Highly sensitive hydrothermally prepared nickel phosphate electrocatalyst as non-enzymatic glucose sensing electrode”, J. Porous Mater., (2020), 1-13 (**I. F. 2.49**).
- 3) **Sachin S. Pujari**, Sujit A. Kadam, Yuan R. Ma, Pranav K. Katkar, Supriya J. Marje, Suraj A. Khalate, Abhishek C. Lokhande, Umakant M. Patil, “Facile synthesis of microstrip-like copper phosphate hydroxide thin films for supercapacitor applications”, J. Electron Mater., 49, (2020), 3890-3901 (**I.F. 1.93**).
- 4) Pranav K. Katkar, Supriya J. Marje, **Sachin S. Pujari**, Suraj A. Khalate, Prashant R. Deshmukh, Umakant M. Patil, “Single-pot hydrothermal synthesis of manganese phosphate microrods as a cathode material for highly stable flexible solid-state symmetric supercapacitors”, Synth. Met., 267, (2020), 116446-116458 (**I.F. 3.26**).
- 5) Pranav K. Katkar, Supriya J. Marje, **Sachin S. Pujari**, Suraj A. Khalate, Abhishek C. Lokhande, Umakant M. Patil, “Enhanced energy density of all-solid-state asymmetric supercapacitors based on morphologically tuned hydrous cobalt phosphate electrode as cathode material”, ACS Sustain. Chem. Eng., 7, (2019), 11205-11218 (**I.F. 8.19**).
- 6) Suraj A. Khalate, Sujit A. Kadam, Yuan R. Ma, **Sachin S. Pujari**, Supriya J. Marje, Pranav K. Katkar, Abhishek C. Lokhande, Umakant M. Patil, “Hydrothermally synthesized Iron Phosphate Hydroxide thin film electrocatalyst for electrochemical water splitting”, Electrochim. Acta, 319, (2019), 118-128 (**I. F. 6.90**).

- 7) Supriya J. Marje, Pranav K. Katkar, **Sachin S. Pujari**, Suraj A. Khalate, Prashant R. Deshmukh, Umakant M. Patil, "Effect of phosphate (anion) precursor on structural and morphology behavior of nickel phosphate thin films and its supercapacitive performance", Mater. Sci. Eng. B, 261, (2020), 114641-114650 (**I.F. 4.70**).
- 8) Supriya J. Marje, Pranav K. Katkar, **Sachin S. Pujari**, Suraj A. Khalate, Abhishek C. Lokhande, Umakant M. Patil, "Regulated micro-leaf like nickel pyrophosphate as a cathode electrode for asymmetric supercapacitor", Synth. Met., 259, (2020), 116224-116234 (**I.F. 3.26**).
- 9) Suraj A. Khalate, Sujit A. Kadam, Yuan R. Ma, **Sachin S. Pujari**, Umakant M. Patil, "Cobalt Doped Iron Phosphate Thin Film: An Effective Catalyst for Electrochemical Water Splitting", J. Alloys Compd., 885, (2021), 160914 (**I.F. 5.31**).

Papers/Poster Presented at National/International Conferences

- 1) **Sachin S. Pujari**, Pranav K. Katkar, Supriya J. Marje, Suraj A. Khalate, Umakant M. Patil, Study of Copper Phosphate Hydroxide Thin Film For Supercapacitor Application, ISMN-2020, SKN Sinhgad College of Engineering, Pandharpur.
- 2) **Sachin S. Pujari**, Pranav K. Katkar, Supriya J. Marje, Suraj A. Khalate, Umakant M. Patil, Synthesis and Supercapacitive Study of Copper Phosphate Hydroxide Thin Film Electrodes, MAS-2019, K. N. Bhise Arts, Commerce and Vinayakrao Patil Science College, Bhosare (Kurduwadi), Solapur.
- 3) **Sachin S. Pujari**, Pranav K. Katkar, Supriya J. Marje, Suraj A. Khalate, Umakant M. Patil, Synthesis and Supercapacitive Study of Copper Phosphate Hydroxide Thin Film Electrodes, 4th ICPM-MDF-2019, Shivaji University, Kolhapur.

Workshops Attended

- 1) Participated in "Biodiversity conservation and biodiversity act 2002" held at D. Y. Patil Education Society (Deemed to be University), Kolhapur at **15th February 2019** organized by Department of Stem Cell and Regenerative Medicine, Centre for Interdisciplinary Research.

CONTENTS

Chapter No.	Chapter Name	Page No.
I	General introduction and literature survey	1-28
II	Theoretical background of hydrothermal, SILAR methods and thin film characterization techniques	29-58
III	Synthesis, characterization and supercapacitive performance of nickel copper phosphate thin films by hydrothermal method	59-88
IV	Synthesis, characterization and supercapacitive performance of nickel copper phosphate thin films by SILAR method	89-114
V	Fabrication of asymmetric supercapacitor device and performance evaluation	115-136
VI	Summary and conclusions	137-142

LIST OF ABBREVIATIONS

AC	Activated carbon	KOH	Potassium hydroxide
ASD	Asymmetric device	LCVD	Laser chemical vapor deposition
BET	Brunauer-Emmett-Teller	LED	Light emitting diodes
CBD	Chemical bath deposition	LiCl	Lithium chloride
C-FP	Carbonized iron cations adsorbed onto polyaniline	MOCVD	Metal organo-chemical vapor deposition
CNT	Carbon nanotube	NaOH	Sodium hydroxide
CP	Carbon paper	NF	Nickel foam
CPE	Constant phase element	NMP	N-methyl 2-pyrrolidone
C_s	Specific capacitance	OHP	Outer Helmholtz plane
CV	Cyclic voltammetry	PANI	Polyaniline
CVD	Chemical vapor deposition	PD	Power density
DDW	Double distilled water	PET	Polyethylene terephthalate
EC	Electrochemical capacitor	PPV	Poly(p-phenylenevinylene)
ED	Energy density	PPy	Polypyrrole
EDL	Electric double layer	PTh	Polythiophene
EDLC	Electric double-layer capacitor	PVA	Poly (vinyl alcohol)
EDS	Energy dispersive X-ray spectroscopy	PVDF	Polyvinylidene fluoride
EIS	Electrochemical impedance spectroscopy	R_{ct}	Charge transfer resistance
ESD	Energy storage device	rGO	Reduced graphene oxide
ESR	Equivalent series resistance	R_s	Solution resistance
FE-SEM	Field emission scanning electron microscopy	SC	Supercapacitor
FT-IR	Fourier transform infrared spectroscopy	SILAR	Successive ionic layer adsorption and reaction
GCD	Galvanostatic charge-discharge	SS	Stainless steel
GF	Graphene foam	SSD	Solid state device
GO	Graphene oxide	TMP	Transition metal phosphate
Hg/HgO	Mercury/mercury oxide	W	Warburg impedance
HPGC	Highly porous graphitic carbon	XPS	X-ray photoelectron spectroscopy
IHP	Inner Helmholtz plane	XRD	X-ray diffraction
IR	Internal resistance		

CHAPTER-1

GENERAL INTRODUCTION AND LITERATURE SURVEY

CHAPTER 1

General Introduction and Literature Survey

Sr. No.	Title		Page no.
1.1	General introduction		1
	1.1.1	Requirement of supercapacitor	1
	1.1.2	Background and evolution of supercapacitor	3
	1.1.3	Present status of supercapacitor	5
	1.1.4	Working principle of supercapacitor	6
1.2	Categories of supercapacitor		7
	1.2.1	Electrochemical double layer capacitors	7
	1.2.2	Pseudocapacitors	9
		1.2.2.1 Intrinsic pseudocapacitor	10
		1.2.2.2 Intercalation pseudocapacitor	10
		1.2.2.3 Extrinsic pseudocapacitor	10
	1.2.3	Hybrid capacitors	11
1.3	Electrode materials for supercapacitors		11
	1.3.1	Carbon materials	12
	1.3.2	Conducting polymers	13
	1.3.3	Metal oxides	13
	1.3.4	Metal phosphates	14
1.4	Literature survey on nickel phosphate, copper phosphate and nickel copper phosphate material for supercapacitor application		14
	1.4.1	Literature survey on nickel phosphate	14
	1.4.2	Literature survey on copper phosphate	21
	1.4.3	Literature survey on nickel copper phosphate	22
1.5	Orientation and purpose of the dissertation		22
1.6	References		25

1.1 General introduction:

1.1.1 Requirement of a supercapacitor:

The world faces critical global issues like inadequate energy, environmental pollution, growing human population, limited natural resources and decreasing fossil fuels [1]. The worldwide rising gasoline prices are accountable for growth of eco-friendly and fuel-efficient transportation development. To overcome these problems, pure and sustainable energy sources are instantly needed. Easily and freely offering renewable energy sources may tackle this problem, so they acquired an extraordinary opportunity for improvement. Harnessing renewable energy sources such as the sun and the wind and sea tides is an appropriate first consideration for the substitution of fossil fuels to enable sustainable energy production [2]. So, the problem may be resolved through renewable energy resources for the continuous creation of energy. But these intermittent energies face challenges such as being influenced by weather and uneven distribution [3]. Therefore, the substitution of fossil fuel employs these renewable energy resources for continuous energy generation is more favourable. Furthermore, energy storage in various types is one of the crucial constituents which can resolve problems. Effective energy storage equipment should be developed since they can store the energy when presented and retrieve it when required. Electrical energy storage equipment plays a crucial role in several practical applications [4, 5]. Therefore, the part of energy storage technologies in the field of renewable energy production and electric vehicles has become a prominent one. To meet future energy requirements, the development of low-cost, flexible, lightweight, high-performance and economically cheap energy storage is essential. The electrochemical energy storage technologies are the most convenient choice for automobiles between various options of energy sources. Capacitors, supercapacitors (SCs), fuel cells and batteries are various types of power sources in electrochemical energy storage systems [6].

Numerous applications need electrical energy storage devices (ESDs) such as hybrid vehicles, solar cells, computers, cell phones, portable electronic devices, etc. In the area of industrial, commercial and domestic, electric machines are broadly utilized and are essential parts of our daily life. Additionally, electrical energy can safely be converted into heat, light and mechanical energy as per necessity. Nevertheless, electrical energy is complicated to available as in-demand. So, there is a requirement of capable ESDs which store the maximum amount of energy. However, there are also some limitations in the application of ESDs, like individual applications require

specific energy and power values. So, we needed ESDs that meet the needs of particular applications. For the application in portable electronics, batteries, electric vehicles, electrochemical ESDs are attractively fascinated. Batteries are the general and most applicable electrical ESDs since they use a smaller volume of active material to accumulate a maximum amount of energy with the appropriate amount of power required for various applications. Batteries are filled with chemicals, and that electrochemical reactions take place and produce charges. Batteries are fabricated by two or more electrochemical cells having terminals to supply energy. The positive and negative electrodes are isolated by the chemical electrolyte. The filled chemical electrolyte can be a liquid or solid, but it is more possible to be a dry powder in an ordinary battery. It generally transforms chemical energy via redox reaction at the interface of anode and cathode. Electrolyte performs as ion carriers in charge storage reaction in a battery. Nowadays, the storage capability of batteries upgrades by using standard design because of their increasing demand in many applications. Still, there is no exchange available to deal with the difficulty of batteries, like their low life span and lowest power. Hence, in the current situation, one needs to progress a design of a device that has special abilities such as high power density (PD), energy density (ED) and long cycle life [7]. In recent years, the SC as alternative ESDs has been fascinated with ample attention because they hold great assurance in a broad range of potential applications [8]. The SCs, due to their favourable characteristics like higher PD ($>10 \text{ kW kg}^{-1}$), faster charge-discharge system as well as cycling stability ($>10^5$ cycles), are extensively used in memory backup systems, portable, electronic devices and hybrid vehicles, etc. [9, 10]. The SCs can deliver and store electrical energy like batteries, but they use various mechanisms. The batteries store electricity chemically, whereas SCs store physically via separating positive and negative charges. The performance of ESDs would be described in terms of their capability to provide power and energy.

Figure 1.1 demonstrates the Ragone plot, which compared all the ESDs in terms of their specific energy and specific power. The conventional capacitors have extremely low ED at PD beyond 10^5 W kg^{-1} , while batteries have high ED and typical PD. The specific power and energy are located against each other, indicating increasing one factor the loss of other. Hence, if we extract energy rapidly from lithium-ion batteries, its capacity is diminished, which implies that we need power from batteries that are executed to extract the lowest amount of energy.

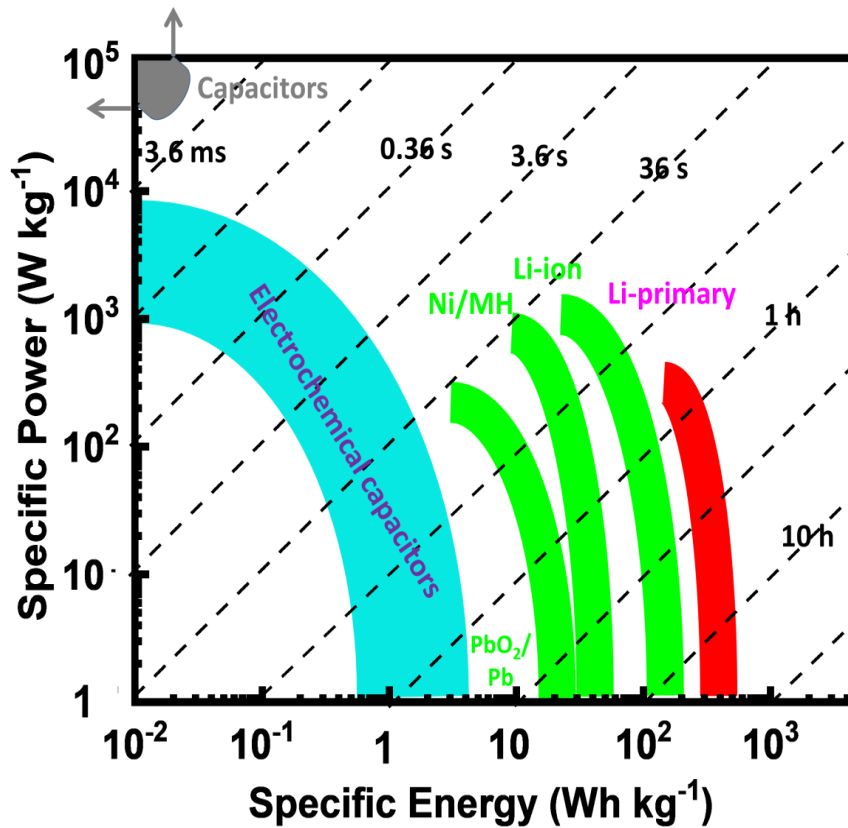


Figure 1.1: Ragone plot for various electrical ESDs [1].

The SCs occupy a prominent position in Ragone plot as they fill out gap between conventional capacitors and fuel cells/batteries. The SCs have high power capabilities and relatively large ED than conventional capacitors. As a result, the SCs can provide a substantial amount of energy at high PD. Moreover, SCs have long cycle life as compare to batteries, low equivalent series resistance (ESR) and high capacitance than the conventional capacitors.

1.1.2 Background and evolution of supercapacitor:

The initial capacitor demonstration occurred in the mid-eighteenth century [11]. A German priest Ewald Georg von Kleist as well as a Dutch scientist Pieter van Musschenbroek constructed the first capacitor, which denominated the "Leyden jar," in 1745 and 1746, respectively. In a glass jar, it included only two metal foils, water, and a conductive chain. The notion of storing static energy at the interface of a solid electrode as well as a liquid electrolyte was created based on this design. Over a century before the creation of the battery (1880), this provided the first idea of an electric double layer (EDL). In the capacitor, the electrical charge-storage mechanisms were first examined by von Helmholtz in 1853 and built the first EDL model by

analysing colloidal suspensions [12]. Between the 19th and early 20th centuries, few pioneering interfacial electrochemists, involving Gouy [13], Chapman [14], Stern [15] and Grahame [16], formulated the advanced theory of EDL capacitance at the interfaces within liquid electrolytes and metal electrodes. At the starting of the 20th century, the first electrochemical capacitor (EC) patent was not implemented until 1954 by H. I. Becker at General Electric. This invention covered ESDs, including porous carbon electrodes dipped in aqueous electrolytes, which accumulate electric energy at the interface as an EDL. Unfortunately this patent was never commercialized. Robert Rightmire founded the first non-aqueous electrolyte-based EC at the Standard Oil Co. of Ohio (SOHIO) [17]. As reported by the broad voltage range of non-aqueous electrolytes, the system explained in this patent could deliver a greater voltages range (3.4–4.0 V) as well as ED than Becker's aqueous EC. Nippon Electric Corp. (NEC), a Japanese business, gained permission for SOHIO's invention, which an EC initially commercialised in 1978 under the name "Super-Capacitor". The NEC's EC application for backup power for clock chips as well as complementary metal oxide semiconductor memory in electronics has been successful in the market. In 1971, ruthenium oxide was used to create a new type of EC termed a pseudocapacitor, which uses Faradaic processes [18, 19]. Based on this discovery, the Pinnacle Research Institute (PRI) started a project in the 1980s based on tantalum/ruthenium oxide pseudocapacitor to develop a high-performance SC named PRI Ultracapacitor. The PRI ultracapacitor was only utilized for military applications such as missile launch and laser weapons systems due to the greater expense of noble metal (ruthenium). As part of their hybrid and electric vehicle initiative, the US Department of Energy (DOE) began assisting a long-term SC research study targeting better ED SCs for use in electric drivelines in 1989 [20]. Currently, the DOE has reached a deal with a world-leading SC manufacturer (Maxwell Technologies, Inc.) to produce high-performance SCs. Companies like Nippon Chemicon (Japan), ELTON (Russia), CAP-XX (Australia), and Nesscap (Korea) have been developing as well as delivering various types of SCs for different applications [21]. Since 2000, the amount of research on SCs has increased dramatically and steadily in response to the growing demand for high-reliability, high-power, and safe ESDs [22]. Presently, transition metal oxide and high surface area carbon-based materials are commercially used to fabricate SC and other metal sulphides, phosphates, and phosphides. Their composites are under study for SC application.

1.1.3 Present status of supercapacitor:

The battery provides high energy but suffers from low power than the capacitor. On the other hand, SCs provide high power with a significant amount of energy and a long lifespan, and low maintenance with ease to fabricate [23]. These special characteristics of SC utilized in present multifunctional technologies where battery technologies are restricted, but their commercial applications are limited because of the self-discharging rate [24]. Nowadays, researchers focusing on enhancing ED of SC by using various features with maintaining all other properties. SCs are three types: electrochemical double-layer capacitors (EDLCs), pseudocapacitors and hybrid capacitors. For EDLCs, carbon based materials (activated carbon (AC), carbon nanotubes (CNTs) and graphene) which deliver high PD and pseudocapacitor employing conducting polymers, transition metal based (metal oxide/hydroxides/phosphates/sulphides) materials which provide high ED [25, 26]. Usually, carbon-based materials are used for SC due to their high surface area and good electrical conductivity. Nevertheless, less capacitance of EDLCs restricts their commercial usage. Presently, many research reports suggest that the pseudocapacitive transition metal oxides are more beneficial electrode materials for SCs due to their large abundance, cost-effectiveness, and environmentally friendly nature [26]. Also, their fast and reversible redox reaction occurs on the surface of the electrode, which delivers high ED and high capacitance value; even so, active material in aqueous electrolytes limits cyclic stability. The issue of less stability could be solved by changing aqueous electrolyte with a solid one, and it overcomes the problem of electrolyte leakage with flexibility and ease of handling [27]. Various types of ionic liquid electrolytes have been developed to enhance the operational potential window and SC's electrochemical performance. They have several advantages such as thermal stability, non-toxicity and non-flammability. Further, the voltage range of SCs with ionic liquid electrolytes can be extent up to 4-6 V [28]. Meanwhile, good electrode material enhances the total capacitance of SC, but other factors like electrolyte, current collector, separator, and other practical elements influence overall performance of SC. The choice of appropriate electrode material and suitable electrolyte effectively increases ED and specific capacitance (C_s) of SC [29]. Biocompatibility, nontoxicity, and lightweight are some benefits of flexible solid state device (SSD) employed in implantable medical devices. Moreover, lightweight and miniature solid-state SC devices can be utilized in portable electronic devices [30].

1.1.4 Working principle of supercapacitor:

The charge storage mechanism of both EC and conventional capacitors are similar, but the difference is in separating medium (electrolyte and dielectric). In a conventional capacitor, two conducting electrodes are isolated by an insulating dielectric material, and the charges accumulate electrostatically. Similarly, EDLC accumulates electric charge at metal/electrolyte surface, and opposite ions on the electrode interface create an EDL. Created EDL is isolated by a distance order of a few Angstrom and depends on electrolytes usage. The schematic diagram of charge storage mechanism in EC is depicted in **Figure 1.2**. EC deliver high ED than conventional capacitors and longer lifespan than batteries. To achieve excellent performance of EC, a higher surface area electrode and a smaller thickness of double layer are required according to following equation (1.1).

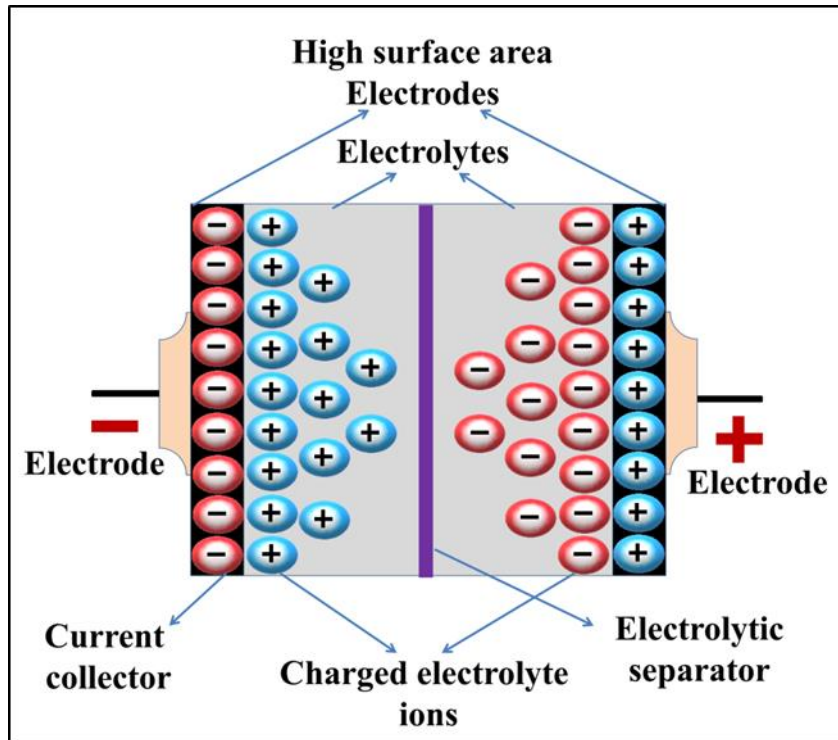


Figure 1.2: Charge storage mechanism of EC.

The EC capacitance C is estimated by using following equation,

$$C = \epsilon_r \frac{A}{d} \quad (1.1)$$

Where ϵ_r is the relative permittivity, A is the surface area of active material, and d is the thickness of double layer. The energy density (E) of EC is calculated as follows,

$$E = \frac{CV^2}{2} \quad (1.2)$$

Where C is capacitance and V is the voltage range of EC.

1.2 Categories of supercapacitor:

Based on the distinct charge storage mechanisms and consumption of electrode material, SCs are categorised into three types: EDLCs, pseudocapacitors, and hybrid capacitors. The charge storage mechanism of EDLC is non-faradaic, where no chemical oxidation-reduction (redox) reactions are involved, which implies charge accumulated by fabricating a double layer between electrode surface electrolyte. The carbon-based electrode materials are utilized for the construction of EDLCs [31-33]. Pseudocapacitors are based upon faradic redox reactions containing high energy electrode materials based on metal oxides/hydroxide, metal phosphides/phosphates/sulphide, metal-doped carbons or conductive polymers [34-37]. A combination of both EDLCs and pseudocapacitive mechanisms i.e. faradic and non-faradic, are hybrid capacitors. Hybrid capacitors are designed by the combination of carbon-based materials along with metal oxides or conducting polymers, or both [35, 38]. This section exhibits an overview of the individual SC in detail. The categorize of SCs with different types and subtypes are demonstrated in **Chart 1**.

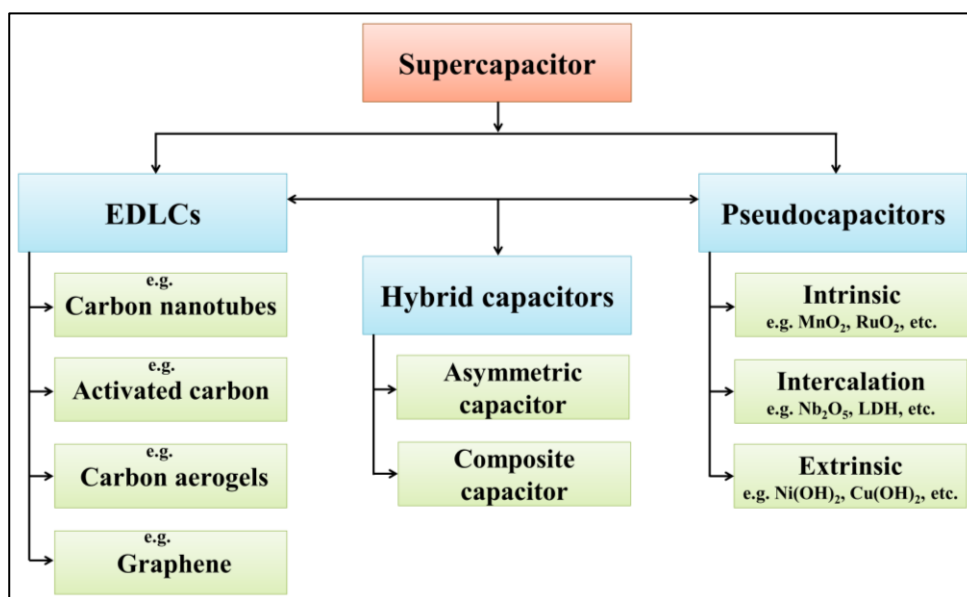


Chart 1: Categories of SCs.

1.2.1 Electrochemical double-layer capacitors:

EDLCs are fabricated from two carbon-based electrodes, a separator and electrolyte as shown in **Figure 1.3**. In EDLC, charge is stored non-faradaically or electrostatically, and no net charge is transferred amongst electrodes and electrolytes. As potential is applied, the charge store on the electrode surface. The ions (unlike charges) are naturally attracted from the electrolyte solution and distributed across the

separator into the pores of the electrode with the opposite charge. Nevertheless, the electrodes are designed to avoid ions recombination. As a result, at each electrode, a double-layer of charge is accumulated. These double-layers coupled with a high surface area of carbon-based electrodes and diminish the distance between electrodes permit EDLCs to perform higher energy densities than conventional capacitors.

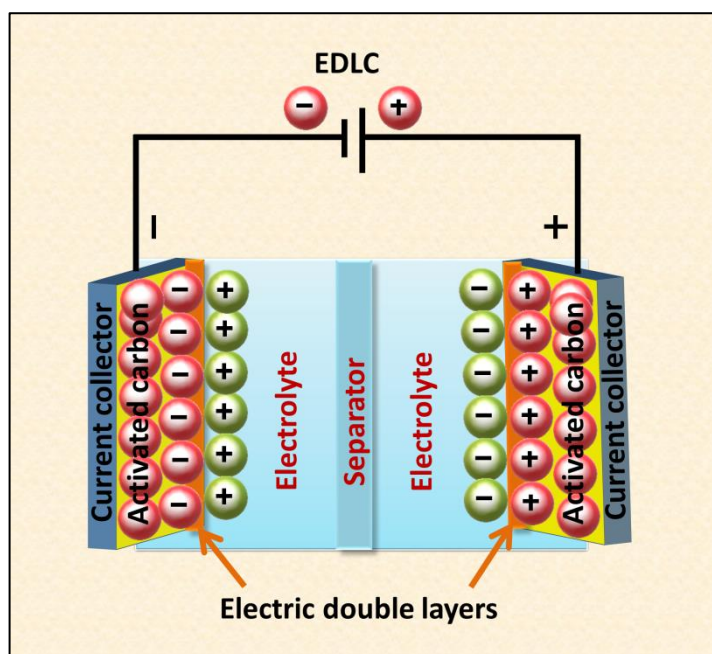


Figure 1.3: Schematic diagram of EDLC.

Faradaic processes do not include any composition or chemical changes because there is no charge transfer among the electrolyte and the electrode. Charge storage in EDLCs is very reversible for this purpose, allowing them to achieve extremely high cycling stability. EDLCs typically have consistent performance characteristics throughout a large number of charge-discharge cycles, up to $\sim 10^6$. Furthermore, electrochemical batteries are usually restricted to 10^3 cycles. This type of capacitor has higher PD but very low energy because of rapid discharge rate [39]. The operating potential restriction of EDLCs is affected by the decomposition potential (1-5 V) of electrolytes. Due to decomposition potential, electric energy accumulates capacity of EDLC is vigorously depends on aqueous or non-aqueous electrolytes. Higher ionic conductivity of aqueous electrolyte than non-aqueous electrolyte exhibits the high specific power of a capacitor. Carbon-based electrode materials typically have the highest surface area, low price, and more constituted techniques than other materials, like metal oxide and conducting polymer [40]. Various types of carbon materials that can be utilised to store charge in EDLC, including AC, CNTs, carbon aerogels, and

currently new verity of carbon fascinated much attention is reduced graphene oxide (rGO).

1.2.2 Pseudocapacitors:

Beyond EDLCs, pseudocapacitor charge storage mechanism is based on the transfer of charges through highly reversible surface redox reactions between electrode and the electrolyte. The schematic illustration of charge storage mechanism in pseudocapacitor is displayed in **Figure 1.4**.

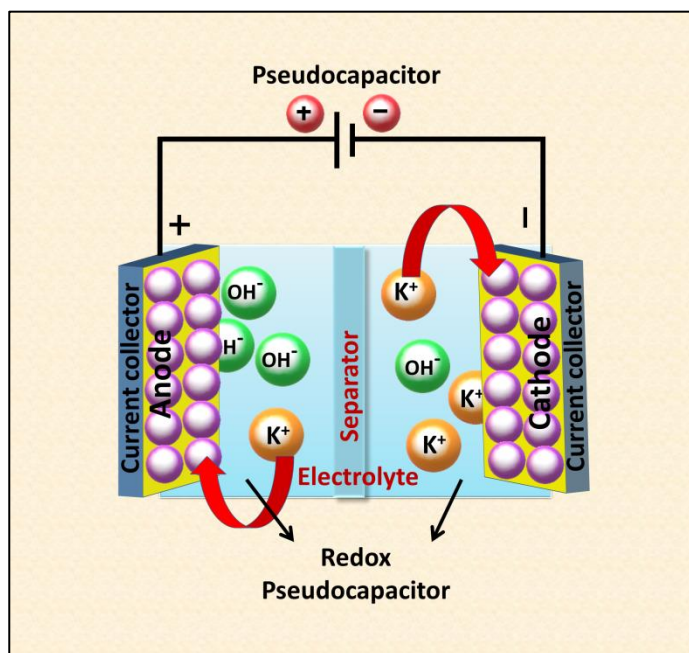


Figure 1.4: Schematic diagram of pseudocapacitor.

This faradaic process leads to pseudocapacitors having higher capacitance and energy densities than EDLCs. However, various factors affect the performance of pseudocapacitor, such as material conductivity, surface area of active electrode and porosity of material, etc. The charge storage mechanism contains redox reactions, insertion and de-insertion, and electrosorption processes, which accomplishes pseudocapacitor. Normally, metal oxide, conducting polymer, sulphides, metal-doped carbon and phosphates are utilized as pseudocapacitors [41-46]. Presently, pseudocapacitive materials are growing interest because of greater C_s and higher ED [47, 48]. Based on the energy storage mechanism, pseudocapacitor is classified into three categories: intrinsic, intercalation, and extrinsic.

1.2.2.1 Intrinsic pseudocapacitors:

In intrinsic material, the redox reaction was recognized as localized on the close surface of material and charges accumulated. Because of multiple valence states, few transition metal oxides (e.g. MnO_2 , RuO_2 and Fe_3O_4) show fast and reversible redox reactions over the electrode surface, making them superior to EDLCs. For many years, MnO_2 and RuO_2 commanded the field of pseudocapacitive materials. Buzzanca and Trasatti [49] firstly reported pseudocapacitive behaviour of MnO_2 from its quasi rectangular curves like its EDLC. However, various studies of intrinsic material have exhibited electrochemical behaviour of bulk MnO_2 depending on the phase and charge-carrying cation in the electrolyte [50, 51].

1.2.2.2 Intercalation pseudocapacitors:

Intercalation pseudocapacitance occurs when ions intercalate into the layers or tunnels of a redox-active material along with a faradaic charge-transfer without crystallographic phase change; such type of charge storage mechanism is reported by Augustyn et. al. [52] and defined as “intercalation pseudocapacitors”. A significant property of intercalation pseudocapacitor is, it avoids structural phase transformation through electrochemical reaction [53]. In conversely to the EDLCs, the charge storage procedure for the intercalation pseudocapacitance is not restricted to the surface, thereby using the bulk of materials for the faradic electrochemical reactions. The intercalation kinetics of layered dichalcogenides are very much influenced by interlayer spacing. Multiple methods are being explored in an exertion to enhance the spacing, ultimately increasing solid-state ion diffusion and rate capability. In intercalation pseudocapacitor, intercalation of ions appears by a solid solution mechanism and do not have a phase change. This process allows enhanced energy storage at higher charge-discharge rates [54].

1.2.2.3 Extrinsic pseudocapacitors:

The materials, who exhibits charge-discharge curves (with plateau) and cyclic voltammetry (strong redox peak) like battery behaviour in their bulk form and they can show pseudocapacitive nature by reducing their particle size (within nanometer). Such phenomenon was reported by Augustyn et al. [52] and defined as “extrinsic pseudocapacitors”. The electrochemical properties change notably, and the materials show a pseudocapacitive response by few battery type materials. The battery-type materials overcome their profile change property when it goes in nanosize (<10 nm) by

decreasing ion diffusion length. The nanosized cobalt and nickel hydroxides are examples of extrinsic pseudocapacitive materials [55, 56].

1.2.3 Hybrid capacitors:

In direction to overcome the restriction of pseudocapacitor and EDLCs the third type of SC has been prepared and is known as hybrid SCs. Hybrid SCs comprise one EDLC type electrode, and another is pure pseudocapacitive type electrode, as depicted in Figure 1.5.

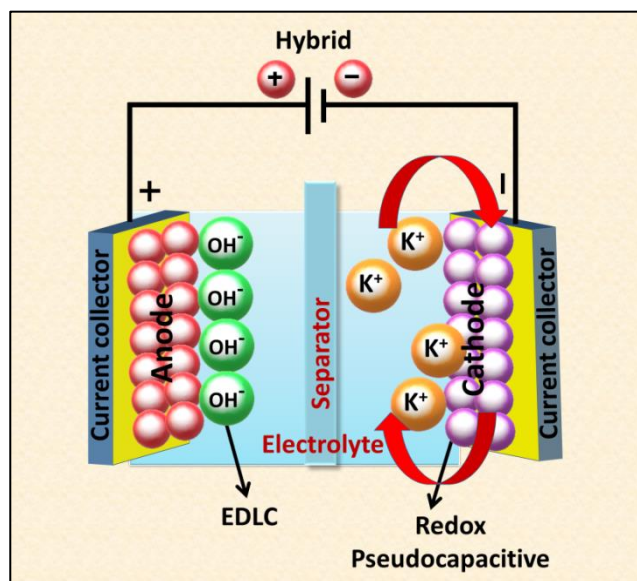


Figure 1.5: Schematic diagram of hybrid capacitor.

The hybrid capacitors store charge by faradic and non-faradic reaction mechanism. In hybrid capacitor, faradic pseudocapacitor electrode material with high capacitance gives higher ED, while the non-faradic EDLC electrode material allows higher PD. The hybrid capacitor is able to achieve higher Cs, ED and PD and cyclic stability than pseudocapacitor or EDLC. The hybrid electrode integrates the carbon-based materials and conducting polymer or metal oxide that leads to the advantage of a chemical and physical charge storage system combined in a single electrode. An asymmetric hybrid capacitor is designed in such a way that one electrode is battery type and another electrode is capacitive type. Such types of devices illustrate the properties of capacitor and battery that mean these devices may be useful for bridge the gap between SCs and batteries [57].

1.3 Electrode materials for supercapacitors:

To execute higher electrochemical results of SC, selection of active material with desired properties is important. For the development of SC, active materials properties

plays important role of such as, high surface area, optimum pores and nanostructured morphology. The ideal SC electrode exhibits following features as listed below.

- ❖ Higher specific surface area to accumulate more ions
- ❖ Electrical conductivity should be high to control PD and rate capability.
- ❖ Controlled porosity can provide facile intercalation of ions.
- ❖ Low cost, as well as non-toxic materials, are needed.
- ❖ Multiple active sites are required to improve electrochemical performance.
- ❖ Thermal and chemical stability should be high to achieve superior electrochemical stability.
- ❖ Economic and facile synthesis process for electrode preparation
- ❖ Minimum ohmic resistance of the actual electrode material and contacts

1.3.1 Carbon materials:

Carbon materials play a vital role in SCs due to their exclusive combination of physical and chemical properties with desirable properties including high conductivity, high active surface area (up to $3000 \text{ m}^2 \text{ g}^{-1}$), good corrosion resistance, high thermal and chemical stability, controlled pore structure, compatibility, and processability in composite materials [58]. The various forms of carbon materials like as fibers, powders, aerogels, monoliths, composites, tubes, sheets, etc. [59-61]. The capacitance predominantly based on the surface area accessible to the electrolyte ions. Carbon-based materials ranging from ACs to CNTs are the broadly explored electrode materials due to the often-cited fetching physical and chemical properties [62]. Knox and co-workers developed the template assisted synthesis of porous carbons [63]. Several porous carbon materials with well-controlled and uniform pore sizes have been designed and synthesized [64]. Templated porous carbons of microporous, mesoporous and macroporous sizes within a tailorable hierarchical structure hold a great promise as SC electrode materials [65]. On the other hand, the development of SC electrodes based on CNTs is of particular interest due to their superior electrical properties and unique tubular porous structures, which favour easy electron and ion transportation. More recently, graphene is a new class of two-dimensional carbon nanostructure, having larger specific surface area as well as unique high electronic qualities, is estimated to have attracted potential in SC application.

1.3.2 Conducting polymers:

Considerable development has been made up in conducting polymer-based materials for storage and electrochemical energy conversion. Conducting polymers have great potential as electrode materials for SCs due to their high conductivity, high capacity, good reversibility, large operating voltage, low cost and low environmental impact [66-70]. Out of different conducting polymers, polyacetylene (PA), polythiophene (PTh), polyaniline (PANI), poly (vinyl alcohol) (PVA), polypyrrole (PPy) and poly(p-phenylenevinylene) (PPV) have been utilized for energy storage application. Conducting polymers mostly including PTh, PANI and PPy has a plenty of unique advantages such as flexibility, easy synthesis, redox behaviour which are meant to resolve challenges in the progress of current SCs. In contrast, pure conducting polymer electrodes show many problems, especially poor cycling stabilities and lower PD. In order to enhance the performance of conducting polymer-based SCs, it is most essential to improve their surface morphology and microstructure through polymerization method, modifying oxidation level, surfactant's type and dopants content.

1.3.3 Metal oxides:

Metal oxides represent an attractive and promising class of electrode material for SCs because of their high cycling stability compared to conducting polymers and high ED compared to the carbon-based material. The fast and reversible electrochemical reactions that occur at the interface of electrode/electrolyte are responsible for the higher value of ED. The various transition metal oxides such as, NiO [71], Fe₂O₃ [72], Co₃O₄ [73], MnO₂ [74], RuO₂ [75], were extensively investigated for SC application. Among these metal oxides, RuO₂ is widely studied because of high electrical conductivity with a wider potential window of 1.2 V. Unfortunately, environmental toxicity and scarce resources of RuO₂ restrict its further development. Recently, binary and ternary transition metal oxides have attracted extensive attention due to their outstanding electrical conductivity, and electrochemical performances compare to single metal oxides. Binary metal oxides such as ZnCo₂O₄, NiCo₂O₄, CuCo₂O₄, MnCo₂O₄ are of the origin of Co₃O₄, and they have delivered excellent performance in SCs [76, 77].

1.3.4 Metal phosphates:

Metal phosphates perform a prominent role in the development of SCs. While carbon-based, conducting polymers and transition metal based oxide/hydroxide materials have been broadly studied for application in SCs. Major attention is being moved into metal phosphides/phosphates recently due to their high theoretical C_s , high chemical stability, high electric conductivity, large abundance and non-toxicity [78-80]. Several transition metal phosphates (TMPs) with an open framework, cavities with multiple channels, and rich redox behaviour exhibit excellent ion/charge conductivity and have thus been investigated as pseudocapacitive electrodes. Also, TMP is probed in many fields such as sensors, SC, catalysts, solar cells, Li-ion batteries, etc., due to their distinctive morphology and excellent electrical and mechanical properties. Generally, different types of monometallic phosphates are fabricated by various chemical methods for SC application. Various metal phosphates were examined for the SC application as, $Ni_3(PO_4)_2$ [81], Ag_3PO_4 [82, 83], $VOPO_4$, [84-86], $Co_3(PO_4)_2$ [87, 88], $Mn_3(PO_4)_2$ [89, 90], $BiPO_4$ [91, 92]. However, bimetallic phosphates exhibited enhanced performance compared to monometallic phosphates because of synergy amongst different metal ions.

1.4 Literature survey on nickel phosphate, copper phosphate and nickel copper phosphate material for supercapacitor application

1.4.1 Literature survey on nickel phosphate:

TMP such as nickel phosphate has been studied for SC applications due to open frame structure, good conductivity, low cost and rich redox behaviour. Different composite materials of nickel phosphate and their structures were fabricated using various synthesis methods such as chemical bath deposition (CBD), sonochemical, hydrothermal, co-precipitation, and calcination method. In addition, the surface morphology of electrode material (nickel phosphate) plays a crucial role in improving C_s and the ED of electrode material.

The earlier reported various types of monometallic and bimetallic nickel phosphate-based electrode materials are summarized in **Table 1.1**. Morphological changes were observed owing to precursor variation studied by Marje et al. [93]. Amorphous nickel phosphate electrode deposited on stainless steel (SS) delivered the C_s of 1031.6 F g^{-1} at 0.5 mA cm^{-2} current density with 80% retention after 3000 cycles. The effect of various calcination temperatures on the structural, morphological and C_s

of nickel phosphate was studied via sonochemical method by Omar et al. [81] the calcined nickel phosphate showed the specific capacity of 620 C g^{-1} at a current density of 0.4 A g^{-1} . The nanocrystal of VSB-5 ($\text{Ni}_{20}[(\text{OH})_{12}(\text{H}_2\text{O})_6][(\text{HP}_4)_8(\text{PO}_4)_4].12\text{H}_2\text{O}$) was produced by Yang et al. [94] via hydrothermal method, and it exhibited the C_s of 2740 F g^{-1} at 3 A g^{-1} current density. Omar et al. [95] reported a sonochemical method monitored by calcination to synthesize nickel phosphate-silver phosphate ($\text{Ni}_3(\text{PO}_4)_2\text{-Ag}_3\text{PO}_4$) it delivers maximum specific capacity of 478 C g^{-1} at 1 A g^{-1} current density. Amorphous $\text{Ni}_3(\text{PO}_4)_2\text{@GO}$ composite is successfully synthesized by Li et. al. [96] via chemical precipitation method. A C_s of 1392.5 F g^{-1} was obtained for $\text{Ni}_3(\text{PO}_4)_2\text{@GO}$ composite sample at a current density of 0.5 A g^{-1} . The $\text{Ni}_{20}[(\text{OH})_{12}(\text{H}_2\text{O})_6][(\text{HPO}_4)_8(\text{PO}_4)_4].12\text{H}_2\text{O}$ prepared by Zhao et al. [97] via hydrothermal method, and it shows maximum C_s of 1494 F g^{-1} at current density 1.25 A g^{-1} . A roe-shaped ternary nanocomposite of $\text{Ni}_3(\text{PO}_4)_2\text{/RGO/Co}_3(\text{PO}_4)_2$ was prepared on cobalt foam by Zhao et al. [98] via hydrothermal method. A C_s of 1137.5 F g^{-1} at 0.56 A g^{-1} was achieved for composite electrode with a capacity retention of 117.8% after 14000 cycles. Peng et. al. [99] synthesized $\text{Ni}_3(\text{PO}_4)_2.8\text{H}_2\text{O}$ via a microwave-assisted chemical method. The prepared $\text{Ni}_3(\text{PO}_4)_2.8\text{H}_2\text{O}$ material delivered C_s of 1301 F g^{-1} at current density 2 A g^{-1} with 83.59% capacitance retention after 1000 cycles. Mirghni et al. [100] prepared $\text{Ni}_3(\text{PO}_4)_2\text{/graphene foam (GF)}$ composite material via hydrothermal method exhibits a specific capacity of 48 mAh g^{-1} at current density 0.5 A g^{-1} . The fabrication of $\text{Ni}_3(\text{PO}_4)_2.8\text{H}_2\text{O}$ nano/micro flakes layer on nickel foam (NF) is reported by Padmanathan et al. [101] via facile one-pot hydrothermal method. The electrode displays a C_s of 1552 F g^{-1} at an applied current of 5 mA cm^{-2} and retains 84% of its initial capacity after 10000 cycles. Pang et al. [102] synthesized amorphous nickel pyrophosphate ($\text{Ni}_2\text{P}_2\text{O}_7$) microstructure by calcining ammonium nickel phosphate ($\text{NH}_4\text{NiPO}_4.6\text{H}_2\text{O}$) microstructures, and it illustrated C_s of 1050 F g^{-1} at current density 500 mA g^{-1} . Sankar et al. [103] synthesized nanorods of $\text{Ni}_2\text{P}_2\text{O}_7$ by hydrothermal method. $\text{Ni}_2\text{P}_2\text{O}_7$ offered capacitance of 5753 mF cm^{-2} at a current density of 5 mA cm^{-2} with addition of $\text{K}_3[\text{Fe}(\text{CN})_6]$ redox additive in 1 M potassium hydroxide (KOH) electrolyte. The amorphous nature of $\text{Ni}_2\text{P}_2\text{O}_7$ prepared by Pramanik et al. [104] via hydrothermal method followed by calcination delivers a C_s of 265 F g^{-1} at scan rate 20 mV s^{-1} . Nanosheets of $\text{Ni}_2\text{P}_2\text{O}_7$ decorated by NiCo-OH composite material synthesized by Chodankar et al. [105] on NF and achieved C_s of 2529 F g^{-1} at current density 1 mA

cm⁻² with stability (92.59%). Nanograins of Ni₂P₂O₇ were prepared by Senthilkumar et al. [106] via simple co-precipitation technique, and it offered a C_s of 1893 F g⁻¹ at current density 2 A g⁻¹. Nickel pyrophosphate was successfully synthesized by Marje et al. [107] using the CBD method, which shows maximum C_s of 482 F g⁻¹ at current density 3 mA cm⁻² and stability (99.73%) after 2500 cycles. Wei et al. [108] prepared Na doped Ni₂P₂O₇ hexagonal tablets via hydrothermal method, which delivered a capacitance of 557.5 F g⁻¹ at current density 1.2 A g⁻¹. Pang et al. [109] studied Ni₁₁(HPO₃)₈(OH)₆ superstructures accumulated by nanotubes under mild hydrothermal conditions and offered C_s 1876 F g⁻¹ at a current density of 0.625 A g⁻¹. Chodankar et al. [110] fabricated by a core-shell structured MnO₂@Ni₂P₂O₇ using hydrothermal followed by a CBD method and achieved a specific capacity of 309 mAh g⁻¹ at current density 1 A g⁻¹ with superior stability (94%) over 12000 cycles. Nickel phosphite [Ni₁₁(HPO₃)₈(OH)₆] hexagonal polyhedrons were prepared by Pang et al. [111] via hydrothermal method, and it exhibited C_s of 295 F g⁻¹ at a current density of 0.625 A g⁻¹ with stability of 99.3% after 1000 cycles. Gao et al. [112] prepared microporous nickel phosphite [Ni₁₁(HPO₃)₈(OH)₆] nanocrystals using a hydrothermal method, and it shows large C_s of 558 F g⁻¹ at current density 0.5 A g⁻¹ with stability (97.7%). Zhao et al. [113] synthesized the mesoporous NH₄NiPO₄.H₂O nanostructures through a hydrothermal method and obtained C_s of 1072 F g⁻¹ at current density of 1.50 A g⁻¹ with stability 95.0% after 3000 cycles. Nickel phosphate nanowires were prepared by Wang et al. [114] via hydrothermal method, and they exhibited C_s of 1472 F g⁻¹ at a current density of 1 A g⁻¹. Li et al. [115] synthesized the co-doped bouquet-like nickel phosphite (Ni₁₁(HPO₃)₈(OH)₆) material via a simple solvothermal method. The electrode exhibited C_s of 751.5 F g⁻¹ at the current density of 0.5 A g⁻¹ with superior stability (98.8%) over 8000 cycles.

Table 1.1: Electrochemical performance comparison of various nickel phosphate based materials for SC application.

Sr. No.	Material and morphology	Substrate	Method of deposition	Electrolyte	Capacitance (F g ⁻¹) at current density (A g ⁻¹)	Stability at cycles	Ref.
1.	Amorphous nickel phosphate (Microsphere)	SS	CBD	1 M KOH	1031 at 0.5 mA cm ⁻²	80%, 6500	[93]

2.	$\text{Ni}_3(\text{PO}_4)_2$ (Nanoparticles)	NF	Sonochemical	1 M KOH	1771 at 0.4	-	[81]
3.	$\text{Ni}_{20}[(\text{OH})_{12}(\text{H}_2\text{O})_6]$ $[(\text{HP}_4)_8(\text{PO}_4)_4] \cdot 12\text{H}_2\text{O}$ (Nanocrystal)	NF	Hydrothermal	1 M KOH	2740 at 3	-	[94]
4.	$\text{Ni}_3(\text{PO}_4)_2\text{-Ag}_3\text{PO}_4$ (Nanoparticles)	NF	Sonochemical & Calcination	1 M KOH	478 C g ⁻¹ at 1	-	[95]
5.	$\text{Ni}_3(\text{PO}_4)_2\text{@GO}$ (Nanoparticles)	NF	Chemical precipitation	2 M KOH	1392.59 at 0.5	93.5%, 1000	[96]
6.	$\text{Ni}_{20}[(\text{OH})_{12}(\text{H}_2\text{O})_6]$ $[(\text{HP}_4)_8(\text{PO}_4)_4] \cdot 12\text{H}_2\text{O}$ (Nanorods)	NF	Hydrothermal	3 M KOH	1497 at 1.25	-	[97]
7.	$\text{Ni}_3(\text{PO}_4)_2\text{/RGO/Co}_3(\text{PO}_4)_2$ (Roe shaped)	Cobalt Foam	Hydrothermal	1 M KOH	1137.5 at 0.56	117.8%, 14000	[98]
8.	$\text{Ni}_3(\text{PO}_4)_2 \cdot 8\text{H}_2\text{O}$ (Microflowers)	NF	Microwave- assisted	3 M KOH	1301 at 2	83.59%, 1000	[99]
9.	$\text{Ni}_3(\text{PO}_4)_2\text{/GF}$ (Nanorods)	NF	Hydrothermal	6 M KOH	48 mAh g ⁻¹ at 0.5	92%, 2000	[100]
10	$\text{Ni}_3(\text{PO}_4)_2 \cdot 8\text{H}_2\text{O}$ (Nano/micro flakes)	NF	One-pot Hydrothermal	1 M NaO H	1552	84% 10000	[101]
11.	$\text{Ni}_2\text{P}_2\text{O}_7$ (Microstructure)	NF	Stirring & Calcination	3 M KOH	1050 at 500 mA g ⁻¹	90.5%, 6000	[102]
12.	$\text{Ni}_2\text{P}_2\text{O}_7$ (Nanorods)	NF	Hydrothermal	1 M KOH	5272 mF cm ⁻² at 5 mA cm ⁻²	83.59%, 5000	[103]
13.	$\text{Ni}_2\text{P}_2\text{O}_7$ (Nano spheres)	Graphite	Hydrothermal & Calcination	3 M KOH	265 at 20 mV s ⁻¹	97%, 1000	[104]
14.	$\text{Ni}_2\text{P}_2\text{O}_7\text{/NiCo-OH}$ (Nanosheets, micro-sheets)	NF	Hydrothermal & Electrodeposit ion	2 M KOH	2529 at 1 mA cm ⁻²	92.59%, 10000	[105]
15.	$\text{Ni}_2\text{P}_2\text{O}_7$ (Nanograins)	CP	Co- precipitation	1 M NaO H	1893 at 2	-	[106]
16.	$\text{Ni}_2\text{P}_2\text{O}_7 \cdot 8\text{H}_2\text{O}$ (Microstrucure)	rGO	CBD	1 M KOH	482 F g ⁻¹ at 3 mA cm ⁻²	99.73% 2500	[107]
17.	$\text{Na-Ni}_2\text{P}_2\text{O}_7$ (Hexagonal tablets)	NF	Hydrothermal	3 M NaO H	557.5 at 1.2	97.3%, 1000	[108]
18.	$\text{Ni}_{11}(\text{HPO}_3)_8$ $(\text{OH})_6$ (Nanotubes)	NF	Hydrothermal	3 M KOH	1876 at 0.625	95%, 2000	[109]
19	$\text{MnO}_2\text{@Ni}_2\text{P}_2\text{O}_7$ (Nanoflakes, micro-sheets)	NF	Hydrothermal & CBD	2 M KOH	309 mAh g ⁻¹ at 1	94%, 12000	[110]

20.	$(\text{Ni}_{11}(\text{HPO}_3)_8(\text{OH})_6)$ (Hexagonal polyhedron)	NF	Hydrothermal	3 M KOH	295 at 0.625	99.3%, 1000	[111]
21.	$(\text{Ni}_{11}(\text{HPO}_3)_8(\text{OH})_6)$ (Nanocrystals)	NF	Hydrothermal	3 M KOH	588 at 0.5	97.7%, 10000	[112]
22.	$\text{NH}_4\text{NiPO}_4 \cdot \text{H}_2\text{O}$ (Nanostructures)	NF	Hydrothermal	3 M KOH	1072 at 1.50	95%, 3000	[113]
23.	NiHPO_4 (Nanowires)	NF	Hydrothermal	3 M KOH	1472 at 1	-	[114]
24.	$\text{Co}-(\text{Ni}_{11}(\text{HPO}_3)_8(\text{OH})_6)$ (Bouquet-like)	NF	Solvothermal	3 M KOH	751.5 at 1	92.8%, 8000	[115]

Using different phases of nickel phosphate fabricated asymmetric device (ASD) for the estimation of practical applicability and reported in **Table 1.2**.

ASD was constructed using amorphous nickel phosphate thin film electrode as cathode electrode and rGO as anode electrode by Marje et al. [93] and it gives C_s of 100.7 F g^{-1} at 6 mA cm^{-2} current density with ED of 45.33 Wh kg^{-1} at 1.5 kW kg^{-1} PD, and delivered 80% C_s retention after 3000 GCD cycles. Omar et al. [81] fabricated ASD by using $\text{Ni}_3(\text{PO}_4)_2$ (positive electrode) and AC (negative electrode) in 1 M KOH electrolyte. The ASD delivered a specific capacity of 355 C g^{-1} at current density 0.4 A g^{-1} with ED of 76 Wh kg^{-1} at PD of 599 W kg^{-1} . Also, the device exhibits 88.5% initial capacity after 3000 cycles. Omar et al. [95] prepared $\text{Ni}_3(\text{PO}_4)_2\text{-Ag}_3\text{PO}_4/\text{AC}$ based supercapattery, which delivered an ED of 32.4 Wh kg^{-1} at PD 399.5 W kg^{-1} with cyclic stability (82%) over 5000 cycles. Li et al. [96] fabricated ASD using $\text{Fe}_2\text{O}_3@\text{GO}/\text{Ni}_3(\text{PO}_4)_2@\text{GO}$ and observed ED of 67.2 Wh kg^{-1} as well as superior long term stability (88%) after 1000 cycle. Zhao et al. [97] fabricated SSD based on $\text{Ni}_{20}[(\text{OH})_{12}(\text{H}_2\text{O})_6][(\text{HP}_4)_8(\text{PO}_4)_4] \cdot 12\text{H}_2\text{O}/\text{graphene}$ using PVA-KOH electrolyte, and it delivered volumetric ED of $0.445 \text{ mWh cm}^{-3}$ at 44 mW cm^{-3} PD with 97.4% capacitive retention after 5000 cycles. Zhao et al. [98] fabricated $\text{Ni}_3(\text{PO}_4)_2/\text{RGO}/\text{Co}_3(\text{PO}_4)_2/\text{AC}$ device, and it delivered C_s of 115.4 F g^{-1} at current density 0.12 A g^{-1} with ED of 44.82 Wh kg^{-1} at PD 428.6 W kg^{-1} , also retention of 91.9% over 18000 cycles. The $\text{Ni}_3(\text{PO}_4)_2 \cdot 8\text{H}_2\text{O}/\text{rGO}$ device fabricated by Peng et al. [99] delivered a large specific capacity of 122.3 C g^{-1} at a current density of 1 A g^{-1} along with ED of 25.48 Wh kg^{-1} at 750 W kg^{-1} PD. It showed cycling performance (84.23%) after 1000 cycles. ASD fabricated by Mirghni et al. [100] using carbonized iron (Fe^{3+}) adsorbed on PANI (C-FP) as the anode electrode and $\text{Ni}_3(\text{PO}_4)_2/90 \text{ mg GF}$

as the cathode delivered ED of 49 Wh kg^{-1} at 499 W kg^{-1} PD with 53% cyclic stability. Padmanathan et al. [101] fabricated ASD based on $\text{Ni}(\text{PO}_4)_2 \cdot 8\text{H}_2\text{O}/\text{NF}/\text{AC}$ has offered specific energy of 33.4 Wh kg^{-1} with the power of 165.5 W kg^{-1} with 89% capacitive retention after 10000 cycles. Sankar et al. [103] fabricated $\text{Ni}_2\text{P}_2\text{O}_7/\text{rGO}$ hybrid SC device, and it exhibited a C_s of 224 F g^{-1} at current density 1 A g^{-1} . Also, it delivered a maximum ED of 70 Wh kg^{-1} at 750 W kg^{-1} PD with superior cycling stability (73%) over 5000 cycles. The $\text{Ni}_2\text{P}_2\text{O}_7/\text{NiCo-OH}/\text{AC}$ device prepared by Chodankar et al. [105] using PVA-KOH gel electrolyte offered C_s of 221 F g^{-1} at current density 3 mA cm^{-2} with cyclic stability (91.83%) over 10000 cycles. Also, it shows ED 78 Wh kg^{-1} at 444 W kg^{-1} PD. Senthilkumar et al. [106] prepared $\text{Ni}_2\text{P}_2\text{O}_7/\text{HPGC}$ ASD, and it exhibited a capacitance of 183 F g^{-1} with ED of 65 Wh kg^{-1} at PD 800 W kg^{-1} as well as 83% capacitive retention. Marje et al. [107] fabricated ASD by using nickel pyrophosphate (positive electrode) and rGO (negative electrode). The ASD shows a capacitance value of 74.81 F g^{-1} and ED of 26.6 Wh kg^{-1} at PD of 870.6 W kg^{-1} . Also, ASD exhibits 87.35% capacitive retention after 5500 cycles. Wei et al. [108] fabricated SSD using Na doped $\text{Ni}_2\text{P}_2\text{O}_7$ (positive electrode) and graphene (negative electrode). The fabricated device delivered C_s of 32.6 mF cm^{-2} at 0.5 mA cm^{-2} current density with ED of 23.4 Wh kg^{-1} at 1.29 kW kg^{-1} PD. Fabricated $\text{MnO}_2@\text{NPO}/\text{AC}$ SSD by Chodankar et al. [110] using PVA-KOH gel electrolyte showed specific capacity of 82 mAh g^{-1} at 1 A g^{-1} current density along with specific energy of 66 Wh kg^{-1} at 640 W kg^{-1} specific power and 93% retention over 10000 cycles. A flexible solid-state ASD was constructed using nanocrystal of $\text{Ni}_{11}(\text{HPO}_3)_8(\text{OH})_6$ (cathode) and graphene nanosheets (anode) by Gao et al. [112]. The device exhibited C_s of 1.64 F cm^{-2} at current density of 5 mA cm^{-2} with ED of 0.45 mWh cm^{-3} at PD of 33 mW cm^{-3} and 93.3% initial capacitance retention after 10000 cycles. ASD cell in which Ni/NiHPO_4 as the cathode and AC as the anode was fabricated by Wang et al. [114]. The device delivered C_s of 98.62 F g^{-1} at 0.5 A g^{-1} current density with ED 26.8 Wh kg^{-1} at 68.8 W kg^{-1} PD and 90.03% retention over 6000 cycles. Li et al. [115] fabricated aqueous and SSD using Co-doped nickel phosphite ($\text{Ni}_{11}(\text{HPO}_3)_8(\text{OH})_6$) (positive electrode) and AC (negative electrode). The aqueous device with 3 M KOH electrolyte delivered C_s of 83.1 mF cm^{-2} at current density 0.5 mA cm^{-2} , also exhibited ED of $15.48 \text{ mWh cm}^{-2}$ at 600 W cm^{-2} PD with cyclic stability (94%) over 5000 cycles. The SSD with PVA-KOH gel electrolyte

delivered C_s of 77.1 mF cm^{-2} at current density 0.5 mA cm^{-2} , also exhibits ED of $14.72 \text{ mWh cm}^{-2}$ at 600 W cm^{-2} PD with cyclic stability (91.2%) over 5000 cycles.

Table 1.2: Literature survey of nickel phosphate based devices.

Sr. No.	Positive electrode (cathode)	Negative electrode (anode)	Electrolyte	Capacitance (F g^{-1}) at current density (A g^{-1})	Energy density (Wh kg^{-1})	Power density (W kg^{-1})	Stability at cycles	Ref.
1.	Amorphous nickel phosphate/SS/rGO/SS	rGO	1 M KOH	100.74 at 6 mA cm^{-2}	45.33	1500	80%, 3000	[93]
2.	$\text{Ni}_3(\text{PO}_4)_2/\text{NF}$	AC/NF	1 M KOH	355 C g^{-1} at 0.4	76	599	88.5%, 3000	[81]
3.	$\text{Ni}_3(\text{PO}_4)_2\text{-Ag}_3\text{PO}_4/\text{NF}$	AC/NF	1 M KOH	146 C g^{-1} at 0.5	32.4	399.5	82%, 5000	[95]
4.	$\text{Ni}_3(\text{PO}_4)_2@\text{GO}/\text{NF}$	$\text{Fe}_2\text{O}_3@\text{GO}/\text{NF}$	-	189 at 0.25	67.2	200.43	85%, 1000	[96]
5.	$\text{Ni}_{20}[(\text{OH})_{12}(\text{H}_2\text{O})_6][(\text{HP}_4)_8(\text{PO}_4)_4]\cdot 12\text{H}_2\text{O}/\text{PET}$	Graphene/PET	PVA-KOH	148.3 F cm^{-2} at 0.5 mA cm^{-2}	$0.445 \text{ mWh cm}^{-3}$	44 mW cm^{-3}	97.4%, 5000	[97]
6.	$\text{Ni}_3(\text{PO}_4)_2/\text{rGO}/\text{Co}_3(\text{PO}_4)_2/\text{Cobalt Foam}$	AC/NF	-	115.4 at 0.12	44.82	428.6	91.9%, 18000	[98]
7.	$\text{Ni}_3(\text{PO}_4)_2\cdot 8\text{H}_2\text{O}$	rGO	-	122.3 C g^{-1} at 1	25.48	750.02	84.23%, 1000	[99]
8.	$\text{Ni}_3(\text{PO}_4)_2/\text{GF}/\text{NF}$	C-FP/NF	-	48 mAh g^{-1} at 0.5	49	499	53%, 10000	[100]
9.	$\text{Ni}(\text{PO}_4)_2\cdot 8\text{H}_2\text{O}/\text{NF}/\text{AC}$	NF	1 M NaOH	161.8 F g^{-1} 2.5 mA cm^{-2}	33.4	165.5	89% 10000	[101]
10.	$\text{Ni}_2\text{P}_2\text{O}_7/\text{NF}$	rGO/NF	1 M KOH	224 at 1	70	750	73%, 5000	[103]
11.	$\text{Ni}_2\text{P}_2\text{O}_7/\text{NiCo-OH}/\text{NF}$	AC/NF	PVA-KOH	221 at 3 mA cm^{-2}	78	444	91.83%, 10000	[105]
12.	$\text{Ni}_2\text{P}_2\text{O}_7/\text{CP}$	HPGC/CP	1 M NaOH	183	65	800	83%, 2000	[106]
13.	$\text{Ni}_2\text{P}_2\text{O}_7//\text{KOH}/\text{rGO}$	rGO	1 M KOH	74.81 F g^{-1} at 0.9 mA cm^{-2}	26.6	870.6	87.35% 5500	[107]
14.	$\text{Na-Ni}_2\text{P}_2\text{O}_7$	Graphene	PVA-NaOH	32.6 mF cm^{-2} at 0.5 mA cm^{-2}	23.4	1292.2	98.5%, 5000	[108]
15.	$\text{MnO}_2@\text{Ni}_2\text{P}_2\text{O}_7$	AC/NF	PVA-KOH	82 mAh g^{-1} at 1	66	640	93%, 10000	[110]
16.	$\text{Ni}_{11}(\text{HPO}_3)_8(\text{OH})_6/\text{PET}$	Graphene/PET	PVA-KOH	1.64 F cm^{-3} at 0.5 mA cm^{-2}	$0.45 \text{ mW h cm}^{-3}$	33 mW cm^{-3}	93.3%, 10000	[112]
17.	Ni/NiHPO_4	AC	3 M KOH	98.62 at 0.5	26.8	68.8	90.3% 6000	[114]

18.	Co- (Ni ₁₁ (HPO ₃) ₈ (OH) ₆)	AC/NF	3 M KOH	83.1 mF cm ⁻² at 0.5 mA cm ⁻²	15.48 mWh cm ⁻²	600 W cm ⁻²	94%, 5000	[115]
		AC/PET	PVA- KOH	77.1 mF cm ⁻² at 0.5 mA cm ⁻²	14.72 mWh cm ⁻²	600 W cm ⁻²	91.2%, 5000	

1.4.2 Literature survey on copper phosphate:

Copper based materials are abundant in nature, and also they are non-toxic, so they are in focus for application in various fields. Copper phosphate is a low-cost, air-stable, environment-friendly material and exhibits electrochemical performance. However, there are very few reports on copper phosphate for SC application and described in **Table 1.3**.

Copper phosphate hydroxide [Cu₂(PO₄)(OH)] thin films were synthesized by Pujari et al. [116] via hydrothermal method and reported maximum C_s of 280 F g⁻¹ at a scan rate 5 mV s⁻¹ with (91%) capacitive retention after 2000 cycles. Karaphun et al. [117] Cu₂P₂O₇ nanocrystals were obtained by calcination of the NH₄CuPO₄·H₂O powder at low temperature. The C_s of 297.521 F g⁻¹ at a current density of 1 A g⁻¹ and cycling stability after a 1000 cycle test of 94.04% was achieved. Binder-free Cu₂P₂O₇ were synthesized by Agarwal et al. [118] via successive ionic layer adsorption and reaction (SILAR) method and reported maximum C_s of 332.9 F g⁻¹ at a scan rate 10 A g⁻¹ with 68% capacitive retention after 4500 cycles.

Table 1.3: Electrochemical performance comparison of various copper phosphate based materials for SC.

Sr. No.	Material and morphology	Substrate	Method of deposition	Electrolyte	Capacitance (F g ⁻¹) at current density (A g ⁻¹)	Stability at cycles	Ref.
1.	Cu ₂ (PO ₄)(OH) (microstrip)	SS	Hydrothermal	1 M KOH	280 at 5 mA cm ⁻²	91%, 2000	[116]
2	Cu ₂ P ₂ O ₇ (Flake like)	--	Hydrothermal	3 M KOH	297.521 at 1 A g ⁻¹	94.04% 1000	[117]
3.	Cu ₂ P ₂ O ₇ (Nanoflakes)	SS	SILAR	1 M LiCl	332.9 At 10 A g ⁻¹	68% 4500	[118]

One report is available on the fabrication of SSD using copper phosphide material as cathode and tabulated in **Table 1.4**.

Agarwal et al. [118] $\text{Cu}_2\text{P}_2\text{O}_7$ based flexible SSD. The device achieves a capacitance value of 102.5 F g^{-1} at 5 A g^{-1} . A specific ED of 11.54 Wh kg^{-1} at 2.76 kW kg^{-1} of PD with retention of 80% at a current density of 12.5 A g^{-1} .

Table 1.4: Literature survey of copper phosphide based devices.

Sr. No.	Positive electrode (cathode)	Negative electrode (anode)	Electrolyte	Capacitance (F g^{-1}) at current density (A g^{-1})	Energy density (Wh kg^{-1})	Power density (W kg^{-1})	Stability at cycles	Ref.
1.	$\text{Cu}_2\text{P}_2\text{O}_7//\text{Cu}_2\text{P}_2\text{O}_7$	$\text{Cu}_2\text{P}_2\text{O}_7$	PVA-LiCl	102.5 F g^{-1} at 5 A g^{-1}	11.54	2760	85% 4500	[118]

1.4.3 Literature survey on nickel copper phosphate:

The fabrication and design of SC electrodes are essential with required properties as wide potential window, high C_s , high PD, and rapid charging-discharging rate. Therefore, combining the benefits of both metal phosphates (nickel and copper phosphate) is a very effective scheme to optimize each metal phosphate for enhancing its electrochemical performance. Unfortunately, to date, there is no report available on nickel copper phosphate based supercapacitor devices. Hence, for the present study, nickel copper phosphate is chosen for SC application.

1.5 Orientation and purpose of the dissertation:

Recently, researchers all over the world focused on the progress of SC performance with high PD and ED, cost-effective electrodes and long cycle lifespan, which are the important backbone of ESDs. An SC device with electrochemical activity as well as low cost may promote its utilization over widespread applications. However, the electrolyte and active surface area of electrode material are key factors and impacts on the performance of SC relating to ED and capacitance. Furthermore, a moderately quick discharge is essential for SC to give pulse power, obtained by lowering ESR. Therefore, the improvement and design of active electrode materials to acquire the above terms become challenging for many electrochemists.

The craze of recent research is concentrated on fabricating binary metal phosphate materials to obtain superior electrochemical efficiency with a high value of ED and PD. Binary metal phosphate-based SCs are a novel incoming class of EC and

are likely to offer high charging-discharging rates with high ED. Enhancements in the C_s , ED and operating potential window of binary metal phosphate-based electrodes considerably extend the whole electrochemical efficiency of the SC. Additionally, the deficiency of one active (nickel) material can be accomplished by another active (copper) material, and synergy between both (nickel copper phosphate) materials can outcome in increased electrochemical performance. With their high electrical conductivity and multiple oxidation states, the nickel and copper promote C_s , ED and PD of SC devices consisting of aqueous or neutral electrolytes.

In preparation of such electrode materials, a simple, convenient and inexpensive synthetic approach to retain the cost of SC cells is essential. Among various other deposition techniques, SILAR and hydrothermal methods have lots of advantages. These two methods are facile to handle, cheap and helpful to deposit materials on a large scale area. These methods offer desired material characteristics such as surface morphology, crystal structure and optimum film thickness. Chemical methods give well adherent, uniformly, and pinhole-free deposited thin films. The nucleation and growth in chemical systems play an important part in the formation of nanocrystalline materials. Also, these methods are utilized for large area deposition, which is favourable for device fabrication.

Therefore, a new class of nickel copper phosphate based electrode materials can be prepared, and ASDs can be constructed using polymer gel electrolytes. Metal phosphates (nickel phosphate, copper phosphate, nickel copper phosphate) with different morphologies could be synthesized by simple chemical methods and applied as electrode materials in SCs. The goal behind fabrication of asymmetric SCs is to examine the feasibility of active electrode material at the device level. Our prior aim of the present work is a facile synthesis of nickel copper phosphate thin films by chemical methods and characterization with different physico-chemical techniques. The chemical methods (SILAR and hydrothermal) can offer additive-less and binder-free thin film electrodes, which can increase the interfacial contact between SS substrates and active material. The oxidation and corrosion of metallic substrates can be controlled utilizing low temperature deposition methods. Preparative factors such as deposition time, concentration of precursor, pH of solution, and deposition temperature are controlled in chemical methods. Moreover, uniform and adherent nickel copper phosphate thin films are characterized for phase analysis, structural explication,

compositional analysis, surface and morphological analysis. The phase confirmation of material is carried out by X-ray diffraction (XRD) technique. Chemical bonding in material is examined by fourier transform infrared spectroscopy analysis (FT-IR). Surface morphology of prepared thin film is visualized by field emission scanning electron microscopy (FE-SEM) technique. The elemental composition of synthesized thin films is recognized by energy dispersive X-ray spectroscopy (EDS) technique. Prepared material confirmation, available chemical composition and oxidation states of thin film are done with X-ray photoelectron spectroscopy (XPS) technique. The electrochemical properties of prepared thin films are investigated by cyclic voltammetry (CV), galvanostatic charge-discharge (GCD) and electrochemical impedance spectroscopy (EIS) techniques. Three electrode cell configuration is employed for the electrochemical study of single electrodes in 1 M KOH electrolyte, where prepared thin films are used as working electrode, platinum plate as a counter and mercury/mercury oxide (Hg/HgO) as a reference electrode. Furthermore, the performance of prepared thin films is estimated in terms of a potential window, C_s , specific energy, specific power and cyclic life.

The main purpose of research is to fabricate asymmetric aqueous and solid state SC devices using nickel copper phosphate thin films as an active cathode material with KOH and PVA-KOH gel electrolyte, respectively. The activity of electrode material and the utility of electrolytes are studied by fabricating aqueous and SSD. The performances of ASDs are examined in terms of capacitance, ED and PD, and cyclic stability. Lastly, conclusions are evaluated based on the performance of nickel copper phosphate based devices.

1.6 References:

1. P. Simon, Y. Gogotsi, *Nat. Mater.*, 7, (2008), 845-854.
2. N. Kumar, J-B Baek *Chem. Commun.*, 50, (2014), 6298-6308.
3. G. Zhou, L. Xu, G. Hu, L. Mai, Yi Cui, *Chem. Rev.*, 119, (2019), 11042-11109.
4. Y. Zhu, J. Li, J. Liu, *J. Power Sources*, 351, (2017), 17-25.
5. Z. Zhang, X. Zhang, W. Chen, Y. Rasim, W. Salman, H. Pan, Y. Yuan, C. Wang, *Appl. Energy*, 178, (2016), 177-188.
6. A. Shukla, S. Sampath, K. Vijayamohanan, *Curr. Sci.*, 79, (2000), 1656-1661.
7. A. Burke, *J. Power Sources*, 91, (2000), 37-50.
8. S. Maiti, A. Pramanik, S. Chattopadhyay, G. De, S. Mahanty, *J. Colloid Interf. Sci.*, 464, (2016), 73-82.
9. H. Jung, H. Wang, T. Hu, *J. Power Sources*, 267, (2014), 566-575.
10. C. Zhou, Y. Zhang, Y. Li, J. Liu, *Nano Lett.*, 13, (2013), 2078-2085.
11. T. Pandolfo, V. Ruiz, S. Sivakkumar, J. Nerkar, In *Supercapacitors: Materials, Systems, and Applications*; Wiley-VCH Verlag GmbH & Co. KGaA, 2013; pp 69-109.
12. S. Zhang, N. Pan, *Adv. Energy Mater.*, 5, (2015), 1401401.
13. W. Raza, F. Ali, N. Raza, Y. Luo, Ki-H Kim, J. Yang, S. Kumar, A. Mehmood, E. Kwon, *Nano Energy*, 52, (2018), 441-473.
14. F. Beguin, V. Presser, A. Balducci, E. Frackowiak, *Adv. Mater.*, (2014), 26, 2219-2251.
15. R. Burt, G. Birkett, X. Zhao, *Phys. Chem. Chem. Phys.*, 16, (2014), 6519-6538.
16. J. Kang, J. Wena, S. Jayaram, A. Yu, X. Wang, *Electrochim. Acta*, 115, (2014), 587-598.
17. R. A. Rightmire, Electrical energy storage apparatus. U.S., Patent 3288641 (1966).
18. S. Trasatti, G. Buzzanca, *J. Electroanal. Chem. Interf. Electrochem.*, 29, (1971), A1-A5.
19. B. Conway, *J. Electrochem. Soc.*, 138, (1991), 1539-1548.
20. Y. Shao, M. El-Kady, J. Sun, Y. Li, Q. Zhang, M. Zhu, H. Wang, B. Dunn, R. Kaner, *Chem. Rev.*, 118, (2018), 9233-9280.
21. J. Miller, *Market and Applications of Electrochemical Capacitors. Supercapacitors*; Wiley-VCH Verlag GmbH & Co. KGaA, 2013; pp 509-526.
22. J. Long, *J. Electrochem. Soc.*, 162, (2015), Y3-Y3.
23. G. Gund, D. Dubal, S. Jambure, S. Shinde, C. Lokhande, *J. Mater. Chem. A*, 1, (2013), 4793-4803.
24. J. Niu, W. Pell, B. Conway, *J. Power Sources*, 156, (2006), 725-740.
25. L. Zhang, X. Zhao, *Chem. Soc. Rev.*, 38, (2009), 2520-2531.
26. C. Lokhande, D. Dubal, O. Joo, *Curr. Appl. Phys.*, 11, (2011), 255-270.
27. H. Pang, X. Li, Q. Zhao, H. Xue, W. Lai, Z. Hu, W. Huang, *Nano Energy*, 35, (2017), 138-145.
28. L. Miao, H. Duan, M. Liu, W. Lu, D. Zhu, T. Chen, L. Li, L. Gan, *Chem. Eng.*, 317, (2017), 651-659.
29. G. Wang, H. Wang, X. Lu, Y. Ling, M. Yu, T. Zhai, Y. Tong, Y. Li, *Adv. Mater.*, 26, (2014), 2676-2682.
30. X. Lu, M. Yu, G. Wang, Y. Tong, Y. Li, *Energy Environ. Sci.*, 7, (2014), 2160-2181.
31. T. Chen, L. Dai, *Mater. Today*, 16, (2013), 272-280.
32. W. Wang, S. Wu, *Appl. Surf. Sci.*, 396, (2017), 1360-1367.

33. X. Li, Y. Zhao, Y. Bai, X. Zhao, R. Wang, Y. Huang, Q. Liang, Z. Huang, *Electrochim. Acta*, 230, (2017), 445-453.
34. M. Stoller, S. Park, Y. Zhu, J. An, R. Ruoff, *Nano Lett.*, 8, (2008), 3498-3502.
35. M. Vangari, T. Pryor, Li. Jiang, *J. Energy Eng.*, 139, (2013), 72-79.
36. B. Zhang, W. Li, J. Sun, G. He, R. Zou, J. Hu, Z. Chen, *Mater. Lett.*, 114, (2014), 40-43.
37. W. Li, G. He, J. Shao, Q. Liu, K. Xu, J. Hu, I. P. Parkin, *Electrochim. Acta*, 186, (2015), 1-6.
38. W. Chen, R. Rakhi, L. Hu, X. Xie, Y. Cui, H. Alshareef, *Nano Lett.*, 11, (2011), 5165-5172.
39. M. Jayalakshmi, K. Balasubramanian, *Int. J. Electrochem. Sci.*, 3, (2008), 1196-1217.
40. E. Frackowiak, F. Beguin, *Carbon*, 39, (2001), 937-950.
41. Z. Wen, W. She, Y. Li, R. Che, *J. Mater. Chem. A*, 2, (2014), 20729-20738.
42. W. Chen, R. Rakhi, H. Alshareef, *Nanoscale*, 5, (2013), 4134-4138.
43. J. Xu, T. Xiao, X. Tan, P. Xiang, L. Jiang, D. Wu, J. Li, S. Wang, *J. Alloys Compd.*, 706, (2017), 351-357.
44. L. Xing, K-J. Huang, L-X. Fang, *Dalton Trans.*, 45, (2016), 17439-17446.
45. S. Lyu, H. Chang, F. Fu, L. Hu, J. Huang, S. Wang., *J. Power Sources*, 327, (2016), 438-446.
46. K. Naoi, P. Simon, *Electrochem. Soc. Interface*, 17, (2008), 7-34.
47. J. Shayeh, M. Sadeghinia, S. Siadata, A. Ehsani, M. Rezaeid, M. Omid, J. *Colloid Interface Sci.*, 496, (2017), 401-406.
48. A. Muzaffara, M. Ahamed, K. Deshmukha, J. Thirumalai, *Renew. Sustain. Energy Rev*, 101, (2019), 123-145.
49. N. Chodankar, H. Pham, A. Nanjundan, J. Fernando, K. Jayaramulu, D. Golberg, Y. Han, D. Dubal, *Small*, 16, (2020), 2002806.
50. O. Ghodbane, J-L. Pascal, F. Favier, *ACS Appl. Mater. Interfaces*, 5, (2009), 1130-1139.
51. S. Devaraj, N. Munichandraiah, *J. Phys. Chem. C*, 112, (2008), 4406-4417.
52. V. Augustyn, P. Simon, B. Dunn, *Energy Environ. Sci.*, 7, (2014), 1597-1614.
53. S. Pawar, B. Pawar, J. Kim, O. Joo, C. Lokhande, *Curr. Appl. Phys.*, 11, (2011), 117-161.
54. J. Cook, T. Lin, H-S. Kim, A. Siordia, B. Dunn, S. Tolbert, *ACS Nano*, 13, (2019), 1223-1231.
55. Y. Wang, Y. Song, Y. Xia, *Chem. Soc. Rev.*, 45, (2016), 5925-5950.
56. H. Li, M. Yu, F. Wang, P. Liu, Y. Liang, J. Xiao, C. Wang, Y. Tong, G. Yang, *Nat. Commun.*, 4, (2013), 1-7.
57. D. Cericol, R. Kotz, *Electrochim. Acta*, 72, (2012), 1-17.
58. S. Bose, T. Kuila, A. K. Mishra, R. Rajasekar, N. H. Kim, J. H. Lee, *J. Mater. Chem.*, 22, (2012), 767-784.
59. M. Zhi, C. Xiang, J. Li, M. Li, N. Wu, *Nanoscale*, 5, (2013), 72-88.
60. H. Jiang, P. S. Lee, C. Li, *Energy Environ. Sci.*, 6, (2013), 41-53.
61. Y. Li, S. Zhang, Q. Yu, *Adv. Mater. Res.*, 750-752, (2013), 894-898.
62. L. Zhang, X. Zhao, *Chem. Soc. Rev.*, 38, (2009), 2520-2531.
63. J. Knox, B. Kaur, G. Millward, *J. Chromatogr. A*, 352, (1986), 3-25.
64. J. Lee, J. Kim, T. Hyeon, *Adv. Mater.*, 18, (2006), 2073-2094.
65. Y. Zhai, Y. Dou, D. Zhao, P. Fulvio, R. Mayes, S. Dai, *Adv. Mater.*, 23, (2011), 4828-4850.

66. C. Xu, Z. Li, C. Yang, P. Zou, B. Xie, Z. Lin, Z. Zhang, B. Li, F. Kang, C. Wong, *Adv. Mater.*, 28, (2016), 4105-4110.
67. M. Zhang, Q. Zhou, J. Chen, X. Yu, L. Huang, Y. Li, C. Li, G. Shi, *Energy Environ. Sci.*, 9, (2016), 2005-2010.
68. Z. Zhang, J. Deng, X. Li, Z. Yang, S. He, X. Chen, G. Guan, J. Ren, H. Peng, *Adv. Mater.*, 27, (2015), 356-362.
69. Y. Li, G. Ren, Z. Zhang, C. Teng, Y. Wu, X. Lu, Y. Zhu, L. Jiang, *J. Mater. Chem. A*, 4, (2016), 17324-17323.
70. G. Cai, P. Darmawan, M. Cui, J. Wang, J. Chen, S. Magdassi, P. Lee, *Adv. Energy Mater.*, 6, (2016), 1501882.
71. L. Zhang, D. Shi, T. Liu, M. Jaroniec, J. Yu, *Mater. Today*, 25, (2019), 35-65.
72. P. Kulal, D. Dubal, C. Lokhande, V. Fulari, *J. Alloys Compd.*, 509, (2011), 2567-2571.
73. Y. Jiang, L. Chen, H. Zhang, Q. Zhang, W. Chen, J. Zhu, D. Song, *Chem. Eng. J.*, 292, (2016), 1-12.
74. W. Wei, X. Cui, W. Chen, D. Ivey, *Chem. Soc. Rev.*, 40, (2011), 1697-1721.
75. S. Makino, T. Ban, W. Sugimoto, *J. Electrochem. Soc.*, 162, (2015), A5001-A5006.
76. D. Dubal, P. Gomez-Romero, B. Sankapal, R. Holze, *Nano Energy*, 11, (2015), 377-399.
77. Y. Zhang, L. Li, H. Su, W. Huang, X. Dong, *J. Mater. Chem. A*, 3, (2015), 43-59.
78. R. Bendi, V. Kumar, V. Bhavanasi, K. Parida, P. Lee, *Adv. Energy Mater.* 6, (2016), 1501833.
79. M. Sun, H. Liu, J. Qu, J. Li, *Adv. Energy Mater.* 6, (2016), 1600087.
80. X. Wang, H.-M. Kim, Y. Xiao, Y.-K. Sun, *J. Mater. Chem. A*, 4, (2016), 14915-14931.
81. F. Omar, A. Numan, N. Duraisamy, S. Bashir, K. Ramesh, S. Ramesh, *RSC Adv.*, 6, (2016), 76298-76306.
82. Y. Zhu, S. Murali, W. Cai, X. Li, J. W. Suk, J. Potts, R. Ruoff, *Adv. Mater.*, 22, (2010), 3906-3924.
83. C. Zheng, H. Yang, Y. Yang, *Mater. Trans.*, 58, (2017), 298-301.
84. N. Chen, J. Zhou, Q. Kang, H. Ji, G. Zhu, Y. Zhang, S. Chen, J. Chen, X. Feng, W. Hou, *J. Power Sources*, 344, (2017), 185-194.
85. Z. Luo, E. Liu, T. Hu, Z. Li, T. Liu, *Ionics*, (2015), 21, 289-294.
86. Y. He, X. Yang, Y. Bai, J. Zhang, L. Kang, Z. Lei, Z. Liu, *Electrochim. Acta*, 178, (2015), 312-320.
87. J. Theerthagiri, K. Thiagarajan, B. Senthilkumar, Z. Khan, R. Senthil, P. Arunachalam, J. Madhavan, M. Ashokkumar, *ChemistrySelect*, 2, (2017), 201-210.
88. P. Katkar, S. Marje, S. Pujari, S. Khalate, A. Lokhande, U. Patil, *ACS Sustainable Chem. Eng.*, 7, (2019), 11205-11218.
89. J. Hao, W. Li, X. Zuo, D. Zheng, X. Liang, Y. Qiang, B. Tan, B. Xiang, X. Zou, *J. Mater. Sci.*, 54, (2019), 625-637.
90. P. Katkar, S. Marje, S. Pujari, S. Khalate, P. Deshmukh, U. Patil, *Synth. Met.*, 267, (2020), 116446.
91. A. Joshi, P. Chanda, V. Singh, *Mater. Today: Proc.*, 32, (2020), 498-503.
92. D. Wang, Z. Fu, Y. Xu, X. Guo, F. Wang, W. Sun, P. Yin, Z. Yang, L. Yang, *Mater. Lett.*, 281, (2020), 128610.
93. S. Marje, P. Katkar, S. Pujari, S. Khalate, P. Deshmukh, U. Patil, *Mater. Sci. Eng. B*, 261, (2020), 114641.

94. J. Yang, J. Tan, D. Ma, J. Power Sources., 260, (2014), 169-173.
95. F. Omar, A. Numan, S. Bashir, N. Duraisamy, R. Vikneswaran, Y. Loo, K. Ramesh, S. Ramesh, Electrochim. Acta, 273, (2018), 216-228.
96. J. Li, M. Liu, L. Kong, D. Wang, Y. Hu, W. Han, L. Kang, RSC Adv., 5, (2015), 41721-41728.
97. J. Zhao, S. Wang, Z. Run, G. Zhang, W. Du, H. Pang, Part. Part. Syst. Charact., 32, (2015), 880-885.
98. C. Zhao, S. Wang, Z. Zhu, P. Ju, C. Zhao, X. Qian, J. Mater. Chem. A, 5, (2017), 18594-18602.
99. X. Peng, H. Chai, Y. Cao, Y. Wang, H. Dong, D. Jia, W. Zhou, Mater. Today Energy, 7, (2018), 129-135.
100. A. Mirghni, M. Madito, K. Oyedotun, T. Masikhwa, N. Ndiaye, S. Ray, N. Manyala, RSC Adv., 8, (2018), 11608-11621.
101. N. Padmanathan, H. Shao, K. Razeeb, ACS Appl. Mater. Interfaces, 10, (2018), 8599-8610.
102. H. Pang, Y. Zhang, Z. Run, W. Lai, W. Huang, Nano Energy, 17, (2015), 339-347.
103. K. Sankar, Y. Seo, S. Lee, S. Jun, ACS Appl. Mater. Interfaces, 10, (2018), 8045-8056.
104. M. Pramanik, R. Salunkhe, M. Imura, Y. Yamauchi, ACS Appl. Mater. Interfaces, 8, (2016), 9790-9797.
105. N. Chodankar, D. Dubal, S. Ji, D. Kim, Small, 15, (2019), 1901145.
106. B. Senthilkumar, Z. Khan, S. Park, K. Kim, H. Ko, Y. Kim, J. Mater. Chem. A, 3, (2015), 21553-21561.
107. S. Marje, P. Katkar, S. Pujari, S. Khalate, A. Lokhande, U. Patil, Synth. Met, 259, (2020), 116224.
108. C. Wei, C. Cheng, S. Wang, Y. Xu, J. Wang, H. Pang, Chem. Asian J., 10, (2015), 1731-1737.
109. H. Pang, C. Wei, Y. Ma, S. Zhao, G. Li, J. Zhang, J. Chen, S. Li, ChemPlusChem, 78, (2013), 546-553.
110. N. Chodankar, D. Dubal, S. Patil, G. Raju, S. Karekar, Y. Huh, Y. Han, Electrochim. Acta, 319, (2019), 435-443.
111. H. Pang, Z. Yan, Y. Wei, X. Li, J. Li, L. Zhang, J. Chen, J. Zhang, H. Zheng, Part. Part. Syst. Charact., 30, (2013), 287-295.
112. Y. Gao, J. Zhao, Z. Run, G. Zhang, H. Pang, Dalton Trans., 43, (2014), 17000-17005.
113. J. Zhao, H. Pang, J. Deng, Y. Ma, B. Yan, X. Li, S. Li, J. Chena, W. Wang, CrystEngComm, 15, (2013), 5950-5955.
114. Z. Wang, F. Chen, P. Kannan, S. Ji, H. Wang, Mater. Lett., 257, (2019), 126742.
115. B. Li, Y. Shi, K. Huang, M. Zhao, J. Qiu, H. Xue, H. Pang, Small, 14, (2018), 1703811.
116. S. Pujari, S. Kadam, Y-R. Ma, P. Katkar, S. Marje, S. Khalate, A. Lokhande, U. Patil, J. Electron. Mater., 49, (2020), 3890-3901.
117. A. Karaphun, P. Chirawatkul, S. Maensiri, E. Swatsitang, J. Sol Gel. Sci. Technol., 88, (2018), 407-421.
118. A. Agarwal, B. Sankapal, Chem. Eng. J., 422, (2021), 130131.

CHAPTER-2

THEORETICAL BACKGROUND OF HYDROTHERMAL, SILAR METHOD AND THIN FILM CHARACTERIZATION TECHNIQUES

CHAPTER 2

Theoretical Background of Hydrothermal, SILAR Method and Thin Film Characterization Techniques

Sr. No.	Title	Page No.
2.1	Introduction to thin films	29
2.2	Hydrothermal method	31
	2.2.1 Theoretical background of hydrothermal method	31
	2.2.2 Basics of hydrothermal method	31
	2.2.3 Effect of preparative parameters	33
	2.2.4 Advantages of hydrothermal method	34
2.3	Successive ionic layer adsorption and reaction (SILAR) method	35
	2.3.1 Theoretical background of SILAR method	35
	2.3.2 Basics of SILAR method	36
	2.3.3 Effect of preparative parameters	40
	2.3.4 Advantages of SILAR method	41
2.4	Physicochemical characterization techniques	42
	2.4.1 X-ray diffraction (XRD)	42
	2.4.2 Fourier transform-infrared spectroscopy (FT-IR)	43
	2.4.3 Brunauer-Emmett-Teller (BET)	45
	2.4.4 X-Ray photoelectron spectroscopy (XPS)	47
	2.4.5 Field emission-scanning electron microscopy (FE-SEM)	48
	2.4.6 Energy dispersive X-ray spectroscopy (EDS)	50
2.5	Electrochemical characterization Techniques	51
	2.5.1 Cyclic voltammetry (CV)	52
	2.5.2 Galvanostatic charge-discharge (GCD)	53
	2.5.3 Electrochemical impedance spectroscopy (EIS)	54
2.6	References	57

2.1 Introduction to thin films:

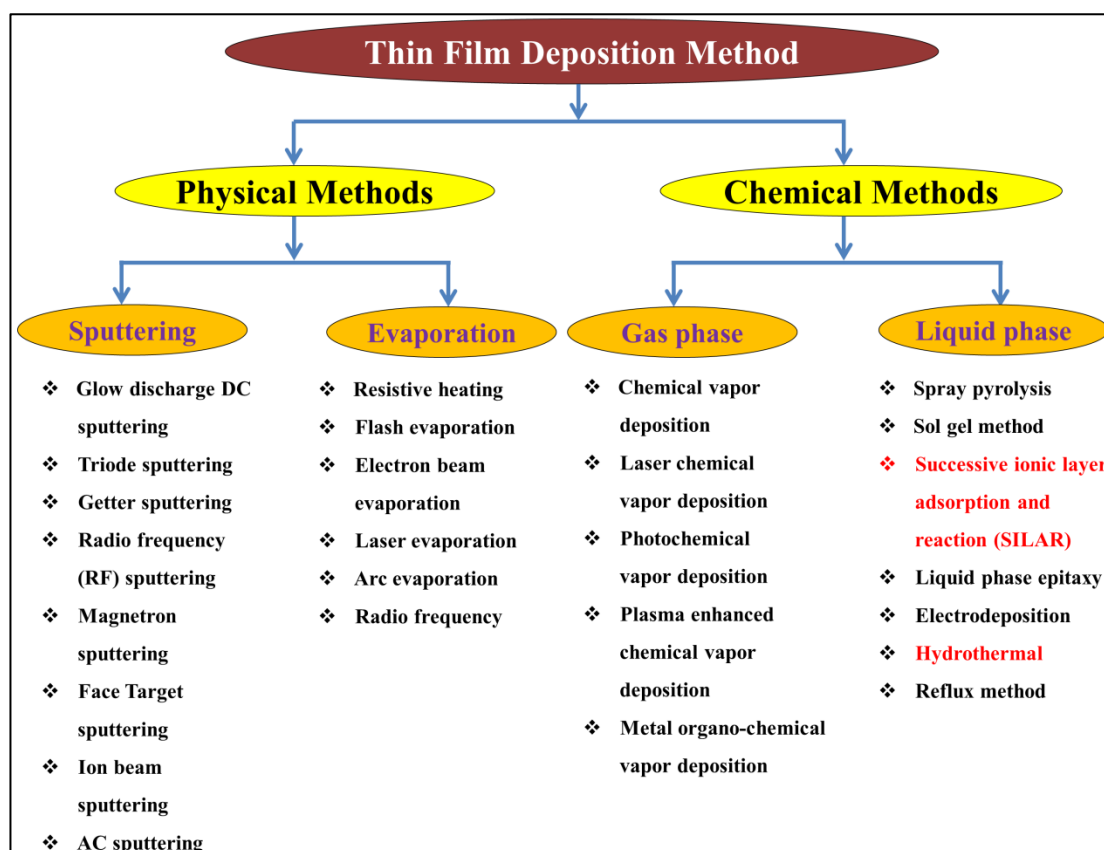
Nowadays, the attention of researchers is focused on thin film technology due to its unique electrical, optical and magnetic properties and its usage in optoelectronic and electronic storage devices [1, 2]. In the fields of energy storage (e.g. batteries), generation (e.g. solar cells) and conversion (e.g. water splitting), material synthesis with desired properties plays a crucial role. In all the above mentioned research areas, different materials are synthesized mostly in two forms: 1) bulk form (powder) and 2) thin film form. The usage of electrically insulating binding agents hinders the actual electrochemical performance of powder material. Thus, the direct deposition of active material on the conducting backbone in thin film form has attracted the attention of many researchers.

Any liquid or solid system that possesses at most 2-D order or periodicity is known as thin film or a surface bounded between two parallel planes extending infinitely in two directions restricted in the dimension along the third direction is called a thin film. Thin film is a layer of material with a thickness of few micrometres, or the process of thin film synthesis on any substrate is called a thin film deposition method. The process of thin film synthesis on any substrate is called a thin film deposition method. The extensive classification of thin film deposition methods is listed in **Chart 2.1**. There are two primary ways to develop nanomaterials in thin film forms: physical and chemical methods. The first approach is to start with bulk material and then break it into smaller pieces using mechanical or other forms of energy (top-down). An opposite way is to synthesize the material from molecular or atomic species via chemical reactions, allowing the precursor particles to grow in size (bottom-up). The recent technologies require various types of thin films for a variety of applications due to their scientific curiosity and potential technical values. The properties such as; a) particle composition, b) particle size, c) particle shape and e) degree of particle agglomeration affects their performance in a particular application. Numerous traditional chemical and novel routes of preparation (bulk/thin films) allow materials to be in nanocrystalline form.

The physio-chemical properties of materials can be modified mostly in thin film form compared with their bulk counterpart. Nanocrystalline thin film materials provide advantages like lower thermal conductivity, higher electrical conductivity, large surface area, and enhanced diffusivity [3]. In general, the properties of thin films are

dependent on the method of deposition. The physical techniques are subdivided into vacuum and sputtering. The deposition performed after the material to be deposited is moved to a gaseous state either by evaporation or an impact procedure. In chemical methods, there are also two branches. One branch is the gas phase, and it contains various types like conventional chemical vapor deposition (CVD), laser chemical vapor deposition (LCVD), photo CVD, plasma enhanced CVD and metal organo-chemical vapor deposition (MOCVD). Another branch is liquid phase which include spray pyrolysis, sol gel process, SILAR, liquid phase epitaxy, electrodeposition, hydrothermal, reflux method, etc. However, physical and gas-phase chemical deposition has some drawbacks, such as sophisticated instrumentation and maintenance, high working temperature and pressure, material wastage, and high cost. On the other hand, the solution phase chemical methods are facile, low cost, economic and convenient for large area deposition of various materials [4, 5]. Therefore, chemical methods are extensively used to prepare nanostructured materials in thin film form for various applications.

Chart 2.1: Classification of thin film deposition method.



2.2 Hydrothermal method:

2.2.1 Theoretical background of hydrothermal method:

A hydrothermal method has been the most efficient and popular method it gathers much interest from researchers and technologists from various fields. The concept of hydrothermal is purely originated from a geological term. The term 'hydrothermal' is described from the Greek words 'hydros' and 'thermos', which defines water and heat. British Geologist Sir Roderick Murchison (1792-1871) used this word for the first time to represent water activity at high temperature and pressure for modifications in the earth crust, which resulted in the production of many minerals and rocks [6, 7]. In the presence of water, elevated temperature, and pressure, most minerals created in metasomatic and post-magmatic phases are considered by hydrothermal origin. It is generally known that, the higher single crystal created in nature (>100 gm of beryl crystals) and number of the highest amount of single crystal formed by man in one experimental run (many hundreds of grams of quartz crystal) both have a hydrothermal origin. Although hydrothermal technique has achieved tremendous development, there is still no unanimity in its evaluation. In the hydrothermal process, heterogeneous reaction executed in aqueous solvents or minerals at elevated temperature and pressure, re-crystallize and dissolve in moderately insoluble materials under standard conditions. As reported by Morey and Niggli (1913), "In a hydrothermal method, the mechanisms are exposed to action of water at temperatures normally close or slightly above critical temperature of water (~370 °C) in closed bombs, and consequently below higher pressure prepared by such solutions" [8]. Lobachev defined it as, "A method where crystallization is carried out from superheated aqueous solution at high pressure" [9]. Laudise [10] defined it as, "hydrothermal growth implies growth from aqueous solution at ambient or nearby ambient conditions." Yoshimura [11] defined it as, "reactions taking place under the conditions of high temperature and pressure (>100 °C, >1 atm) in aqueous solutions under a closed system". Rabenau in 1985 defined as, "hydrothermal synthesis as the heterogeneous reactions in aqueous media above 100 °C temperature and 1 bar pressure" [12].

2.2.2 Basics of hydrothermal method:

Nowadays, some chemical reactions in the existence of minerals or water under pressure and temperature conditions are called hydrothermal reaction processes. The

preparation of nanomaterials by hydrothermal method provides numerous advantages over other conventional methods. It offers a synthesis of various dimensional nanomaterials relevant to the cost effective for instrumentation, precursors salt and energy used. Significant features of the hydrothermal method, such as heat capacity, ionic product, dielectric constant, thermal conductivity, and viscosity, depend on extreme pressure and temperature. The stoichiometric control is less for the materials synthesized at higher temperature reaction processes due to volatilization of components and stress-induced defects caused by phase transformations. But, a relatively low temperature hydrothermal process can prevent such undesirable problems and provides the capability to precipitate the powders directly from the solution; also, uniformity of nucleation regulates the rate, ageing and growth, which impact the size, aggregation control and morphology. Hydrothermal methods can synthesise materials with different particle sizes and morphologies that can be obtained by varying different growth parameters.

Pressure-temperature interchange is one of the well-known physical processes in hydrothermal solution, and due to that, it isn't easy to synthesize various phases of the materials [13]. The main consideration of researchers about hydrothermal experiments is that the system should operate reliably under extreme pressure-temperature conditions [7]. **Figure 2.1** exhibits a conventional hydrothermal synthesis process, where precursors are directly dissolved in a water bath. The bath is placed in an autoclave, which can endure high temperature and pressure. A reaction container/vessel called an autoclave is desired for crystal growth under hydrothermal conditions. The autoclave is enclosed and heated to the requisite temperature, and most of the time, pressure is self-generated. The pressure greater than several hundred bars can be simply achieved even at low temperatures and is dependent on the degree of autoclave filling. The extreme temperature and pressure can be as high as 1273 K and 500 bar. For commercial applications, a purpose temperature under 773 K is generally preferred [14]. Temperature fluctuations due to the rise in temperature of the growth medium which leads to a higher dissolution rate. This method is also favourable to the industrial production of morphologically controlled materials with desired shape and size.

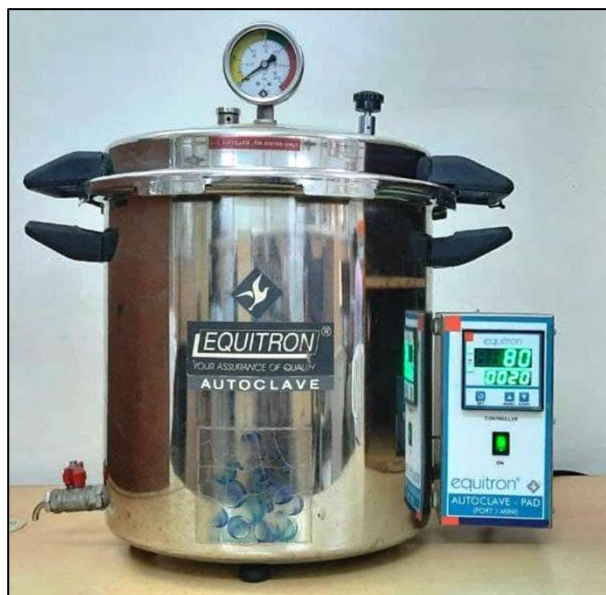


Figure 2.1: The photograph of programmable hydrothermal equipment used for preparation of thin films.

2.2.3 Effect of preparative parameters:

The deposition of thin film with well uniform and adherent nature by hydrothermal method depends on rate of the chemical reaction. The number of nucleation centres responsible for the rate of deposition and thickness of thin film. Different parameters decide growth kinetics of film, such as the nature of substrate, precursors, temperature and pressure, pH, and complexing agent. Effect of preparative parameters on growth mechanism is discussed below;

a) Nature of substrate:

The creation of thin film strongly depends on the reaction kinetics and film adhesion. The substrate surface is very significant for nucleation and further growth since it provides nucleation centres as an essential building block. Therefore, substrate purification is a primarily important step in the method of thin film preparation. The high deposition rate and terminal thickness can be achieved when the lattice parameters of substrates and growing material match well with each other. However, for thin film deposition, any kind of substrates such as conducting (SS) and non-conducting (glass) substrates can be used with the only condition that they should provide a nucleation centre.

b) Temperature & pressure:

Temperature and pressure is another very important parameter which influences the reaction rate of a bath. The rise in bath temperature and pressure enhances the

diffusion rate and increases ionic mobility, consequently the increase bath reaction rate. As a result, the film thickness increases until specific reaction temperature and pressure; after that, the film thickness decrease. At high temperatures and pressure, the high reaction rate in solution creates more precipitate, reducing the thin film thickness.

c) pH of solution:

The supersaturation condition determines the rate of chemical reaction as well as the rate of deposition. As the pH value of the reaction bath increases, the metal complex usually becomes more stable by reducing the availability of free metal ions, which will decrease the reaction rate resulting in higher terminal thickness.

d) Complexing agent:

In hydrothermal method, most of the depositions are executed in alkaline solution. Therefore, to avoid the precipitation of metal ions, a complexing agent is added. It helps to decrease the concentration of free metal ions in solution bath, which prevent the rapid bulk formation of the desired product. A high concentration of complexing agents decreases the concentration of free metal ions.

2.2.4 Advantages of hydrothermal method:

The hydrothermal synthesis method gives many advantages, which are listed below: [15, 16]

- This procedure is eco-friendly since it is conducted in an enclosed system, and contents can be reutilized and retrieved after cooling down to ambient temperature.
- By controlling the hydrothermal pressure and temperature, different crystalline products and crystal structures can be achieved.
- The processing and equipment required are easier and consumes low energy.
- The morphology and crystalline size can be modified to nanoscale simply by changing the preparative parameters, e.g. pH, temperature, deposition time, precursor concentration, etc.
- A hydrothermal method is unique for the preparation of thermodynamically metastable phases.
- A variety of particle sizes and morphologies are possible through hydrothermal technique.

- This method is also favourable for the industrial production of morphologically controlled materials.

2.3 Successive ionic layer adsorption and reaction (SILAR) method:

2.3.1 Theoretical background of SILAR method:

SILAR is one of the latest solution methods for the deposition of thin film, also known as a modified version of the CBD process. In CBD method, the cations and anions are represented in the same chemical bath, while in SILAR method, separate chemical baths are prepared from cationic and anionic precursor solutions. Thus, SILAR is a low-cost, simple, and hence low energy consumption method that is beneficial for preparing uniform, large area and well adherent thin films.

SILAR process was developed for thin films preparation in the mid-1980s [17-22]. The name SILAR was first given to this method by Nicolau [23]. In 1985, Ristov et al. [24] developed a new chemical method for the deposition of oxide thin film by using SILAR technique. The distinguishing property of SILAR is the usage of alternating cationic solution (a metal salt solution) and anionic solution (a hydrolyzing solution) baths. In principle, this is the purpose to allow ion-by-ion growth of the thin film via sequential addition of separate atomic layers.

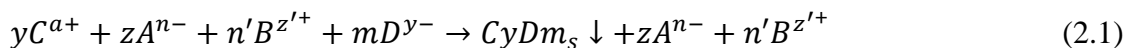
In most chemical methods, a thin film is generated on a substrate when heterogeneous precipitation performs on a substrate surface, and homogeneous precipitation performs in a precursor solution or bath. Nevertheless, the chemical method exhibits an unwanted precipitate formation in precursor solution and can't be eliminated. To avoid such a problem, the CBD method is modified and reported in a new method known as the SILAR method. **Figure 2.2** and **2.6** shows the schematic presentation and actually used of SILAR method, respectively. In modified method, thin films are made from the insertion of a substrate in specifically positioned cationic and anionic precursors, and the substrate is washed with ion-exchange water during every immersion.

The theoretical background and basics of SILAR are reported with details in the review article of Pathan and Lokhande [25]. The SILAR method depends on pre-adsorption followed by reaction of ions in precursors solution and rinsing in double distilled water (DDW) during every immersion. Pre-adsorption is an essential backbone of the SILAR system. It is predicted that the contact between heterogeneous phases expedited the growth of material. Liquid-solid, gas-solid, and gas-liquid are

three adsorption systems. SILAR system utilized in this work concerned on adsorption in a liquid-solid system. Adsorption is a surface phenomenon generated by attractive forces (Van-der Waals or chemical attractive or cohesive forces) among surface of a substrate and solution of ions. Due to Van-der Waals or chemical attractive or cohesive forces, the cations adsorbed on a substrate surface are significant to the formation of a monolayer. In the reaction process, the adsorbed ion reacted with anions aimed at the desired material's monolayer formation. By repeating such cycles, layer-by-layer formation of film occurs on the substrate surface. The adsorption process depends on the physical preparative parameters like the nature of substrate, temperature, the concentration of a solution, area of a substrate, etc.

2.3.2 Basics of SILAR method:

The SILAR process is aimed to grow $CyDm$ type through a heterogeneous chemical reaction on the solid surface via a reaction among adsorbed yC^{a+} (cations) and mD^{y-} (anion) as per following reaction,



With, $my = nz = n'z'$.

Where, C cation (Cu^+ , Ni^{2+} , Co^{2+} , Mn^{2+} , Fe^{3+} , etc.); y : number of cations, a^+ : numerical value of charge on cation, A : an ion in cationic precursors having a negative charge ($A = NO_3^{2-}$, Cl^{2-} , SO_4^{2-} , etc.) z : represent the number of A in cationic precursors, and n is the numerical value of charges on A . z' : the numerical value of charge on B , B : the ion in anionic precursor having a positive charge, n' : number of B in the anionic solutions, D : represent the anion (O^- , OH^- and PO_4^{3-}), m : the number of anions and y^- is charge on D .

Basically, the SILAR method works in four beakers system, which is generally used to deposition of metal oxide and sulfide films. However, this system has been modified into a three-beaker system for deposition of binary metal phosphate films.

Figure 2.2: displays a schematic of the experimental setup of SILAR in 3 steps.

The first and second beakers contain cationic and anionic precursors, respectively, whereas the third beaker contains DDW for rinsing purposes. Thus, the substrate is successively immersed in separate beakers one by one during the deposition process beginning from 1st.

1. Adsorption:

In this first step of SILAR process, when the substrate is dipped into a cationic precursor, different layers of charges are formed on its surface (**Figure 2.2** and **2.3**). Nearest to the substrate, a very thin layer is formed of solvent molecules (water molecules in the current case) called as an inner layer. This inner layer sometimes contains other species called specifically adsorbed anions [26].

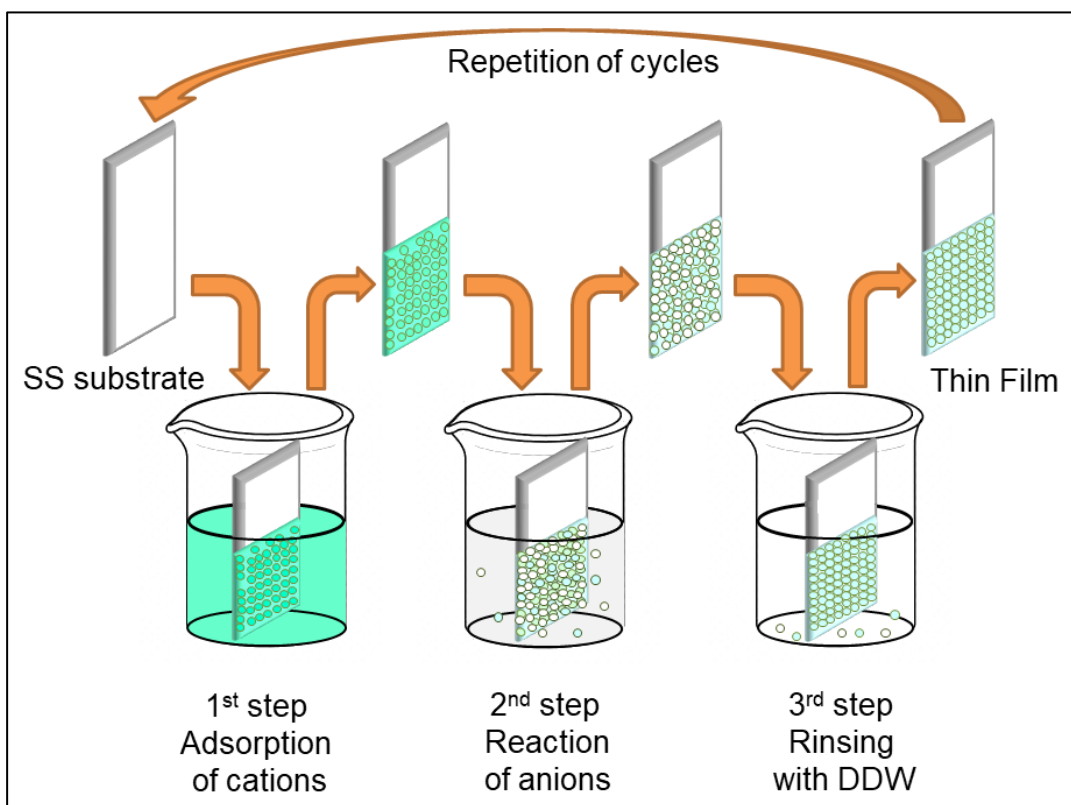


Figure 2.2: Schematic illustration of SILAR method.

The points of the electrical centres of these specifically adsorbed anions are called as inner Helmholtz plane (IHP). The solvated (complexed by solvent molecules or solvated ions are surrounded) cations present in solution closer to the substrate and get adsorbed on to surface for charge equilibrium. This adsorption is possible because of the Van-der Waals or chemical attractive or cohesive forces among them [25]. The location of points of these closest solvated cations is called the outer Helmholtz plane (OHP). From bulk of solution to OHP non-specifically adsorbed solvated cations are present. This layer of non-specifically adsorbed solvated cations is called as a diffuse layer. The thickness of this diffuse layer depends on the surface charge of the substrate. Surface charge of the substrate decides the thickness of this diffuse layer. In the CBD process anions and cations both are present in a single chemical bath hence

one could not eliminate the unwanted homogeneous precipitation. While in the SILAR method there is no chance of homogeneous precipitation until substrates are appropriately rinsed.

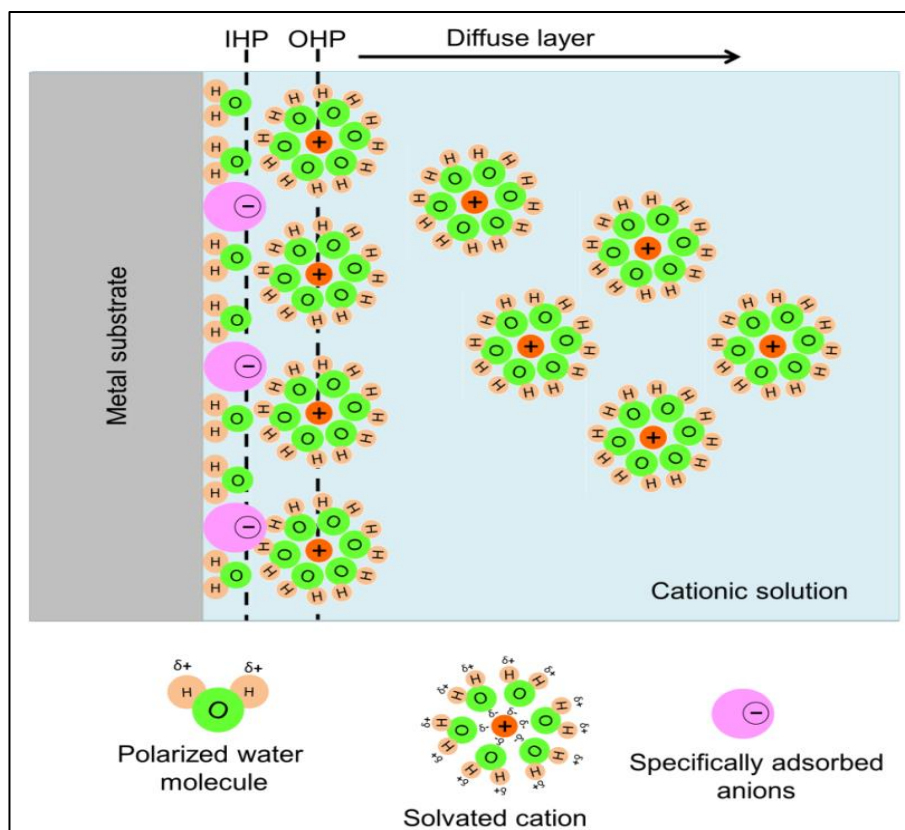


Figure 2.3: Schematic of development of Helmholtz double layer during 1st step of SILAR.

2. Reaction:

In this step, the chemical interaction among solvated adsorbed cations and anions is achieved by dipping the substrate in the solution to generate stable solid layer at the interface as shown in **Figure 2.4**. Some of the counter ions also get attached to this solid layer.

3. Rinsing:

In this last step, the unreacted and excess species and reaction by-products are eliminated. At this last step, a monolayer of targeted material grows uniformly on the substrate as exhibited in **Figure 2.5**.

These three steps combinly complete one SILAR deposition cycle. After few cycles, enough material is deposited on the substrate in the form of adherent and

uniform thin film. The standard of the thin film in SILAR method (in terms of uniformity, adherence, etc.) is strongly influenced by the adsorption, reaction and rinsing time.

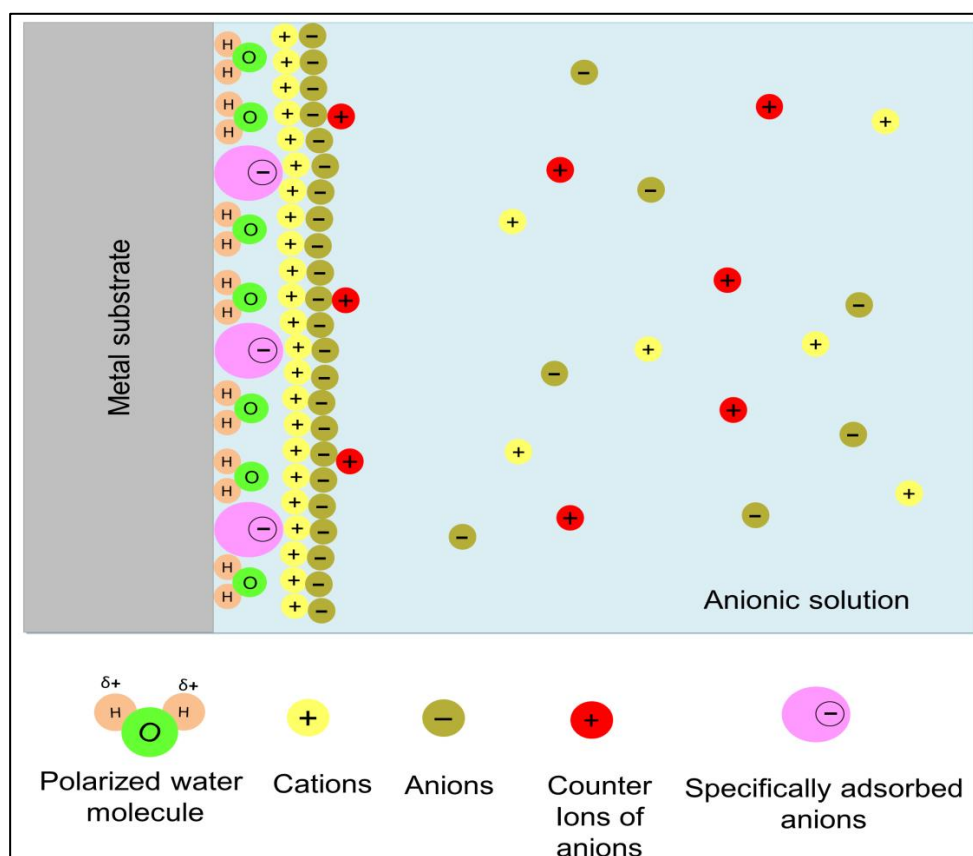


Figure 2.4: Schematic of development of water insoluble solid compound during 2nd step of SILAR.

In this study, many attempts were performed in order to obtain uniform and adherent deposition of material and eventually experimental parameters optimized by varying adsorption, reaction and rinsing time.

The SILAR deposition process can be operated by three ways,

1. Manual operation: In which dipping of the substrate in each beaker is carried out manually. So, this process is a time-consuming.
2. Computer-based operation: The computer program operates the translational and vertical movement of the spindle to which substrates are attached.
3. Microprocessor-based: The substrates are suspended to a horizontal robotic spindle in the vertical direction and a microprocessor regulates its movements in translational and vertical movements. Presently, a microprocessor-based SILAR instrument (displayed in **Figure 2.6**) is popular among researchers

because of its easy and facile operation settings, also applicability for the binary, ternary metal phosphate as well as composite materials synthesis.

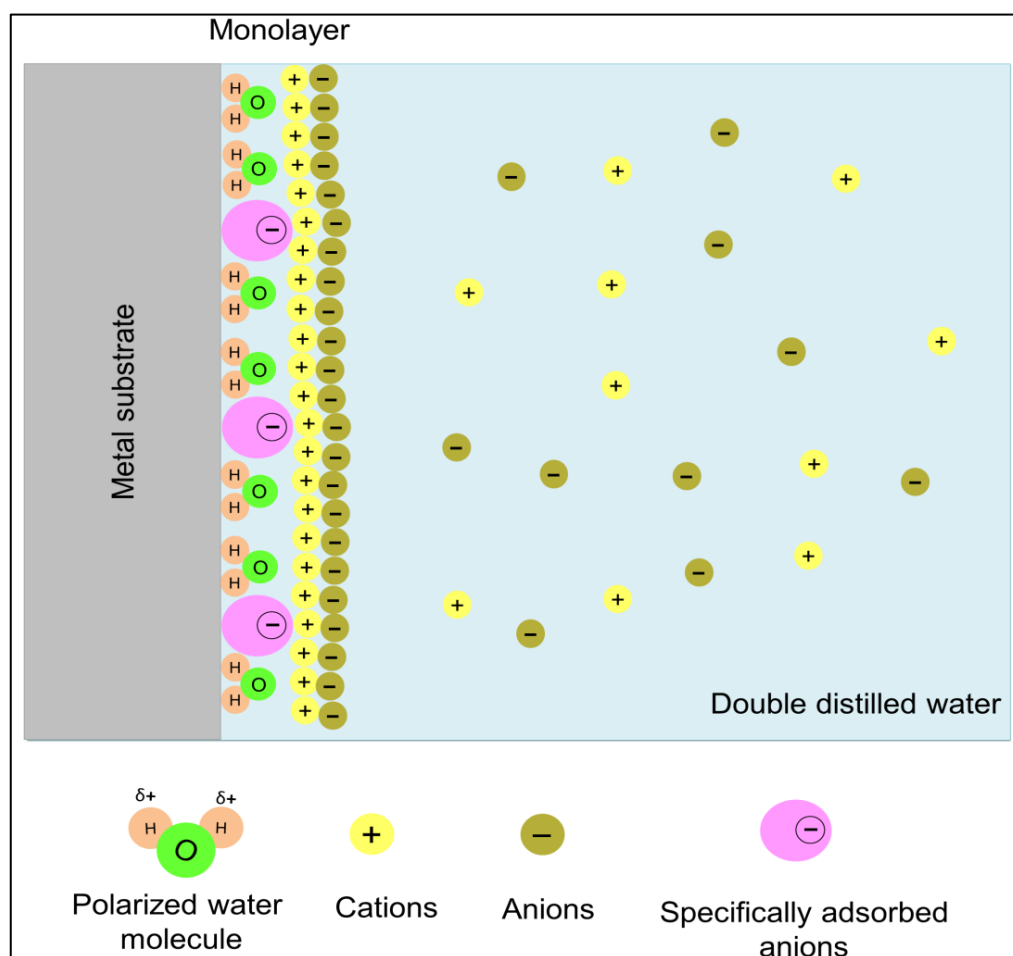


Figure 2.5: Schematic of formation of a monolayer of targeted material during 3rd step of SILAR.

2.3.3 Effect of preparative parameters:

In SILAR method, the growth kinetic depends on various parameters such as, substrate nature, ion concentration, adsorption, reaction, and rinsing time. The effect of different deposition parameters on film growth formation are discussed below:

a) Concentration of cation and anion:

From higher concentration of precursor solution thick film can be achieved while for lower concentration precursor solution non-uniform thin film with lower thickness can be obtained. Since, at lower concentration solution there is a deficiency of required number of ionic species for the superior quality of film. Also, stoichiometric formation of thin film can be obtained by changing precursor concentrations.



Figure 2.6: Photograph of programmable SILAR machine used for deposition of thin film electrode.

b) Adsorption and reaction time:

Adsorption and reaction time have the crucial role in the thin film production process. As the adsorption time is more than that of reaction time the film creation takes place by assorted reaction and it outcomes into higher terminal thickness. Equal adsorption time and reaction time, leads to consistent reaction and steady growth can give uniform film formation.

c) Rinsing Time:

To remove poorly bonded species from the substrate surface and to evade the precipitation in reaction bath, rinsing of substrate is required. A superior quality of thin film can be obtained by sufficient rinsing time.

2.3.4 Advantage of SILAR method:

Besides the simplicity, SILAR method has many advantages as given below:

- SILAR is a facile, inexpensive method and it is convenient for deposition over a large area.
- Foreign elements can be doped into thin film material by easily including it into the cationic solution.
- In several applications, the thickness of thin film plays a key role and it can be easily controlled in SILAR method by varying the deposition cycles.

- It is a low temperature process, so various kinds of substrates such as metal, semiconductor, insulator and polymer can be used. Also, it prevents oxidation or corrosion of metallic substrates.
- It does not need any sophisticated instrumentation.
- The deposition rate, film thickness and morphology can be effectively manipulated by changing the preparative conditions.
- There are practically no limitations on the substrate material and dimensions.

2.4 Physicochemical characterization techniques:

The effective performance of a material is strongly associated with its different physicochemical properties. Therefore, the characterization of material through different techniques and careful study of obtained results is essential task in the research field. The as-deposited thin film electrodes in the current study were examined through different material characterizations like XRD, FT-IR, BET, FE-SEM, EDS and XPS techniques.

2.4.1 X-ray diffraction (XRD):

XRD is a well-known analytical technique to get the information of crystallite phase and orientation of growth of the material [27]. Lattice parameters, grain size, strain, defect structure, epitaxy, structure identification and preferred orientation of the materials can be analysed by the XRD pattern. XRD is a fundamental non-destructive technique and gives detail information based on scattering of X-rays from the structures [28]. Due to improved detection methods of X-rays, commercial monochromators, and intense micro-focused X-ray source, the XRD technique is applicable to probe thin films of 100 Å thickness [29]. To identify the unknown material, obtained diffraction data is compared with American Standard for Testing of Materials (ASTM) or Joint Committee Powder Diffraction Standards (JCPDS) cards [30]. The intensities measured by XRD can give accurate and quantitative information about the atomic arrangements at interfaces (e.g. in multilayers). The basic principles of XRD are found in textbooks e.g. Tayler [31], Buerger [32], Cullity [30] and Guinier [33]. Schematic representation of diffractometer is exhibited in **Figure 2.7**, where 2θ is the angle between the incident and diffracted X-ray. Typically, diffraction pattern is provided by diffracted intensity with function of (2θ) orientation of specimen. The wavelength of X-ray is in the range of 0.7-2 Å with corresponding energies.

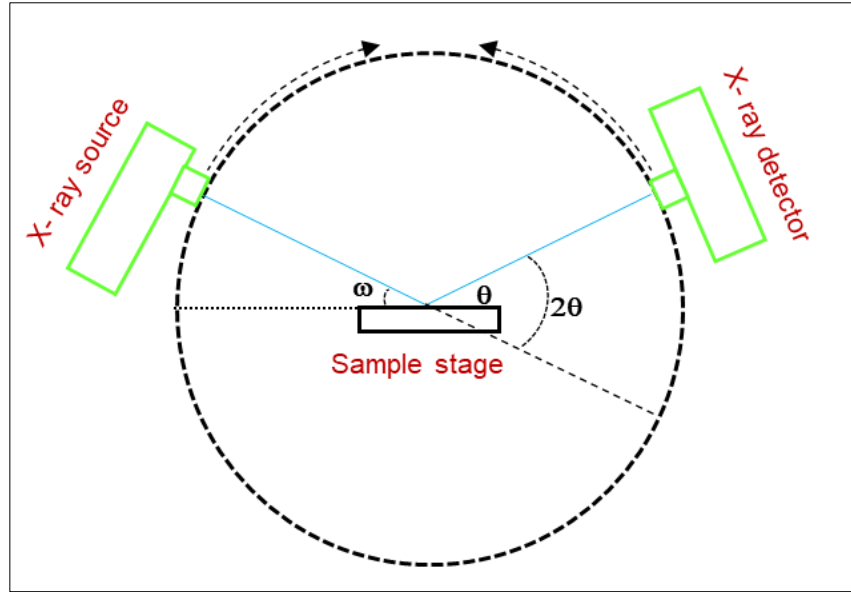


Figure 2.7: Schematic diagram of the XRD diffractometer.

For the structural investigation of thin films, several researchers have been using an XRD system. Monochromator is used in the XRD technique as a source of diffraction beam and X-ray beam diffracts from the film surface and detected by oscillating detector around the mean diffraction position. Monochromatic radiation is most significant in XRD technique for the analysis of accurate d-spacing from observed diffraction angles, according to Bragg's law as exhibited following equation [34],

$$2d \sin \theta = n\lambda \quad (2.2)$$

Where, d , λ , n and θ are the interplaner distance, wavelength of monochromatic X-ray, order of diffraction and θ is diffraction angle, respectively.

2.4.2 Fourier transform infrared spectroscopy (FT-IR):

FT-IR spectroscopy is powerful tools for identifying inter atomic forces and atomic arrangement in the crystal lattice. FT-IR can be utilize to analysis a wide range of materials in thin film or bulk forms, pastes, fibres, liquids, solids, powders and other forms. FT-IR spectroscopy is a technique that delivers information about the molecular structure or chemical bonding of materials, either organic or inorganic. It is used to recognize unknown materials present in a specimen. In an electromagnetic field, two energy levels (E_1 and E_2) are located in a material where energy level difference is equal to ' h ' times of incident radiation frequency (ν) and it is written as,

$$\Delta E = h\nu \quad (2.3)$$

The positive ΔE defines molecule absorbs energy; when ΔE is negative defines it emits energy in form of radiation, and thus emission spectrum is obtained. When equation 2.4 is satisfied, a unique spectrum for the molecule is found. The intensity plot versus frequency called as a spectrum and peaks found after the satisfaction of equation (2.4).

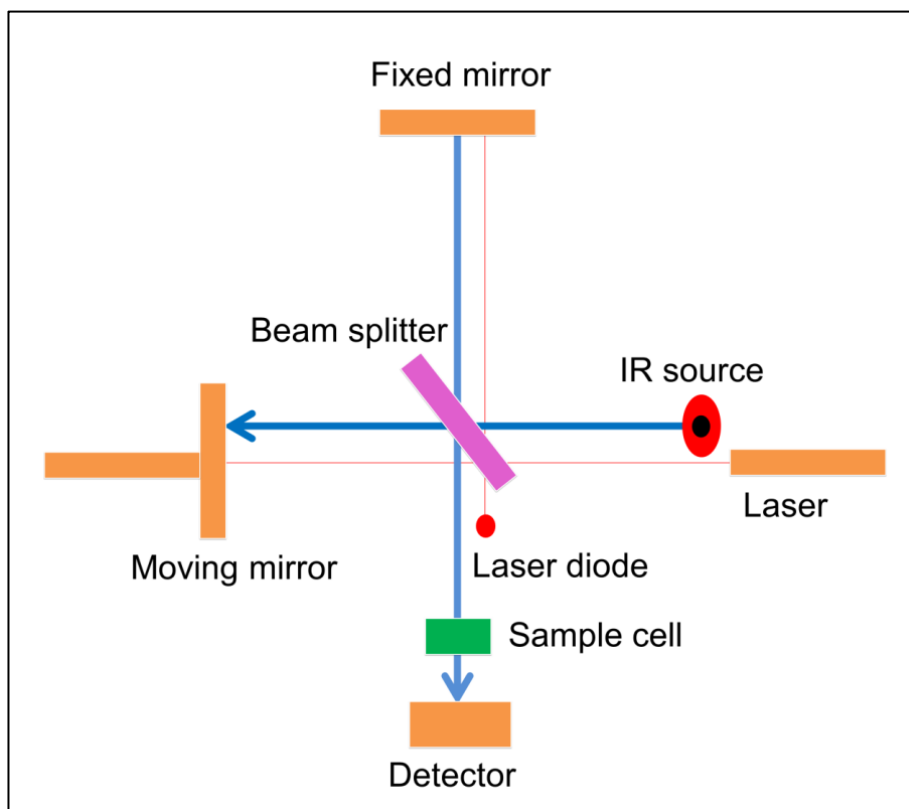


Figure 2.8: Basic ray diagram of FT-IR spectrometer.

In FT-IR analysis, a small portion of spectrum (near to visible) can be investigated, which includes UV, visible and IR regions (10^{-6} - 10^{-3} cm). In atom, the absorption illustrates transition among the different allowed levels for the orbital electrons in molecules, illustrates the atoms within the molecule as a rotates or a vibrate and the entire energy contributions can be represented by the equation [35, 36],

$$E_{total} = E_{elect} + E_{vib} + E_{rot} + E_{trans} \quad (2.4)$$

Where, E_{elect} , E_{vib} , E_{rot} , and E_{trans} are the electronic energy, vibrational energy, rotational energy and translation energy, respectively. **Figure 2.8** depicts the basic schematic ray diagram of FT-IR spectrometer. Electronic, rotational and vibrational energies are possible only for certain transitions because of quantized energy levels and small quantity translational energy can be neglected. Infrared spectrum can be

employed as a finger print for identification of material, in support of X-ray technique for material characterization.

2.4.3 Brunauer-Emmett-Teller (BET):

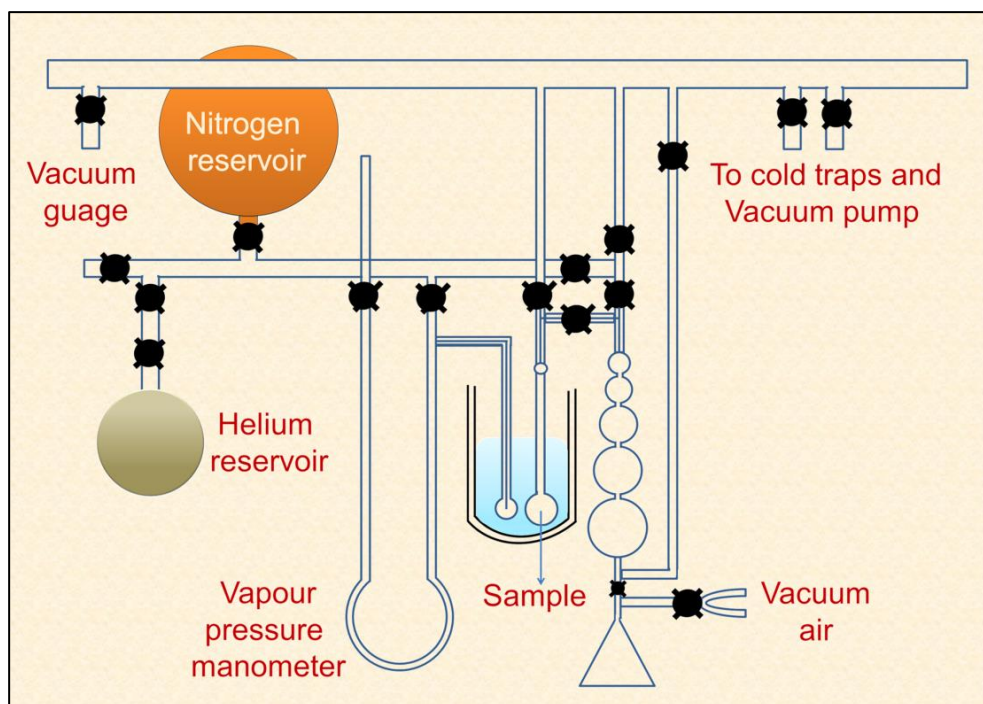


Figure 2.9: Schematic representation of the dynamic flow method [37].

BET is generally used for the analysis of specific surface area and porosity of the materials. The specific surface area of thin film material is evaluated by the adsorption of gas molecules on solid surface by calculating the quantity of adsorbate gas corresponding to a monomolecular layer on the specimen surface. The quantity of gas condense or adsorbed on the surface of solid at a constant temperature (at 77 K temperature of the liquid nitrogen) depends on the pressure of gas. The gas is adsorbed in the pores as well as on the surface of the specimen. The quantity of gas condensed or adsorbed at a given pressure delivers the detail information about pore structure. In general, the non-corrosive gases like nitrogen are utilized for BET measurement. Specific surface area is a scale-dependent property, with no single true value of specific surface area definable, and thus quantities of specific surface area determined through BET theory may depend on the adsorbate molecule utilized and its adsorption cross-section [38]. The schematic representation of the dynamic flow method apparatus utilized for the determination of specific surface area is indicated in **Figure 2.9**.

The specific surface area in the $\text{m}^2 \text{g}^{-1}$ offering crucial information about the impact of particle size and surface porosity. In general, BET isotherm data collected and plotted as adsorbed amount of N_2 gas concentration as a function of relative pressure of system. Six types of adsorption isotherms are possible [38, 39].

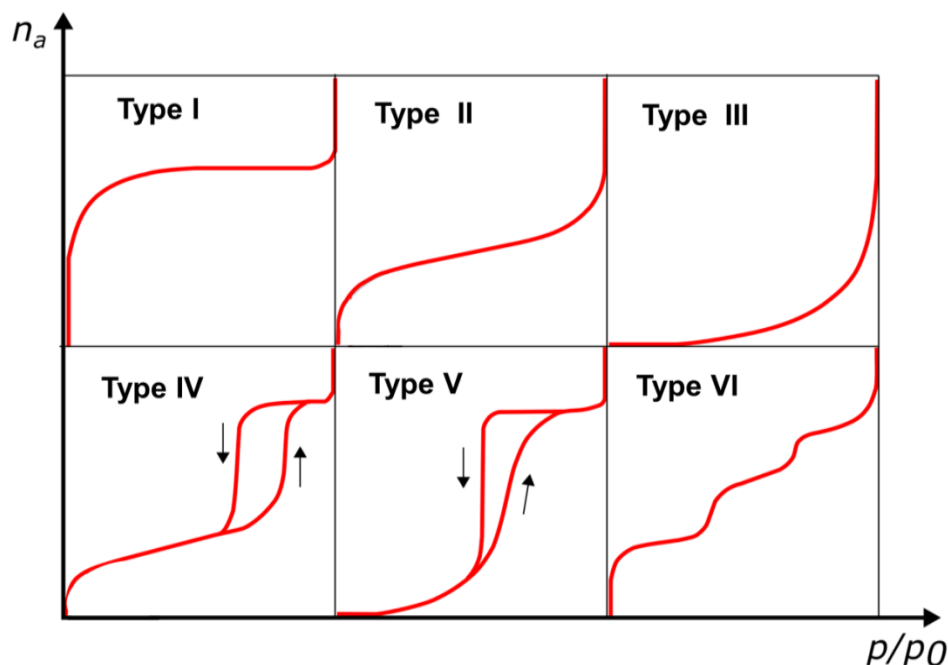


Figure 2.10: Six types of adsorption isotherms in BET study [38].

- 1) **Type I:** When, $P/P_0 < 1$ and $c > 1$, where P/P_0 is a relative pressure and c is the BET constant which is related to obtained adsorption energy of first monolayer. The micro porous materials having pore diameter less than 2 nm illustrates such type of isotherm as shown in **Figure 2.10**.
- 2) **Type II:** It occurs if $c > 1$ in BET equation and most usually observed. Monolayer formation begins at knee point and at medium pressure multilayer formation occurs.
- 3) **Type III:** A type III isotherm is possible when $c < 1$ and directly multilayer formation takes place, it means multilayers are not formed, and where BET is not applicable.
- 4) **Type IV:** This curve detected when capillary condensation is formed. Monolayer formation happens at low pressure followed by multilayer produced by increase in pressure. A material with 2 to 50 nm called mesoporous materials expresses such type of isotherm.
- 5) **Type V:** It is associated to the Type III isotherm in that the adsorbent-adsorbate interaction is weak, but obtained with certain porous adsorbents.

- 6) Type VI:** In which the sharpness of the steps depends on the system and the temperature, denotes stepwise multilayer adsorption on a uniform non-porous surface.

The BET theory is an extension of the Langmuir theory, which is a theory for monolayer of molecular adsorption to multilayer adsorption with the following hypotheses:

- (a) Gas molecules physically adsorb on the solid surface.
- (b) There is no interaction among each adsorption layer.
- (c) The Langmuir theory can be implemented to each layer.

The BET technique is commonly used in surface science for the evaluation of solids surface areas by the physical adsorption of gas molecules. The total specific surface area (S_T) as well as surface area (S_B) are analysed from the following expression;

$$S_T = \frac{V_m N_s}{V} \quad (2.5)$$

and

$$S_B = \frac{S_T}{a} \quad (2.6)$$

Where, S , N , V_m and a are the adsorption cross section of the adsorbing species, Avogadro's number, molar volume of the adsorbate gas and mass of the adsorbent, respectively [40].

2.4.4 X-Ray photoelectron spectroscopy (XPS):

XPS also known as Electron Spectroscopy for Chemical Analysis (ESCA) is the most widely used surface analysis technique because it can be applied to a broad range of materials and provides valuable quantitative and chemical state information from the surface of the material or thin film. XPS technique is based on the photoelectric effect and monochromatic X-rays are used as a source of photons [41]. In XPS investigation, when X-ray beam is incident on the surface of thin film it causes electrons to release from a top surface layer of material and these electrons are mentioned as photoelectrons. These photoelectrons (released electrons) are essential to decide the elemental structure, stoichiometry, quantity of an element and chemical state present in a thin film material. The binding energy of photoelectron is calculated by the following equation,

$$E_{binding} = E_{photon} - E_{kinetics} + \varphi \quad (2.7)$$

Where,

$E_{binding}$ = Binding energy of atomic orbital

E_{photon} = Photon energy

$E_{kinetics}$ = Ejected photoelectrons of kinetic energy

φ = Spectrometer work function

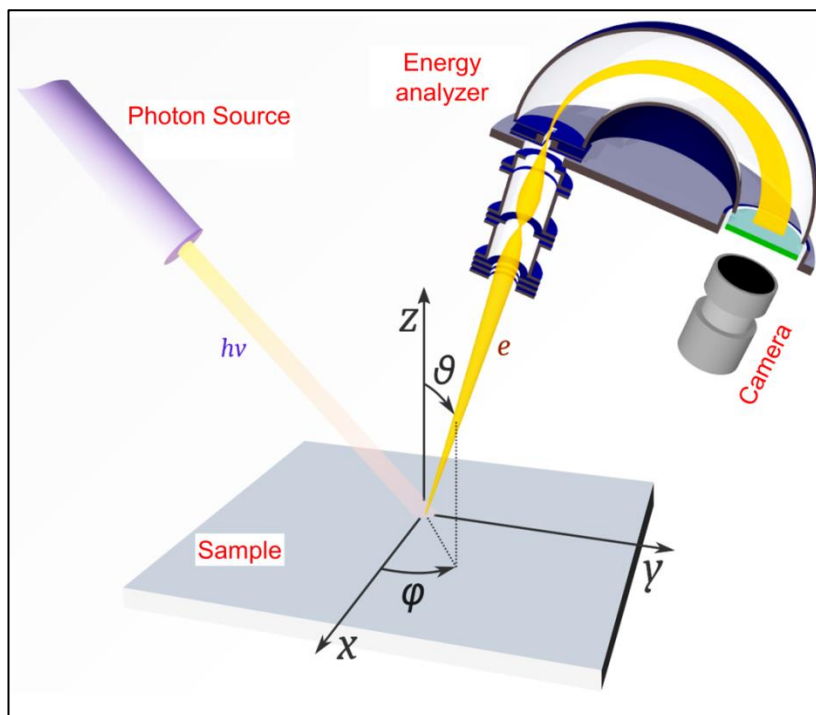


Figure 2.11: Ray diagram of XPS technique.

During the photoelectron emission, there is a probability of emission of an auger electron. The electrons of different energy ranges are released because of different energy levels present in different atoms. Electrons undergo far more interactions with matter than photons, this result in extreme short path length of electrons in comparison to photons. The peak in spectra indicates the background signal and presence of escaped electrons occur due to absorption in material. The schematic diagram of XPS technique is displayed in **Figure 2.11**. The energy, spatial and depth distribution of specific electrons are three main basic modes of data arrangement from XPS technique. The elemental mapping and chemical state of an element is executed by depth distribution and spatial distribution gives the probability of electron emission.

2.4.5 Field emission-scanning electron microscopy (FE-SEM):

FE-SEM is a versatile and convenient tool for studying surface morphology of thin and bulk samples. FE-SEM microscopy is a type of microscope which uses a

focused beam of electrons to scan a surface of a specimen to create a high resolution image. FE-SEM produces image that can show information of a material's surface topography and elemental analysis [42].

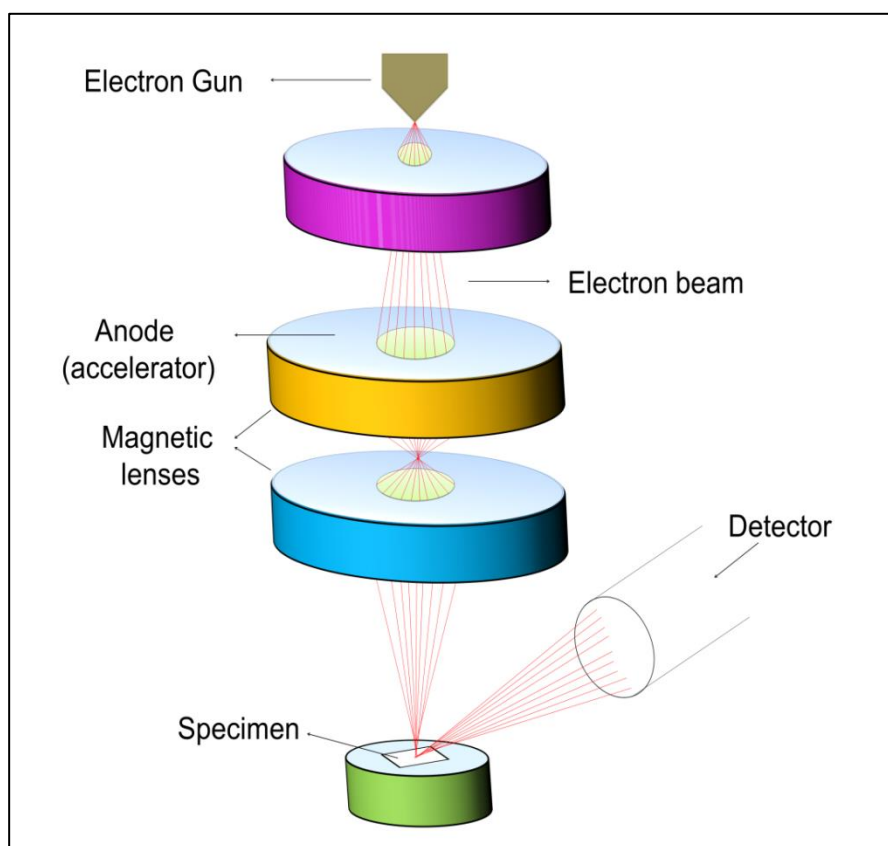


Figure 2.12: Schematic of FESEM instrument.

The resolution of the FE-SEM can approach up to a few nm. Also, it can operate at magnifications that are simply adjusted from about 10X to 300,000X and larger depth of field up to 100 times than that of optical microscope [43]. The ray diagram of FE-SEM exhibited in **Figure 2.12**. In the FE-SEM, a source of primary electrons (high-energy electrons) is focused (in vacuum) into a fine probe (through electromagnetic lenses) and rastered on the surface of the specimen as exhibited in **Figure 2.13**. As electrons bombard on the surface, a number of interactions produce that can result in the emission of electrons or photons from (or through) the surface. This interaction includes the emission of back-scattered electrons, auger electrons, elemental X-rays and secondary electrons as displayed in **Figure 2.13**.

When the electron beam hits the surface of the sample, it penetrates the sample to a depth of few microns, depending on the density of sample and accelerating voltage. Backscattered and secondary electrons are conventionally separate out

according to their energies. The secondary and backscattered electrons are used for the formation of a sample image by amplifying and transforming the signals. When a high-energy primary electron interacts with a specimen atom, it undergoes either inelastic or elastic scattering with the atomic nucleus. In scattering, if transferred energy is not enough then electron cannot emit from the specimen, and when transferred energy is higher than work function of specimen then electron emits from the specimen, surface. Details about the specimen, such as specimen composition, surface characteristics and topography etc. can be achieved from each signal.

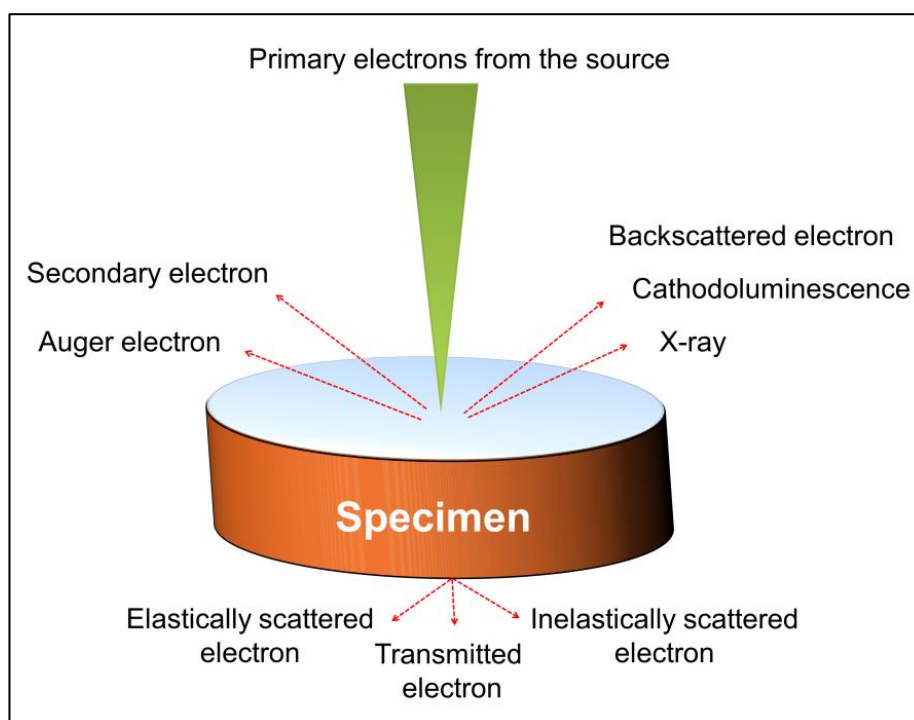


Figure 2.13: Ray diagram of the released different categories of electrons during interaction between beam and specimen.

2.4.6 Energy dispersive X-ray spectroscopy (EDS):

EDS (also known as EDS, EDX, or EDAX) is a powerful technique that enables the user to analyze the elemental composition or elemental analysis of a desired sample. The major operating principle that allows EDS to function is the capacity of high energy of electromagnetic radiation (X-rays) to eject 'core' electrons (electrons that are not in the outermost shell) from an atom. This principle is known as Moseley's Law, which determine direct correlation between the frequency of light released and atomic number of the atom. The EDS analysis works as an integrated property of FE-SEM and cannot be operated its own without the latter.

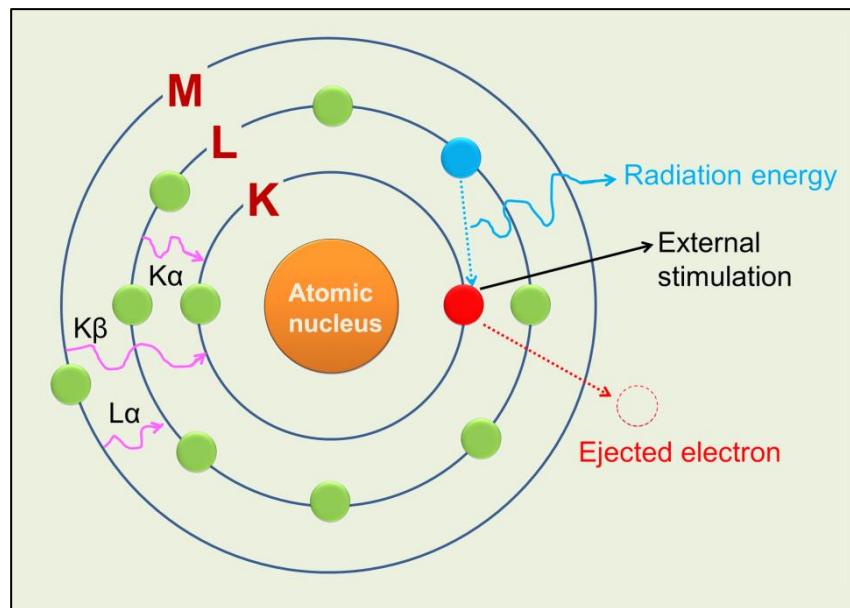


Figure 2.14: Principle of Energy-dispersive X-ray spectroscopy [44].

In this investigation, high energy beams of X-ray incident on the specimen to initiate the emission of characteristics X-ray or Continuum or background X-rays. At rest, an atom within the sample consists of ground state (or unexcited) electrons in discrete energy. An electron from an inner shell is excited by an incident beam, thereby removing electron from its shell and generating a hole (as shown in **Figure 2.14**). This hole can be occupied by an electron of a higher-energy shell. The difference in energies of the higher- and lower- energy shells is emitted in form of X-ray. Quantitative measurement of the energy and number of X-rays can be done with energy-dispersive analysis of X-rays. Since, the energy of these X-rays is characteristic feature of energy difference between two shells and atomic structure of discharging element. Thus, this technique can be used for elemental analysis. When K shell electrons are excited, they emit characteristic X-rays which are termed as “K Lines” and those emitted from L and M shells are called “L Lines” and “M Lines” respectively. If the element is heavy then its characteristics X-rays energies are also higher, therefore incident electrons of higher energies are required.

2.5 Electrochemical characterization techniques:

The SC gained much attention in electronics and power engineering, due to its high PD compared to the batteries and high capacitance compared to ordinary dielectric capacitors [45]. The SCs are categorized into two groups i.e. EDLCs (charge stored by non-faradic mechanism) and pseudocapacitors (charge stored by faradic

mechanism). Generally, suitable porous electrodes and electrolytes are used in the SC device. Using following equation the C_s of SC device can be calculated [46, 47].

$$C_s = \frac{I \times \Delta t}{m \times \Delta V} \quad (\text{For GCD}) \quad (2.8)$$

Where, C_s , I , ΔV , m and Δt are the C_s (F g⁻¹), current density (mA cm⁻²), potential window (V), deposited mass of material (g), and discharging time (s), respectively. The ED and PD of SC are calculated using by following equations:

$$ED = \frac{1}{2} CV^2 \quad (2.9)$$

$$PD = \frac{E}{\Delta t} \quad (2.10)$$

Where, ED , C , V , PD and Δt are the ED (Wh Kg⁻¹), C_s (F g⁻¹), operating voltage (V), PD (W kg⁻¹) and discharging time (s). The C_s and operating potential window of electrode material must be large to get the higher values of ED and PD. Electrolyte and active material are important to obtain wide potential window and large capacitance of SC device. Therefore, electrochemical features of electrode are significant for successful utilization in SC device and to know the electrochemical behavior of prepared electrode, CV, GCD and EIS techniques are necessary and used for analysis.

2.5.1 Cyclic voltammetry (CV):

CV is a potentiodynamic electrochemical measurement technique. In CV, the potential of the working electrode is ramped forward and backward through a predefined range with a constant sweep rate and the corresponding current is measured. **Figure 2.15** shows a typical CV curve when the potential of the working electrode is ramped between V1 and V2. As the potential increases, the current increases and the anodic peak is obtained. This anodic peak is called an oxidation peak. As the potential comes back the current decreases at a certain potential cathodic peak is obtained which is called a reduction peak.

As the CV begins from V1 the negative ions from the electrolyte get adsorbed on the surface of working electrode. As the potential of the working electrode increases slowly the concentration of positive charge also increases and resultantly more and more negative ions get adsorbed. Hence, a double layer of charge is formed on the surface of the electrode. This is called charge storage by double layer or non-faradic mechanism. But when the potential of the working electrode further increases, at a potential value the current suddenly starts to increase and an anodic peak is obtained.

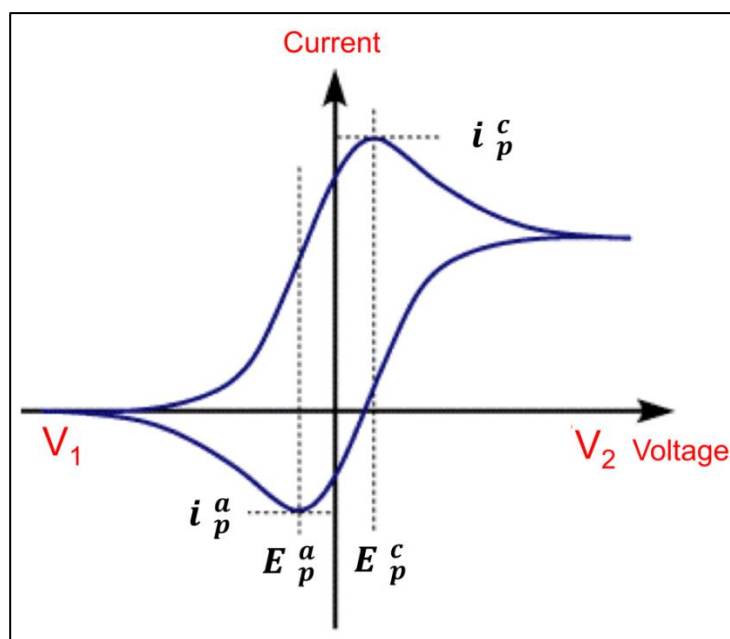


Figure 2.15: A typical cyclic voltammogram for a reversible single electrode transfer reaction.

This positive current is due to the oxidation of the electrode material. After reaching V_2 , the direction of ramping reversed from V_2 to V_1 . In this reverse scan, the oxidized material gets reduced and the cathodic peak is obtained. This oxidation and reduction of material in a higher potential region are combined called a redox reaction of a material and the charge storage through this process is called a redox or faradic mechanism [48].

2.5.2 Galvanostatic charge-discharge (GCD):

GCD also called as a chronopotentiometry which is a prominent measurement technique that can provide valuable information about C_s , ED and PD, capacitance, cycle life as well as internal resistance (IR). In this technique, a constant current is provided to working electrode and corresponding potential measured with respect to reference electrode as a function of time. The charging-discharging are governed at constant current until the set voltage is attained. When reverse current is applied, the measured potential is quickly changed because of the IR drop, and after that it gradually changes. The schematic illustration of charge-discharge curve is displays in **Figure 2.16**.

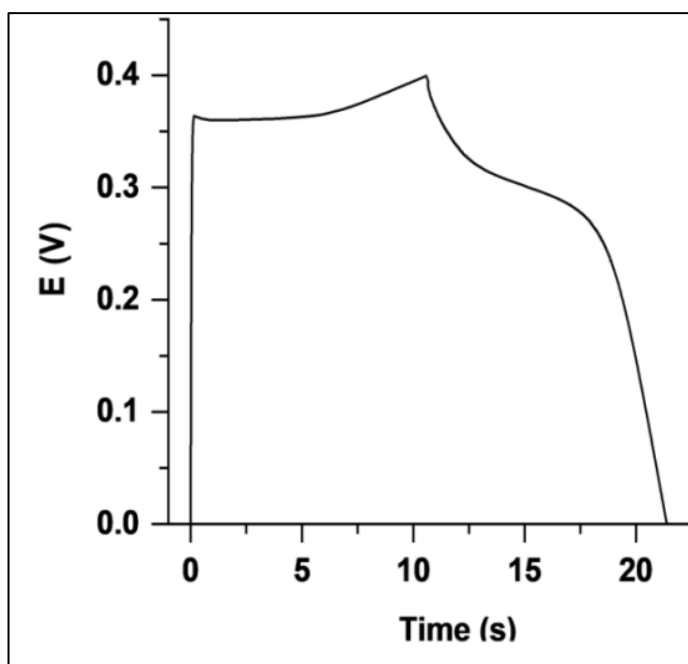


Figure 2.16: Schematic of charge-discharge curve.

The nature of charge-discharge curve and charge storage mechanism is depend on the prepared electrode. Symmetric linear nature of charge-discharge curve indicates the EDL mechanism and asymmetric non-linear nature indicates pseudocapacitive mechanism used for charge storage in electrodes [49].

2.5.3 Electrochemical impedance spectroscopy (EIS):

In EIS technique, response of current and electrochemical impedance is measured by providing AC signal of potential in wide range of frequencies (from mHz to MHz) to a electrochemical cell. EIS technique is beneficial to obtain information about the resistance of electrode-electrolyte interface and charge transfer process [50]. Impedance is nothing but the AC resistance of the cell, which contains imaginary and real parts. The electrochemical cell consists of resistive, capacitive and inductive properties. Resistive properties determined in the real part, while capacitive and inductive properties obtained in the imaginary part of impedance Z' vs Z'' plots called Nyquist plot [51]. **Figure 2.17** displays a typical Nyquist plot obtained from EIS analysis. Where Z' and Z'' indicate the real and imaginary parts of EIS, respectively. The intercept of Nyquist plot to the X-axis (i.e. real part) in the higher frequency region denote the solution resistance (R_s). While the intercept of semicircle in the higher frequency region denote the sum of R_s , and charge transfer resistance (R_{ct}). After semicircle at initial curve the straight line at low frequency indicates the

Warburg constant. In this study, EIS is measured with a nominal root-mean-square amplitude potential (V_{rms}) of 10 mV.

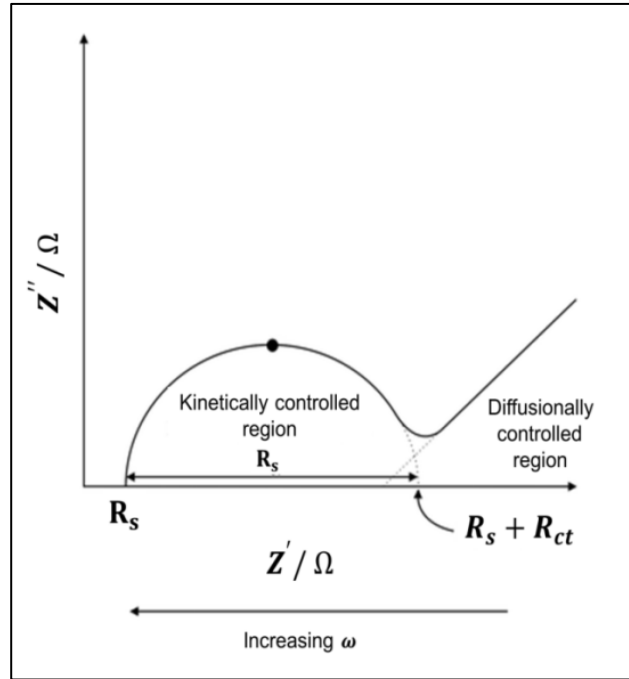


Figure 2.17: A typical Nyquist plot obtained from EIS [52].

The EIS technique is significant because it estimates the frequency independent and dependent parts of the Nyquist plot individually. If the input signals of a sinusoidal voltage $V_{(\omega)} = V_0 \sin \omega t$ and $I_{(\omega)} = I_0 \sin(\omega t + \Phi)$ be its output response, then the impedance of the electrode material is given by,

$$Z_{(\omega)} = \frac{V_{(\omega)}}{I_{(\omega)}} = \frac{V_0 \sin \omega t}{I_0 \sin(\omega t + \Phi)} \quad (2.11)$$

$$Z_{(\omega)} = Z_0 \frac{\sin(\omega t)}{\sin(\omega t + \Phi)} \quad (2.12)$$

The impedance is expressed in terms of magnitude, (Z_0) and phase shift (ϕ).

In order to forecast the performance of a SCs dependent on operating conditions and load, simulations based on an equivalent circuit model are broadly used [53]. The generalized method to recognise equivalent circuit models is presented in **Figure 2.18**. Initially the parameters of the model have to be assessed. Thus impedance spectra acquired by the equivalent circuit are fitted to experimental data via numerical optimization. After that the assessed parameters are executed into a cell model. Finally, the model is authenticated by evaluation to experimental data.

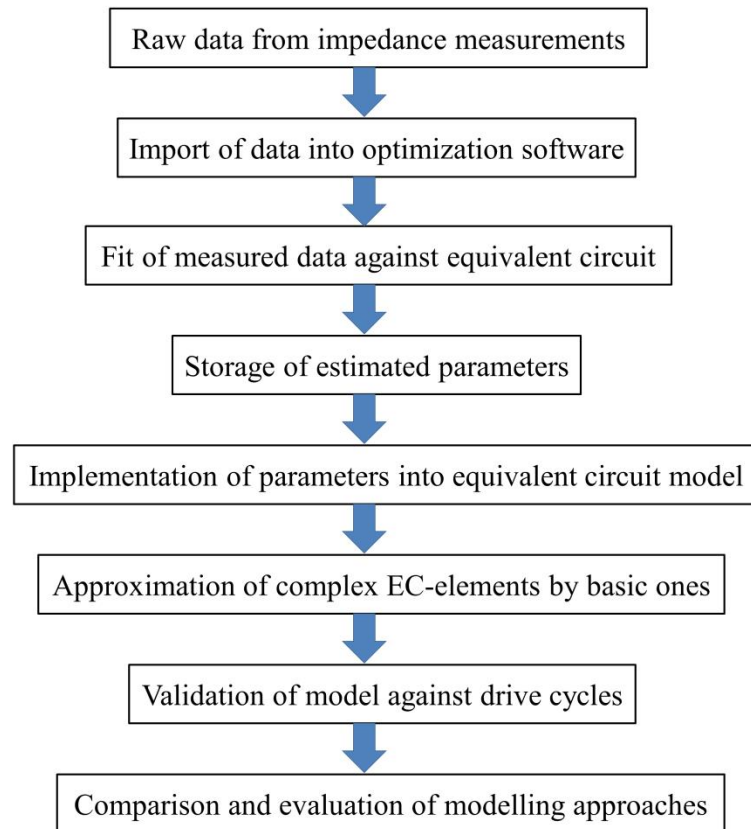


Figure 2.18: Approach of system identification for an equivalent circuit model [53].

2.6 Reference:

1. D. Dubal, O. Ruiz, P. Gomez–Romero, *Chem. Soc. Rev.*, 44, (2015), 1777-1790.
2. E. Rogers, P. F. Smet, P. Dorenbos, D. Poelman, E. Kolk, *J. Phys.: Condens. Matter*, 22, (2010), 015005.
3. I. Gurrapp, L. Binder, *Sci. Technol. Adv. Mater.*, 9, (2008), 043001.
4. C. Lokhande, *Mater. Chem. Phys.*, 27, (1991), 1-43.
5. U. Patil, S. Kulkarni, V. Jamadade, C. Lokhande, *J. Alloys Compd.*, 509, (2011), 1677-1682.
6. K. Byrappa, N. Keerthiraj, S. M. Byrappa, *Handbook of Crystal Growth* (2nd Edition), Bulk Crystal Growth, (2015), 535-575.
7. K. Byrappa, T. Adschiri, *Prog. Cryst. Growth Ch.*, 53, (2007), 117-166.
8. G. Morey, P. Niggli, *J. Am. Chem. Soc.*, 35, (1913), 1086-1130.
9. A. N. Lobachev, (ed.), *Crystallization Processes under Hydrothermal Conditions*, Consultants Bureau, New York, (1973), pp. 1-255.
10. R. A. Laudise, *The Growth of Single Crystals*, Prentice-Hall, Englewood Cliffs, New Jersey, (1970), pp. 278-281.
11. M. Yoshimura, H. Suda, *Hydrothermal Processing of Hydroxyapatite: Past, Present, and Future in: Hydroxyapatite and Related Materials* (P. W. Brown and B. Constanz, eds.), CRC Press, Inc, (1994), pp. 45-72.
12. A. Rabenau, *Angew. Chem. Int. Ed.*, 24, (1985), 1026-1040.
13. W. Cho, M. Yashima, M. Kakihana, A. Kudo, T. Sakata, M. Yoshimura. *Appl. Phys. Lett.*, 66, (1995), 1027-1029.
14. R. I. Walton, *Chem. Soc. Rev.*, 31, (2002), 230-238.
15. M. Shandilya, R. Rai, J. Singh, *Adv. Appl. Ceram.*, 115, (2016), 354-376.
16. W. Suchanek, R. Riman, *Adv. Sci. Tech*, 45, (2006), 184-193.
17. B. Ghosh, M. Das, P. Banerjee, S. Das, *Appl. Surf. Sci.*, 254, (2008), 6436-6440.
18. H. Pathan, S. Kale, C. Lokhande, S. Han, O. Joo, *Mater. Res. Bull.*, 42, (2007), 1565-1569.
19. S. Kale, R. Mane, H. Pathan, A. Shaikh, O. Joo, S. Han, *Appl. Surf. Sci.*, 253, (2007), 4335-4337.
20. T. Niesen, M. De Guire, *J. Electroceram.*, 6, (2001), 169-207.
21. S. Sartale, C. Lokhande, *Mater. Chem. Phys.*, 72, (2001), 101-104.
22. T. Niesen, M. De Guire, *Solid State Ion.*, 151, (2002), 61-68.
23. Y. Nicolau, *Appl. Surf. Sci.*, 22, (1985), 1061-1074.
24. M. Ristov, G. Sinadinovski, I. Grozdanov, *Thin Solid Films.*, 123, (1985), 63-67.
25. H. M. Pathan, C. D. Lokhande, *Bull. Mater. Sci.*, 27, (2004), 85-111.
26. X. Cao, X. Zheng, J. Tian, C. Jin, K. Ke, R. Yang, *Electrochim. Acta.*, 191, (2016), 776-783.
27. Gary Hodes, "Chemical Solution Deposition of Semiconductor Films", Marcel Dekker Inc, New York, (2001), pp. 64.
28. B. Ezekoye, P. Offor, V. Ezekoye, F. Ezema, *Int. J. Sci. Res.*, 2, (2013), 452-456.
29. K. L. Chopra, *Thin Film Phenomena*, McGraw Hill Book Co. New York, (1969), pp. 864.
30. B. Cullity, S. Stock, "Elements of X-rays Diffraction", 3rd Edition, Prentice Hall, (2014), 284-285.
31. A. Taylor, "X-ray Metallography", Wiley, New York, (1942).
32. M. J. Buerger, "X-ray Crystallography", Wiley, New York, (1942).
33. A. Guinier, "X-ray Diffraction", Freeman, San Francisco, (1963).

34. A. Bunaciu, E. gabriela Udriștioiu, H. Aboul-Enein, *Crit. Rev. Anal. Chem*, 45, (2015), 289-299.
35. R. A. Nyquist, R. O. Kagel, *Infrared Spectra of Inorganic Compounds*, Academic Press INC, New York, (1971).
36. J. Preudhomme, P. Tarte, *Spectrochim. Acta*, 27, (1971), 1817-1835.
37. <http://iitk.ac.in/dord/facilities>.
38. J. B. Condon, *Surface Area and Porosity Determinations by Physisorption: Measurements and Theory* (Elsevier, Amsterdam, 2006), pp. 6-14.
39. K. Sing, D. Everett, R. Haul, L. Moscou, R. Pierotti, J. Rouquerol, T. Siemieniewska, *Pure Appl. Chem.*, 57, (1985), 603-619.
40. Y. Shi, Y. Meng, D. Chen, S. Cheng, P. Chen, T. Yang, Y. Wan, D. Zhao, *Adv. Funct. Mater.*, 16, (2006), 561-567.
41. C. D. Wagner, W. M. Riggs, L. E. Davis, J. F. Moulder, *X ray Photoelectron Spectroscopy in: G.E. Muilenberg (Eds.), X ray Photoelectron Spectroscopy*, Perkin Elmer Corporation, Minnesota, (1979), pp. 1-28.
42. Y. Hunge, M. Mahadik, A. Moholkar, C. Bhosale, *Appl. Surf. Sci.*, 420, (2017), 764-772.
43. L. D. Hanke, *Handbook of Analytical Methods for Materials, Materials Evaluation and Engineering*, Inc. Plymouth, (2001).
44. <https://www.thermofisher.com/blog/microscopy/edx-analysis-with-sem-how-does-it-work/>, EDX Analysis with SEM: How Does it Work?
45. A. Burke, *J. Power Sources*, 91, (2000), 37-50.
46. P. Katkar, S. Marje, S. Pujari, S. Khalate, A. Lokhande, U. Patil, *ACS Sustain. Chem. Eng.*, 7, (2019), 11205-11218.
47. A. Bard, L. Faulkner, *Electrochemical Methods: Fundamentals and Applications*, 2nd edition, John Wiley & Sons, Inc, New York, (2001), pp. 864.
48. C. G. Zoski, *Handbook of electrochemistry*, Elsevier Science, Netherlands (2006).
49. S. Dai, Y. Xi, C. Hu, X. Yue, L. Cheng, G. Wang, *J. Power Sources*, 274, (2015), 477-482.
50. A. Chu, P. Braatz, *J. Power Sources*, 112, (2002), 236-246.
51. M. E. Orazem, B. Tribollet, *Preliminary Graphical Methods in: Electrochemical Impedance Spectroscopy*, A John Wiley & Sons, Inc., New Jersey, (2008), pp. 333.
52. E. Randviir, C. Banks, *Anal. Methods*, 5, (2013), 1098-1115.
53. D. Andrea, M. Meiler, K. Steiner, H. Walz, T. Soczka-Gutha, D. Sauerb, *J. Power Sources*, 196, (2011), 5349-5356.

CHAPTER-3

SYNTHESIS AND CHARACTERIZATION OF NICKEL COPPER PHOSPHATE THIN FILMS BY HYDROTHERMAL METHOD

CHAPTER 3

Synthesis and characterization of nickel copper phosphate thin films by hydrothermal method

Sr. No.	Title	Page No.
3.1	Introduction	59
SECTION – A		
Hydrothermal synthesis and characterization of nickel copper phosphate thin films		
3.2.A.1	Introduction	59
3.2.A.2	Experimental details	60
	3.2.A.2.1 Substrate	60
	3.2.A.2.2 Substrate cleaning	61
	3.2.A.2.3 Chemicals	61
	3.2.A.2.4 Synthesis of nickel copper phosphate thin films	61
	3.2.A.2.5 Materials characterization	63
3.2.A.3	Results and discussion	63
	3.2.A.3.1 Film formation and reaction mechanism	63
	3.2.A.3.2 XRD study	65
	3.2.A.3.3 FT-IR study	66
	3.2.A.3.4 BET study	67
	3.2.A.3.5 XPS study	69
	3.2.A.3.6 FE-SEM study	71
	3.2.A.3.7 EDS study	73
3.2.A.4	Conclusions	74
SECTION – B		
Supercapacitive performance evaluation of nickel copper phosphate thin films		
3.2.B.1	Introduction	75
3.2.B.2	Experimental configuration for electrochemical performance measurements	75
3.2.B.3	Results and discussion	76
	3.2.B.3.1 CV study	76
	3.2.B.3.2 GCD study	81
	3.2.B.3.3 EIS study	83

	3.2.B.3.4	Stability study	84
3.2.B.4	Conclusions		85
3.3	References		86

3.1 Introduction:

Developed energy storage and energy conversion devices have been actively implemented in the background of rapid growth of energy demand and insufficient of fossil fuel resources [1]. Amongst the different ESDs, SCs are the best option for clean and green ESD [2]. The attractive characteristics of SCs are their better cycling performance, high PD, quick charging and discharging rate. These fantastic characteristics of SC motivate its usage in different applications, either single or into combined [3]. SCs are currently employed in consumer electronics, aircrafts, electric vehicles, smart grids and hybrid vehicles [4-7]. Depending on the mechanism of charge storage, SCs are generally divided into two types such as, EDLCs and pseudocapacitors.

TMPs demonstrated good electrochemical performances in various applications [8] such as lithium-ion batteries [9], electrocatalysis [10], photocatalysis [11] and SCs [12]. The outstanding performance of metal phosphates would be associated their metallic property like excellent electrical conductivity, which performs high PD and fast electron transport [13, 14]. As a result of various TMPs based on Ni, Cu, Fe, Co, etc. was reported as earth-abundant electroactive materials [15]. Motivated by research interests in the synergistic impact of binary TMPs for SC application, nickel copper phosphate thin films are deposited directly (binder-free approach) on SS substrate at various concentrations of nickel and copper using hydrothermal method. Further, the influence of nickel and copper concentrations on physico-chemical properties of nickel copper phosphate thin films is examined. This chapter is divided into two sections (section A and B). Section 'A' deals with the synthesis of nickel copper phosphate thin films by hydrothermal method and their morphological and structural characterization. Section 'B' is associated with the SC performance analysis of nickel copper phosphate thin film electrodes.

SECTION – A

Hydrothermal synthesis and characterization of nickel copper phosphate thin films

3.2.A.1 Introduction:

For the large scale commercialization of SCs electrode material must have high electrochemical performance (high PD and ED), long durability, and low cost. From these points of view, the Ni-Cu based compound are prepared by simple, additive-free,

scalable, binder-less, low temperature, low cost, and eco-friendly hydrothermal method. Some successful works have been done to prepare nickel copper phosphide by hydrothermal method [16]. The hydrothermal is a most convenient method to prepare large scale thin films with environmental friendly nature and low cost. A hydrothermal method is broadly utilized to prepare functional nano/micro materials with certain sizes and shapes. The predicted micro/nanostructured thin films can be simply achieved by controlling the growth and rate of reaction through hydrothermal method. According to the literature survey, analyse on the development of nickel copper phosphate material by a hydrothermal method for energy-relevant SC applications is scarcely examined. So, there is opportunity to analyse the performance of a novel nickel copper phosphate electrode for SC application. This chapter is about the characterization of nickel copper phosphate thin film electrodes synthesized by hydrothermal method with changing concentrations of nickel and copper.

3.2.A.2 Experimental details:

3.2.A.2.1 Substrate:

The deposition substrate properties play a vital role in the construction of flexible SC electrodes. The mechanical strength and flexibility of SCs electrode are based upon the substrate material. Several substrates such as carbon-based paper, flexible metal substrates, conventional paper, graphene sponges, textiles, cables, Ti foil, carbon cloth, SS, NF, etc. act as a conductive backbone to assist active materials [17]. Till now cost-effective and, eco-friendly, flexible substrates are employed for the fabrication of flexible devices. It is known that the high surface area, mechanical flexibility, high porosity and good conductivity of support substrates help to improve the performance of SCs.

The carbon based substrates provide high capacitance and offer high surface area but synthesizing methods for material preparation are expensive and sluggish, also they have low conductivity. The CPs are light weight and highly flexible but they suffer from low surface area and conductivity. The textiles substrate used for bendable, wearable and flexible device purposes, but they have naturally low capacitance and it is main restriction in the practical application [18]. The cable natured substrates caught major attraction because of their adaptability of shapes, but they limit in practical application due to low ED, high processing and preparation cost [17].

In present work, flexible SS is used as a current collector for the direct growth of metal phosphate. The material is directly grown on SS conductive substrate without using any polymer binder (binder-free). The direct (in-situ) growth of active materials on conductive current collector has been regarded as an effective route to improve the interfacial contact than the conventional binder enriched coating technique. Also, the SS substrate is stable in acidic and basic conditions than the other metallic substrates. Moreover, the lightweight and flexible nature of SS substrate is prominent features for the construction of flexible SCs. The efficient electrochemical performance may be delivered due to direct electrical contact between active material and substrate [18]. Earlier reports have displayed that, the enhanced morphology and structure of active materials with good adhesion on the current collector assist the charge transfer process more efficiently [19-21].

3.2.A.2.2 Substrate cleaning:

To deposit adherent, contaminant free, pinhole free and uniform thin films, the substrate surface plays a crucial role during deposition. The heterogeneous growth of material in chemical deposition methods initiates from nucleation sites delivered by substrate. A substrate with a contamination is responsible for the uncontrolled growth and results into non-uniform thin film. The SS substrates for thin film deposition of nickel copper phosphate were cleaned employing following steps;

Step 1: The SS substrate was wiped out with acetone to eliminate the dirt.

Step 2: The SS substrate was mirror polished by applying zero grade polish paper.

Step 3: The substrate was washed with detergent and DDW.

Step 4: Finally, the substrate was ultrasonically cleaned in DDW for 15 minutes and dried at ambient condition, and further utilized for deposition.

3.2.A.2.3 Chemicals:

Analytical grade nickel sulphate ($\text{NiSO}_4 \cdot 6\text{H}_2\text{O}$), copper sulphate ($\text{CuSO}_4 \cdot 5\text{H}_2\text{O}$), potassium dihydrogen orthophosphate (KH_2PO_4) and urea (NH_2CONH_2) were purchased from Sigma Aldrich and used as received without any purification. SS substrates with thickness of 0.5 mm (purchased from a local dealer) were used for film deposition. The DDW was used as solvent during the experiment.

3.2.A.2.4 Synthesis of nickel copper phosphate thin films:

In the Ni-Cu phosphate material synthesis $\text{NiSO}_4 \cdot 6\text{H}_2\text{O}$, $\text{CuSO}_4 \cdot 5\text{H}_2\text{O}$ and KH_2PO_4 were used as a source of Ni, Cu and phosphate, respectively. For the

controlled reaction procedure, urea is added and it acts as a hydrolyzing agent in the synthesis. $\text{NiSO}_4 \cdot 6\text{H}_2\text{O}$ (0.0333M), $\text{CuSO}_4 \cdot 5\text{H}_2\text{O}$ (0.0333M) and KH_2PO_4 (0.0667M) sources were dissolved in 50 ml of DDW with hydrolyzing agent (0.075M), consecutively. The above mixture was stirred vigorously till preparation of homogenous solution, then it was utilized for further Ni-Cu phosphate. The effect of variation in Ni and Cu content examined via varying the ratio between them. Herein, the molar ratio of Ni and Cu varied as 0.0333:0 (1:0), 0.0249:0.0083 (0.75:0.25), 0.0166:0.0166 (0.50:0.50), 0.0083:0.0249 (0.25:0.75) and 0:0.0333 (0:1) M, and named as H-NCP-1, H-NCP-2, H-NCP-3, H-NCP-4, and H-NCP-5, respectively.

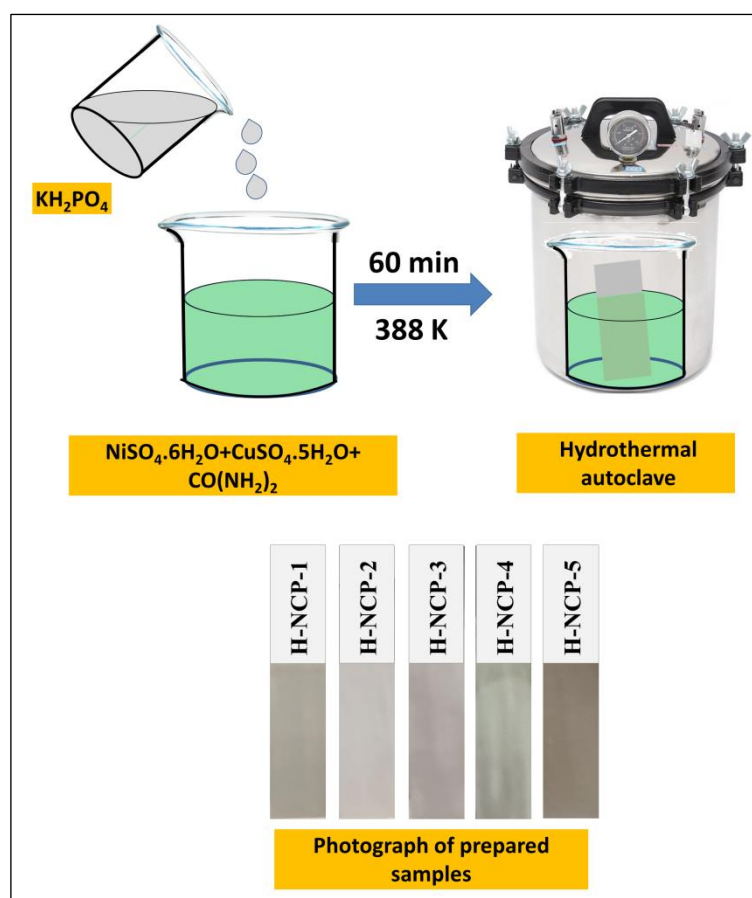


Figure 3.1: Schematic presentation of nickel copper phosphate thin films preparation by hydrothermal method at different nickel and copper molar ratio.

In prepared solution baths with different Ni and Cu molar ratio (intimated above), well cleaned SS substrates were dipped vertically. After dipping the substrate, the solution baths put into a hydrothermal autoclave and kept at a constant 388 K temperature for 60 min. The schematic representation of thin film preparation by hydrothermal method is displayed in **Figure 3.1**. After continuous 60 min heating, the reaction bath was removed from hydrothermal autoclave and deposited substrate taken

out from solution. The substrates with deposited material rinsed several times in DDW for removal of loosely bonded particles from the surface and dried at ambient conditions. The prepared thin film electrodes of nickel copper phosphate on SS substrates were directly employed for different characterization.

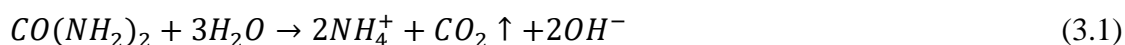
3.2.A.2.5 Materials characterization:

The structural characterization of the Ni-Cu phosphate thin films were examined by XRD from Rigaku miniflex-600 with Cu K α ($\lambda = 0.15406$ nm) in the 2θ range of 10-80°. The FT-IR spectra were recorded by an FT-IR 4600 type-A instrument using a KBr pellet at ambient temperature for the detection of functional groups. The XPS (K-alpha XPS System, Thermo Fisher Scientific, U.K.) was analyzed for identifying oxidation states and chemical composition of Ni-Cu phosphate thin film. The surface area and porosity were measured from BET analysis using (Belsorp II mini) instrument. The FE-SEM (JSM-6500F, JEOL) was utilized to examine surface morphology of prepared material and EDS (Oxford, X-max) was used to observe elemental analysis. All electrochemical activities were evaluated by using ZIVE MP1 multichannel electrochemical workstation.

3.2.A.3 Results and discussion:

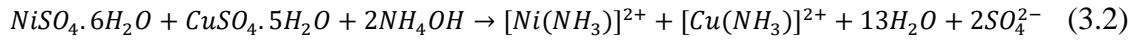
3.2.A.3.1 Film formation and reaction mechanism:

Hydrothermal synthesis mainly depends on the controlled precipitation through direct heating under enclosed system and the development of solid phase during the conversion of supersaturated state to the saturated state of a solution [22]. The film formation process contributes two significant steps, initial one is nucleation monitored by the crystal growing process. In film formation procedure, nucleation on substrate surface performed and promotes growth of nucleation sites [23]. The deposition of nickel copper phosphate thin films are executed for different molar ratios (H-NCP-1, H-NCP-2, H-NCP-3, H-NCP-4 and H-NCP-5) of nickel and copper via a hydrothermal method. Nickel sulphate, copper sulphate and potassium dihydrogen phosphate are utilized as precursors of nickel, copper and phosphate. In this process, urea is utilized as a hydrolyzing agent when the reaction bath is heated at 363 K temperature. Then urea decomposes delicately producing CO_2 and NH_3 as [24, 25].



According to the equation (3.1), released NH_4^+ ions represent as a complexing agent in the bath, and Ni^{2+} and Cu^{2+} ions in solution complexed as $Ni(NH_3)_2^{2+}$ of

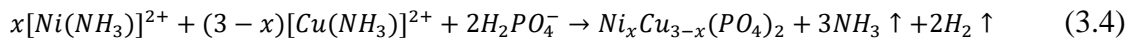
$Cu(NH_3)^{2+}$ (equation 3.2). This complex gradually releases Ni^{2+}/Cu^{2+} ions and which inhibits fast nucleation, control the reaction rate and subsequent homogeneous nucleation in the solution.



On the other hand, phosphate decomposes as follows,



Finally, Ni^{2+}/Cu^{2+} ions from nickel/copper complex and $H_2PO_4^-$ ions from phosphate precursor react with each other and produces $Ni_xCu_{3-x}(PO_4)_2$ material in thin film form, as per the following reaction,



Reaction temperature (388 K) and reaction time (1 h) are optimized for the uniform deposition of material on SS substrate. Before 1 h deposition time, the film was not uniform.

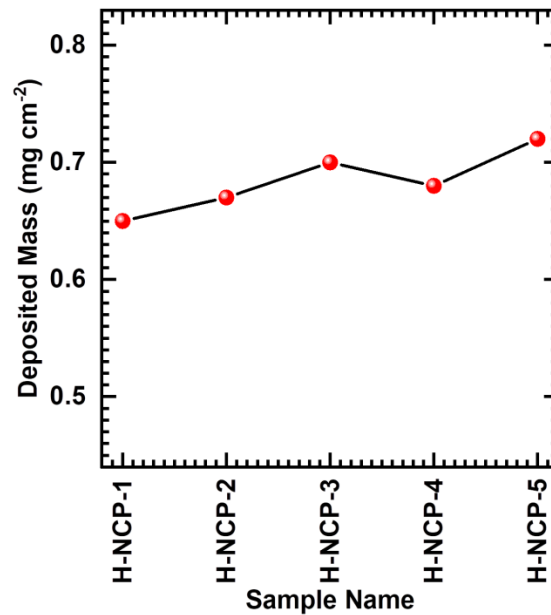


Figure. 3.2: Deposited mass of nickel copper phosphate thin film for different compositions (H-NCP-1 to H-NCP-5).

The mass of deposited nickel copper phosphate material on SS substrate with different nickel:copper compositions is analysed by weight difference method (**Figure 3.2**). For samples H-NCP-1, H-NCP-2, H-NCP-3, H-NCP-4, and H-NCP-5, the deposited weights are 0.65, 0.67, 0.70, 0.68, and 0.72 mg cm⁻², respectively. The growth rate of materials is different due to combination of transition metals (Ni and Cu) which may impact the terminal thickness of thin films.

3.2.A.3.2 XRD study:

The XRD patterns of nickel copper phosphate (H-NCP-1 to H-NCP-5) electrodes synthesized by hydrothermal method at various concentration ratios of Ni and Cu are illustrated in **Figure 3.3**. The H-NCP-1 and H-NCP-5 are pristine nickel phosphate and copper phosphate samples, respectively. The XRD pattern of H-NCP-1 (indicated as “●” in **Figure 3.3**) matches with the JCPDS card no. 033-0951 and confirms the formation of $\text{Ni}_3(\text{PO}_4)_2 \cdot 8\text{H}_2\text{O}$. In H-NCP-1 XRD pattern, diffraction peaks at angles of 11.54, 13.60, 18.64, 20.93, 22.38, 23.63, 28.42, 30.76, 33.63, 36.19, 39.60, 41.47, 42.10 and 55.80° are ascribed to the (1 1 0), (0 2 0), (2 0 0), (0 1 1), (1 3 0), (1 0 1), (0 3 1), ($\bar{3}$ 0 1), ($\bar{3}$ 2 1), (1 4 1), ($\bar{1}$ 1 0), ($\bar{2}$ 5 1), ($\bar{2}$ 2 0), and (0 8 0) crystal planes. Similarly, the XRD pattern of H-NCP-5 (indicated as “▲” in **Figure 3.3**) matches with JCPDS card no. 01-070-0494 and confirms the formation of $\text{Cu}_3(\text{PO}_4)_2$. In H-NCP-5, diffraction peaks at an angle of 15.32, 18.84, 24.06, 30.88, 34.27, 35.25, 37.34, 50.62, 58.32 and 64.11° corresponds to the (0 0 1), (0 1 0), ($\bar{1}$ 0 1), (0 1 2), (1 2 1), ($\bar{1}$ 0 2), (2 1 0), ($\bar{2}$ 1 1), (2 3 2) and ($\bar{3}$ $\bar{2}$ 1) crystal planes of copper phosphate.

The peaks marked with an asterisk (*) are ascribed to the SS substrate. It can be noticed that, the diffraction peaks relate to nickel phosphate are more prominent in H-NCP-1 and H-NCP-2 than others, where nickel concentration is higher than copper in nickel copper phosphate films. In addition, peaks related to copper phosphate are more dominant than nickel phosphate for sample H-NCP-3 to H-NCP-5, since copper concentration is higher. Detected peaks and crystal planes represent the creation of monoclinic crystal structure of nickel phosphate and copper phosphate in H-NCP series thin films. So, it confirms the formation of nickel copper phosphate material. The creation of sharp diffraction peaks in the patterns implies that, nickel copper phosphate is highly crystalline. Moreover, good crystallinity of nickel copper phosphate may be favourable for enhancing the electrochemical performance by providing excellent electrochemical conductivity [6].

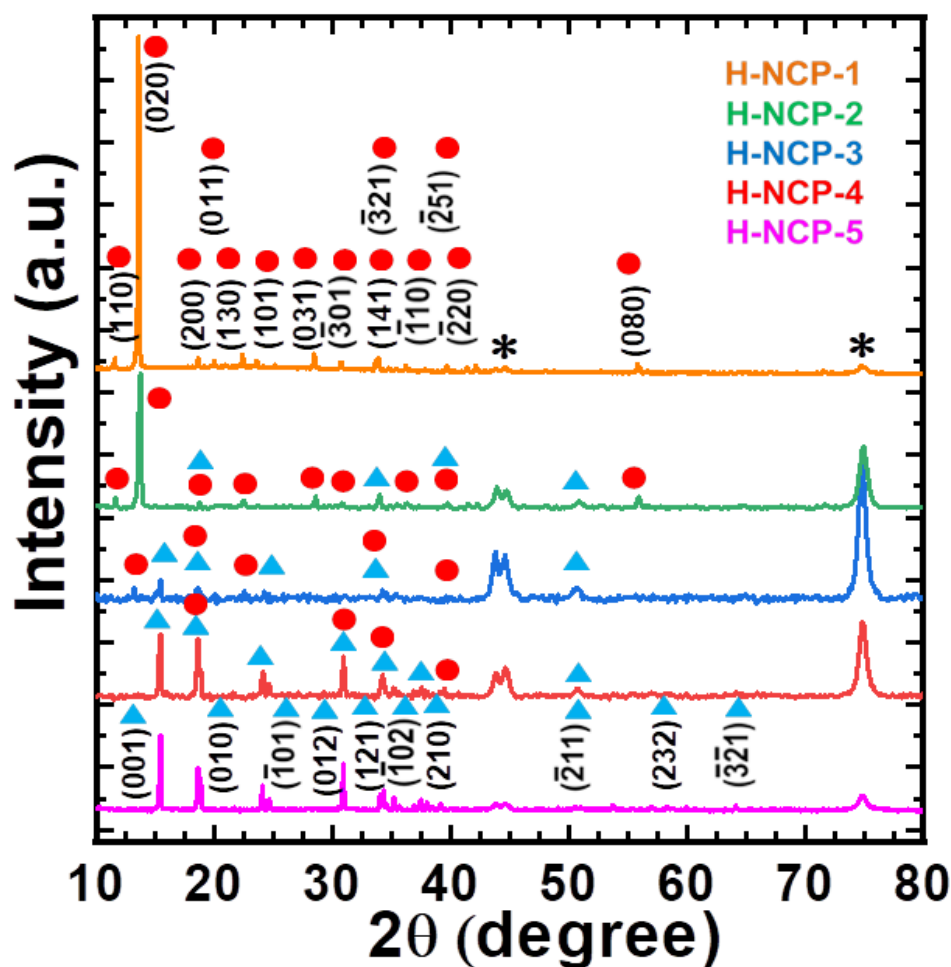


Figure 3.3: XRD patterns of nickel copper phosphate (H-NCP series) thin films.

3.2.A.3.3 FT-IR study:

FT-IR spectroscopic investigation was performed to examine the functional groups and molecular chemical bonds present in the synthesized H-NCP thin films. **Figure 3.4** reveals the characteristic peak at 559 cm^{-1} due to metal-oxygen bonding of Ni-O in H-NCP-1 sample [26] and peak at 620 cm^{-1} reveals Cu-O bonding in H-NCP-5 thin film [27]. The peak at 620 cm^{-1} relates to the stretching vibration mode of phosphate molecules (P-O-P) [28]. The vibrational bands of PO_4^{3-} anion are noticed around wavenumbers of 750 cm^{-1} [29, 30]. The absorption peaks at 1003 and 1049 cm^{-1} are attributed to P-O symmetric stretching vibration, and 1134 cm^{-1} is antisymmetric stretching of PO_4^{3-} group [31-33]. The absorption peak of 1361 cm^{-1} reveals bending mode of H-O-P bond [34]. The peak of 1593 to 1698 cm^{-1} illustrates H-O-H bending vibration of structural water form H-NCP series samples. Also, the broad band from 3004 to 3387 cm^{-1} represent the adsorbed water content in the synthesized material [35, 36]. The prepared samples denote almost similar range of peaks which confirms occurrence of similar chemical bonding in the samples. The FT-IR result confirms

presence of structural water and phosphate content in the prepared samples. The FT-IR investigation indicates successful synthesis of the hydrous nickel copper phosphate thin films.

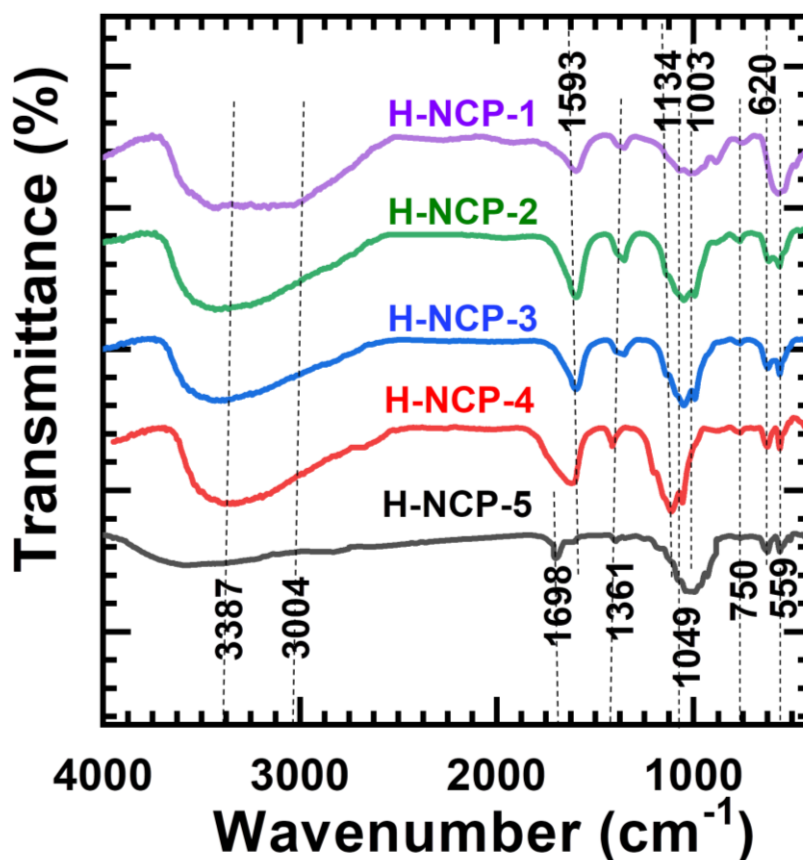


Figure 3.4: FTIR spectra of nickel copper phosphate (H-CMP series) thin films.

3.2.A.3.4 BET study:

The N_2 adsorption-desorption experiments were executed for the analysis of specific surface area and pore characteristics of H-NCP series samples (at 77 K temperature of the liquid nitrogen) and depicted in **Figure 3.5 (a-f)**. The detected isotherms of sample H-NCP-1 (a), H-NCP-2 (b), H-NCP-4 (d) and H-NCP-5 (f) reveal a type III isotherm with H3 type hysteresis loop, and sample H-NCP-3 (c) reveals IV isotherm with H2 type hysteresis loop of physisorption, according to distribution of International Union of Pure and Applied Chemistry (IUPAC) [37]. The type III isotherm represents most likely macroporous structural of material, and a lower energy of adsorption and type IV isotherm indicates characteristic property of mesoporous material [38]. A typical H3 type hysteresis loop of H-NCP-1, H-NCP-2, H-NCP-4 and H-NCP-5 samples represent plate-like particles generating slit-shaped pores, and H2 type hysteresis loop of H-NCP-3 (c) sample represents well ordered pores with narrow

as well as wide portions due to interconnecting channels [39, 38]. According to the determination of BET equation, the surface areas were calculated as 16.74, 25.66, 83.74, 24.25 and 19.41 $\text{m}^2 \text{g}^{-1}$ for samples (a) H-NCP-1, (b) H-NCP-2, (c) H-NCP-3, (d) H-NCP-4 and (e) H-NCP-5, respectively.

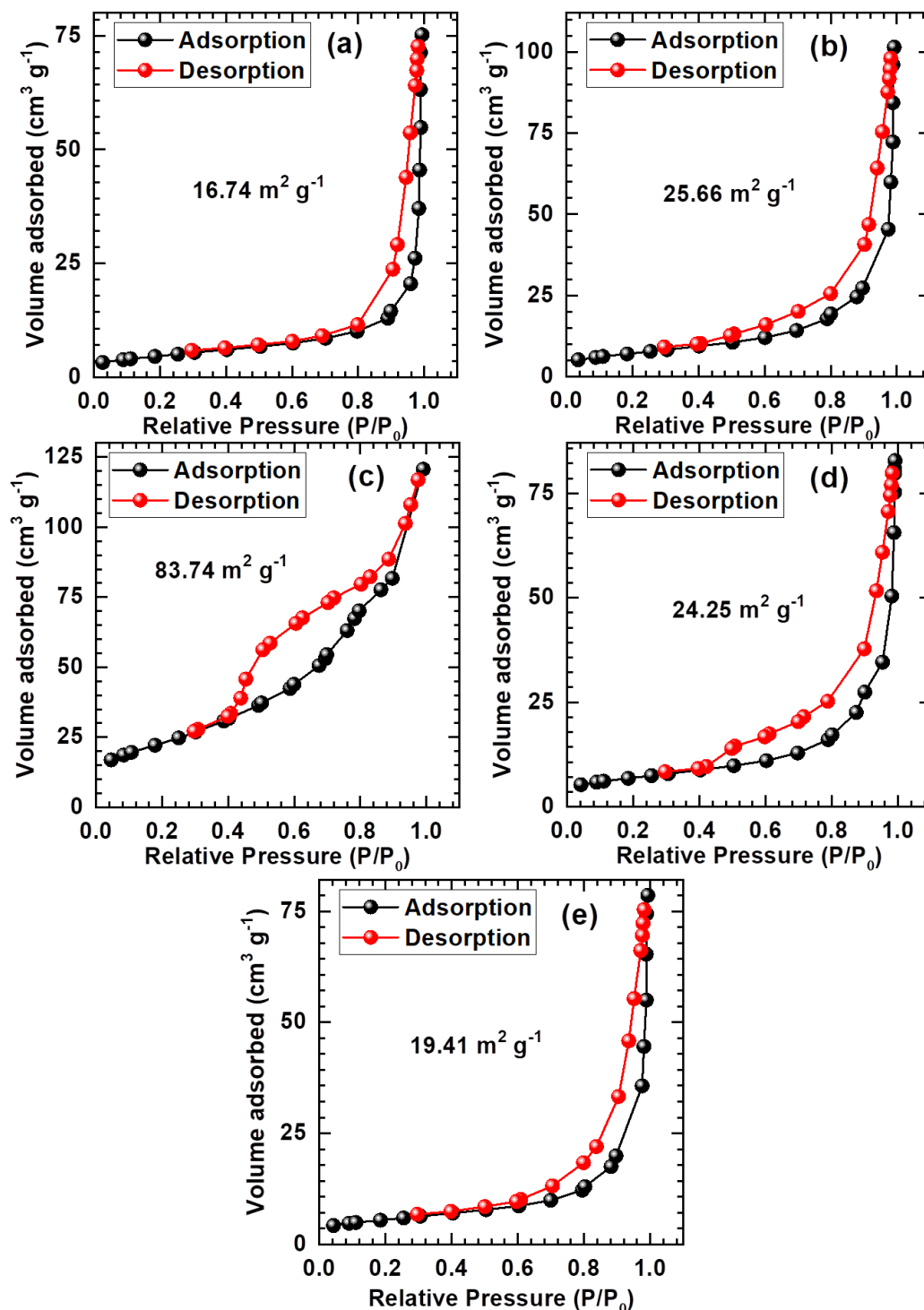


Figure 3.5: Nitrogen adsorption-desorption isotherm of samples (a) H-NCP-1, (b) H-NCP-2, (c) H-NCP-3, (d) H-NCP-4 and (e) H-NCP-5.

The BET results reveal that, electrode with optimum composition (50:50) exhibits high surface area of $83.74 \text{ m}^2 \text{ g}^{-1}$. The obtained high surface area assists more active sites for electrochemical interactions with electrolyte ions and it is convenient for energy storage application. The distribution of pore size of H-NCP series samples is exhibited in **Figure 3.6**. An average pore diameter of 26.83, 23.79, 8.90, 24.03 and 20.76 nm for samples H-NCP-1, H-NCP-2, H-NCP-3, H-NCP-4 and H-NCP-5, respectively. This macroporosity and higher surface area of the electrodes could be beneficial for high electrochemical capacitive performance.

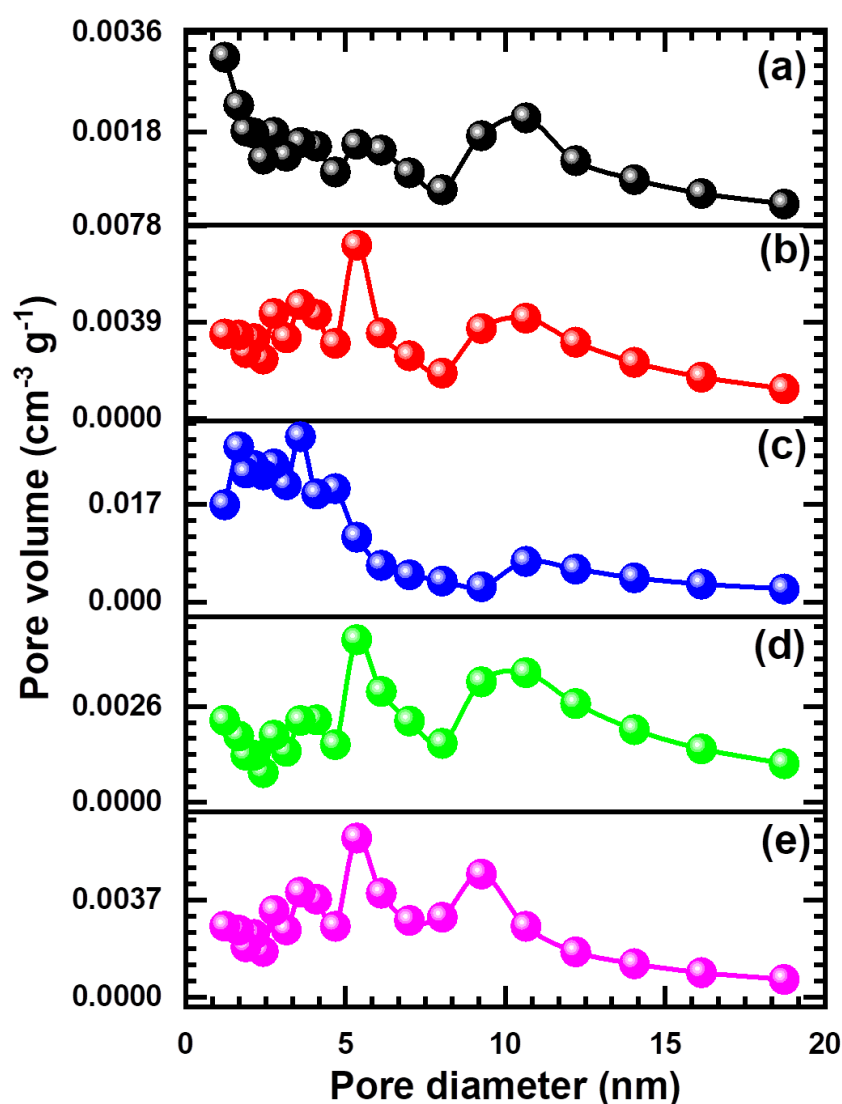


Figure 3.6: Pore size distribution curves of samples (a) H-NCP-1, (b) H-NCP-2, (c) H-NCP-3, (d) H-NCP-4 and (e) H-NCP-5.

3.2.A.3.5 XPS study:

The chemical environment and composition of the elements are analysed by employing XPS analysis. The survey spectrum of XPS for sample H-NCP-3 (**Figure**

3.7 (a) displays presence of nickel, copper, phosphorous and oxygen elements. The Ni2p XPS spectrum in **Figure 3.7 (b)** exhibits two peaks at binding energies of 874.6 and 856.90 eV corresponding to Ni2p_{1/2} and Ni2p_{3/2}, respectively which are characteristic to Ni²⁺ states with satellite peaks at 861.7 and 879.9 eV [40, 41].

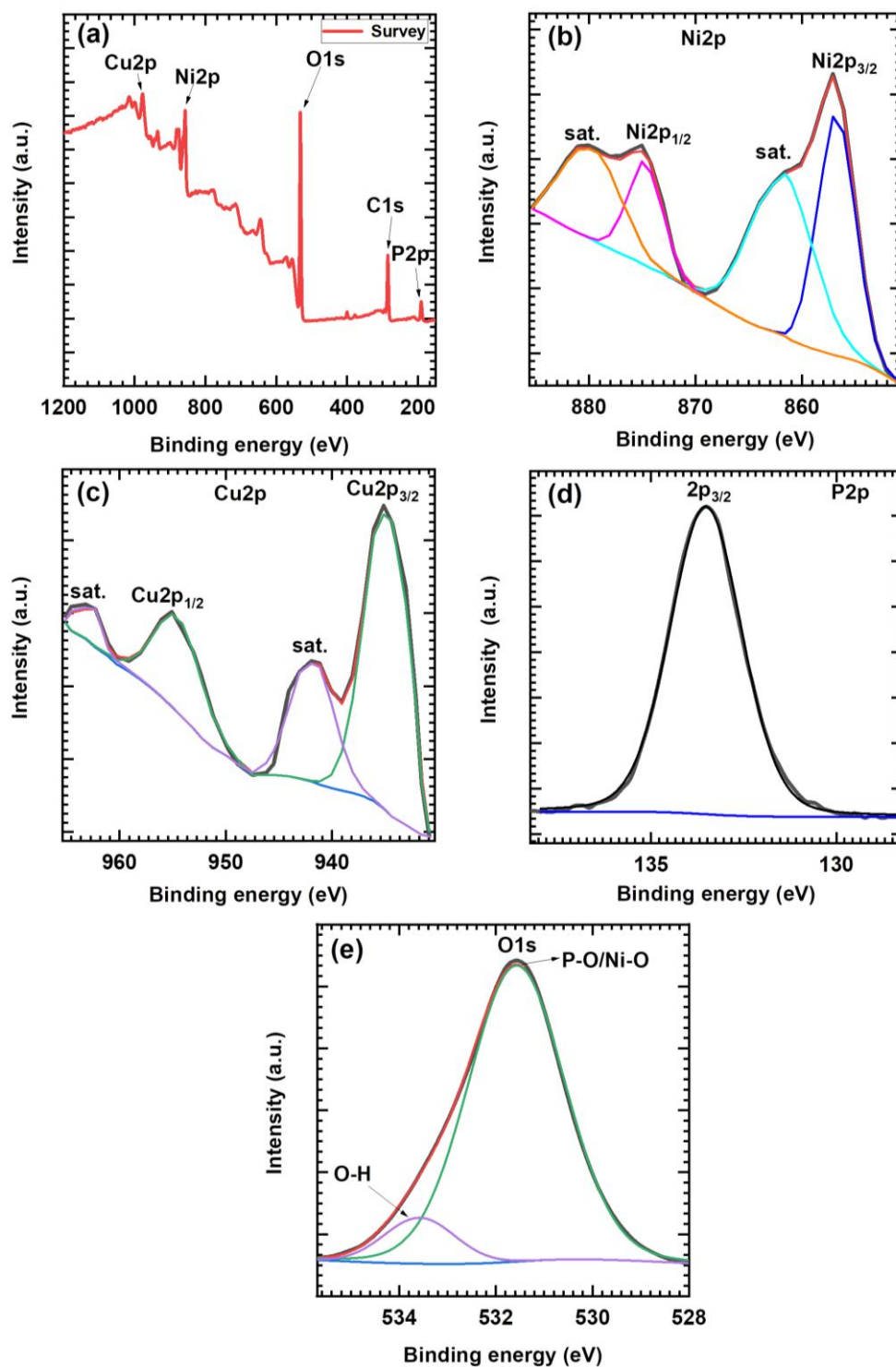


Figure 3.7: (a) Survey, (b) Ni2p, (c) Cu2p, (d) P2p and (e) O1s XPS spectra of sample H-NCP-3.

For the XPS spectrum of Cu2p region (**Figure 3.7 (c)**), the peak at 935.0 eV binding energy corresponds to Cu2p_{3/2} along with satellite peak at 941.9 eV binding energy, indicating the presence of Cu⁺ [42]. Similarly, the intense peak at 955.1 eV binding energy implies Cu2p_{1/2} and the satellite peak at 963.3 eV reveal Cu²⁺ oxidation state [16]. The P2p spectrum reveals a peak at a binding energy of 133.5 eV is due to 2P_{3/2} state represent P-O bonding (**Figure 3.7 (d)**), and confirms pentavalent state of phosphorous (PO₄³⁻) [43, 44]. **Figure 3.7 (e)** displays the core level spectrum of O1s with fitted peaks at 533.5 and 531.9 eVs which could be attributed to O1s in P-O/Ni-O and O-H compounds [45].

3.2.A.3.6 FE-SEM study:

The change in microstructure of nickel copper phosphate thin film electrodes is visualized by FE-SEM images due to the ratio variation in synthesis process. The SEM micrographs of nickel copper phosphate thin film electrodes at two different magnifications (X500 and X2000) are depicted in **Figure 3.8 (a1-e2)**. The FE-SEM images of H-NCP-1 for pristine nickel phosphate displayed in **Figure 3.8 (a1, a2)**, indicates microplates like architecture consisting of irregularly shapes with average length of 12.23 μm and average thickness of about 1.43 μm . The FE-SEM images of H-NCP-2 electrode are shown in **Figure 3.8 (b1, b2)**, the increased concentration of copper in H-NCP-2 thin film changes from dense microplates like network to microflower with interconnected microflakes. It is observed that, the microflakes are interconnected with each other and microflowers are over grown on the surface of interconnected microflakes. Also, reveals a microsheets having an average thickness of 0.67 μm . Further increase in the content of copper for H-NCP-3 thin film sample shows the microflakes like morphology with some individually overgrown microrods as displayed in **Figure 3.8 (c1, c2)**. Also, these microflakes are connected to each other forming into interconnected networks. The average thickness of nanoflakes is 0.50 μm and an average length of microrod is 6.47 μm . The nanoflakes network of H-NCP-3 can give abundant space for diffusion of electrolyte ions, which is highly desirable for SC electrodes [46]. Similarly, the H-NCP-4 thin film (**Figure 3.8 (d1, d2)**) shows a microrod -like structure with an average thickness of 6.59 μm over microflakes. FE-SEM images of H-CMP-5 for pristine copper phosphate exhibited in **Figure 3.8 (e1, e2)** represents the sample consists of uneven structured microrods with an average length of 12.11 μm . H-CMP series thin films surface morphologies with microplates

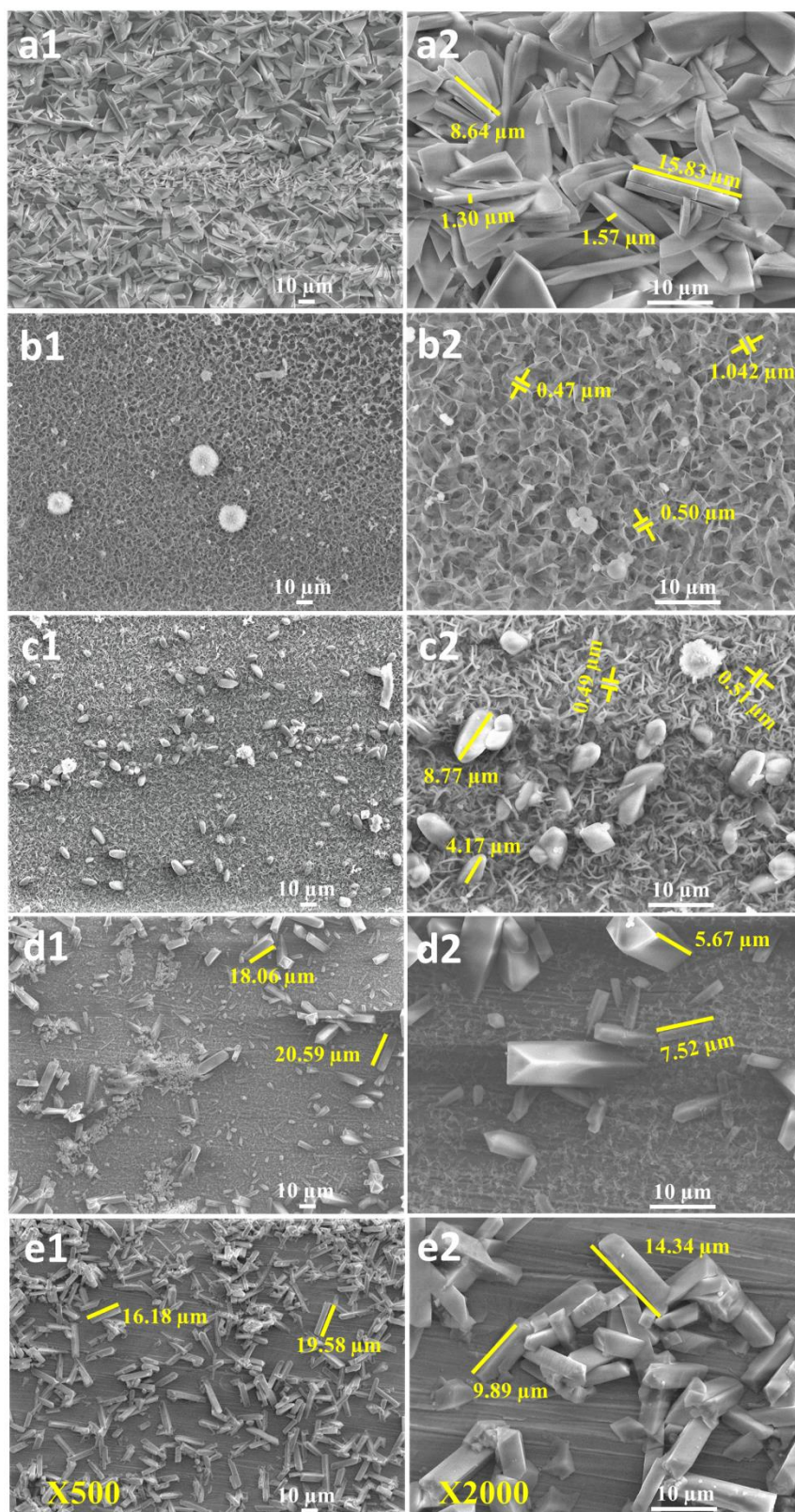


Figure 3.8: FE-SEM micrographs of nickel copper phosphate electrodes: (a1, a2) H-NCP-1, (b1, b2) H-NCP-2, (c1, c2) H-NCP-3, (d1, d2) H-NCP-4, and (e1, e2) H-NCP-5 at two magnifications (X500 and X2000).

to microrod like structure may assists largely for easy accessibility of active sites in faradic reactions to deliver high capacitive performance. Such a microplates to microrods like morphology can allow faster charge transport and rapid ion accessibility during an electrochemical reaction [47].

3.2.A.3.7 EDS study:

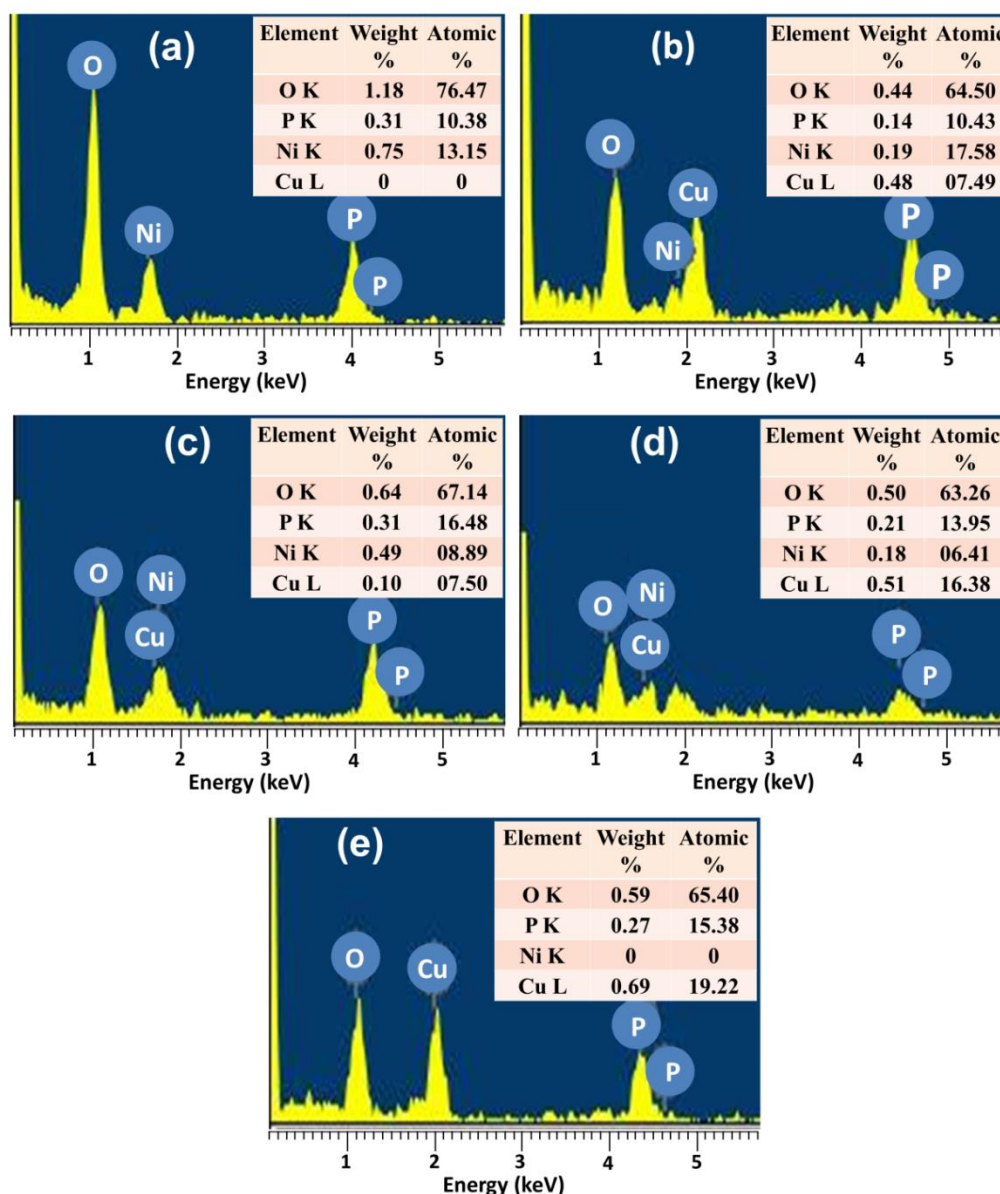


Figure 3.9: EDS spectra of nickel copper phosphate electrodes: (a) H-NCP-1, (b) H-NCP-2, (c) H-NCP-3, (d) H-NCP-4, and (e) H-NCP-5.

The chemical composition of Ni:Cu phosphate samples was investigated by EDS analysis and displayed in **Figure 3.9 (a-e)**. The H-NCP-1 sample exhibits nickel, phosphorous and oxygen elements, and confirms formation of nickel phosphate. Similarly, the H-NCP-5 sample exhibits copper, phosphorous and oxygen elements

and confirms formation of copper phosphate material. The other samples (H-NCP-1 to H-NCP-5) exhibit nickel, copper, phosphorous and oxygen elements in the EDS analysis without any other impurity, which confirm successful preparation of nickel copper phosphate material in thin film form. The observed Ni:Cu atomic ratios of H-NCP-1 to H-NCP-5 electrodes along with experimental chemical compositions are provided in **Table 3.2**.

Table 3.2: Experimental and observed Ni and Cu atomic ratio with an obtained phase of H-CMP-series thin films.

Sample name	Experimental ratio (Ni:Cu)	Observed ratio (Ni:Cu)	Obtained phase
H-NCP-1	1:0	1:0	$\text{Ni}_3(\text{PO}_4)_2 \cdot \text{H}_2\text{O}$
H-NCP-2	0.75:0.25	0.70:0.30	$\text{Ni}_{2.10}\text{Cu}_{0.90}(\text{PO}_4)_2 \cdot \text{H}_2\text{O}$
H-NCP-3	0.50:0.50	0.54:0.45	$\text{Ni}_{1.62}\text{Cu}_{1.35}(\text{PO}_4)_2 \cdot \text{H}_2\text{O}$
H-NCP-4	0.25:0.75	0.29:0.71	$\text{Ni}_{0.87}\text{Cu}_{2.13}(\text{PO}_4)_2 \cdot \text{H}_2\text{O}$
H-NCP-5	0:1	0:1	$\text{Cu}_3(\text{PO}_4)_2 \cdot \text{H}_2\text{O}$

3.2.A.4 Conclusions:

In conclusion, nickel copper phosphate thin films were directly deposited on SS substrate using a facile hydrothermal method at 388 K for 60 min. The XRD study confirmed, monoclinic crystal structure and FTIR exhibited the hydrous nature of nickel copper phosphate thin films. Also, XPS results confirmed that the obtained material is a nickel copper phosphate compound in thin film form. H-NCP series thin films illustrate different morphologies from microplates to microds and they significantly enhanced electrochemical performance. Furthermore, EDS confirmed that the chemical composition of nickel copper phosphate varies from H-NCP-1 to H-NCP-5. The overall result complements each other and confirms that the obtained material is hydrous nickel copper phosphate in thin film form.

SECTION – B

Supercapacitive performance evaluation of nickel copper phosphate thin films

3.2.B.1 Introduction:

In this section, hydrothermally synthesized nickel copper phosphate thin films are employed as SC electrodes for electrochemical capacitive testing. The concentration effect of nickel and copper on the electrochemical performance of nickel copper phosphate thin films is analyzed in conventional three-electrode system by various electrochemical measurements such as CV, GCD, cyclic stability, and EIS.

3.2.B.2 Experimental configuration for electrochemical performance measurements:

The conventional three electrode system is utilized for electrochemical measurements of nickel copper phosphate thin film electrodes in 1 M KOH electrolyte solution. For the three electrode system, nickel copper phosphate thin films were employed as a working electrode, platinum sheet as a counter electrode and Hg/HgO as a reference electrode. The 1 cm² area of working electrode was immersed in the electrolyte for precise electrochemical measurement. The arrangement of the experiment for the electrochemical performance evaluation is displayed in **Figure 3.10**. The electrochemical studies are executed using the ZIVE MP1 workstation. The CV is considered a favourable technique for the evaluation of redox involved and potentials electron-transfer redox reactions. The GCD technique is employed to evaluate the capacitive retention of electrode material in terms of C_s (equation 2.8), ED (equation 2.9), and PD (equation 2.10) of the electrode.

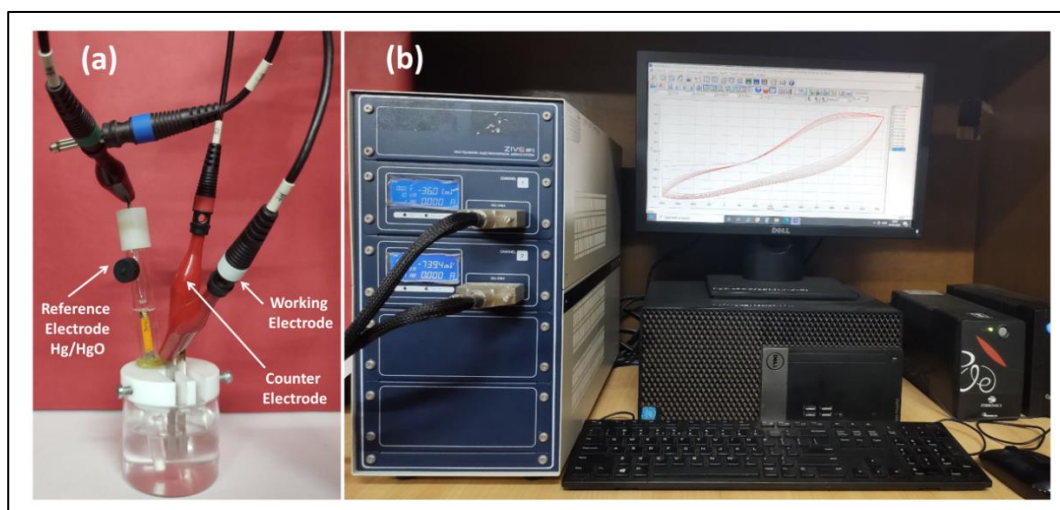


Figure 3.10: Photographs of (a) Three electrode system and, (b) experimental set up consisting of an electrochemical workstation.

3.2.B.3 Results and discussion:

3.2.B.3.1 CV study:

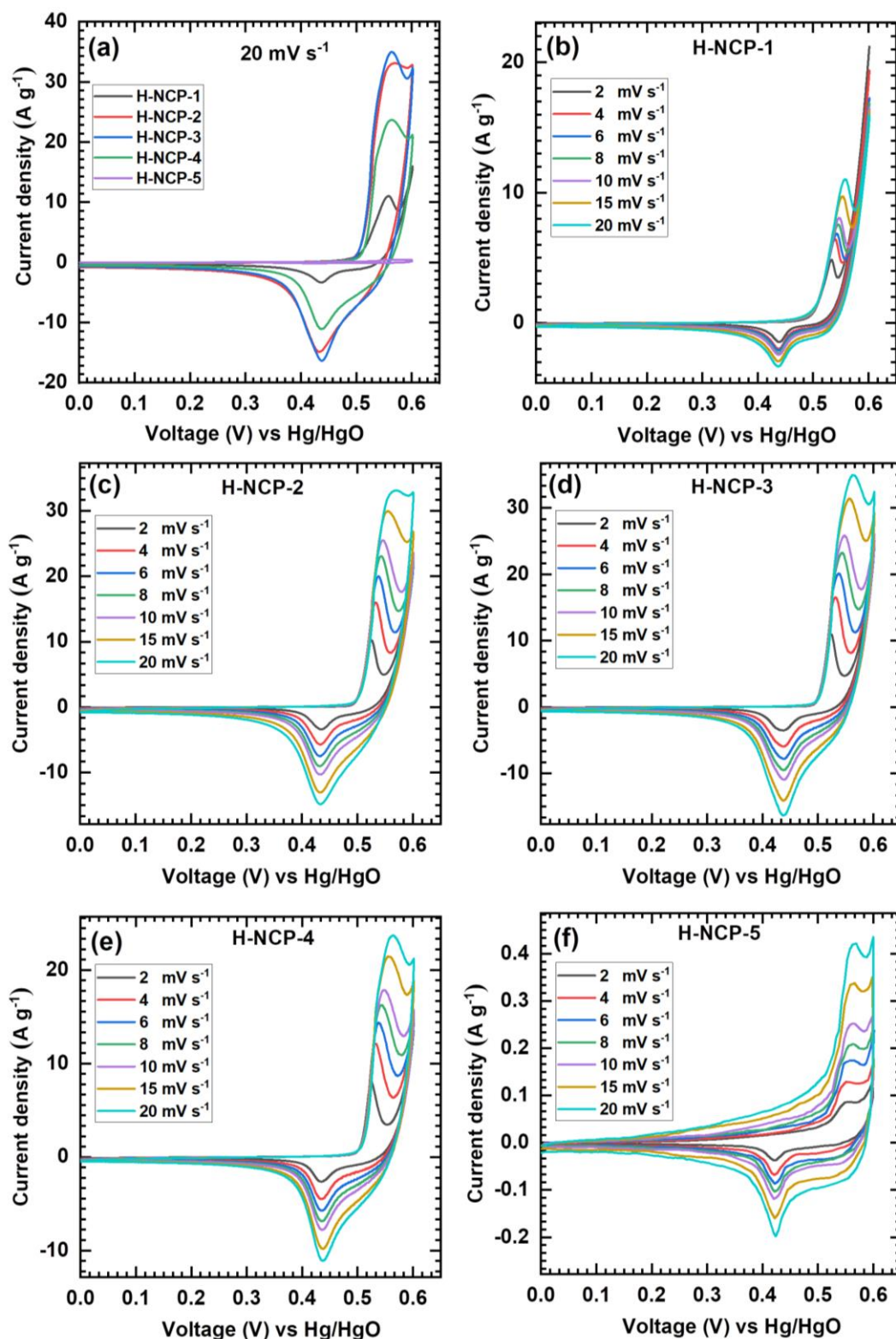


Figure 3.11: (a) The comparative CV curves of H-NCP series electrodes at 20 mV s⁻¹ scan rate, the CV curves at different scan rates from 2-20 mV s⁻¹ for (b) H-NCP-1, (c) H-NCP-2, (d) H-NCP-3, (e) H-NCP-4 and (f) H-NCP-5 electrodes.

The morphology altered caused by molar ratio variation of nickel and copper in nickel copper phosphate material and its effect on supercapacitive performance was examined in electrochemical cell of three electrode system. **Figure 3.11** shows CV curves of H-NCP series electrodes in the optimized potential window of 0 to 0.6 V (vs Hg/HgO). The comparative CV curves of H-NCP series electrodes at 20 mV s⁻¹ scan rate are revealed in **Figure 3.11**. The area under CV curve of H-NCP-3 electrode is higher than nickel phosphate (H-NCP-1), copper phosphate (H-NCP-5) and other nickel copper phosphate electrodes. Combined microstructure of microflakes and microsheets reveal higher area under the curve than single microplates and microrods like structure due to large number of electrochemical active sites.

The CV curves of H-NCP series electrodes at various scan rates from 2-20 mV s⁻¹ are displayed in **Figure 3.11 (b-f)**. The nickel phosphate electrode (H-NCP-1) and copper phosphate electrodes (H-NCP-5) show well-established redox peaks (**Figure 3.11 (b and f)**) confirm pseudocapacitive nature of material. Increasing copper content affects the morphology that ultimately influence on the electrochemical performance in terms of area under CV curves. The changing of CV nature from nickel phosphate to copper phosphate electrode (H-NCP-1 to H-NCP-5) is very clearly noticed in the **Figure 3.11** from **(b)** to **(f)**. Area under the curve increases for each sample (**Figure 3.11**) with increasing scan rates from 2-20 mV s⁻¹, which exhibits the voltammetric current is directly proportional to the scan rate. At lower scan rate, due to more time for the diffusion process, electrolytic ions get accessibility to it works in inner surface of the material which increases the utilization of electrode material and at the higher scan rate, only the outer surface of material is utilized for the storage of electrolytic ions. The charge storage kinetics from CV curves of prepared nickel copper phosphate thin film electrodes were examined by using power's law. The scan rate dependent CV current represented by the powers law using the following equation.

$$i_p = av^b \quad (3.5)$$

Where, i_p denotes peak current, a and b are adjustable parameters, v is scan rate, while b has determined values. For H-NCP series electrode, graph of log (i) vs log (v) plotted in **Figure 3.12** and calculated their b values from slope of graph.

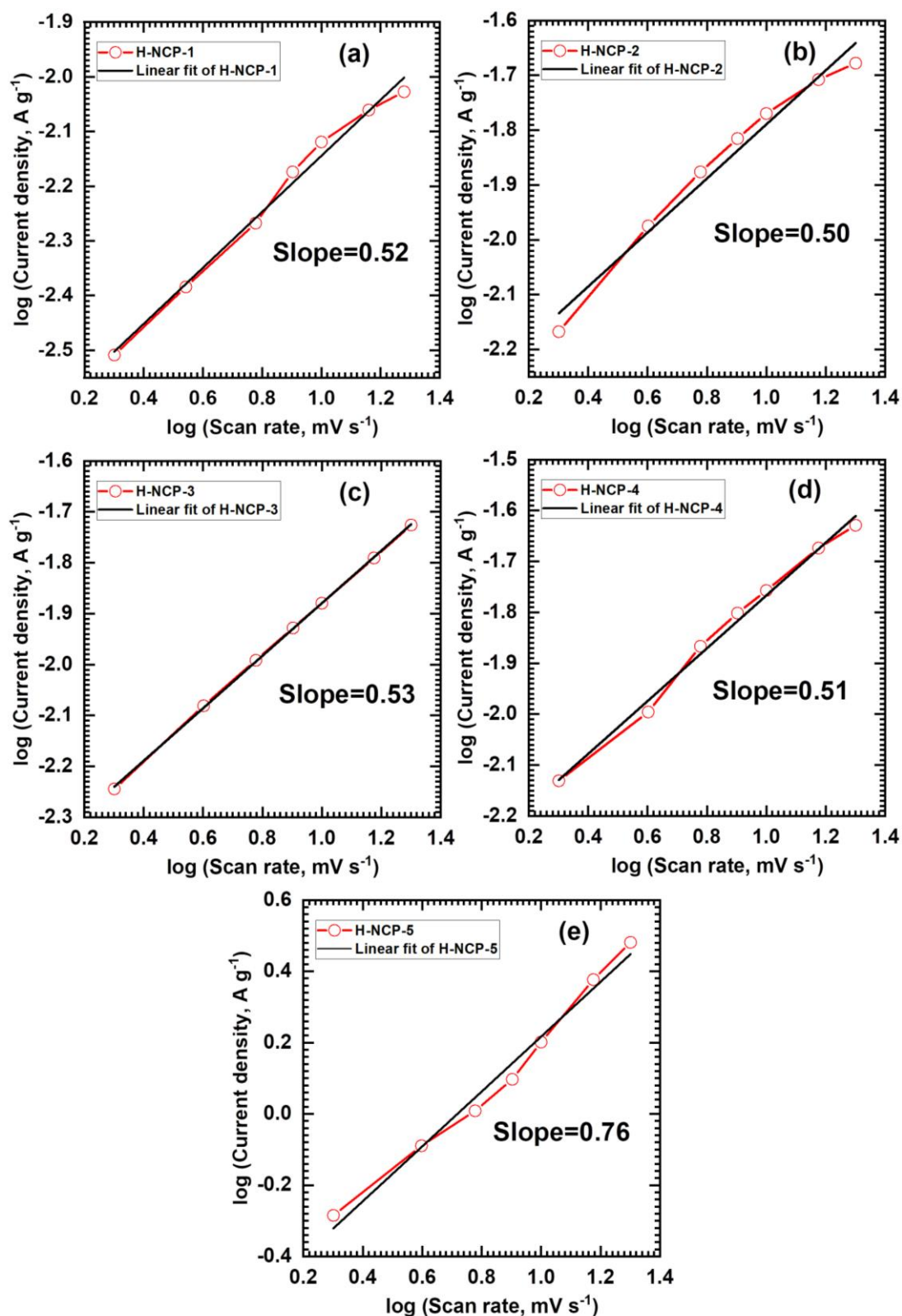


Figure 3.12: Plots of $\log(\text{current density, A g}^{-1})$ versus $\log(\text{scan rate, mV s}^{-1})$ for electrodes (a) H-NCP-1, (b) H-NCP-2, (c) H-NCP-3, (d) H-NCP-4, and (e) H-NCP-5.

The basic conditions for the b value is, when it is 0.5 then the faradic electrochemical process and if it is 1 then the electrochemical process is capacitive

[48]. The prepared H-NCP-1, H-NCP-2, H-NCP-3, H-NCP-4, and H-NCP-5 electrodes exhibit b values of 0.52, 0.50, 0.53, 0.51, and 0.76, respectively. The values of b for H-NCP series electrodes ranging from 0.5 to 1 illustrate both (diffusive and capacitive) processes are responsible for charge storage. To identify the individual contribution of surface pseudo-capacitive and battery process modified Power's law can be used as expressed in following equation.

$$I_p = C_s v + C_b v^{1/2} \quad (3.6)$$

Where, I_p represent peak current density, v is the scan rate, and $C_s v$ and $C_b v^{1/2}$ illustrate current contribution from surface pseudo-capacitive (I_{surface}) and bulk process (I_{bulk}) [49]. The contribution of current density from the surface pseudo-capacitive (I_{surface}) and battery-like (I_{bulk}) process for nickel copper phosphate thin film electrodes at various scan rates 2-20 mV s^{-1} are expressed in **Figure 3.13 (a-e)**. It observed that, with increasing scan rate the contribution from pseudocapacitive surface process increases, which concluded that capacitive process is dominant at high scan rate and diffusive process is dominant at low scan rate and so, the active material shows battery like nature at low scan rate and more capacitive nature at high scan rates. The H-NCP-5 electrode (copper phosphate) shows highest capacitive contribution (24%) than the other samples at scan rate of 2 mV s^{-1} . Conversely, the nickel phosphate electrode (H-NCP-1) shows ~10% capacitive current contribution in total current at scan rate of 2 mV s^{-1} . The H-NCP-3 electrode shows moderate capacitive current contribution of ~13% and other sample reveals different values of current contribution owing to different chemical compositions (nickel and copper) and morphology.

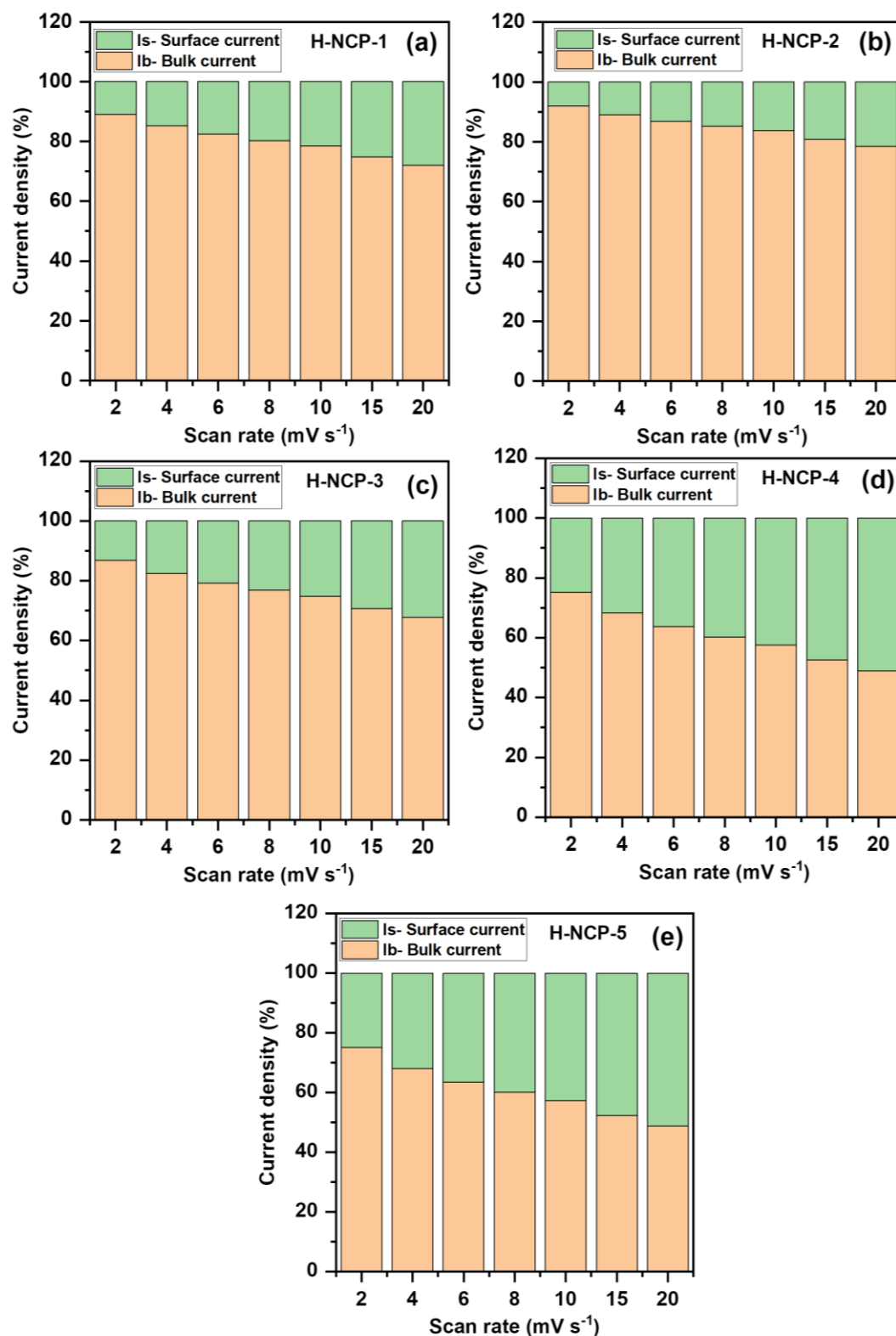


Figure 3.13: Graphs of calculated contribution of pseudocapacitive (surface current) and battery type (bulk current) in current density at various scan rates (2 to 20 mV s^{-1}) of (a) H-NCP-1, (b) H-NCP-2, (c) H-NCP-3, (d) H-NCP-4 and (e) H-NCP-5 electrodes.

3.2.B.3.2 GCD study:

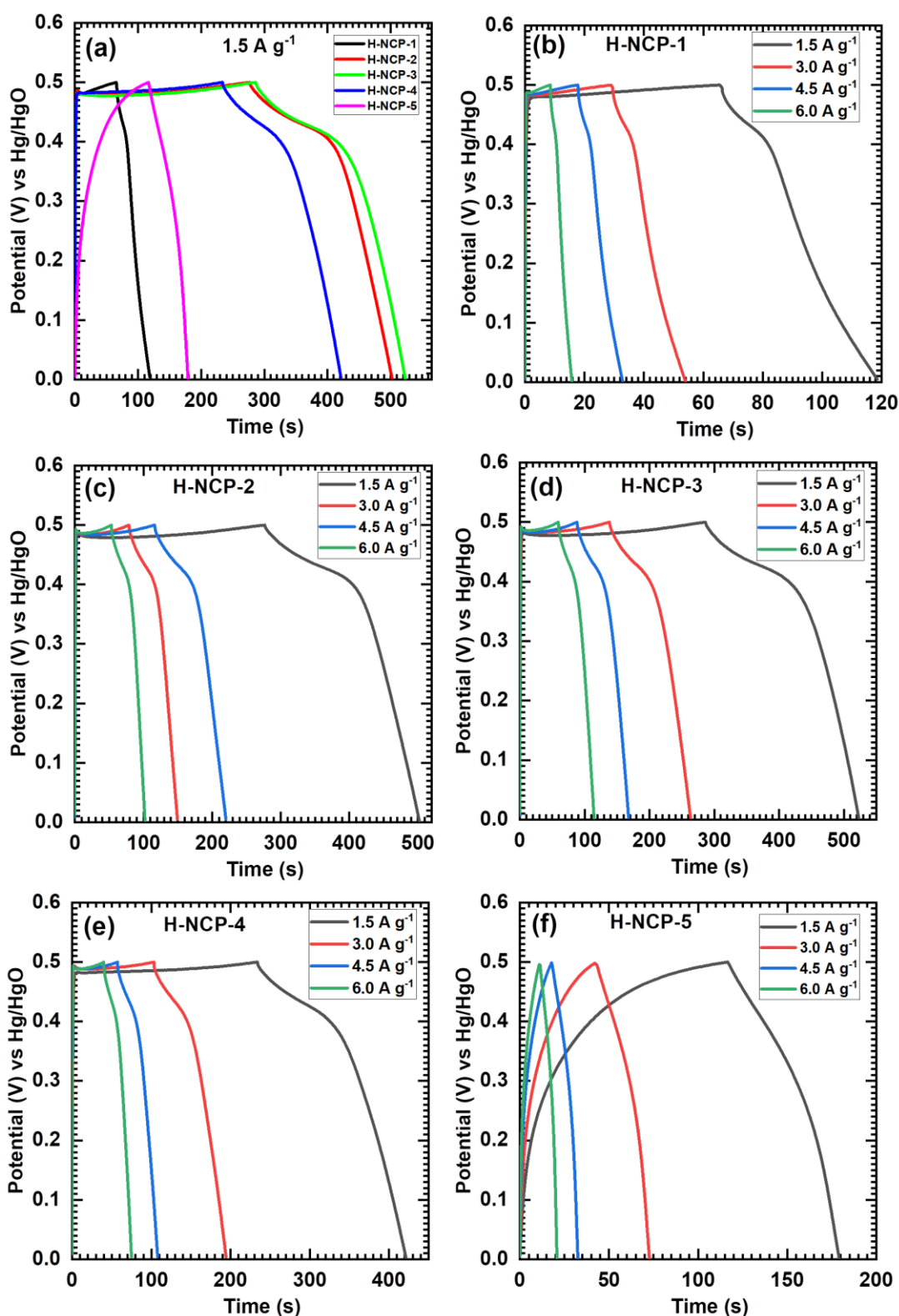


Figure 3.14: (a) Comparative GCD curves of H-NCP series electrodes at 1.5 A g⁻¹ current density, GCD curves at various current densities from 1.5-6.0 A g⁻¹ of (b) H-NCP-1, (c) H-NCP-2, (d) H-NCP-3, (e) H-NCP-4 and (f) H-NCP-5 electrodes.

The electrochemical capacitive performance of H-NCP-series electrodes was investigated by the GCD technique. The GCD curves of H-NCP-series electrodes at different current densities in the optimized potential of 0.0 to 0.5 V (vs Hg/HgO) are displayed in **Figure 3.14**. Comparative GCD curves of H-NCP series electrodes at 1.5 A g⁻¹ current density are exhibited in **Figure 3.14 (a)**. The nickel phosphate (H-NCP-1) and copper phosphate (H-NCP-5) electrodes show distinct nature of charge-discharge curve as shown in **Figure 3.14 (b-f)**. The non-linear (quasi-triangular) profile of the charge and discharge curves reveals the intercalation pseudocapacitive nature of nickel copper phosphate thin films [50, 51].

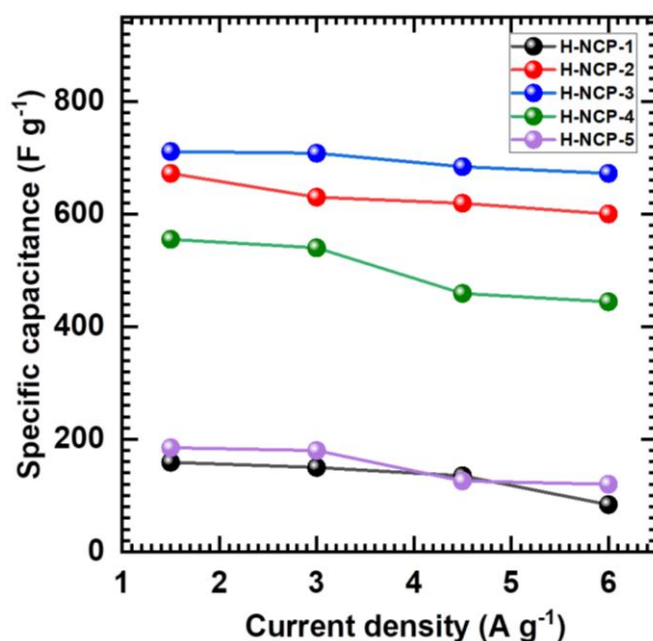


Figure 3.15: C_s of H-NCP series thin films at various current densities (1.5-6.0 A g⁻¹).

The C_s calculated from GCD curves for H-NCP series electrodes using the equation 2.8 are plotted in **Figure 3.15**. The H-NCP-3 electrode with optimum Ni:Cu ratio shows high discharging time and reveal higher C_s than other electrodes. The H-NCP-3 electrode shows maximum C_s of 711 F g⁻¹ at 1.5 A g⁻¹ current density and it decreases up to 672 F g⁻¹ at 6 A g⁻¹ current density confirms good capacitive retention even at high current density. Similarly, the H-NCP-1, H-NCP-2, H-NCP-4 and H-NCP-5 thin film electrodes show maximum C_s of 159, 672, 555 and 185 F g⁻¹, respectively at 1.5 A g⁻¹ current density. It indicated that, at high current density C_s value decreases due to fast charging-discharging rate. Conversely, at lower current density maximum utilization of active material is feasible due to more penetration time for electrolyte ions in the interior surface of the material which contributes in the high capacitance [52]. The better electrochemical capacitive performance of H-NCP-3

electrode is originated from synergistic effect of nickel and copper species (50:50 ratio) and high surface area offered by nanoflakes-like morphology.

3.2.B.3.3 EIS study:

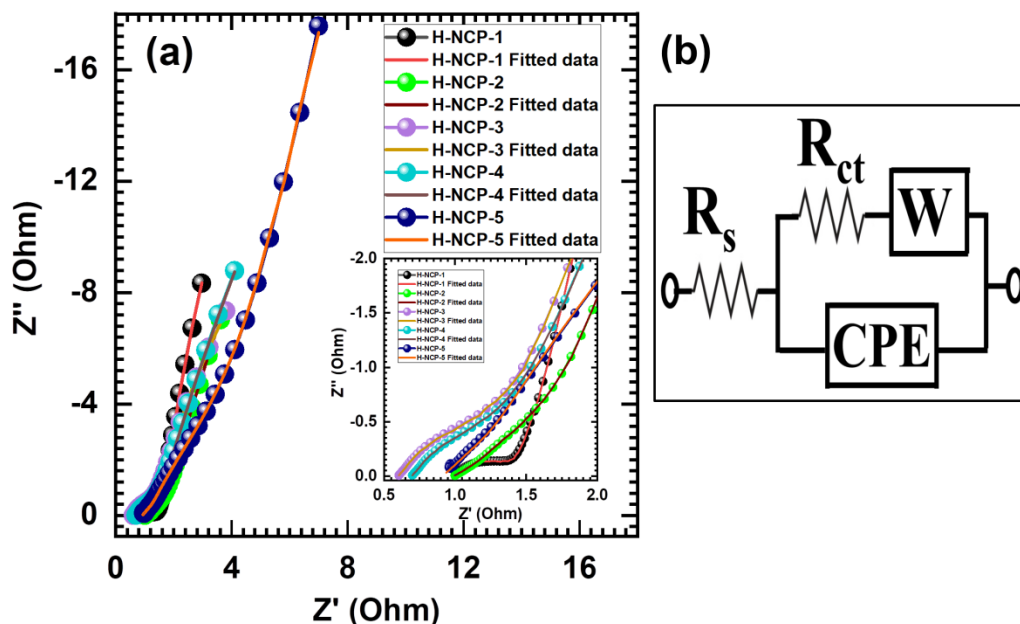


Figure 3.16: (a) The Nyquist plots of H-NCP series electrodes (H-NCP-1 to H-NCP-5) and (b) the fitted equivalent circuit for the EIS data.

The measured electrochemical impedance quantitatively examines the electrochemical characteristics of thin film electrodes and electrolytes. The EIS study was conducted in the range of 100 kHz to 100 MHz with an amplitude of 10 mV at open circuit potential. The Nyquist plots of H-NCP series electrodes are presented in **Figure 3.16 (a)**. Typically, all Nyquist plots display two different portions: the semi-circle in the high-frequency portion indicates R_s and R_{ct} , the middle frequency portion associated with the diffusion-controlled process denoted by the Warburg element (W), and the low-frequency (straight line) portion indicates the capacitive behaviour [53, 54].

An equivalent circuit is shown in **Figure 3.16 (b)** and the fitted parameters of the equivalent circuit are provided in **Table 3.3**. The R_s and R_{ct} interface resistance with a constant phase element (CPE) exhibit general imperfect capacitors (when $n = 1$ and $Q = C$) ascribed to semi-infinite diffusion charges [55]. The R_s values for H-NCP-1, H-NCP-2, H-NCP-3, H-NCP-4, and H-NCP-5 electrodes are found to be 0.81, 0.98, 0.59, 0.68, and 0.90 Ω , respectively, and the R_{ct} values are 1.73, 5.33, 2.30, 12.8, and 3.50 Ω , respectively. The smaller values of R_s and R_{ct} for H-NCP series thin films indicate a good attachment of active material with SS substrate acting as a current collector and the

spontaneous electrochemical reaction among the electrolyte and active electrode material. Also, it is revealed good ionic conductivity of electrolyte and very low IR value of material which lead to a high capacitance of H-NCP-3 electrode.

Table 3.3: Electrochemical impedance spectroscopic fitted circuit parameters.

Sample name	R_s (Ω)	R_{ct} (Ω)	CPE (mF)	n	W (Ω)
H-NCP-1	0.81	1.73	0.19	1.0	0.15
H-NCP-2	0.98	5.33	0.32	0.93	0.40
H-NCP-3	0.59	1.60	0.39	0.61	0.49
H-NCP-4	0.68	2.80	0.67	0.62	0.48
H-NCP-5	0.90	3.50	0.78	0.74	0.45

3.2.B.3.4 Stability study:

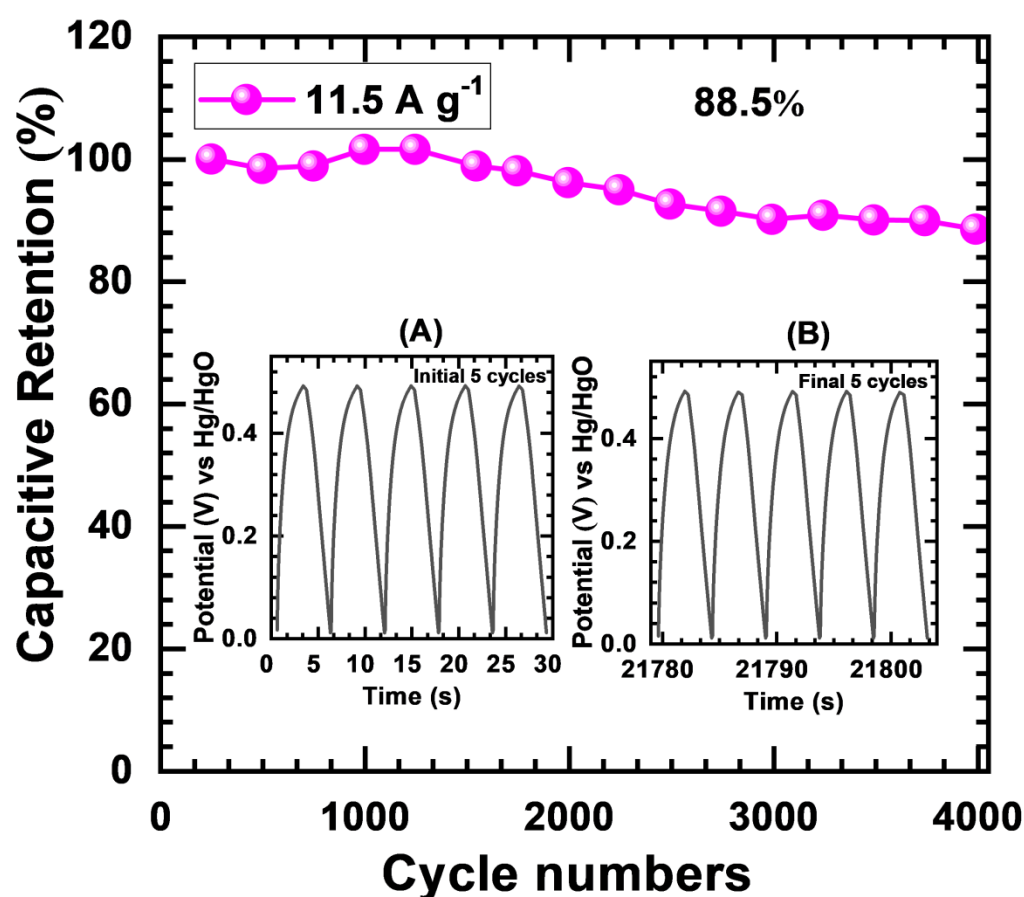


Figure 3.17: The plot of capacitive retention of H-NCP-3 electrode at 11.5 A g⁻¹ current density for 4000 cycles (inset: GCD curves of (A) initial and (B) final 5 cycles).

Electrochemical cycling stability is essential parameter for the SC application. The electrochemical stability of H-NCP-3 electrode was tested for 4000 GCD cycles at 11.5 A g^{-1} current density as exhibited in **Figure 3.17**. The H-NCP-3 electrode exhibits 88.5% capacitive retention after 4000 GCD cycles. The GCD curves of initial 5 cycles and final 5 cycles are presented as inset of **Figure 3.17** as (A) and (B), respectively. The decrement in charge-discharge time is observed in initial and final GCD cycles (inset **Figure 3.17**). Such, decrease in capacitance after 4000 cycle is observed due to the loss of active material by the dissolution or detachment during the early charging-discharge cycles [56].

3.2.B.4 Conclusions:

In this chapter, the electrochemical performance of nickel copper phosphate (H-NCP series) thin film electrodes was tested by a three-electrode system in aqueous 1 M KOH electrolyte. The maximum C_s of 711 F g^{-1} is obtained for H-NCP-3 ($\text{Ni}_{1.62}\text{Cu}_{1.35}(\text{PO}_4)_2 \cdot \text{H}_2\text{O}$) electrode at 1.5 A g^{-1} current density. Also, a small value of R_s ($0.59 \text{ } \Omega$) and R_{ct} ($1.30 \text{ } \Omega$) implies high electrochemical conductivity and good charge transfer kinetics of the H-NCP-3 electrode. Moreover, the H-NCP-3 electrode revealed excellent capacitive retention of 88.5% over 4000 cycles. Among H-NCP series thin films, the H-NCP-3 electrode displayed high electrochemical capacitive performance and it can be utilized as a cathode in asymmetric SC device fabrication.

3.3 References:

1. H. Chen, S. Jiang, B. Xu, C. Huang, Y. Hu, Y. Qin, M. Heb, H. Cao, J. Mater. Chem. A, 7, (2019), 6241-6249.
2. L. Feng, Y. Zhu, H. Ding, C. Ni, J. Power Sources, 267, (2014), 430-444.
3. S. Marje, P. Katkar, S. Pujari, S. Khalate, A. Lokhande, U. Patil, Synth. Met., 259, (2020), 116224.
4. J. Li, D. Chen, Q. Wu, Eur. J. Inorg. Chem., 10, (2019), 1301-1312.
5. A. Mirghni, K. Oyedotun, O. Olaniyan, B. Mahmoud, N. Sylla, N. Manyala, RSC Adv., 9, (2019), 25012-25021.
6. N. Padmanathan, H. Shao, K. Razeeb, ACS Appl. Mater. Interfaces, 10, (2018), 8599-8610.
7. P. Simon, Y. Gogotsi, Nat. Mater., 7, (2008), 845-854.
8. Y. Lu, T. Wang, X. Li, G. Zhang, H. Xue, H. Pang, RSC Adv., 6, (2016), 87188-87212.
9. N. Mohamed, N. Allam, RSC Adv., 10, (2020), 21662-21685.
10. S. Khalate, S. Kadam, Y-R. Ma, S. Pujari, S. Marje, P. Katkar, A. Lokhande, U. Patil, Electrochim. Acta, 319, (2019), 118-128.
11. K. Mi, Y. Ni, J. Hong, J. Phys. Chem. Solids, 72, (2011), 1452-1456.
12. H. Wan, L. Li, Y. Chen, J. Gong, M. Duan, C. Liu, J. Zhang, H. Wang, Electrochimica Acta, 229, (2017), 380-386.
13. M. Cheng, H. Fan, Y. Xu, R. Wang, X. Zhang, Nanoscale, 9, (2017), 14162-14171.
14. S. Carenco, D. Portehault, C. Boissière, N. Mézailles, C. Sanchez, Chem. Rev., 113, (2013), 7981-8065.
15. E. Farahi, N. Memarian, Chem. Phys. Lett., 730, (2019), 478-484.
16. Y. Ni, K. Liao, J. Li, CrystEngComm, 12, (2010), 1568-1575.
17. L. Yu, J. Zhang, Y. Dang, J. He, Z. Tobin, P. Kerns, Y. Dou, Y. Jiang, Y. He, S. Suib, ACS Catal., 9, (2019), 6919-6928.
18. H. Sharkawy, D. Sayed, A. Dhmees, R. Aboushahba, N. Allam, ACS Appl. Energy Mater., 3, (2020), 9305-9314.
19. D. Dubal, J. Kim, Y. Kim, R. Holze, C. Lokhande, W. Kim, Energy Technol., 2, (2014), 325-341.
20. S. Palchoudhury, K. Ramasamy, R. Gupta, A. Gupta, Front. Mater., 5, (2019), 1-9.
21. P. Katkar, S. Marje, V. Parale, C. Lokhande, J. Gunjekar, H-H. Park, U. Patil, Langmuir, 37 (17), 5260-5274.
22. S. Marje, P. Katkar, S. Pujari, S. Khalate, P. Deshmukh, U. Patil, Mater. Sci. Eng. C, 261, (2020), 114641.
23. P. Katkar, S. Marje, S. Pujari, S. Khalate, A. Lokhande, U. Patil, ACS Sustainable Chem. Eng., 7, (2019), 11205-11218.
24. G. Gund, D. Dubal, S. Jambure, S. Shinde, C. Lokhande, J. Mater. Chem. A, 1, (2013), 4793-4803.
25. G. Cai, J. Tu, D. Zhou, L. Li, J. Zhang, X. Wang, C. Gu, CrystEngComm, 16, (2014), 6866-6872.
26. U. Patil, J. Sohn, S. Kulkarni, S. Lee, H. Park, K. Gurav, J. Kim, S. Jun, ACS Appl. Mater. Interfaces, 6, (2014), 2450-2458.
27. Y. Zhao, J. Wang, H. Chen, T. Pan, J. Zhang, C. Cao, Electrochim. Acta, 50, (2004), 91-98.
28. S. Navale, V. Mali, S. Pawar, R. Mane, M. Naushad, F. Stadler, V. Patil, RSC Adv., 5, (2015), 51961-51965.

29. B. Ameri, S. Davarani, R. Roshani, H. Moazami, A. Tadjarodi, J. Alloys Compd., 695, (2017), 114-123.
30. N. Prokopchuk, V. Kopilevich, L. Voitenko, Russ. J. Appl. Chem., 81, (2008), 386-391.
31. S. Kullyakool, C. Danvirutai, K. Siri Wong, P. Noisong, J. Therm. Anal. Calorim., 115, (2014), 1497-1507.
32. P. Noisong, C. Danvirutai, T. Srithanratana, B. Boonchom, Solid State Sci., 10, (2008), 1598-1604.
33. H. Wen, M. Cao, G. Sun, W. Xu, D. Wang, X. Zhang, C. Hu, J. Phys. Chem. C, 112, (2008), 15948-15955.
34. P. Katkar, S. Marje, S. Kale, A. Lokhande, C. Lokhande, U. Patil, CrystEngComm, 21, (2019), 884-893.
35. B. Liang, Y. Chen, J. He, C. Chen, W. Liu, Y. He, X. Liu, N. Zhang, V. Roy, ACS Appl. Mater. Interfaces, 10, (2018), 3506-3514.
36. D. Wang, Y. Xu, W. Sun, X. Guo, L. Yang, F. Wang, Z. Yang, Electrochim. Acta, 337, (2020), 155827.
37. S. Sartale, C. Lokhande, Mater. Chem. Phys., 65, (2000), 63-67.
38. Z. Jiang, W. Lu, Z. Li, K. H. Ho, X. Li, X. Jiao, D. Chen, J. Mater. Chem. A, 2, (2014), 8603-8606.
39. K. Sing, D. Everett, R. Haul, L. Moscou, R. Pierotti, J. Rouquerol, T. Siemieniewska, Pure Appl. Chem., 57, (1985), 603-619.
40. J. B. Condon, Surface Area and Porosity Determinations by Physisorption: Measurements and Theory (Elsevier, Amsterdam, 2006), pp. 6-14.
41. J. Gunjekar, T. Kim, H. Kim, I. Kim, S. Hwang, J. Am. Chem. Soc., 133, (2011), 14998-15007.
42. X. Peng, H. Chai, Y. Cao, Y. Wang, H. Dong, D. Jia, W. Zhou, Mater. Today Energy, 7, (2018), 129-135.
43. W. Bian, Y. Huang, X. Xu, M. Din, G. Xie, X. Wang, ACS Appl. Mater. Interfaces, 10, (2018), 9407-9414.
44. A. Han, H. Zhang, R. Yuan, H. Ji, P. Du, ACS Appl. Mater. Interfaces, 9, (2017), 2240-2248.
45. R. Yuan, J. Yuan, Y. Wu, P. Ju, L. Ji, H. Li, L. Chen, H. Zhou, J. Chen, Colloids Surf. A, 547, (2018), 56-63.
46. G. Hu, X. Deng, Z. Peng, K. Du, Electrochim. Acta, 53, (2008), 2567-2573.
47. X. Wang, H. Jian, Q. Xiao, S. Huang, Appl. Surf. Sci., 459, (2018), 40-47.
48. K. Malaie, M. Ganjali, T. Alizadeh, J Mater Sci: Mater Electron 28, (2017), 14631-14637.
49. K. Sankar, Y. Seo, S. Lee, S. Jun, ACS Appl. Mater. Interfaces, 10, (2018), 8045-8056.
50. M. Sathiya, A. Prakash, K. Ramesha, J. Tarascon, A. Shukla, J. Am. Chem. Soc., 133, (2011), 16291-16299.
51. S. Pujari, S. Kadam, Y-R. Ma, P. Katkar, S. Marje, S. Khalate, A. Lokhande, U. Patil, J. Electron. Mater., 49, (2020), 3890-3901.
52. F. Omar, A. Numan, S. Bashir, N. Duraisamy, R. Vikneswaran, Y. Loo, K. Ramesh, S. Ramesh, Electrochim. Acta, 273, (2018), 216-228.
53. S. Kandalkar, H. Lee, S. Seo, K. Lee, C. Kim, J. Mater. Sci., 46, (2011), 2977-2981.
54. J. Cherusseria, K. Kar, J. Mater. Chem. A, 4, (2016), 9910-9922.
55. B. Xie, Y. Chen, M. Yu, X. Shen, H. Lei, T. Xie, Y. Zhang, Y. Wu, Nanoscale Res. Lett, 10, (2015), 332.

56. J. Xiao, S. Yang, *J. Mater. Chem.*, 22, (2012), 12253-12262.
57. P. Deshmukh, S. Pusawale, V. Jamadade, U. Patil, C. Lokhande, *J. Alloys Compd.*, 509, (2011), 5064-5069.
58. Y-K. Hsu, Y-C. Chen, Y-G. Lin, *Electrochim. Acta*, 139, (2014), 401-407.

CHAPTER-4

SYNTHESIS AND CHARACTERIZATION OF NICKEL COPPER PHOSPHATE THIN FILMS BY SILAR METHOD

CHAPTER 4

Synthesis and characterization of nickel copper phosphate thin films by SILAR method

Sr. No.	Title	Page No.
4.1	Introduction	89
SECTION – A		
SILAR synthesis and characterization of nickel copper phosphate thin films		
4.2.A.1	Introduction	89
4.2.A.2	Experimental details	90
	4.2.A.2.1 Chemicals	90
	4.2.A.2.2 Synthesis of nickel copper phosphate thin films	90
4.2.A.3	Results and discussion	92
	4.2.A.3.1 Film formation and reaction mechanism	92
	4.2.A.3.2 XRD study	93
	4.2.A.3.3 FT-IR study	94
	4.2.A.3.4 BET study	95
	4.2.A.3.5 XPS study	97
	4.2.A.3.6 FE-SEM study	99
	4.2.A.3.7 EDS study	101
4.2.A.4	Conclusions	102
SECTION – B		
Supercapacitive performance evaluation of nickel copper phosphate thin films		
4.2.B.1	Introduction	102
4.2.B.2	Results and discussion	103
	4.2.B.2.1 CV study	103
	4.2.B.2.2 GCD study	107
	4.2.B.2.3 EIS study	109
	4.2.B.2.4 Stability study	110
4.2.B.3	Conclusions	111
4.3	References	112

4.1 Introduction:

Recently, TMPs, as an emerging variety of essential functional material, have been widely investigated for several applications such as photocatalytic reactions [1, 2], rechargeable batteries [3, 4], catalytic water splitting [5, 6] and SCs [7, 8] owing to their outstanding electrical conductivity and excellent electrochemical performance. Furthermore, TMPs exhibit prominent thermal stability as well as good resistance to the ambient environment, permits them to be employed as stable electrode materials. Hence, various TMPs such as cobalt phosphate [7], nickel phosphate [8], silver phosphate [9], and copper phosphate [10] have been explored as an electrode material for SC application.

The various phases and morphologies of metal phosphates are obtained using various synthesis processes. The different polymorphs of nickel phosphate such as, $\text{Ni}_{11}(\text{HPO}_3)_8(\text{OH})_6$ [11], $\text{Ni}_3(\text{PO}_4)_2$ [12], $\text{Ni}_2\text{P}_2\text{O}_7$ [13], etc. were synthesized for SC application. Similarly, the polymorphs of copper phosphate such as $\text{Cu}_2\text{P}_2\text{O}_7$ [14], $\text{Cu}_2(\text{PO}_4)(\text{OH})$ [10], etc. were prepared and studied for SC application. It is known that, the synergistic effect between the nickel and copper species can offer large electrochemical response for nickel copper binary phosphate material [15].

So considering benefits of synergistic effect, nickel and copper species are combined and binder-free nickel copper phosphate thin film electrodes are synthesized by SILAR method. The simple SILAR method was employed for the preparation of nickel copper phosphate thin films on SS substrate. The ratio of nickel and copper species varied in nickel copper phosphate to obtain better performance by tuning morphological as well as structural properties of electrodes. The present chapter is distributed into two sections (section A and B). Section 'A' deals with the synthesis of nickel copper phosphate thin films by SILAR method and their characterization. Section 'B' is related with the supercapacitive performance of SILAR deposited nickel copper phosphate thin film electrodes.

SECTION – A

SILAR synthesis and characterization of nickel copper phosphate thin films

4.2.A.1 Introduction:

The present section (A) deals with the characterization of nickel copper phosphate thin films prepared by facile and convenient SILAR method. The

preparative conditions such as precursor concentration, adsorption, reaction, and rinsing time are optimized to obtain superior quality of nickel copper phosphate thin films. It provides many advantages such as ion-by-ion growth mode, greater precursor utilization capability, and deposition technique is simple to control appropriate thickness film [16, 17]. Successively, nickel copper phosphate thin films are characterized employing various characterization techniques such as XRD for structural investigation, FT-IR for detection of functional group, XPS to analyse oxidation states, FE-SEM for surface morphological studies and BET for surface area and porosity. The purpose of this work is to examine synergistic effect in combined transition bimetallic phosphate (various concentrations of nickel:copper) on electrochemical activities.

4.2.A.2 Experimental details:

4.2.A.2.1 Chemicals:

Dipotassium hydrogen orthophosphate (K_2HPO_4), nickel sulphate ($NiSO_4 \cdot 6H_2O$), and copper sulphate ($CuSO_4 \cdot 5H_2O$) was purchased from Sigma Aldrich (AR grade) and utilized as received without any further purification.

4.2.A.2.2 Synthesis of nickel copper phosphate thin films:

Nickel copper phosphate thin film electrodes were synthesized by SILAR method. **Figure 4.1** reveals the schematic representation of SILAR method for synthesis of nickel copper phosphate on the SS substrate using a three-beaker system at ambient temperature. The SS substrates were firstly wiped with acetone and smoothened with polish paper prior to an ultra-sonication in DDW (complete procedure of substrate cleaning is given in the earlier chapter). A varied concentration of nickel sulphate (0.0333-0.0249 M) and copper sulphate (0.0249-0.0333 M) (serving Ni^{2+} and Cu^{2+} ions) was prepared by dissolving stoichiometric amounts of $NiSO_4$ and $CuSO_4$ in 50 ml DDW, which serves as the cationic precursor source. A 0.075 M dipotassium hydrogen orthophosphate (serving PO_4^{3-} ions) was formulated in 50 ml DDW which serves as the anionic precursor source. Detailed proportions of nickel (Ni) and copper (Cu) precursors are used as shown in **Table 4.1**, for deposition of nickel copper phosphate materials. In typical synthesis, the precleaned SS substrate was sequentially dipped in the cationic and anionic solutions for 10 s each. After that, the substrate was rinsed in DDW for 20 s. At ambient temperature, such 70 cycles were repeated to get a uniform deposition of material.

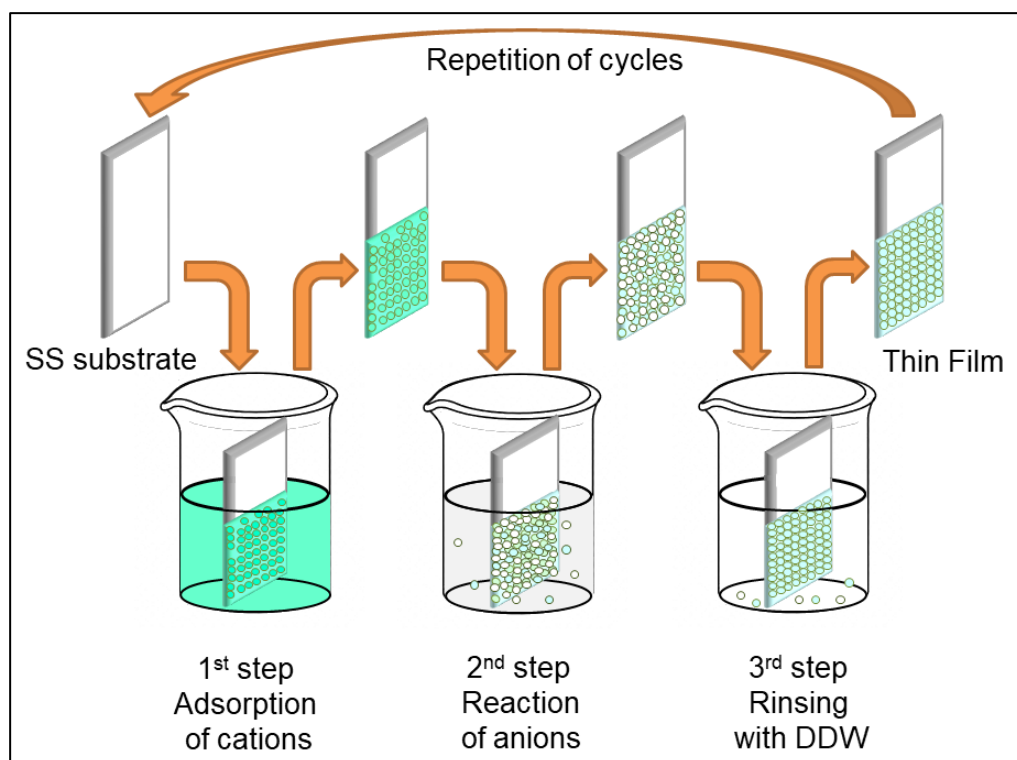


Figure 4.1: Schematic representation of SILAR method for nickel copper phosphate thin films deposition.

The adsorption, reaction, as well as rinsing time in this experiment are optimized by some trials to get uniform and adherent film. In the first beaker, the metal cations (Ni^{2+} and Cu^{2+} ions) are adsorbed on the surface of substrate and react with freshly adsorbed anions (PO_4^{3-} ions) in the second beaker to form a solid thin film. After 70 deposition cycles, light blue-colored thin films were obtained on surface of SS substrates as displayed in **Figure 4.2**. The thin film electrodes prepared by using different compositions of Ni and Cu precursor are denoted as, S-NCP-1, S-NCP-2, S-NCP-3, S-NCP-4, and S-NCP-5, (given in **Table 4.1**).

Table 4.1: Different compositions of nickel, copper and phosphate precursors for synthesis of nickel copper phosphate thin film and corresponding notations.

Sr. No.	Sample name	$\text{NiSO}_4 \cdot 6\text{H}_2\text{O}$ (M)	$\text{CuSO}_4 \cdot 5\text{H}_2\text{O}$ (M)	K_2HPO_4 (M)
1.	S-NCP-1	0.0333	0	0.075
2.	S-NCP-2	0.0083	0.0249	0.075
3.	S-NCP-3	0.0166	0.0166	0.075
4.	S-NCP-4	0.0249	0.0083	0.075
5.	S-NCP-5	0	0.0333	0.075

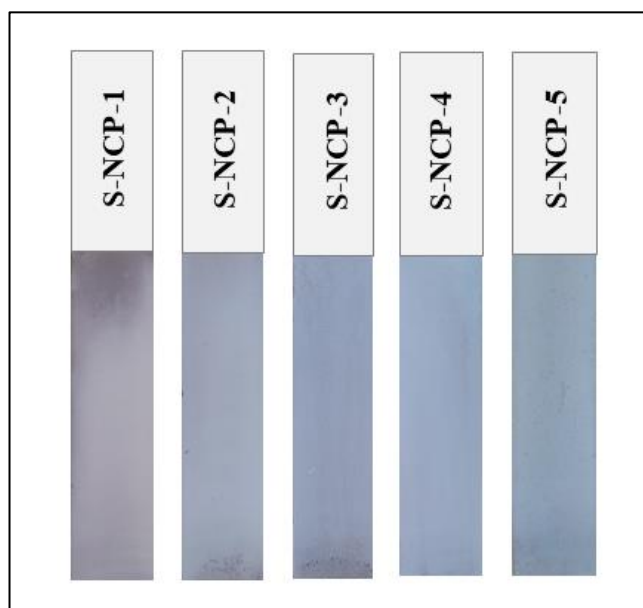
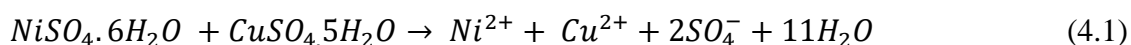


Figure 4.2: Photograph of SILAR synthesized nickel copper phosphate thin films (S-NCP series) with different concentrations of Ni:Cu.

4.2.A.3 Results and discussion:

4.2.A.3.1 Film formation and reaction mechanism:

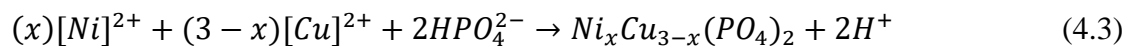
Schematic **Figure 4.1** demonstrates the preparation procedure of nickel copper phosphate thin films by SILAR method. Nickel copper phosphate thin films were developed on the SS substrate via electrostatic adsorption as well as reaction between cations and anions on the SS surface (as displays in scheme **Figure 4.1**). In concise, a three beaker SILAR system, the first beaker contains a mixture of nickel sulphate and copper sulphate ($\text{NiSO}_4 \cdot 6\text{H}_2\text{O}/\text{CuSO}_4 \cdot 5\text{H}_2\text{O}$) aqueous solution with different compositions as a cationic precursor. Then, the adsorbed cations react with anions from precursor (K_2HPO_4) in the second beaker. Moreover, DDW in third beaker was employed for rinsing purpose. The reaction mechanism for nickel copper phosphate thin film development by SILAR method is as follows; thin layer of $\text{Ni}^{2+}/\text{Cu}^{2+}$ ions get adsorbed on SS substrate while dipping the substrate in a cationic precursor solution (kept at ambient temperature).



An anionic precursor of dipotassium hydrogen orthophosphate dissociates as per equation (4.2),



Furthermore, the reaction executed after dipping of the wet substrate in the K_2HPO_4 anionic solution, where a chemical reaction among HPO_4^{2-} and adsorbed Ni^{2+}/Cu^{2+} ions leads to the deposition of adherent nickel copper phosphate layer as,



Thus, the thin film is developed by the ion-by-ion growth mechanism, where film growth occurs by the nucleation of ions at nucleation centre on the dipped surface of substrate. The weight of nickel copper phosphate on SS substrate was measured by the gravimetric mass difference method (**Figure 4.3**). The deposited mass of material for electrodes S-NCP-1, S-NCP-2, S-NCP-3, S-NCP-4, and S-NCP-5 are 1.22, 1.10, 0.90, 1.02, and 1.12 mg cm⁻², respectively.

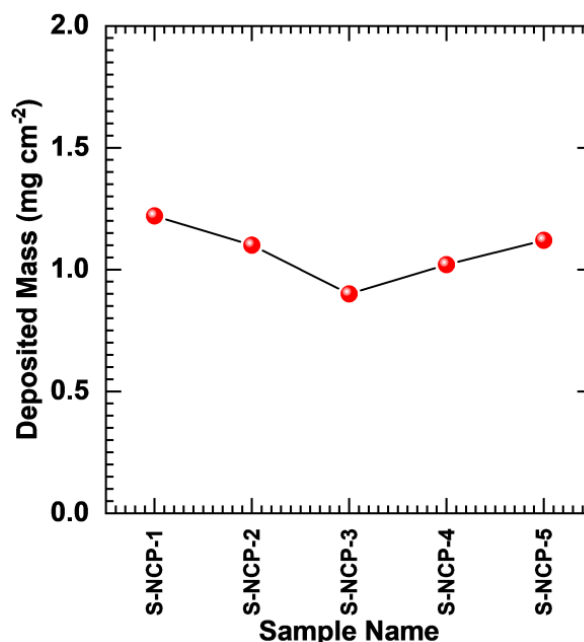


Figure 4.3: Deposited mass of nickel copper phosphate thin film for different composition of nickel and copper.

4.2.A.3.2 XRD study:

The crystallinity of S-NCP-1 to S-NCP-5 electrodes was examined by XRD analysis. As displayed in **Figure 4.4**, amorphous phase of as-prepared nickel copper phosphate is observed, since no significant diffraction peaks were observed in the XRD patterns. The peaks represented as ‘SS’ are related to stainless steel conducting substrate. The absence of diffraction peak from XRD patterns of NCP-series electrodes indicates formation of amorphous phase of material. The amorphous phase of material is feasible for the improvements of electrochemical activities due to large active sites

can be obtained by irregular structure of material. Such, amorphous structure of material can provide facile access to ions in nickel copper phosphate material [18]. An amorphous material permits a continuous redox reaction on the surface, aimed to enhance performance compared to crystalline structures [19].

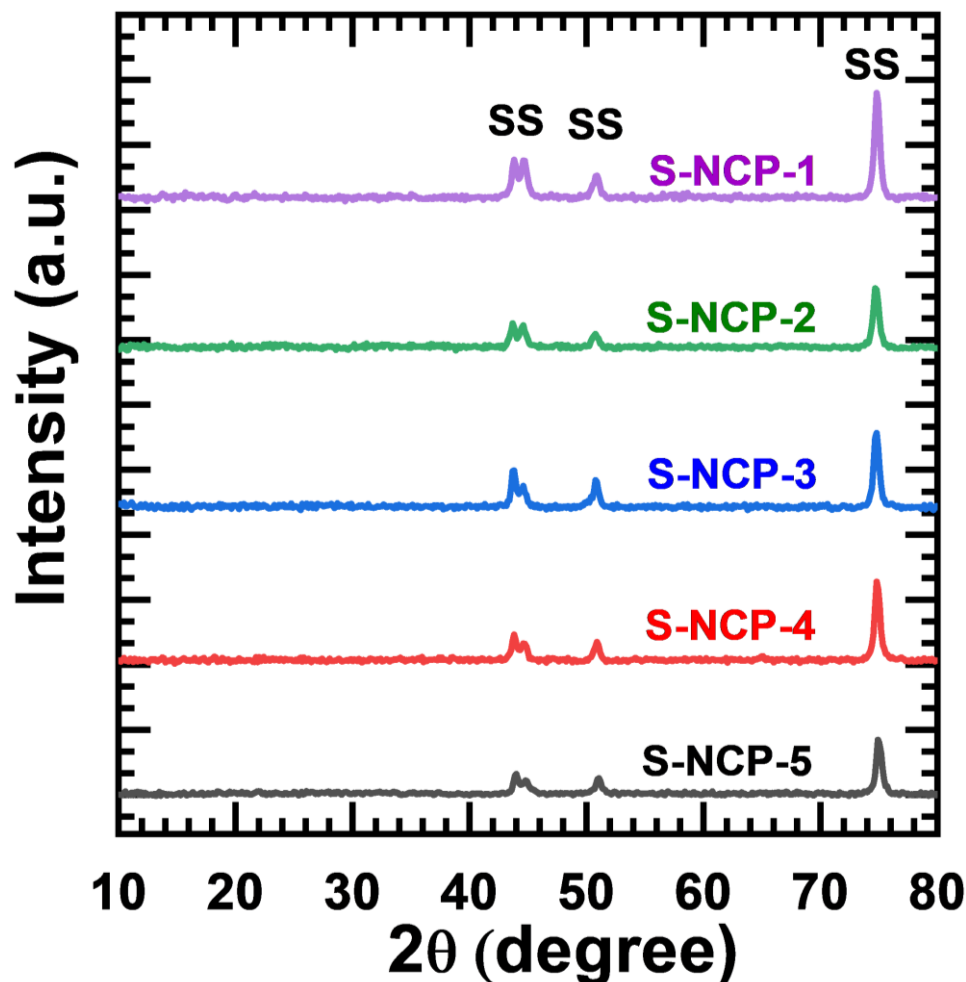


Figure 4.4: XRD patterns of nickel copper phosphate (S-NCP series) thin films.

4.2.A.3.3 FT-IR study:

The FT-IR spectra of S-NCP series thin films was examined in the region of $4000\text{--}400\text{ cm}^{-1}$ and presented in **Figure 4.5**. The presence of chemical bonding in prepared electrodes was studied by FT-IR analysis. **Figure 4.5** displays the characteristic peak at 563 cm^{-1} can be ascribed to Ni-O bonding [20] and peak at 623 cm^{-1} to Cu-O bonding in thin films [21]. The observed peak at 765 cm^{-1} attributed to the symmetric stretching of P-O-P linkage [22]. The symmetric and asymmetric (P-O) stretching vibrational mode of PO_4^{3-} anions are confirmed by peaks observed at wavenumbers of 995 and 1050 cm^{-1} [23–26]. The peak at 1385 cm^{-1} assigned to the H-O-P bending vibrations [27]. The absorption peak at 1598 cm^{-1} assign to the bending

mode of water molecule (H-O-H). Furthermore, a wide band at 3480 cm^{-1} is observed due to O-H stretching vibration mode from structural water molecules captured during synthesis [28, 29]. The FT-IR spectra reveals characteristic properties of nickel, copper, phosphate water molecule bonding and indicating successful formation of hydrous nickel copper phosphate.

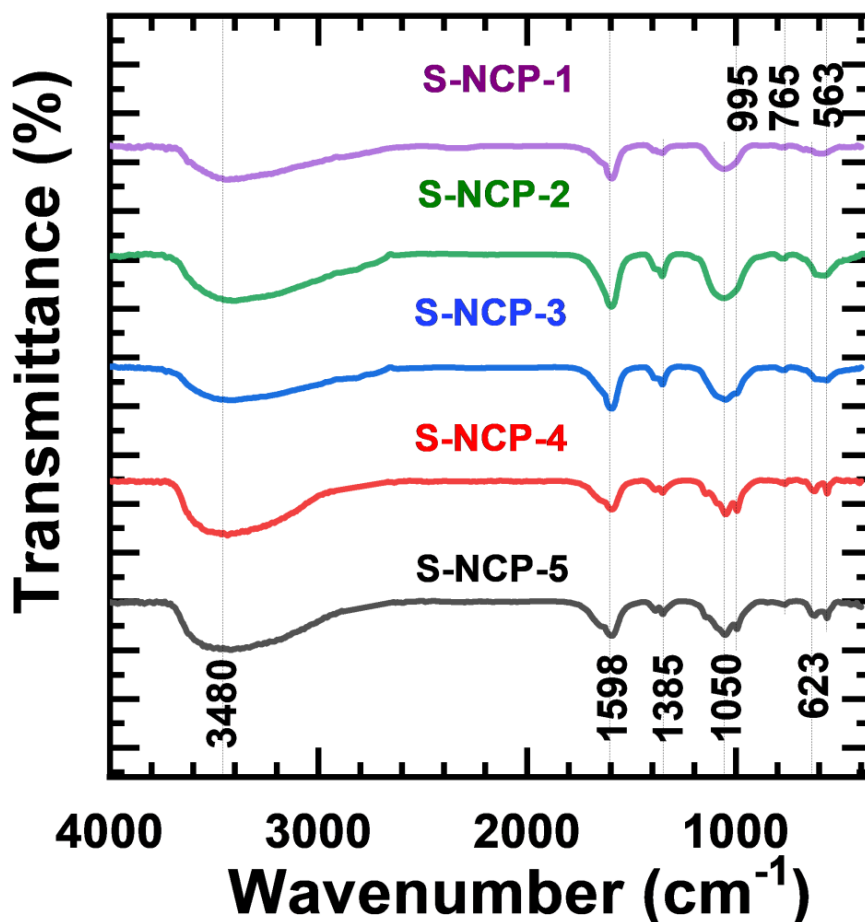


Figure 4.5: FT-IR spectra of nickel copper phosphate thin films (S-NCP-1 to S-NCP 5).

4.2.A.3.4 BET study:

The surface area (**Figure 4.6**) and pore size (**Figure 4.7**) distribution of the S-NCP series samples was examined using N_2 adsorption–desorption isotherms. The detected isotherms of sample (a) S-NCP-1, (b) S-NCP-2, (c) S-NCP-3 (d) S-NCP-4 and (e) S-NCP-5 reveals a type III isotherm with H3 type hysteresis loop which signifies a lower energy of adsorption and characteristics features of mesoporous material [30]. According to the BET equation, the surface areas were calculated as 23.77, 36.91, 37.30, 16.02 and 17.09 $\text{m}^2\text{ g}^{-1}$ for sample S-NCP-1, S-NCP-2, S-NCP-3, S-NCP-4 and S-NCP-5, respectively. The distribution of pore size of S-NCP series

samples revealed in **Figure. 4.7**. An average pore diameter of 28.82, 21.49, 18.48, 27.90 and 25.67 nm is obtained for samples S-NCP-1, S-NCP-2, S-NCP-3, S-NCP-4 and S-NCP-5, respectively.

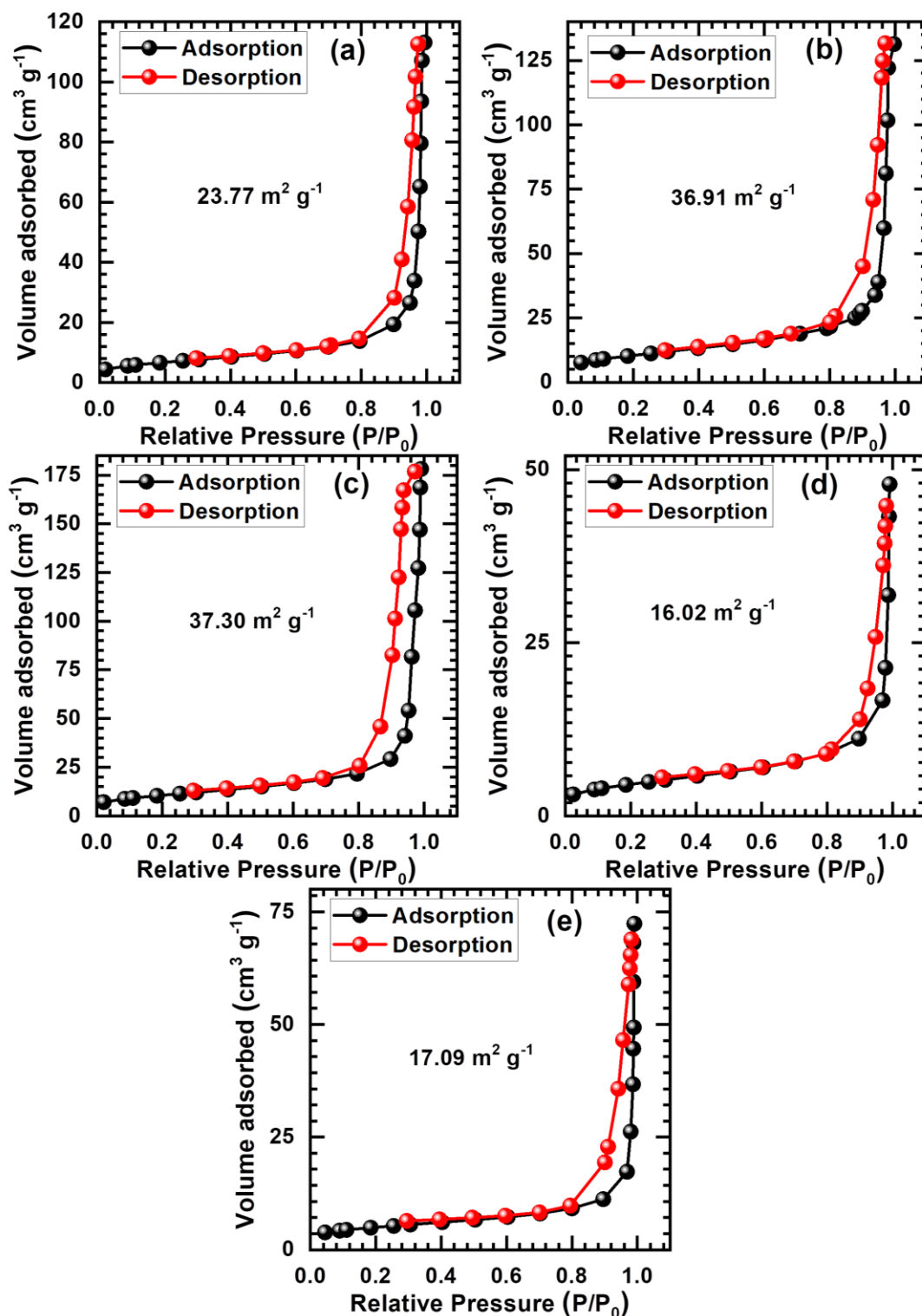


Figure 4.6: Nitrogen adsorption-desorption isotherm of samples; (a) S-NCP-1, (b) S-NCP-2, (c) S-NCP-3, (d) S-NCP-4 and (e) S-NCP-5 samples.

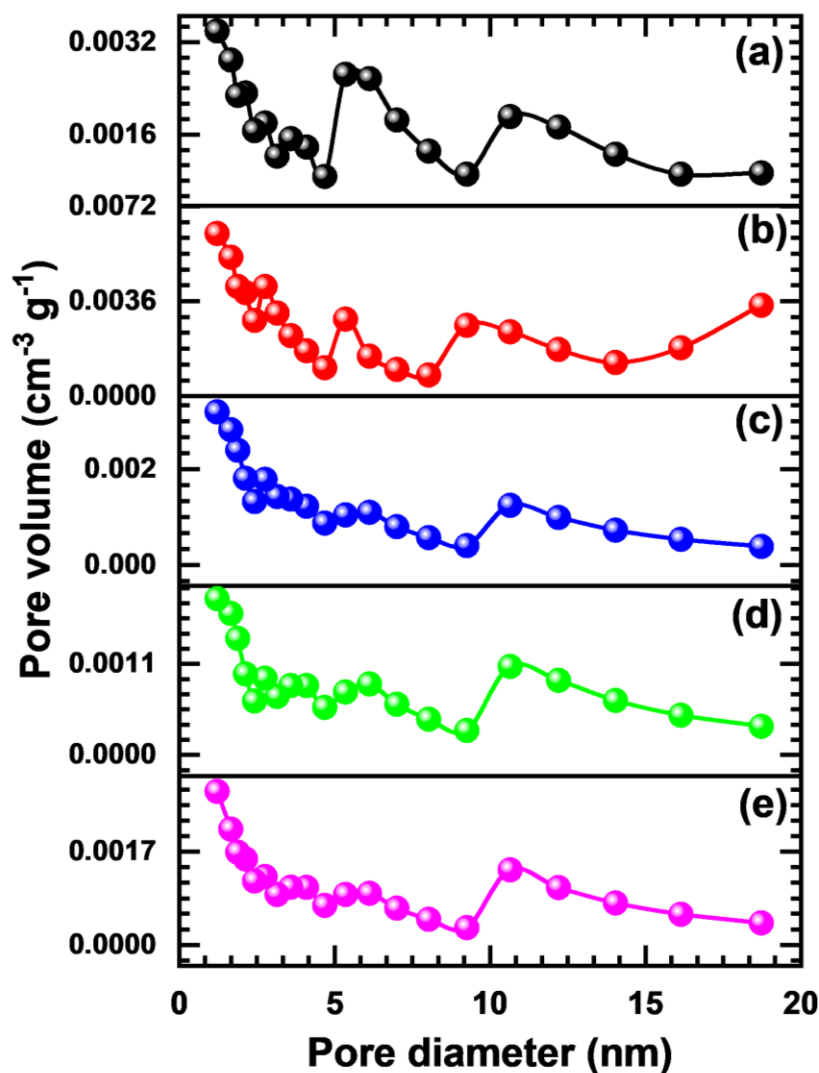


Figure 4.7: Pore size distribution curves of samples (a) S-NCP-1, (b) S-NCP-2, (c) S-NCP-3, (d) S-NCP-4 and (e) S-NCP-5 samples.

4.2.A.3.5 XPS study:

The surface information and composition of SILAR deposited amorphous nickel copper phosphate thin films were further examined by the XPS and the results are presented in **Figure 4.8**. The existence of Ni, Cu, P and O elements were identified from a survey scan of nickel copper phosphate for S-NCP-3 electrode (**Figure 4.8 (a)**). The **Figure 4.8 (b-e)** exhibits the high resolution emission spectra of Ni2p, Cu2p, P2p and O1s respectively. In the Ni2p spectra (**Figure 4.8 (b)**), the peaks located at 875.9 eV from Ni2p_{1/2} and 858.4 eV from Ni2p_{3/2} electrons associate with two satellite peaks at 880.1 and 862.6 eVs can be attributed to nickel species with the chemical states of Ni²⁺ [31].

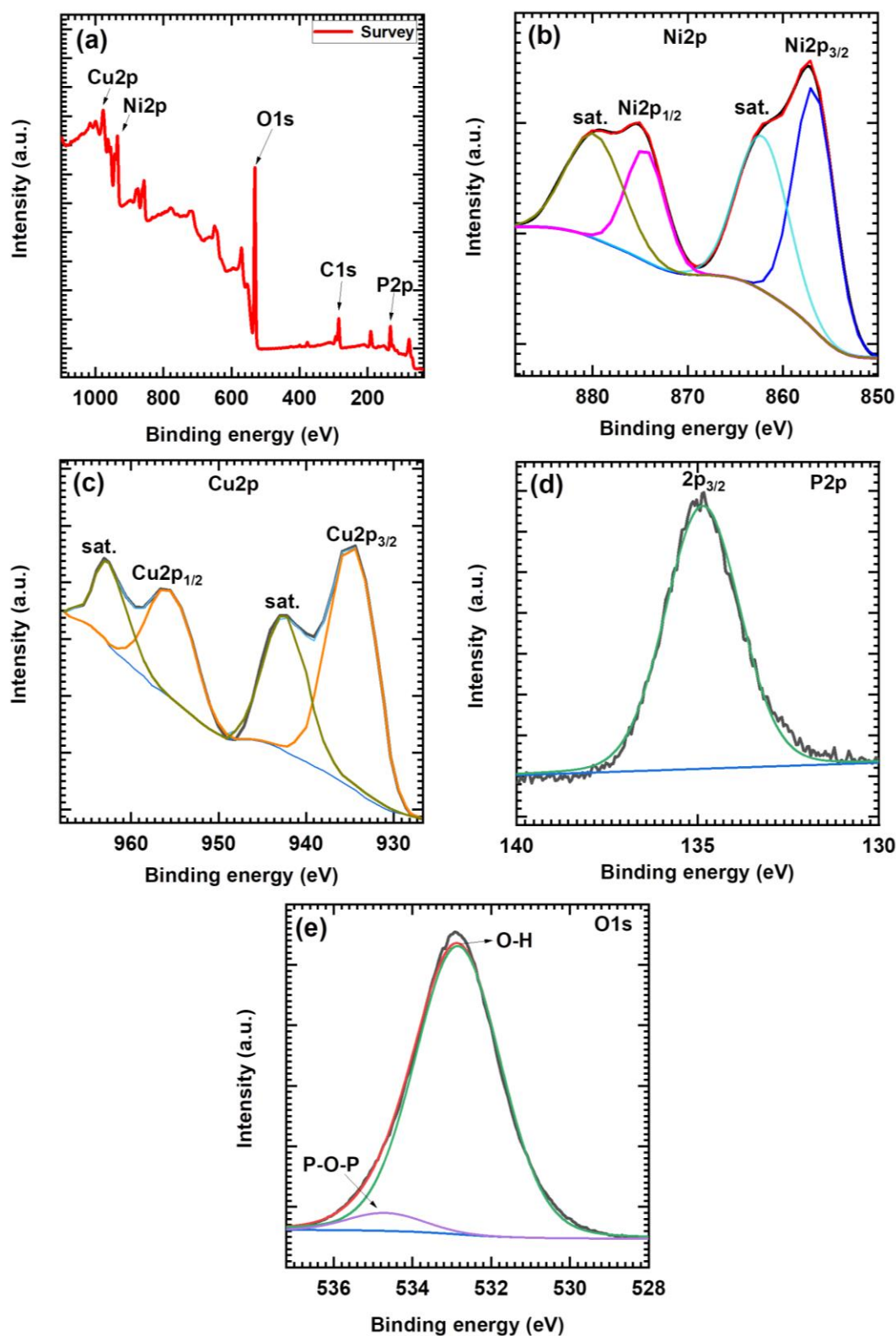


Figure 4.8: (a) Survey, (b) Ni2p, (c) Cu2p, (d) P2p and (e) O1s XPS spectra of sample S-NCP-3.

For the Cu2p spectra (**Figure 4.8 (c)**), the peaks located at 956.5 eV from Cu2p_{1/2} and 934.3 eV from Cu2p_{3/2} electrons associate with two satellite peaks at 963.1

and 943.9 eVs can be attributed to copper phosphate with the chemical states of Cu^{2+} [15]. The P2p XPS spectra (**Figure 4.8 (d)**) of the P element reveals one peak at 134.8 eV, agreeing well with P-O and P=O in nickel copper phosphate thin film [32]. Further, the O1s band (**Figure 4.8 (e)**) was deconvoluted into two peaks at 534.7 and 532.8 eVs attributed to metal-oxygen molecules and O-H group from adsorbed water, respectively [33, 34].

4.2.A.3.6 FE-SEM study:

FE-SEM investigation is used for the surface morphology analysis of SILAR deposited nickel copper phosphate thin films. The **Figure 4.9** displays the morphologies of SILAR deposited thin films at different magnifications (X30000 and X100000). The morphological evolution is observed from S-NCP-1 to S-NCP-5 sample due to variation in nickel and copper composition. FE-SEM images in **Figure 4.9** reveal porous morphology consisting of a nanoparticle-like structure of material.

The FE-SEM images of pristine nickel phosphate (S-NCP-1) exhibited in **Figure 4.9 (A1, A2)**, reveals that the sample consists of nanoparticle like structure having average particle size of 110 nm. Likewise, nanoparticles-like morphology is detected for S-NCP series electrodes (**Figure 4.9 (B2-D2)**) with different average particle sizes of ~135 nm (S-NCP-2), ~86.50 nm (S-NCP-3) and ~91.5 nm (S-NCP-4). Moreover, the FE-SEM images of pristine copper phosphate (S-NCP-5) (**Figure 4.9 (E1, E2)**) indicate that thin film contains nanoparticle-like morphology having average particle size is 94 nm. In the lower magnification (**Figure 4.9 (A1-E1)**), the as-prepared (S-NCP series) samples seem to be uniform, dense, compact and well covered nanoparticle structure. A nanoparticle like structure exhibits delivers a more porous surface area which can result in a maximum capacitance value through electroactive cavities. Conversely, in the higher magnification (**Figure 4.9 (A2-E2)**) these particles consist of numerous uniform nanoparticles and possess loosely packed structure, which is beneficial for the accessibility of electrolyte ions to active materials. Such porous nanoparticle like morphology can promote the rapid diffusion of electrolytic ions in electrodes which can offer excellent capacitive retention at high charge discharge rates.

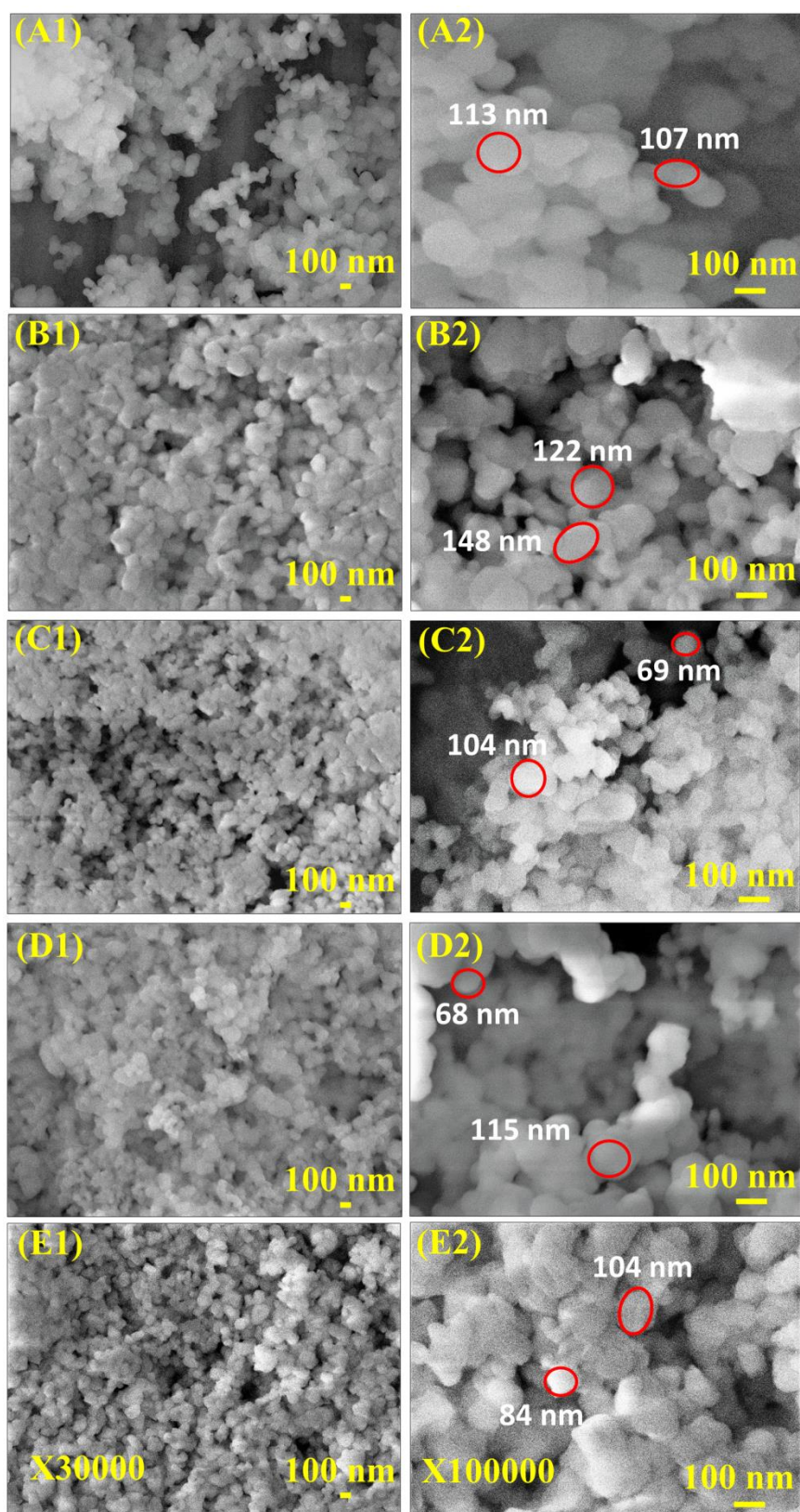


Figure 4.9: FE-SEM micrographs of nickel copper phosphate electrodes: (A1, A2) S-NCP-1, (B1, B2) S-NCP-2, (C1, C2) S-NCP-3, (D1, D2) S-NCP-4, and (E1, E2) S-NCP-5 at different magnifications (X30000 and X100000).

4.2.A.3.7 EDS study:

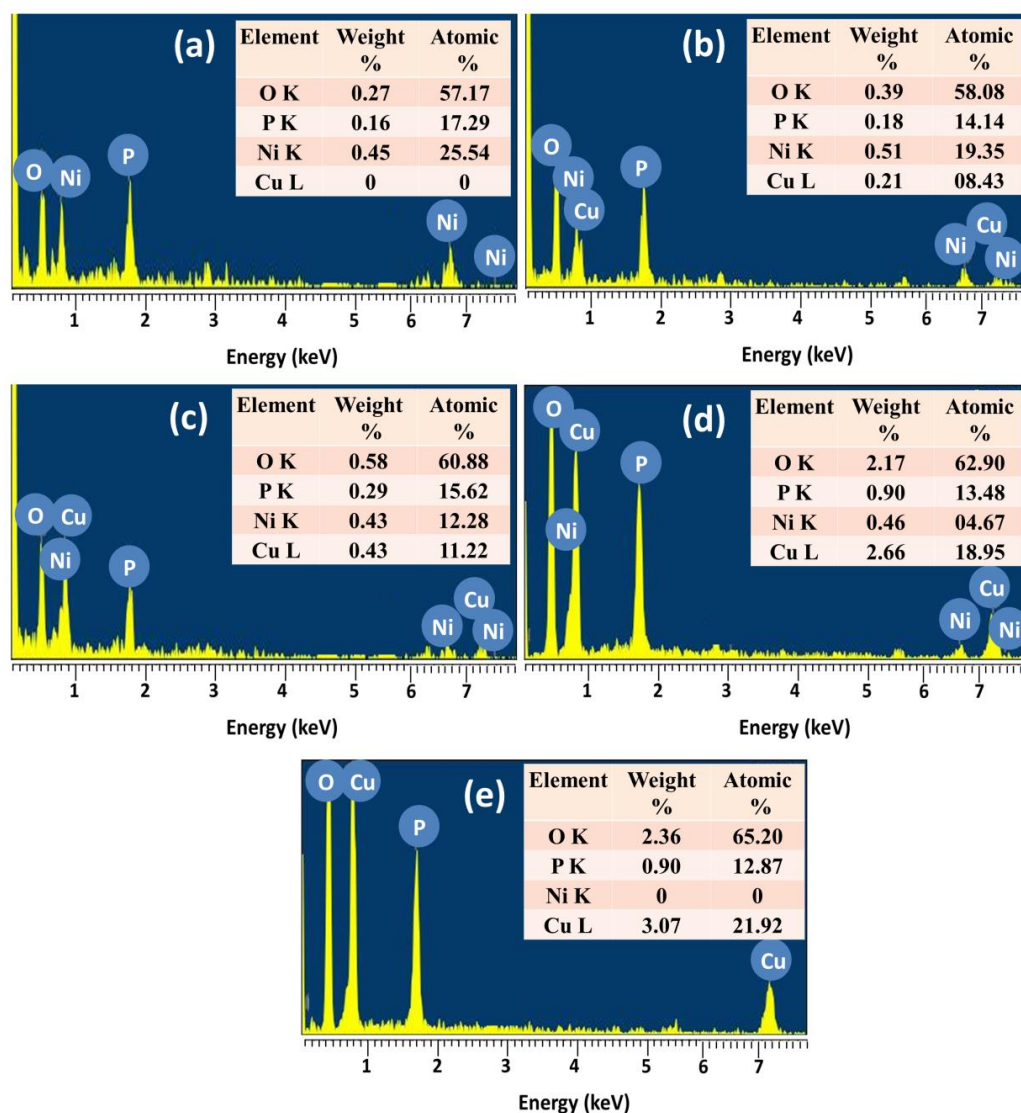


Figure 4.10: EDS spectra of nickel copper phosphate electrodes: (a) S-NCP-1, (b) S-NCP-2, (c) S-NCP-3, (d) S-NCP-4, and (e) S-NCP-5.

Elemental mapping of S-NCP series thin film samples was examined using EDS analysis and presented in **Figure 4.10 (a-e)**. The presence of nickel, copper, phosphorous and oxygen elements in the sample S-NCP-2 to S-NCP-4 confirm the successful deposition of nickel copper phosphate material on SS substrate in thin film form via SILAR deposition method. Also, the absence of copper in S-NCP-1 and nickel in S-NCP-5 samples confirm formation of nickel phosphate and copper phosphate materials, respectively. The experimental and observed nickel and copper ratios for S-NCP series samples are provided in **Table 4.2**. It is found that, the experimental and observed ratios of nickel and copper contents are almost similar. Therefore, EDS result confirm formation of nickel copper phosphate ($\text{Ni}_x\text{Cu}_{3-x}(\text{PO}_4)_2 \cdot \text{H}_2\text{O}$) in thin film form.

Table 4.2: Experimental and observed nickel and copper atomic ratio in S-NCP series thin films.

Sample name	Experimental ratio (Ni:Cu)	Observed ratio (Ni:Cu)	Obtained phase
S-NCP-1	1:0	1:0	$\text{Ni}_3(\text{PO}_4)_2 \cdot \text{H}_2\text{O}$
S-NCP-2	0.75:0.25	0.70:0.30	$\text{Ni}_{2.10}\text{Cu}_{0.90}(\text{PO}_4)_2 \cdot \text{H}_2\text{O}$
S-NCP-3	0.50:0.50	0.52:0.48	$\text{Ni}_{1.56}\text{Cu}_{1.44}(\text{PO}_4)_2 \cdot \text{H}_2\text{O}$
S-NCP-4	0.25:0.75	0.20:0.80	$\text{Ni}_{0.60}\text{Cu}_{2.40}(\text{PO}_4)_2 \cdot \text{H}_2\text{O}$
S-NCP-5	0:1	0:1	$\text{Cu}_3(\text{PO}_4)_2 \cdot \text{H}_2\text{O}$

4.2.A.4 Conclusions:

In brief, the binder-free synthesis of nickel copper phosphate thin film electrodes (S-NCP-series) at ambient environment was achieved by facile SILAR method. S-NCP-series thin films revealed porous nanoparticles-like morphology and XRD study affirmed formation of amorphous nickel copper phosphate. The variation in compositions of existing S-NCP series thin film materials with phase of nickel copper phosphate ($\text{Ni}_x\text{Cu}_{3-x}(\text{PO}_4)_2 \cdot \text{H}_2\text{O}$) is affirmed from the EDS analysis. The FTIR study confirms the structural water exists in the prepared nickel copper phosphate thin films. Also, the XPS result affirms similar result that, the prepared material is a nickel copper phosphate compound. The overall results demonstrated that, the prepared material by SILAR method in thin film form is amorphous and hydrous nickel copper phosphate [$\text{Ni}_x\text{Cu}_{3-x}(\text{PO}_4)_2 \cdot \text{H}_2\text{O}$].

SECTION – B

Supercapacitive performance evaluation of nickel copper phosphate thin films

4.2.B.1 Introduction:

In this section, electrochemical analysis of nickel copper phosphate (S-NCP-1 to S-NCP-5) thin films in 1 M KOH electrolyte was examined by CV, GCD and EIS techniques. Furthermore, the effect of scan rate and current density on electrochemical performance of nickel copper phosphate thin films was studied using above mentioned electrochemical techniques, to select appropriate electrode material for the assembly of SC device.

4.2.B.2 Results and discussion:

4.2.B.2.1 CV study:

Electrochemical activity of S-NCP series thin film electrodes in electrolyte (1 M KOH) was examined by CV analysis. Typical CV curves of S-NCP series electrodes at 20 mV s^{-1} scan rate within potential window of 0 to 0.65 V (vs Hg/HgO) are plotted in **Figure 4.11 (a)**. In these plots, the S-NCP-3 electrode demonstrates more area under the CV curve than other electrodes. Redox peaks in CV curves exhibit pseudocapacitive (surface and bulk process) nature of the material [35].

The electrodes nickel (S-NCP-1) and copper (S-NCP-5) phosphate shows distinct nature of CV curves. Also, it is noticed that, the nickel and copper ratio variation affects the morphology of material and that eventually influence the electrochemical performance. The CV curves of electrodes (S-NCP-1 to S-NCP-5) at $2\text{-}20 \text{ mV s}^{-1}$ sweep rates are demonstrated in **Figure 4.11 (b-f)** and it is noted that, all CV curves of S-NCP-series electrodes exhibits the redox behaviour. It is observed that, area under the CV curve increases with increasing scan rate. The equal composition of nickel and copper in S-NCP-3 sample having aggregated nanoparticle like morphology displays higher CV area than the other electrodes.

The charge stored in the electrode can be the combination of two mechanisms (electrochemical pseudocapacitive type and battery type) and it is analysed by Power's law using scan rate dependent CV curves. The b value of S-NCP series electrodes is estimated from the slope of graph $\log(i)$ vs $\log(v)$ [36] and displayed in **Figure 4.12**. The graph illustrates b values of S-NCP-1, S-NCP-2, S-NCP-3, S-NCP-4, and S-NCP-5 electrodes are 0.68, 0.51, 0.59, 0.52 and 0.84, respectively. The values of b for S-NCP series electrodes ranging from 0.5 to 1 [37] that represent both (capacitive and diffusive) processes leads to charge storage. The contribution in current density from the surface pseudo-capacitive (surface) and battery-like (bulk) process for nickel phosphate thin film electrodes at various scan rates $2\text{-}20 \text{ mV s}^{-1}$ are expressed in **Figure 4.13**.

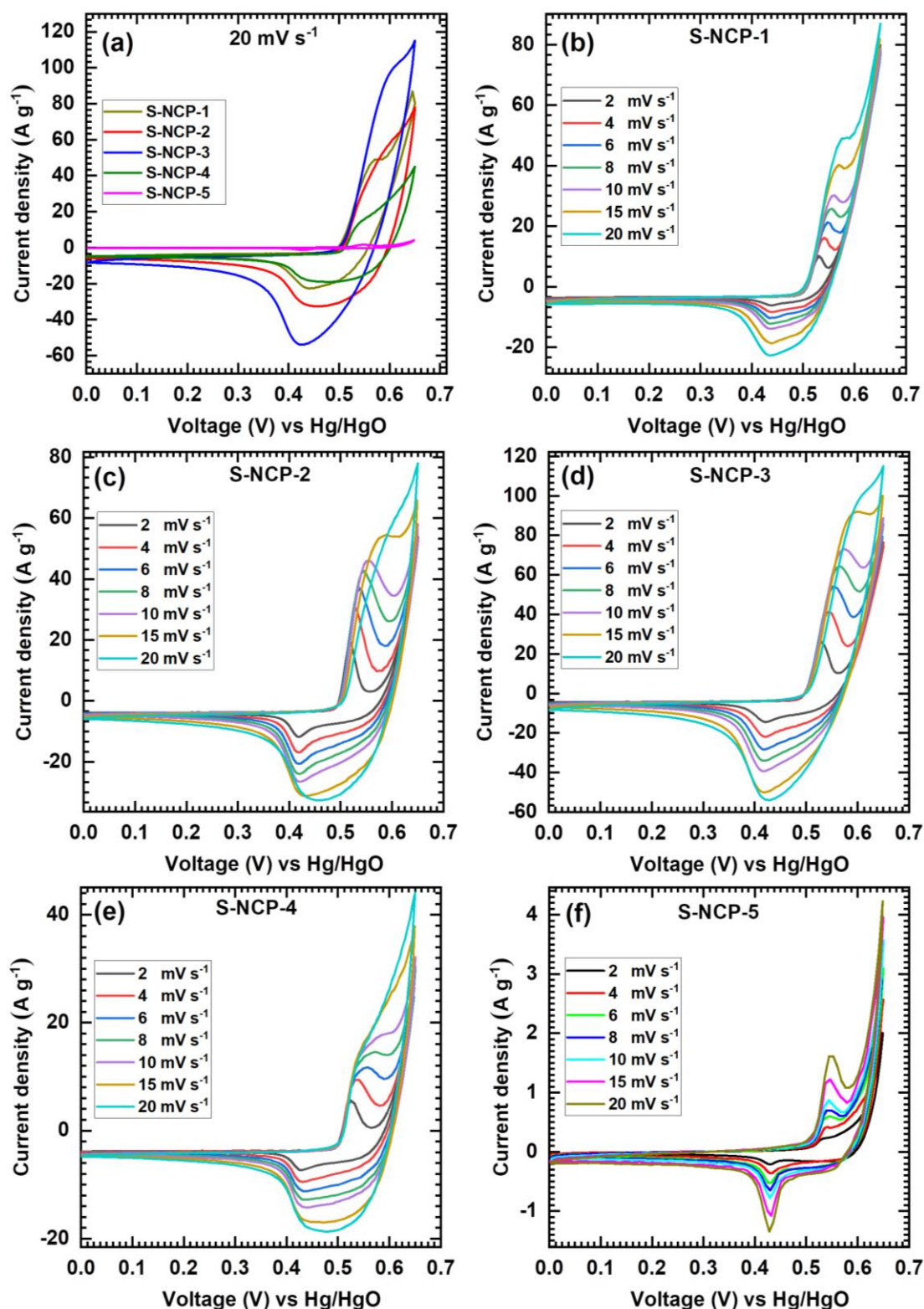


Figure 4.11: (a) The comparative CV curves of S-NCP series electrodes at 20 mV s⁻¹ scan rate, the CV curves at different scan rates from 2-20 mV s⁻¹ for (b) S-NCP-1, (c) S-NCP-2, (d) S-NCP-3, (e) S-NCP-4 and (f) S-NCP-5 electrodes.

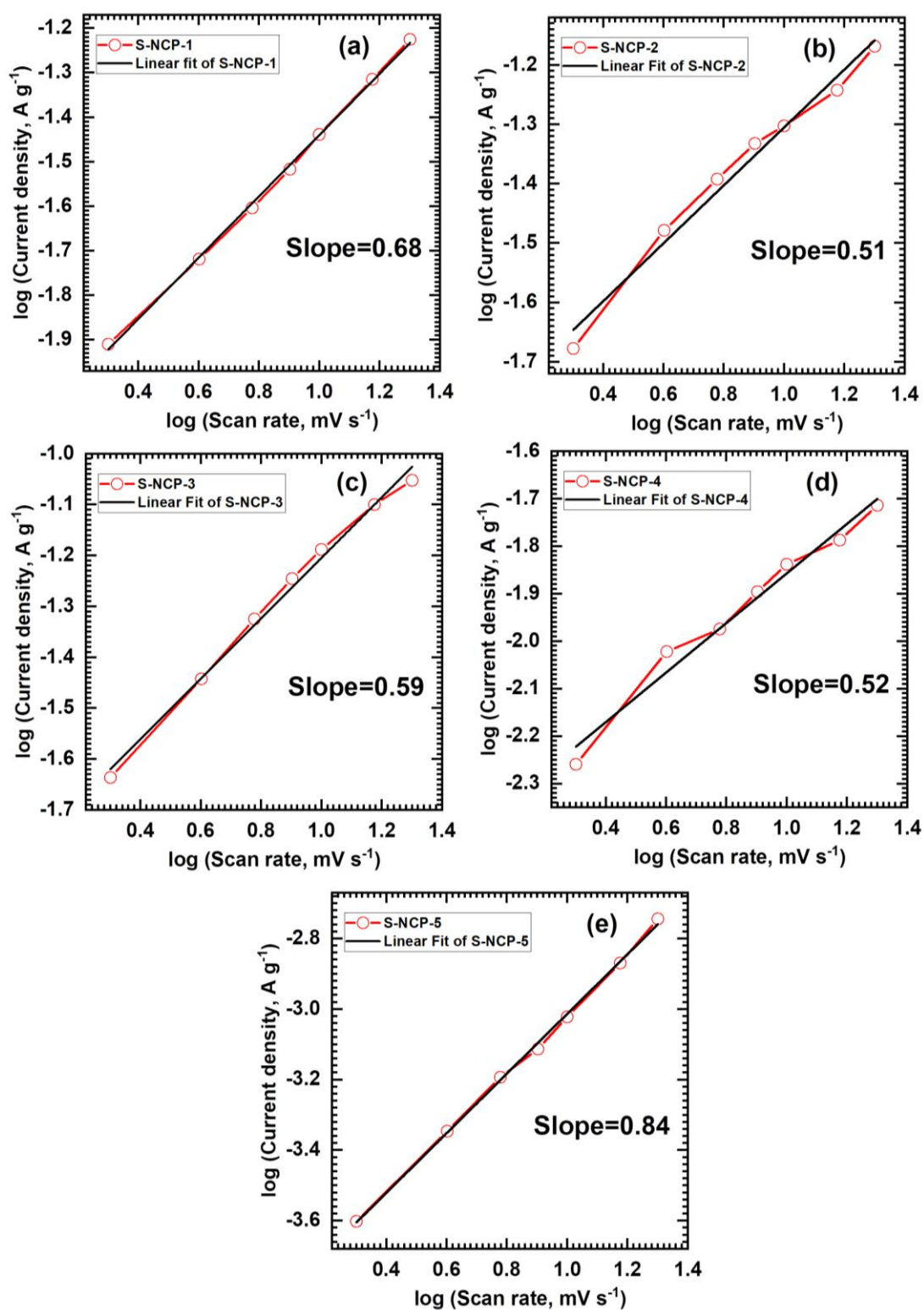


Figure 4.12: Plots of $\log(\text{current density, A g}^{-1})$ versus $\log(\text{scan rate, mV s}^{-1})$ for (a) S-NCP-1, (b) S-NCP-2, (c) S-NCP-3, (d) S-NCP-4 and (e) S-NCP-5 electrodes.

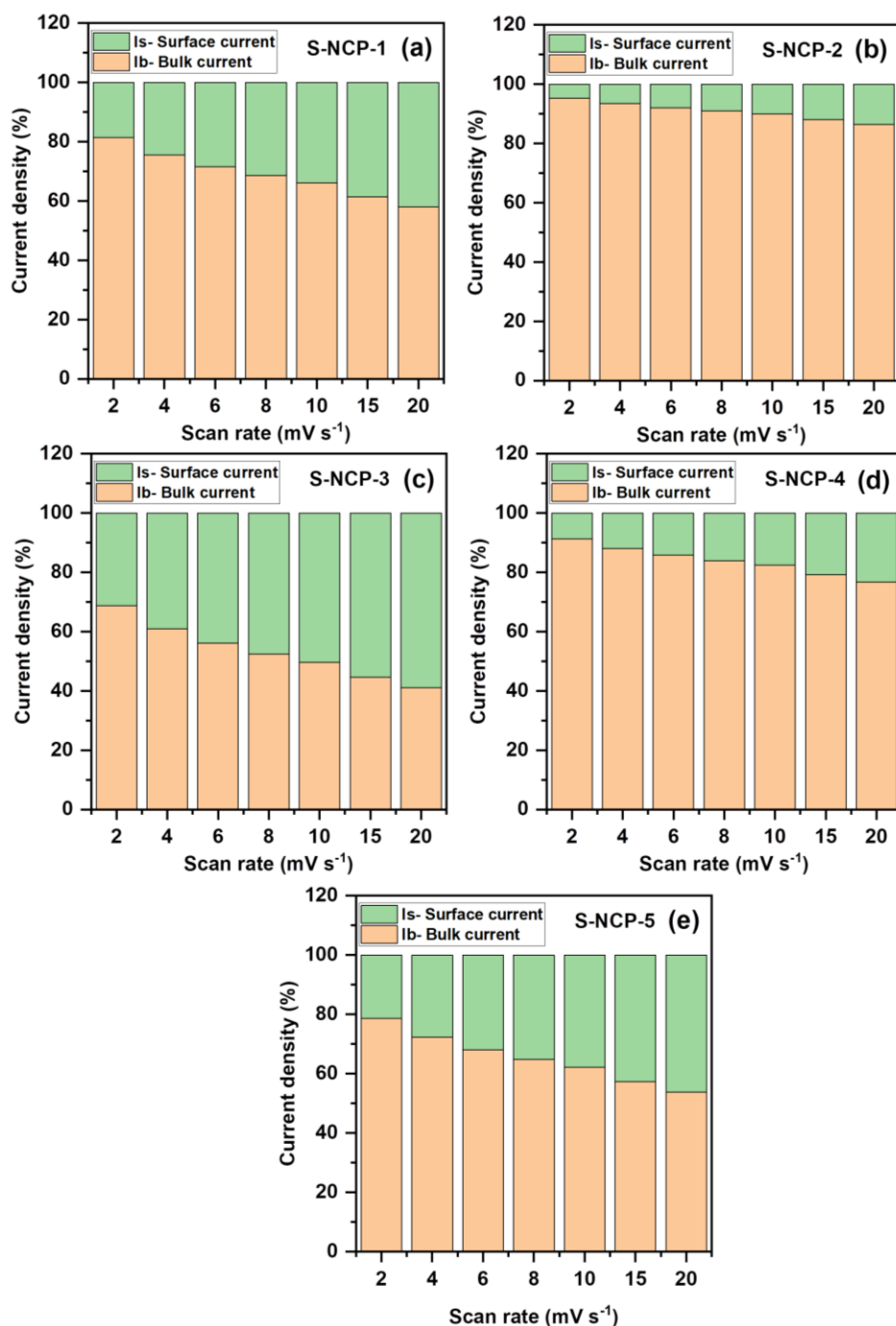


Figure 4.13: Graph of calculated contribution of battery type (bulk current) and pseudocapacitive (surface current) current density at different scan rates (2 to 20 mV s^{-1}) for (a) S-NCP-1, (b) S-NCP-2, (c) S-NCP-3, (d) S-NCP-4 and (e) S-NCP-5 electrodes.

To recognize the individual contribution of surface pseudo-capacitive and battery process by using modified Power's law [38-41]. Pseudocapacitive and battery type current contribution for S-NCP series electrodes are calculated at various scan rates

and presented in **Figure 4.13**. It is noted that, the contribution of surface pseudocapacitance is more for high scan rate and more bulk battery type at low scan rate. Also, the result confirms that bulk battery current contribution is dominant over surface pseudocapacitive current at lower scan rates and vice versa. Also, other electrode displays different current contribution values due to different concentration of nickel and copper in the material. The S-NCP-3 electrode offers ~58% capacitive current contribution at 20 mV s^{-1} scan rate and it is higher than nickel phosphate (S-NCP-1) (~42%) and copper phosphate (S-NCP-5) (~46%) electrode.

4.2.B.2.2 GCD study:

The GCD analysis was executed within optimized potential window of 0 to 0.55 V (vs Hg/HgO) for S-NCP series electrodes. At constant current density of 1 A g^{-1} , GCD analysis of S-NCP series electrodes is analyzed and revealed in **Figure 4.14 (a)**. In a comparative study, S-NCP-3 electrode reveals large charging and discharging time than other electrodes. The GCD curves of S-NCP series electrodes at various current densities from 1-4 A g^{-1} are present in **Figure 4.14 (b-f)**. Likewise CV curves, the nickel (S-NCP-1) and copper (S-NCP-5) phosphate electrode exhibits different charge-discharge curves like battery type and surface redox type, respectively. Non-linear discharging curves of S-NCP series electrodes exhibits in-deep ion intercalation due to redox reaction, and indicate pseudocapacitive behaviour of the material [42-44]. GCD analysis concludes that, the S-NCP-3 electrode gives higher charge-discharge response may be due to large surface area offered by nanostructure and optimum composition of nickel and copper. From the GCD graph, the C_s of S-NCP series electrodes are calculated and plotted in **Figure 4.15**. The S-NCP-3 electrode displays higher discharging time that accountable for high C_s than other electrodes. The S-NCP-3 electrode shows maximum C_s of 750 F g^{-1} at 1 A g^{-1} current density and it decreases up to 618 F g^{-1} at 4 A g^{-1} current density. Similarly, the S-NCP-1, S-NCP-2, S-NCP-4 and S-NCP-5 thin film electrodes offer maximum C_s of 540, 640, 594, and 83 F g^{-1} , respectively at 1 A g^{-1} current density. The decrement in C_s is noted with respect to increase in current density due to shorter time for electrochemical reaction with nanostructure by electrolytic ion at higher current density [45]. At the same time, the longer interaction of electrolyte ions with the inner and outer surface of electrode material at lower charge-discharge rate gives high C_s values [46].

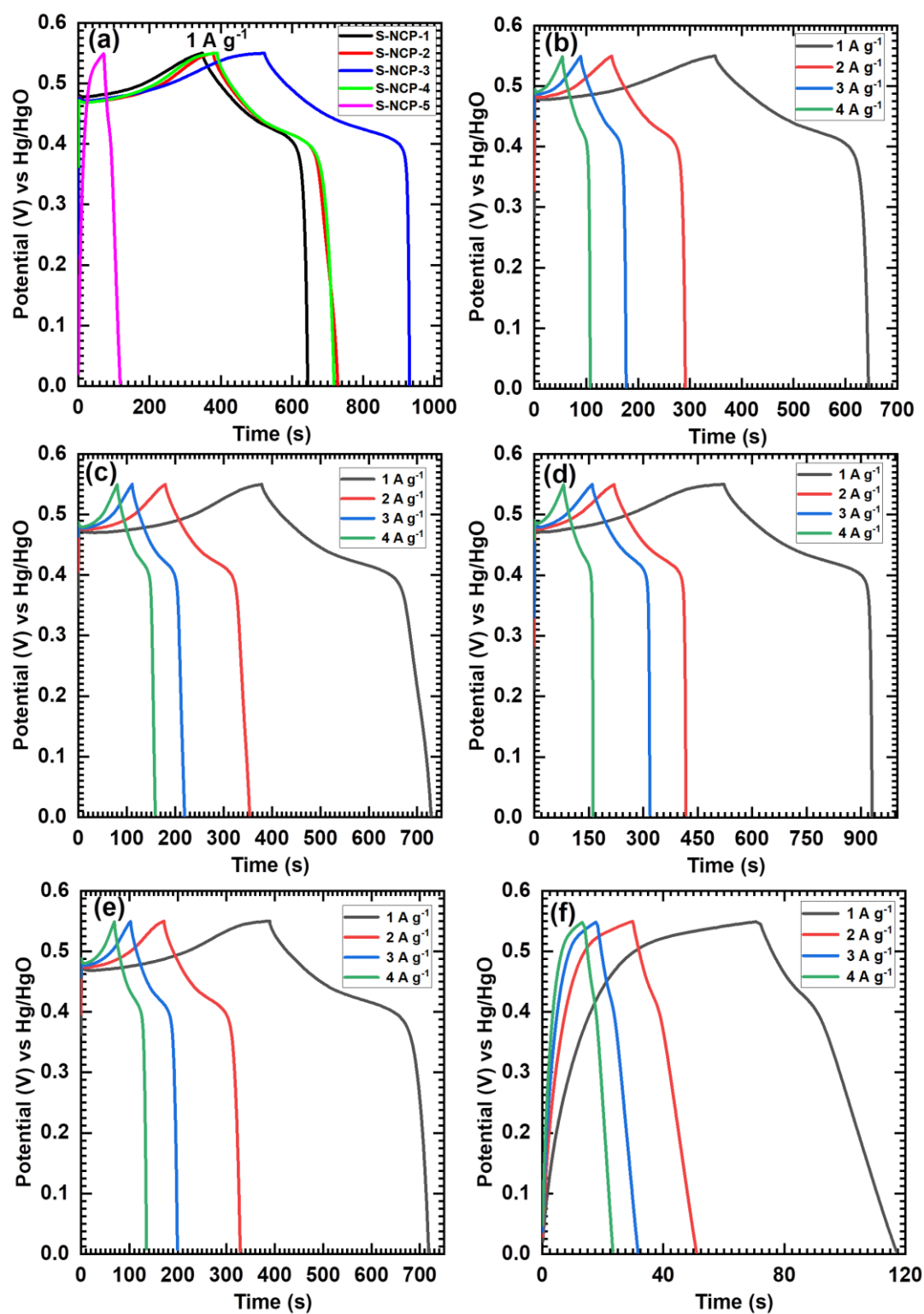


Figure 4.14: (a) The comparative GCD curves of S-NCP series electrodes at current density of 1 A g⁻¹. The GCD curves at various current densities from 1-4 A g⁻¹ for (b) S-NCP-1, (c) S-NCP-2, (d) S-NCP-3, (e) S-NCP-4 and (f) S-NCP-5 electrodes.

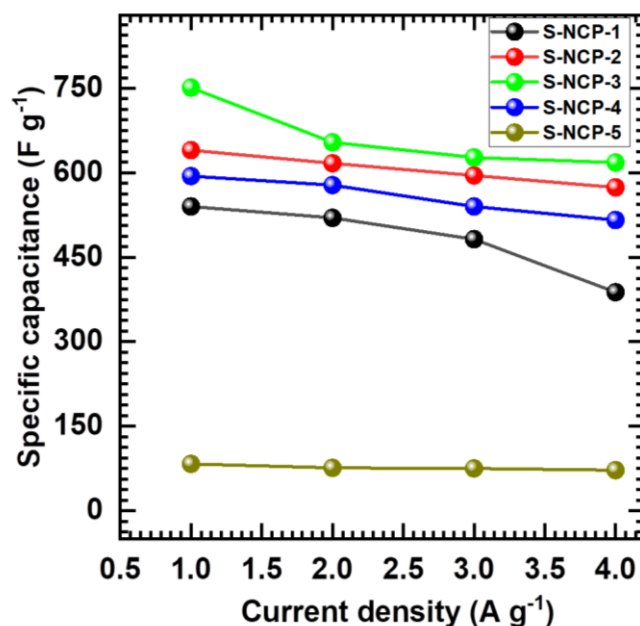


Figure 4.15: C_s of S-NCP series thin films at various current densities (1 to 4 $A g^{-1}$).

4.2.B.2.3 EIS study:

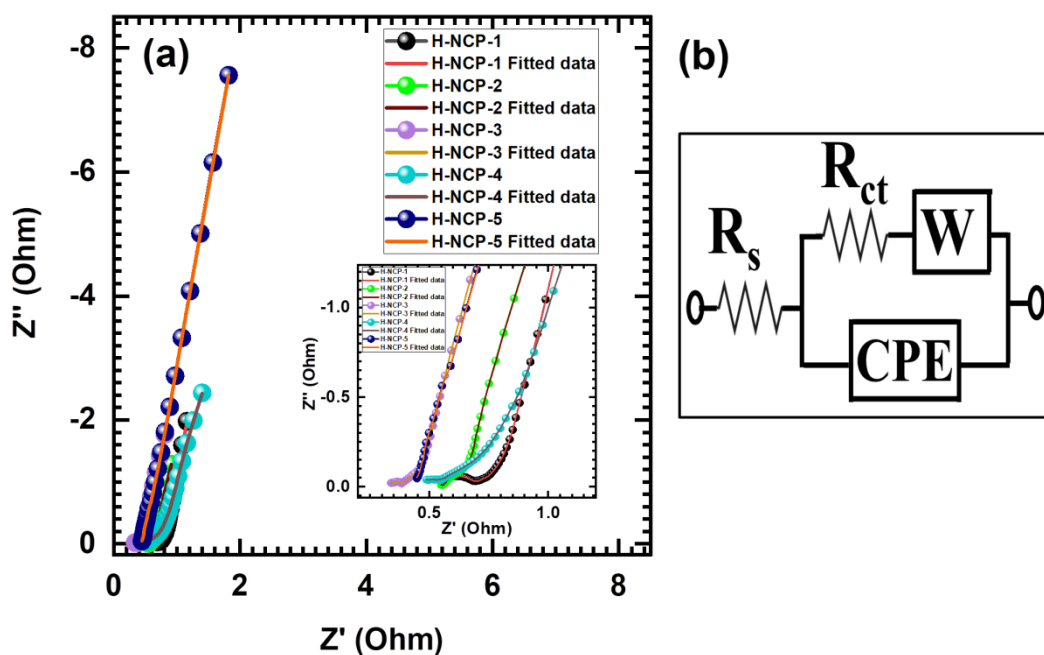


Figure 4.16: The Nyquist plots of S-NCP series electrodes (S-NCP-1 to S-NCP-5) (inset: magnified Nyquist plot at higher frequencies portion).

The Nyquist plots of S-NCP series electrodes are presented in **Figure 4.16 (a)**. The EIS technique is employed to examine ion transfer and electrochemical conductivities of electrodes. The equivalent circuit is displayed in **Figure 4.16 (b)** and it is found to fit with experimental data of S-NCP series electrodes. The values of fitted parameters of equivalent circuit are tabulated in **Table 4.3**.

Table 4.3 : Electrochemical impedance spectroscopic fitted circuit parameters of S-NCP series.

Sample name	R_s (Ω)	R_{ct} (Ω)	CPE (mF)	n	W (Ω)
S-NCP-1	0.55	0.70	0.81	0.98	0.61
S-NCP-2	0.45	1.04	1.19	0.88	0.82
S-NCP-3	0.33	0.38	0.90	0.93	0.90
S-NCP-4	0.48	0.87	0.61	1.0	0.16
S-NCP-5	0.38	1.20	2.53	1.36	0.44

The lower values of R_s (0.55, 0.45, 0.33, 0.48 and 0.38 Ω) and R_{ct} (0.70, 1.04, 0.38, 0.87 and 1.20 Ω) are obtained for S-NCP series electrodes. The small values of R_s (0.33 Ω) and R_{ct} (0.38 Ω) for S-NCP-3 thin films electrode denote a good attachment of the active material with the substrate and the spontaneous electrochemical reaction between the electrolyte and active electrode material.

4.2.B.2.4 Stability study:

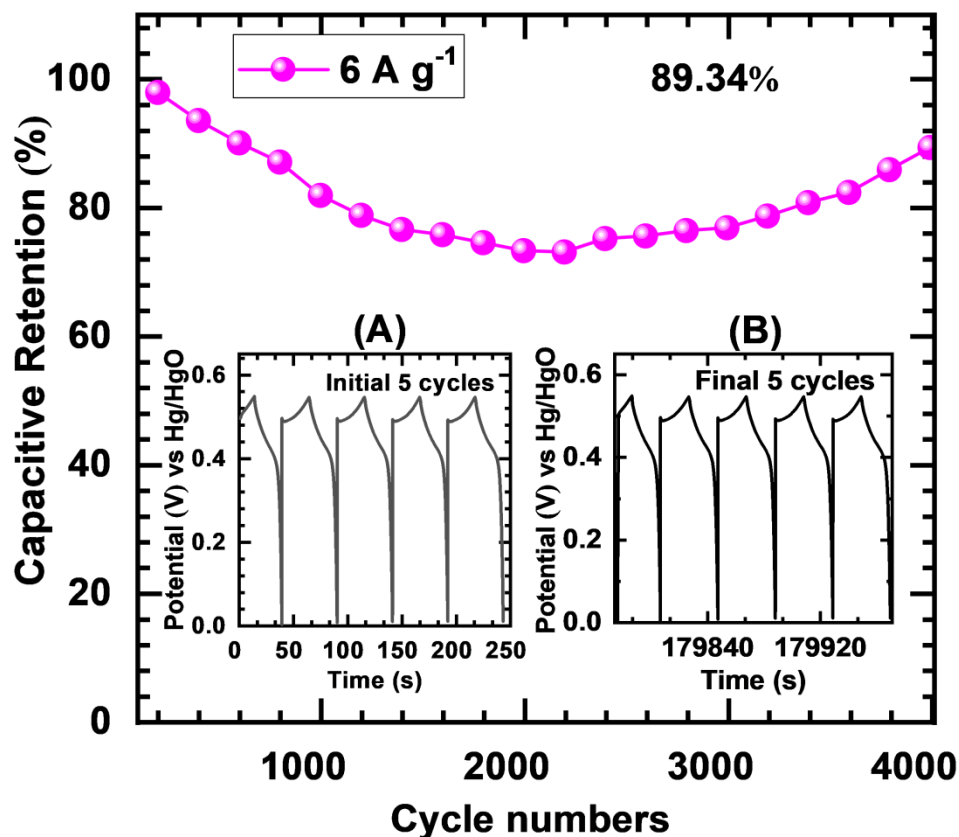


Figure 4.17: The plot of capacitive retention of S-NCP-3 electrode at 6 A g⁻¹ current density for 4000 GCD cycles (inset: GCD curve of (A) initial and (B) final 5 cycles).

The **Figure 4.17** displays cyclic stability of S-NCP-3 electrode at 6 A g^{-1} current density. Stability study reveals that, the S-NCP-3 electrode shows 89.34% capacitive retention over 4000 GCD cycles. The GCD curves of initial (A) and final (B) 5 cycles are revealed as inset of **Figure.4.17**. The decrement in capacitance is noted because of minute depletion of active material after several charge-discharge cycles due to swelling and shrinking of material.

4.2.B.3 Conclusions:

It is concluded that, the electrochemical capacitive performance of nickel copper phosphate (S-NCP series) depends on the different compositions of nickel and copper. The optimized nickel copper phosphate ($\text{Ni}_{1.56}\text{Cu}_{1.44}(\text{PO}_4)_2 \cdot \text{H}_2\text{O}$) electrode revealed the highest C_s of 750 F g^{-1} at a current density of 1 A g^{-1} with good cyclic stability up to 89.34% after 4000 GCD cycles. A small R_{ct} value ($0.38 \text{ } \Omega$) of S-NCP-3 electrode indicates high electrical conductivity and good charge transfer kinetics, which attributed to superior capacitive performance. The electrochemical analysis shows that, S-NCP-3 thin film electrode is suitable as a cathode for asymmetric SC device fabrication.

4.3 References:

1. T. Xu, Y. Zhu, J. Duan, Y. Xia, T. Tong, L. Zhang, D. Zhao, *Chem. Eng. J.*, 395, (2020), 124991.
2. J-K. Liu, C-X. Luo, J-D. Wang, X-H. Yang, X-H. Zhong, *CrystEngComm*, 14, (2012), 8714-8721.
3. B. Ellis, W. R. Makahnouk, Y. Makimura, K. Toghill L. Nazar, *Nat. Mater.*, 6, (2007), 749-753.
4. S. Fedotov, N. Khasanova, A. Samarin, O. Drozhzhin, D. Batuk, O. Karakulina, J. Hadermann, A. Abakumov, E. Antipov, *Chem. Mater.*, 28, (2016), 411-415.
5. P. Menezes, C. Panda, C. Walter, M. Schwarze, M. Driess, *Adv. Funct. Mater.*, 29, (2019), 1808632.
6. M. Sial, H. Lin, X. Wang, *Nanoscale*, 10, (2018), 12975-12980.
7. P. Katkar, S. Marje, S. Pujari, S. Khalate, P. Deshmukh, U. Patil, *Synth. Met.*, 267, (2020), 1-13.
8. J. Zhao, H. Pang, J. Deng, Y. Ma, B. Yan, X. Li, S. Li, J. Chen, W. Wang, *CrystEngComm*, 15, (2013), 5950-5955.
9. S. Li, F. Teng, M. Chen, N. Li, X. Hua, K. Wang, M. Li, *Chem. Phys. Lett.*, 601, (2014), 59-62.
10. S. Pujari, S. Kadam, Y-R. Ma, P. Katkar, S. Marje, S. Khalate, A. Lokhande, U. Patil, *J. Electron. Mater.*, 49, (2020), 3890-3901.
11. Y. Gao, J. Zhao, Z. Run, G. Zhang, H. Pang, *Dalton Trans.*, 43, (2014), 17000-17005.
12. X. Peng, H. Chai, Y. Cao, Y. Wang, H. Dong, D. Jia, W. Zhou, *Mater. Today Energy*, 7, (2018), 129-135.
13. F. Omar, A. Numan, N. Duraisamy, S. Bashir, K. Ramesh, S. Ramesh, *RSC Adv.*, 6, (2016), 76298-76306.
14. A. Agarwal, B. Sankapal, *Chem. Eng. J.*, 422, (2021), 130131.
15. H. Sharkawy, D. Sayed, A. Dhmees, R. Aboushahba, N. Allam, *ACS Appl. Energy Mater.*, 3, (2020), 9305-9314.
16. S. Kale, R. Mane, H. Chung, M. Yoon, C. Lokhande, S. Han, *Appl. Surf. Sci.*, 253, (2006), 421-424.
17. R. Patil, C. Lokhande, R. Mane, H. Pathan, O. Joo, S. Han, *Mat. Sci. Eng. B*, 129, (2006), 59-63.
18. P. Kulal, D. Dubal, C. Lokhande, V. Fulari, *J. Alloys Compd.*, 509, (2011), 2567-2571.
19. Y. Zhang, W. Sun, X. Rui, B. Li, H. Tan, G. Guo, S. Madhavi, Y. Zong, Q. Yan, *Small*, 11, (2015), 3694-3702.
20. S. Navale, V. Mali, S. Pawar, R. Mane, M. Naushad, F. Stadler, V. Patil, *RSC Adv.*, 5, (2015), 51961-51965.
21. B. Ameri, S. Davarani, R. Roshani, H. Moazami, A. Tadjarodi, *J. Alloys Compd.*, 695, (2017), 114-123.
22. H. Liu, T. Chin, S. Yung, *Mater. Chem. Phys.*, 50, (1997), 1-10.
23. D. Yang, Q. Yu, L. Gao, L. Mao, J. Yang, *Appl. Surf. Sci.*, 416, (2017), 503-510.
24. N. Priyadharsini, A. Shanmugavani, L. Vasylechko, R. Selvan, *Ionics*, 24, (2018), 2073-2082.
25. N. Prokopchuk, V. Kopilevich, L. Voitenko, *Russ. J. Appl. Chem.*, 81, (2008), 386-39.
26. C. Lee, F. Omar, A. Numan, N. Duraisamy, K. Ramesh, S. Ramesh, *J. Solid State Electrochem.*, 21, (2017), 3205-3213.

27. D. Wang, Y. Xu, W. Sun, X. Guo, L. Yang, F. Wang, Z. Yang, *Electrochim. Acta*, 337, (2020), 135827.
28. S. Sartale, C. Lokhande, *Mater. Chem. Phys.*, 65, (2000), 63-67.
29. Z. Jiang, W. Lu, Z. Li, K. H. Ho, X. Li, X. Jiao, D. Chen, *J. Mater. Chem. A*, 2, (2014), 8603-8606.
30. J. B. Condon, *Surface Area and Porosity Determinations by Physisorption: Measurements and Theory* (Elsevier, Amsterdam, 2006), pp. 6-14
31. H. Pang, C. Wei, Y. Ma, S. Zhao, G. Li, J. Zhang, J. Chen, S. Li, *Chempluschem*, 78, (2013), 546-553.
32. J. Li, M. Liu, L. Kong, D. Wang, Y. Hu, W. Han, L. Kang, *RSC Adv.*, 5, (2015), 41721-41728.
33. M. Chen, D. Butenko, I. Zatonovsky, J. Li, W. Han, N. Klyui, *Dalton Trans.*, 49, (2020), 8226-8237.
34. M. Jiang, J. Li, J. Li, Y. Zhao, L. Pan, Q. Cao, D. Wang, Y. Du, *Nanoscale*, 11, (2019), 9654-9660.
35. X. Bai, Q. Liu, Z. Lu, J. Liu, R. Chen, R. Li, D. Song, X. Jing, P. Liu, J. Wang, *ACS Sustain. Chem. Eng.*, 5, (2017), 9923-9934.
36. M. Sathiya, A. Prakash, K. Ramesha, J. Tarascon, A. Shukla, *J. Am. Chem. Soc.*, 133, (2011), 16291-16299.
37. N. Chodankar, I. Bagal, S. Ryu, D. Kim, *Chem. Eng. J.*, 362, (2019), 609-618.
38. P. Katkar, S. Marje, S. Pujari, S. Khalate, A. Lokhande, U. Patil, *ACS Sustainable Chem. Eng.*, 7, (2019), 11205-11218.
39. J. Duay, S. Sherrill, Z. Gui, E. Gillette, S. Lee, *ACS Nano*, 7, (2013), 1200-1214.
40. H. Kim, J. Cook, H. Lin, J. Ko, S. Tolbert, V. Ozolins, B. Dunn, *Nat. Mater.*, 16, (2017), 454-460.
41. P. Yang, Z. Wu, Y. Jiang, Z. Pan, W. Tian, L. Jiang, L. Hu, *Adv. Energy Mater.*, 8, (2018), 1801392-1801402.
42. F. Omar, A. Numan, S. Bashir, N. Duraisamy, R. Vikneswaran, Y. Loo, K. Ramesh, S. Ramesh, *Electrochim. Acta*, 273, (2018), 216-228.
43. S. Kandalkar, H. Lee, S. Seo, K. Lee, C. Kim, *J. Mater. Sci.*, 46, (2011), 2977-2981.
44. K. Sankar, Y. Seo, S. Lee, S. Jun, *ACS Appl. Mater. Interfaces*, 10, (2018), 8045-8056.
45. F. Butt, M. Tahir, C. Cao, F. Idress, R. Ahmed, W. Khan, Z. Ali, N. Mohmood, M. Tanveer, A. Mohmood, I. Aslam, *ACS Appl. Mater. Interfaces*, 16, (2014), 13635-13641.
46. J. Cherusseria, K. Kar, *J. Mater. Chem. A*, 4, (2016), 9910-9922.

CHAPTER-5

FABRICATION OF ASYMMETRIC SUPERCAPACITOR DEVICE AND PERFORMANCE EVALUATION

CHAPTER 5

Fabrication of asymmetric supercapacitor device and performance evaluation

Sr. No.	Title	Page No.
5.1	Introduction	115
SECTION – A Synthesis, characterization and supercapacitive performance evaluation of reduced graphene oxide (rGO) electrode		
5.2.A.1	Introduction	116
5.2.A.2	Experimental details	116
	5.2.A.2.1 Chemicals	116
	5.2.A.2.2 Synthesis of graphene oxide	116
	5.2.A.2.3 Synthesis of reduced graphene oxide	117
5.2.A.3	Results and discussion	117
	5.2.A.3.1 XRD study	117
5.2.A.4	Supercapacitive performance evaluation	118
	5.2.A.4.1 CV study	118
	5.2.A.4.2 GCD study	118
	5.2.A.4.3 EIS study	119
	5.2.A.4.4 Stability study	120
5.2.A.5	Conclusions	120
SECTION – B Fabrication of asymmetric supercapacitor device		
5.2.B.1	Introduction	121
5.2.B.2	Experimental details	121
	5.2.B.2.1 Electrode preparation	121
	5.2.B.2.2 Preparation of PVA-KOH gel electrolyte	121
	5.2.B.2.3 Fabrication of asymmetric aqueous device	122
	5.2.B.2.4 Fabrication of asymmetric solid-state device	122
5.2.B.3	Conclusions	123
SECTION – C Electrochemical performance evaluation of aqueous and solid-state device (For S-NCP-3//rGO)		
5.2.C.1	Introduction	123
5.2.C.2	Results and discussion	123
	5.2.C.2.1 Electrochemical performance evaluation of S-NCP-3//KOH//rGO aqueous asymmetric device	123
	5.2.C.2.1.1 CV study	124
	5.2.C.2.1.2 GCD study	125

		5.2.C.2.1.3	EIS study	126
		5.2.C.2.1.4	Ragone plot	127
		5.2.C.2.1.5	Stability study	127
	5.2.C.2.2	Electrochemical performance evaluation of S-NCP-3//PVA-KOH//rGO asymmetric solid-state device		128
		5.2.C.2.2.1	CV study	128
		5.2.C.2.2.2	GCD study	129
		5.2.C.2.2.3	EIS study	131
		5.2.C.2.2.4	Ragone plot	131
		5.2.C.2.2.5	Stability study	132
		5.2.C.2.2.6	Demonstration of S-NCP-3//PVA-KOH//rGO asymmetric solid-state device	133
5.2.C.3	Conclusions			134
5.3	References			135

5.1 Introduction:

The fabrications of SCs with flexible, portable and small size are essential to complete the current demand in ESDs [1, 2]. Currently, researchers are trying to design the materials, which can boost up energy and power capability of present ESDs. Nowadays, the SCs have fascinated significant attention as favourable and analogous ESDs because of good capabilities like rapid charge-discharge efficiency, long lifespan and superior PD, as compared to the batteries technology [3-6]. For the purpose to commercialize SCs; it is significant to enhance the specific energy as well as potential window without excluding other features. In addition, the fabrication of solid-state SC devices has paid enormous attention in order to fulfil the future energy demand which is largely dependent on electrochemical energy storage systems [7].

Consider a win-win condition where the fundamental principles behind SCs and batteries work together to achieve common purpose of higher energy and power efficiency. One such design is asymmetric SCs unlike traditional SCs, which consist of two distinct electrodes [8]. The different and same (EDLCs types and pseudocapacitive types) of electrode materials are employed to design the symmetric and asymmetric SC devices. The asymmetric configuration of SC is a beneficial approach to improve the operating potential window of device and it can be capable to deliver high power among other ESDs [9]. The ED and C_s of asymmetric SCs are greater as compared to the symmetric SCs [10, 11]. For this reason, the ASDs have been constructed by combining electrodes with different charge storage mechanisms and operating potential windows.

In this chapter, asymmetric aqueous and solid state SC devices are prepared using best performing nickel copper phosphate thin film as a cathode and rGO as an anode material to obtain high capacitive performance. This chapter is splitted into three sections (A, B and C). Section 'A' deals with synthesis and electrochemical performance evaluation of rGO electrode. Section 'B' describes the fabrication of aqueous and solid state asymmetric SC devices and section 'C' is related to the electrochemical performance evaluation of S-NCP-3//rGO aqueous and solid-state ASDs.

SECTION – A**Synthesis, characterization and supercapacitive performance evaluation of reduced graphene oxide (rGO) electrode****5.2.A.1 Introduction:**

In the progress of asymmetric SC devices, various forms of carbon materials have been largely investigated as a negative electrode due to their better cycling stability, high surface area, high C_s , strong mechanical properties, superior electrical conductivity and higher PD [12-16]. Typically, carbon based materials like as carbon aerogels, AC, CNTs, graphene oxide (GO), etc. were employed as negative electrode in the ASDs [16-18]. Among these materials, rGO offers high charge carrier mobility, ultrahigh specific surface area with high electrical conductivity, good chemical stability, great flexibility and strong mechanical strength [19]. Present section describes the preparation of GO by modified Hummer's method and reduction of GO by hydrothermal method. Additionally, the rGO films are characterized by different techniques and supercapacitive performance is probed in 1 M KOH electrolyte.

5.2.A.2 Experimental details:**5.2.A.2.1 Chemicals:**

Graphite flakes, potassium permanganate (KMnO_4), sulfuric acid (H_2SO_4), N-Methyl-2-Pyrrolidone (NMP), sodium nitrate (NaNO_3), hydrochloric acid (HCl), polyvinylidene fluoride (PVDF), carbon black, KOH and hydrogen peroxide (H_2O_2) were purchased from Sigma Aldrich. All the chemicals were AR grade and utilized without further purification.

5.2.A.2.2 Synthesis of graphene oxide:

The GO was prepared by modified Hummer's method [20, 21]. In primary stage, graphite flakes (5 g) and NaNO_3 (2.5 g) were mixed with 120 mL of H_2SO_4 and stirred in an ice bath for 25 min. After that, 15 g of KMnO_4 were slowly added in the mixture with constant stirring, while the temperature of the mixture maintained below 293 K. Thereafter, the mixture was continuously stirred for overnight (12 h) at ambient environment. DDW (150 ml) with 30% H_2O_2 (5 ml) was added (30 min) dropwise. Later, the reaction product was washed with 5% HCl and DDW repeatedly. Then, resultant mixture was centrifuged at 2000 rpm to eliminate unreacted graphite flakes and further centrifuged at 10000 rpm to collect GO nanosheets. The centrifuged and washed GO is utilized for the preparation of rGO.

5.2.A.2.3 Synthesis of reduced graphene oxide:

The rGO was synthesized by reducing the GO by hydrothermal method. The well dispersed 50 ml GO solution (4 mg mL^{-1}) was prepared and heated at 423 K for 12 h in a hydrothermal autoclave. Prepared product (rGO) was cooled via liquid nitrogen for solidification and freeze dried for 48 h to avoid aggregation of rGO during elimination of water content. At last, the rGO foam was obtained and it further crushed into powder. Furthermore, the rGO (negative) electrode was prepared as follows: 75 wt% of as-prepared rGO material, 20 wt% of carbon black and 5% polyvinylidene fluoride (PVDF) in N-methyl 2-pyrrolidone (NMP) was used to make homogeneous slurry. Then, formed slurry was coated on SS substrate ($1 \times 1 \text{ cm}^2$ area) and dried at 333 K for 2 h. Then, prepared rGO electrode was employed as anode in the asymmetric SC device.

5.2.A.3 Results and discussion:

5.2.A.3.1 XRD study:

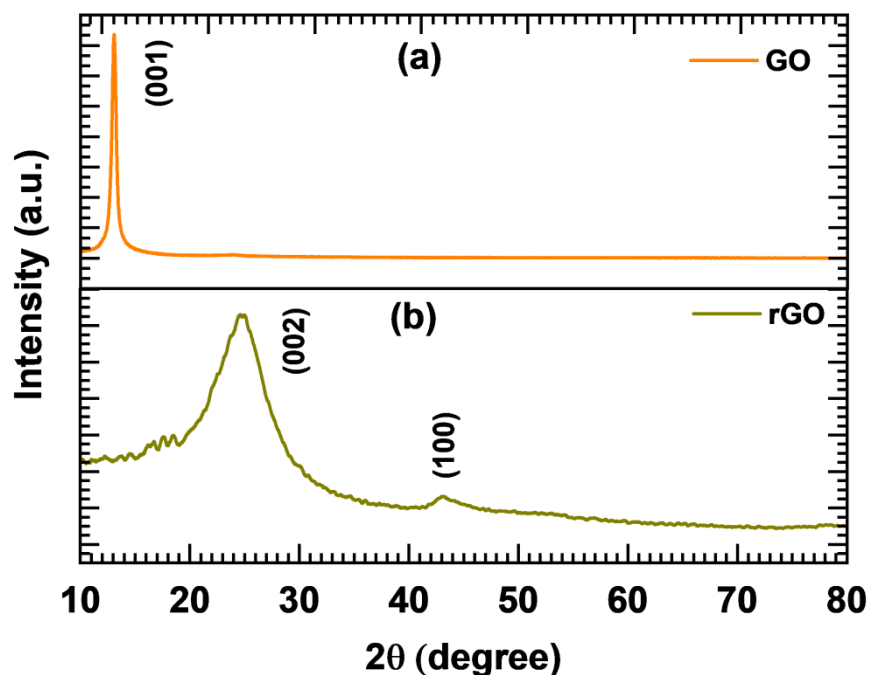


Figure 5.1: XRD patterns of (a) GO and (b) rGO samples.

XRD patterns of GO and rGO are presented in **Figure 5.1 (a and b)**. The prepared GO sheet showed the strong characteristic peak at 11.13° assigned to the (0 0 1) plane in the XRD. Also, the characteristic diffraction peaks are detected at 24.71° and 43.09° assigned to the (0 0 2) and (1 0 0) planes [22]. The scattered XRD peak at

24.71° confirms a reduction of GO material and formation of few layered rGO nanosheets [23].

5.2.A.4 Supercapacitive performance evaluation:

The electrochemical characteristics of rGO electrode tested by CV, GCD, EIS and stability techniques in 1 M KOH electrolyte using three-electrode cell configuration.

5.2.A.4.1 CV study:

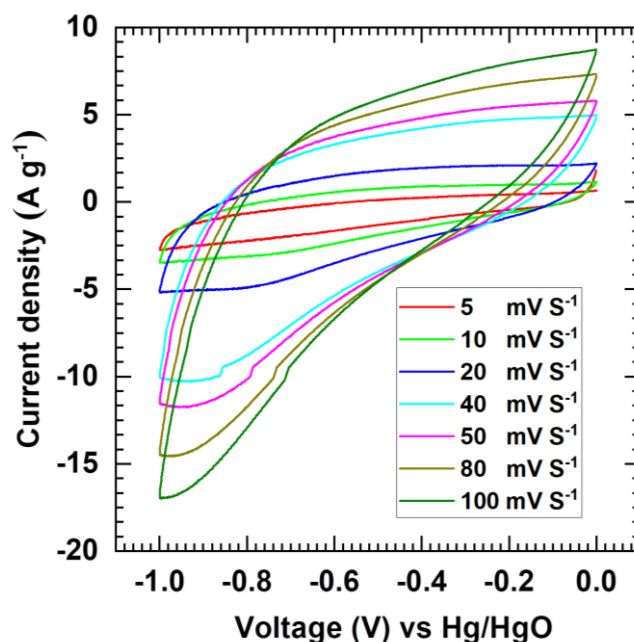


Figure 5.2: CV plots of rGO electrode at scan rates from 5-100 mV s^{-1} .

The CV curves of rGO (negative) electrode at various scan rates from 5-100 mV s^{-1} within the potential range of 0 to -1 V vs Hg/HgO in 1 M KOH electrolyte are displayed in **Figure 5.2**. **Figure 5.2** shows that, the area under the CV curve increases with increasing scan rate, this displays voltammetric current is proportional to the scan rate of CV and signifies typical EDLC behaviour of electrode. The quasi-rectangular profile of CV curves affirms EDLC based capacitive nature of rGO electrode.

5.2.A.4.2 GCD study:

The GCD plots of rGO electrode evaluated at different current densities from 1.5 to 3.5 A g^{-1} within the potential range of 0 to -1 V vs Hg/HgO and presented in **Figure 5.3 (a)**. The charge-discharge plot shows nearly linear curve, which is the indicative of its double layer capacitive nature. The GCD analysis was used to calculate C_s of rGO electrode and plotted in **Figure 5.3 (b)** as a function of current density. The maximum

C_s of 159 F g^{-1} is obtained for rGO electrode at 1.5 A g^{-1} current density and it decreases to 114 F g^{-1} at the current density of 3.5 A g^{-1} .

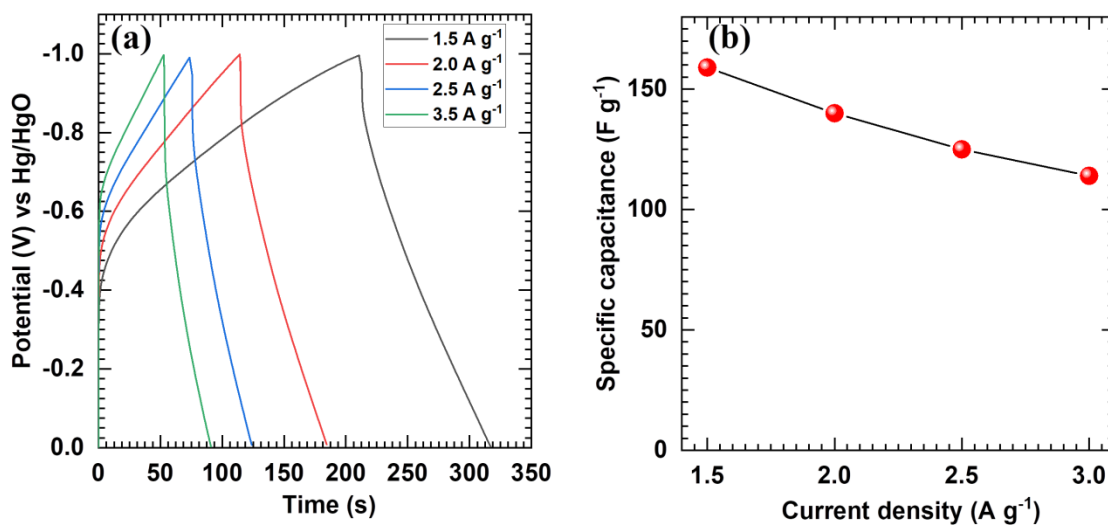


Figure 5.3: (a) The GCD curves of rGO electrode at different current densities from 1.5 to 3.5 A g^{-1} and (b) the plot of C_s of rGO electrode at 1.5 to 3.5 A g^{-1} current densities.

5.2.A.4.3 EIS study:

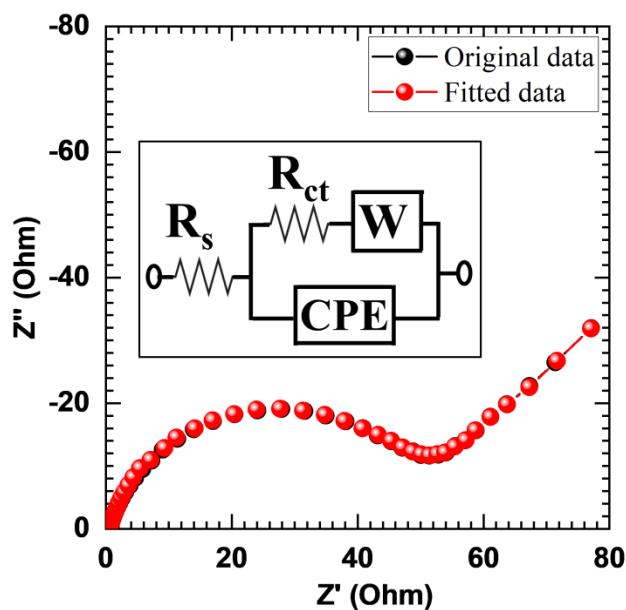


Figure 5.4: Nyquist plot of rGO electrode [Inset: equivalent circuit for fitted with Nyquist plot].

The EIS study of rGO electrode was executed to examine its electrochemical conductivity. The Nyquist plot of rGO electrode is exhibited in **Figure 5.4**. The fitted equivalent circuit is displayed as inset of **Figure 5.4**. In fitted circuit, $R_s = 0.48 \Omega$, R_{ct}

$=47.61 \Omega$, $CPE = 0.843 \text{ mF}$ and $W = 0.282 \Omega$. A small value (R_s and R_{ct}) of total impedance denotes excellent electrical conductivity of rGO electrode.

5.2.A.4.4 Stability study:

The cyclic stability of the rGO electrode was tested over 3000 GCD cycles at current density of 4 A g^{-1} and presented in **Figure 5.5**. This stability test revealed 77.42% retention of the C_s after 3000 GCD cycles. A reduction in charge-discharge time in initial (A) and final (B) GCD cycles is observed and revealed as inset **Figure 5.5**. Furthermore, observed reduction in capacitance may be due to depletion of minute active material during cycling.

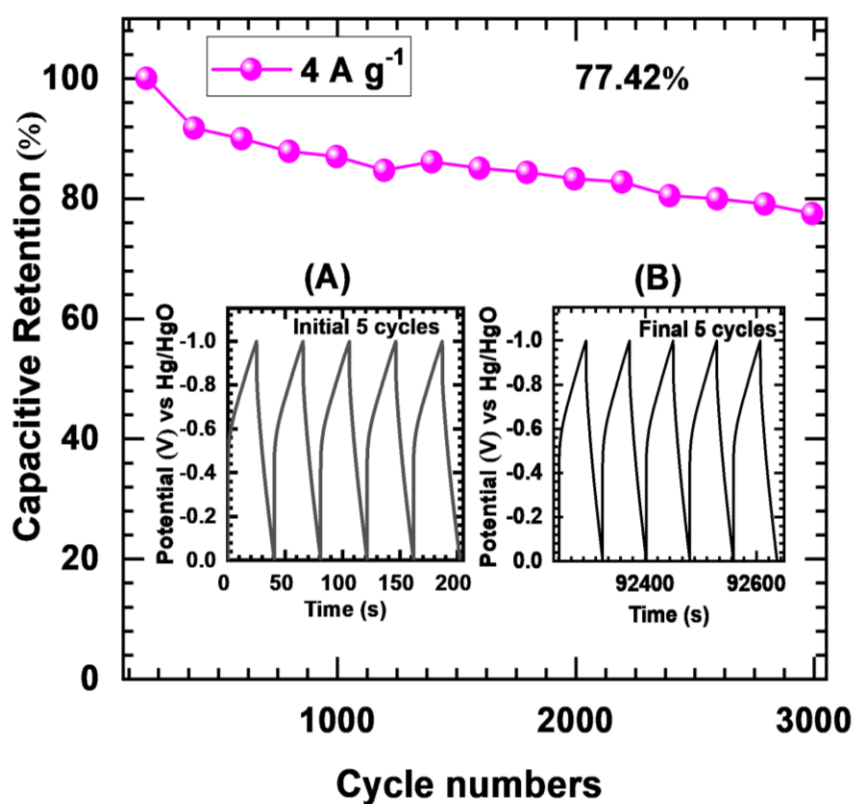


Figure 5.5: Stability of rGO electrode during 3000 cycles at current density of 4 A g^{-1} . Inset displays the GCD curves of the initial (A) and final (B) 5 GCD cycles.

5.2.A.5 Conclusions:

In summary, GO was successfully synthesized by the modified Hummer's method and further reduced using hydrothermal method. The successful reduction of GO to rGO is affirmed by XRD study. The rGO electrode displayed superior supercapacitive performance with maximum C_s of 159 F g^{-1} at 1.5 A g^{-1} current density. Also, it exhibited 77.42% capacitive retention over 3000 GCD cycles. The

results suggest that, rGO electrode can be excellent candidate (anode) for SC device application.

SECTION – B

Fabrication of asymmetric supercapacitor device

5.2.B.1 Introduction:

The choice of electrode material plays a key role that can effectively enhance the potential window of device. Aqueous or solid-state gel electrolyte is fabricated amongst two different charge storage materials in an asymmetric construction to perform high ED while sustaining PD [24, 25]. In general, the operating potential window of an asymmetric SCs device is associated with the electrolytes overpotential as well as the work function difference of the negative and positive electrodes [26, 27]. Furthermore, a wider potential window of device can enhance the ED and can be achieved through different electrolytes (aqueous and solid-state).

5.2.B.2 Experimental details:

5.2.B.2.1 Electrode preparation:

As concluded from **chapter 3** and **4**, the SILAR deposited nickel copper phosphate material reveals high performance as compare to hydrothermally synthesized nickel copper phosphate electrode. Therefore, SILAR deposited nickel copper phosphate on the flexible SS substrate is used as cathode for ASD fabrication. The preparative parameters described in **chapter 4** are used for the preparation of large area ($5 \times 5 \text{ cm}^2$) nickel copper phosphate thin film (cathode electrode). The rGO (anode) electrode was prepared as discussed in section A of this chapter. These cathode and anode electrodes are used for aqueous and SSD fabrication.

5.2.B.2.2 Preparation of PVA-KOH gel electrolyte:

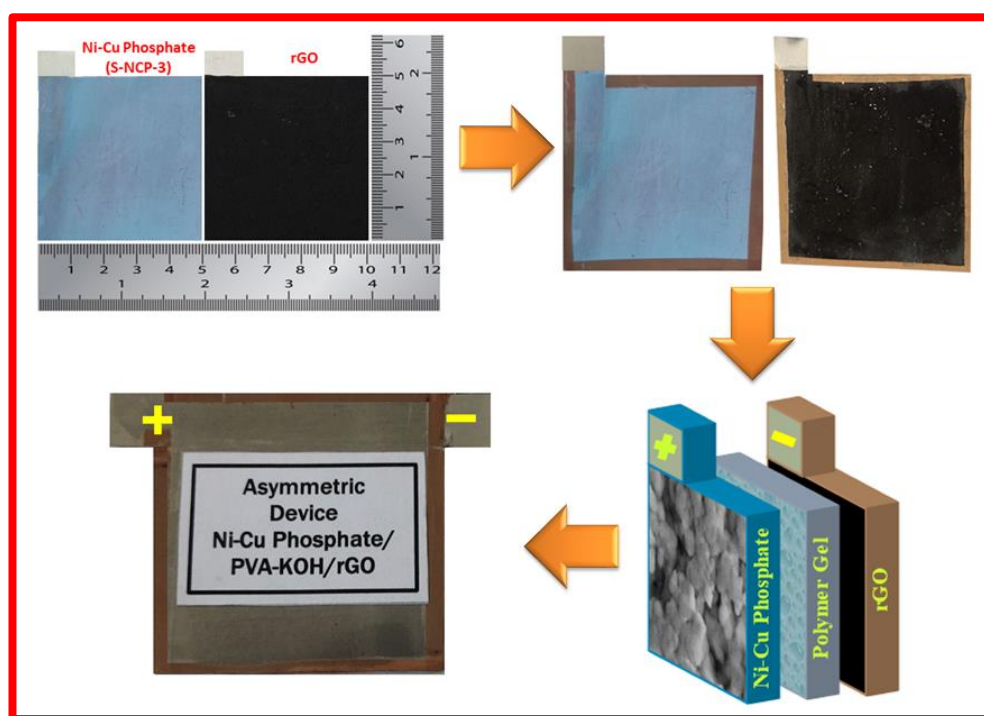
To prepare the SSD, the water soluble PVA polymers with KOH were utilized for the preparation of gel electrolyte. Initially, 2 g PVA is taken in 20 ml DDW and dissolved at 363 K temperature under constant stirring up to a solution become transparent and clear. After that, 1 M KOH solution (in 10 mL of DDW) was added in PVA solution and stirred rigorously up to viscous, clear and homogeneous appearance of solution [28]. The viscous and transparent gel (PVA-KOH) is utilized as gel electrolyte and separator in SSD fabrication.

5.2.B.2.3 Fabrication of asymmetric aqueous device:

The important condition in asymmetric aqueous device fabrication is that, both electrodes (cathode and anode) should have different potential windows. An asymmetric aqueous device was fabricated using SILAR deposited nickel copper phosphate (S-NCP-3) as a cathode and rGO as anode in 1 M KOH electrolyte and analysed with different electrochemical parameters.

5.2.B.2.4 Fabrication of asymmetric solid-state device:

To make the ASD, SILAR prepared nickel copper phosphate (S-NCP-3) as a positive and rGO as a negative electrode with PVA-KOH gel electrolyte were used as illustrated in **Scheme 5.1**.



Scheme 5.1: Schematic illustration of SSD fabrication.

An asymmetric SSD was fabricated employing a large area ($5 \times 5 \text{ cm}^2$) nickel copper phosphate and rGO electrodes. Furthermore, those two electrodes were painted with PVA-KOH gel to form a thin layer of electrolyte and dried at ambient environment. After drying, the edges of electrodes were enclosed with insulating tape to inhibit any shortening through electrodes sides. One more time the gel electrolyte painted on the surface of active material for making proper contact among electrode and electrolyte. Later, both electrodes were assembled to form a SSD with gel electrolyte. The assembled solid-state ASD is further packed with transparent plastic strips. Lastly, the prepared device was pressed under 1 ton pressure for 12 h to increase

the interfacial contact of active electrode materials with gel electrolyte. The SSD was successfully fabricated by aforementioned steps.

5.2.B.3 Conclusions:

In summary, a large area nickel copper phosphate thin films were prepared by SILAR method and rGO electrode via drop-casting method on SS substrate. The asymmetric aqueous and solid-state SC devices were successfully fabricated using nickel copper phosphate (S-NCP-3) as a positive electrode and rGO as a negative electrode. The 1 M KOH and PVA-KOH as aqueous and gel electrolyte, respectively are used to fabricate SC aqueous and SSD.

SECTION – C

Electrochemical performance evaluation of aqueous and solid-state device (For S-NCP-3//rGO)

5.2.C.1 Introduction:

To develop an ASD, the most important condition is that the electrode material must have different operating potential windows (positive and negative). Aqueous asymmetric SC device was fabricated using SILAR deposited nickel copper phosphate as positive and rGO as negative electrodes in 1 M KOH electrolyte. Moreover, the crucial task for preparation of ASD is that, charges of both electrodes ($q^+ = q^-$) should be equal to obtain the maximum electrochemical performance. Therefore, the mass loading of both electrodes was determined by the following charge balance formula: [29]

$$\frac{m_+}{m_-} = \frac{C_- \times \Delta V_-}{C_+ \times \Delta V_+} \quad (5.1)$$

Where, $m_{(+ or -)}$, $\Delta V_{(+ or -)}$ and $C_{(+ or -)}$ are the mass of active substance (g), potential window (V) and C_s ($F g^{-1}$) of the positive and negative electrodes. In the present case, the operative potential window (0 to 0.65 and -1 to 0 V vs Hg/HgO) and capacitances (750 and $159 F g^{-1}$ at 1 and $1.5 A g^{-1}$, respectively) of positive and negative electrodes are dissimilar. So calculated optimal mass ratio of positive and negative electrode is obtained to be $0.38:1$ in present work. Therefore, the obtained optimum masses were utilized to construct ASD.

5.2.C.2 Results and discussion:

5.2.C.2.1 Electrochemical performance evaluation of S-NCP-3//KOH//rGO aqueous asymmetric device:

5.2.C.2.1.1 CV study:

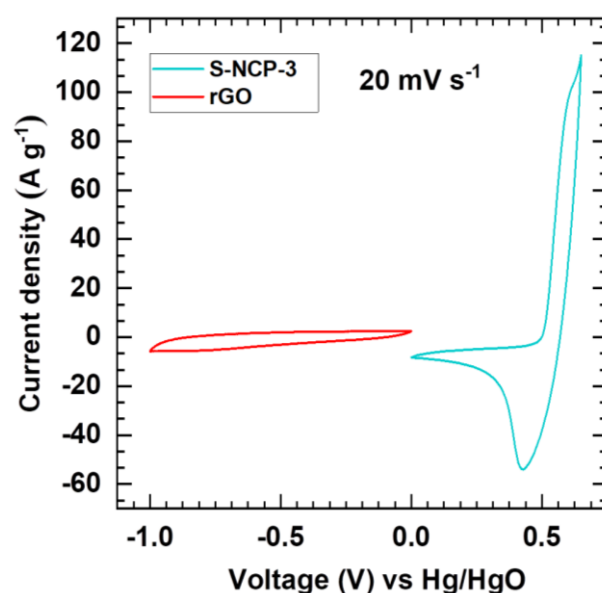


Figure 5.6: The CV plots of S-NCP-3 and rGO electrodes in 1 M KOH electrolyte.

To examine the supercapacitive performance of an aqueous ASD (S-NCP-3//KOH//rGO), CV, GCD and EIS techniques were employed. The CV graphs of rGO and S-NCP-3 electrodes in different voltage ranges at 20 mV s^{-1} scan rate are presented in **Figure 5.6**. The **Figure 5.6** shows that, two individual pseudocapacitive electrodes with practical integration can achieve a wide voltage window for aqueous asymmetric SC device. The electrochemical performance of S-NCP-3//KOH//rGO asymmetric SC device was analysed by two electrode cell system. The voltage window of S-NCP-3//KOH//rGO ASD were optimized in the range of 1.2 to 1.7 V at a fixed scan rate 50 mV s^{-1} as presented in **Figure 5.7 (a)**. Increases in the operating voltage window from 1.2 to 1.7 V, current contribute of the CV curve increases. The quasi-rectangular nature of CV curves is achieved up to voltage window of 0 to 1.6 V and abruptly increase in current is observed owing to oxygen evolution reaction process at 1.7 V, which may be contribute for irreversible reaction [30, 31]. Hence, the voltage window of 0.0 to 1.6 V was selected for the electrochemical of S-NCP-3//KOH//rGO ASD. The CV curves of S-NCP-3//KOH//rGO device at various scan rates from $5\text{--}100 \text{ mV s}^{-1}$ within the operating voltage window of 0 to 1.6 V are exhibited in **Figure 5.7 (b)**. The device displays similar and reversible shape of CV curves with good rate capability at different scan rates [32].

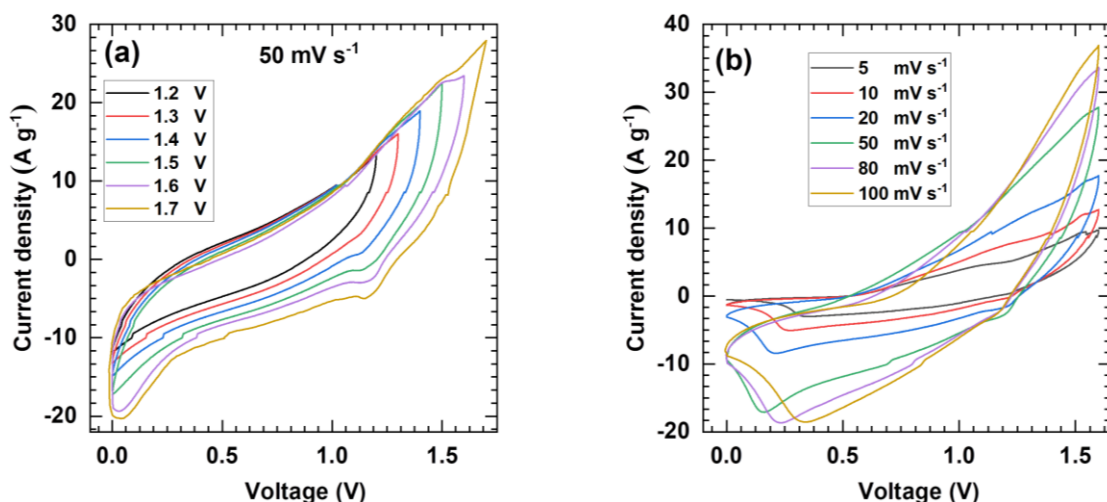


Figure 5.7: The CV curves of S-NCP-3//KOH//rGO ASD (a) in different voltage windows from 1.2-1.7 V and (b) at various scan rates from 5-100 mV s^{-1} .

5.2.C.2.1.2 GCD study:

The GCD curves of S-NCP-3//KOH//rGO ASD in different voltage windows (1.2 to 1.7 V) at a constant current density of 3.6 A g^{-1} are exhibited in **Figure 5.8 (a)**. The GCD curves display better performance within the voltage window of 0 to 1.6 V by showing symmetric charge-discharge nature. So, from CV and GCD studies, the operational voltage window of 0 to 1.6 V was selected for ASD and applied for further study. The GCD plots of S-NCP-3//KOH//rGO device at different current densities from 3.0 - 3.9 A g^{-1} are presented in **Figure 5.8 (b)**. The non-linear GCD curves are observed for NCP-3//KOH//rGO device.

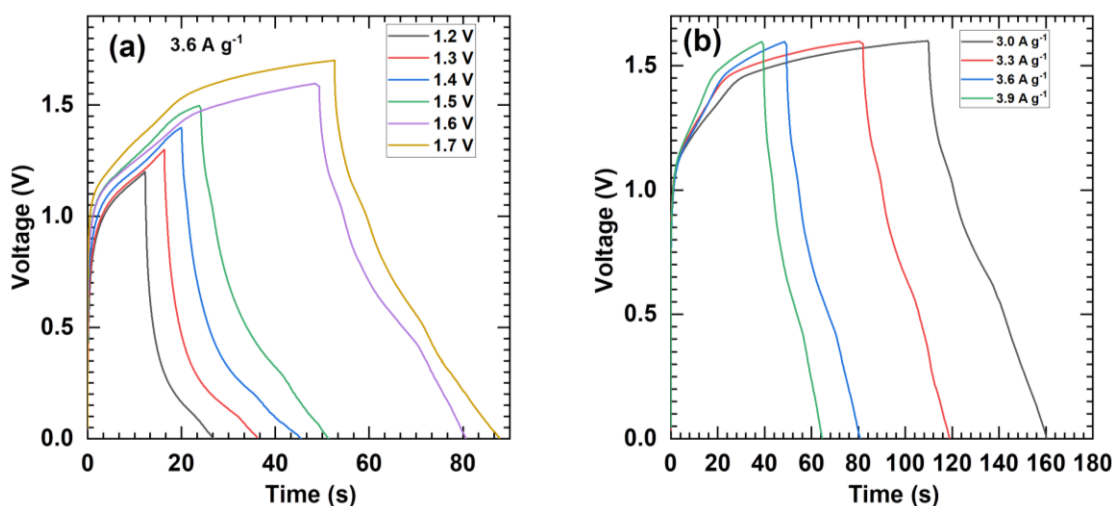


Figure 5.8: The GCD curves of S-NCP-3//KOH//rGO ASD (a) in different voltage windows from 1.2-1.7 V and (b) at various current densities from 3.0 - 3.9 A g^{-1} .

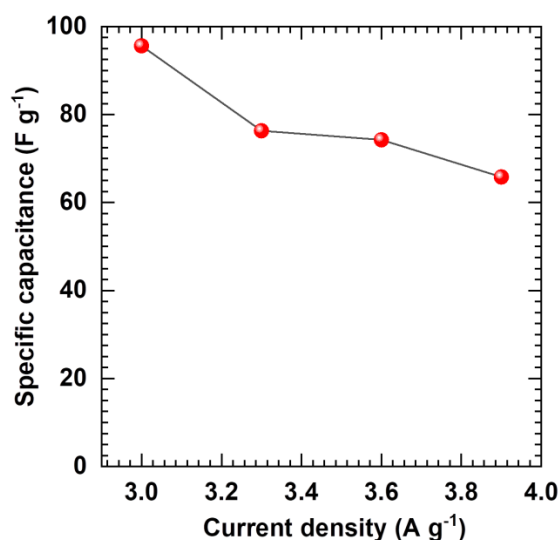


Figure 5.9: The C_s of S-NCP-3//KOH//rGO device at different current densities.

The C_s of S-NCP-3//KOH//rGO ASD calculated from GCD curves are shown in **Figure 5.9**. The S-NCP-3//KOH//rGO device achieves highest C_s of 95.62 F g^{-1} at 3.0 A g^{-1} current density and it decreases up to 65.81 F g^{-1} at current density of 3.9 A g^{-1} . The small decrement of capacitance at higher current density suggests excellent rate capability of aqueous asymmetric SC device. The C_s of the device decreases with increase in current density, due to inadequate electrode-electrolyte interaction at high current density [33, 34].

5.2.C.2.1.3 EIS study:

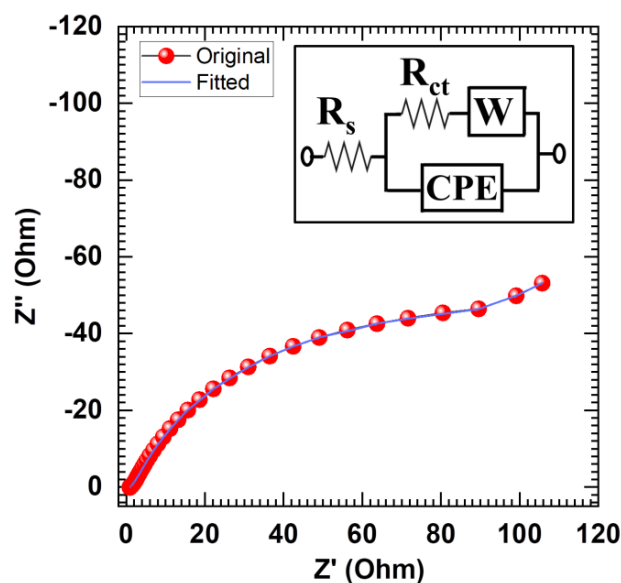


Figure 5.10: The Nyquist plot of S-NCP-3//KOH//rGO asymmetric aqueous device [inset: equivalent circuit of the fitted data].

The properties of ion transfer in asymmetric aqueous device were investigated by EIS analysis. The Nyquist plot of S-NCP-3//KOH//rGO asymmetric aqueous device is presented in **Figure 5.10**. The equivalent circuit of impedance spectroscopy is depicted as inset of **Figure 5.10**. Low R_s (0.87Ω) and R_{ct} (96.92Ω) values are observed due to high electrochemical conductivity of electrodes. Also, the value of W and CPE is 0.811 mF and 0.205Ω , respectively. The mutual nature of both electrodes is responsible for better electrochemical performance of S-NCP-3//KOH//rGO asymmetric aqueous device with enhanced operating voltage window, C_s as well as ED.

5.2.C.2.1.4 Ragone plot:

The ED and PD are two essential factors in the SC performance evaluation. The ED and PD of asymmetric aqueous device are calculated and illustrated in **Figure 5.11**.

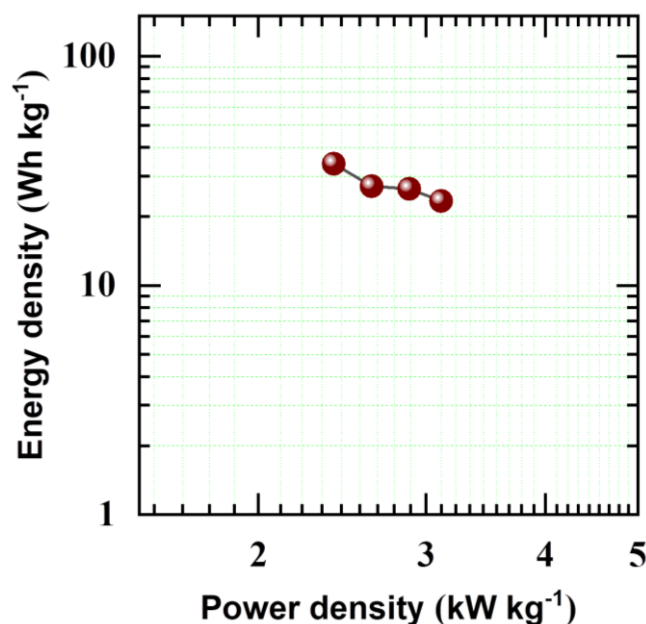


Figure 5.11: Ragone plot of S-NCP-3//KOH//rGO asymmetric aqueous device.

The ED of S-NCP-3//KOH//rGO ASD reached up to 34 Wh kg^{-1} with a PD of 2.40 kW kg^{-1} . Moreover, the ED remained 23.39 Wh kg^{-1} at a high PD of 3.11 kW kg^{-1} . The ASD with two different EDLC and pseudocapacitive material has improved the working potential window and the resulting ED as well as PD.

5.2.C.2.1.5 Stability study:

The cyclic stability of the S-NCP-3//KOH//rGO asymmetric cell was studied by continuous 5000 GCD cycles at a current density of 13 A g^{-1} (**Figure 5.12**). The

capacitance retention with respective cycles is plotted in **Figure 5.12** and the GCD curves of initial (A) and final (B) 5 cycles are depicted as inset of figure. The S-NCP-3//KOH//rGO asymmetric cell shows 94.11% capacitive retention after 5000 GCD cycles. The asymmetric cell illustrate decrement in the C_s at initial cycles then increase in C_s owing to expansion of electrochemical active volume of material after many GCD cycles. The stable nature with superior capacitance of S-NCP-3//KOH//rGO ASD encourages further usage of SILAR deposited nickel copper phosphate thin films and rGO electrodes in the hybrid solid state ESD application.

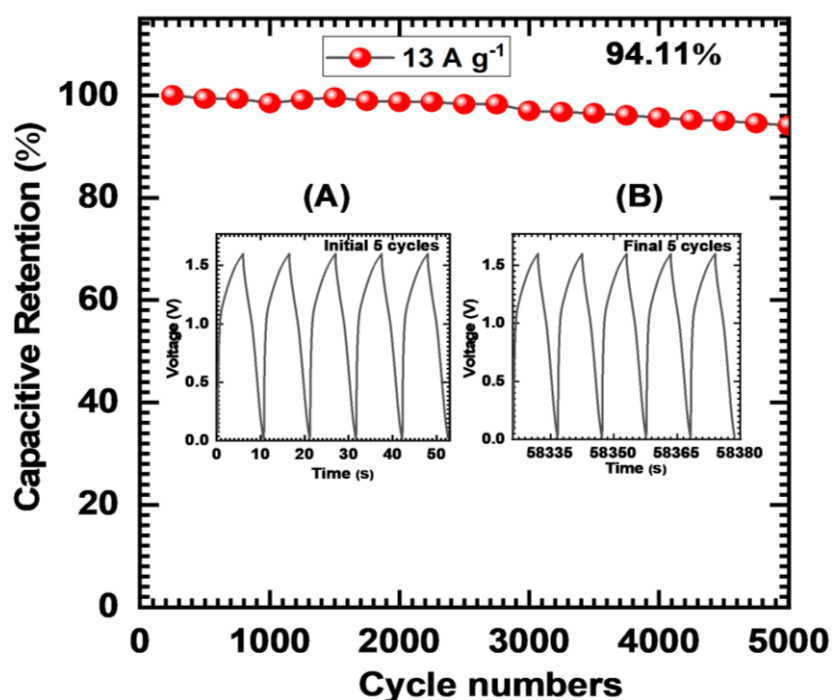


Figure 5.12: The plot of capacitive retention of S-NCP-3//KOH//rGO ASD at the current density of 13 A g^{-1} with respect to cycle numbers (5000) (inset: initial (A) and final (B) 5 GCD cycles).

5.2.C.2.2 Electrochemical performance evaluation of S-NCP-3//PVA-KOH//rGO asymmetric solid-state supercapacitor device:

An all-solid-state asymmetric SC device is prepared as described in sub-section 5.2.B.2.4 of section B. The electrochemical performance of an asymmetric SSD is tested (CV, GCD and EIS) by a two-electrode configuration.

5.2.C.2.2.1 CV study:

Figure 5.13 (a) shows the CV curves of S-NCP-3//PVA-KOH//rGO asymmetric SSD at constant scan rate of 50 mV s^{-1} for different voltage ranges from +1.2 to +1.7

V. Area under CV curve increases in anodic and cathodic regions up to 1.6 V and thereafter, abruptly increase in current is observed at 1.7 V voltage window which demonstrate that, oxygen evolution reaction. Hence, the voltage window of 0 to 1.6 V was selected for S-NCP-3//PVA-KOH//rGO asymmetric SSD and used for further electrochemical analysis.

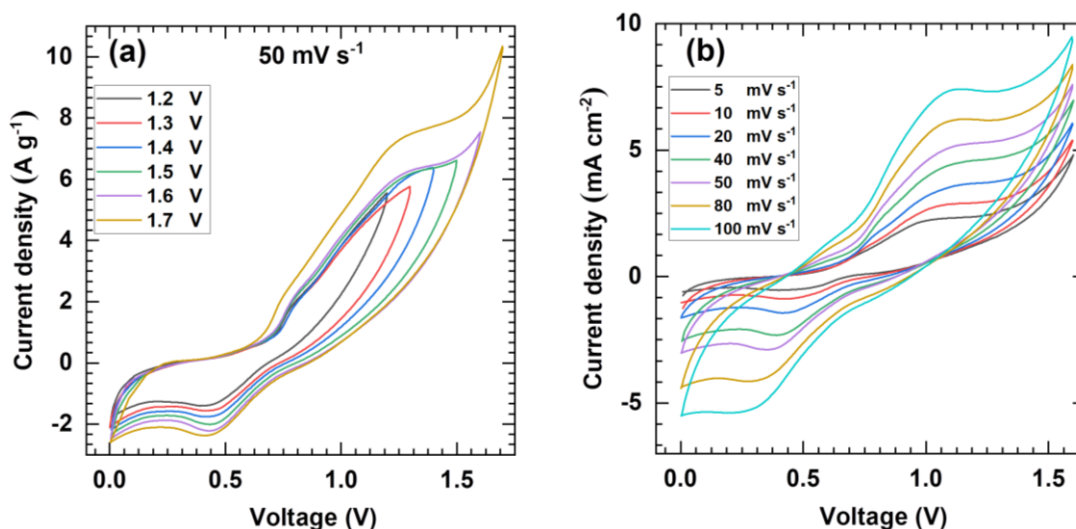


Figure 5.13: The CV curves of S-NCP-3//PVA-KOH//rGO asymmetric SSD (a) in different voltage windows from 1.2 to 1.7 V and, (b) at different scan rates from 5-100 mV s^{-1} .

Figure 5.13 (b) illustrates the CV curves of S-NCP-3//PVA-KOH//rGO asymmetric SSD at different scan rates ranging from 5-100 mV s^{-1} . The shape of CV curves reveal larger area under the curve with perfect pseudocapacitive behaviour of S-NCP-3//PVA-KOH//rGO asymmetric SSD. All the CV curves maintain their shape irrespective of scan rate, signifying that the S-NCP-3//PVA-KOH//rGO asymmetric SSD displays excellent capacitive behaviour.

5.2.C.2.2.2 GCD study:

The electrochemical capacitive performance of S-NCP-3//PVA-KOH//rGO asymmetric SSD is further investigated by the charge-discharge study. The GCD curves of S-NCP-3//PVA-KOH//rGO asymmetric SSD at different voltage windows (1.2 to 1.7 V) at a constant current density of 2.8 A g^{-1} are exhibited in **Figure 5.14 (a)**. Up to voltage of 1.6 V, the GCD curve shows better performance for S-NCP-3//PVA-KOH//rGO asymmetric SSD. The GCD curves of S-NCP-3//PVA-KOH//rGO asymmetric SSD at different current densities from 0.7 to 2.8 A g^{-1} are shown in **Figure 5.14 (b)**.

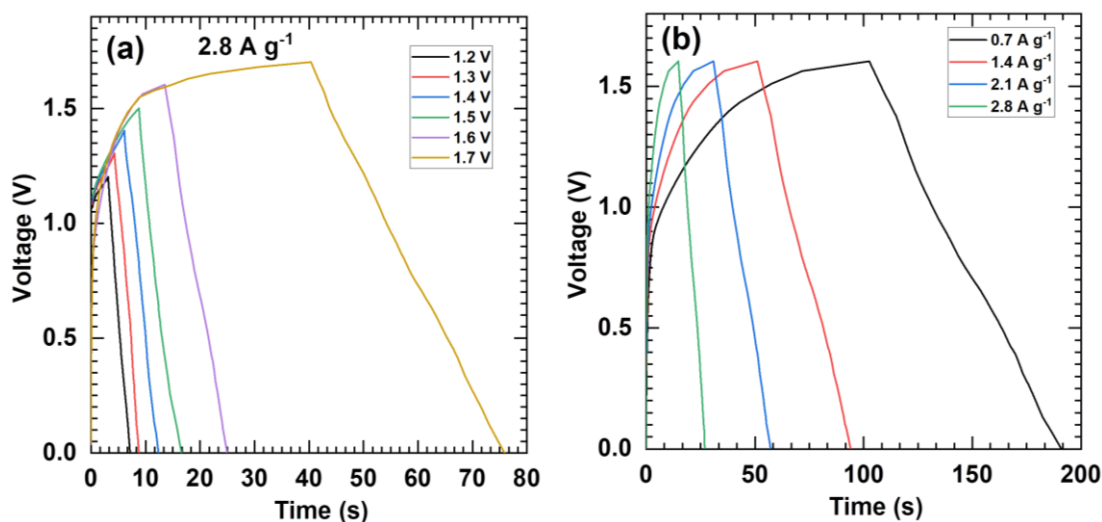


Figure 5.14: The GCD curves of S-NCP-3//PVA-KOH//rGO asymmetric SSD (a) in different voltage windows from 1.2-1.6 V and (b) at various current densities from 0.7-2.8 A g⁻¹.

Meanwhile, the non-linear charge-discharge profile illustrates a better electrochemical capacitive behaviour based on good reversible redox reactions. The C_s of S-NCP-3//PVA-KOH//rGO asymmetric SSD calculated from GCD curves is showed in **Figure 5.15**. The S-NCP-3//PVA-KOH//rGO asymmetric SSD achieves highest C_s of 37.62 F g⁻¹ at 0.7 A g⁻¹ current density and it decreases up to 22.75 F g⁻¹ at current density of 2.8 A g⁻¹.

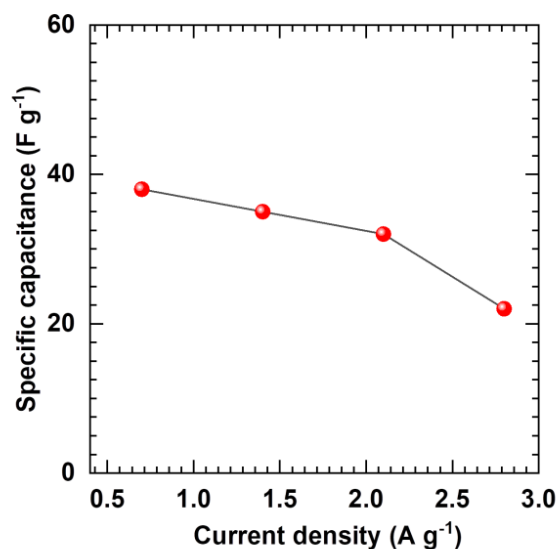


Figure 5.15: The C_s of S-NCP-3//PVA-KOH//rGO asymmetric SSD at different current densities.

5.2.C.2.2.3 EIS study:

The Nyquist plot for S-NCP-3//PVA-KOH//rGO asymmetric SSD was studied by using EIS analysis and exhibited in **Figure 5.16** with an equivalent circuit as inset of figure. The low values of R_s (0.24Ω) and R_{ct} (144Ω) attributed to the superior ionic conductivity of gel electrolyte and its compatibility with electrode material. The W and CPE are found to be 0.28Ω and 0.568 mF , respectively in equivalent circuit. The EIS result confirms that, the gel electrolyte offers low IR.

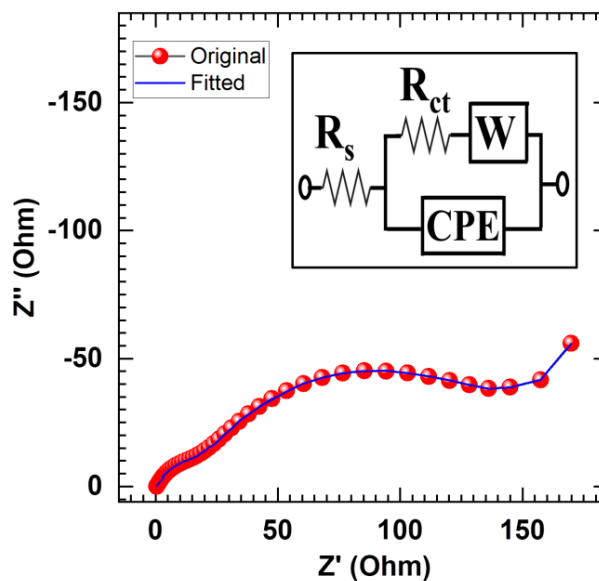


Figure 5.16: The Nyquist plot of S-NCP-3//PVA-KOH//rGO asymmetric SSD [inset: equivalent circuit of the fitted data].

5.2.C.2.2.4 Ragone plot:

The Ragone plot of S-NCP-3//PVA-KOH//rGO asymmetric SSD is presented in **Figure 5.17**. The fabricated device delivered highest ED of 13.51 Wh kg^{-1} with a PD of 0.55 kW kg^{-1} and maintained 7.82 Wh kg^{-1} ED at a maximum PD of 2.16 kW kg^{-1} . This result illustrates enhanced ED and good rate capability for the SSD that can be understood from good C_s and broad working voltage window.

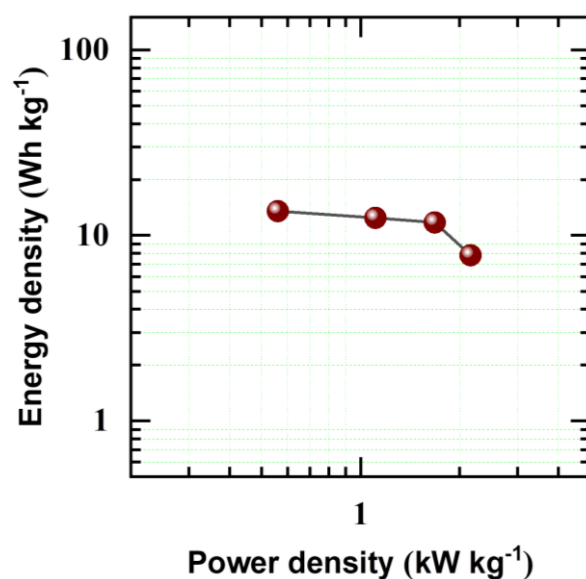


Figure 5.17: Ragone plot of S-NCP-3//PVA-KOH//rGO asymmetric SSD.

5.2.C.2.2.5 Stability study:

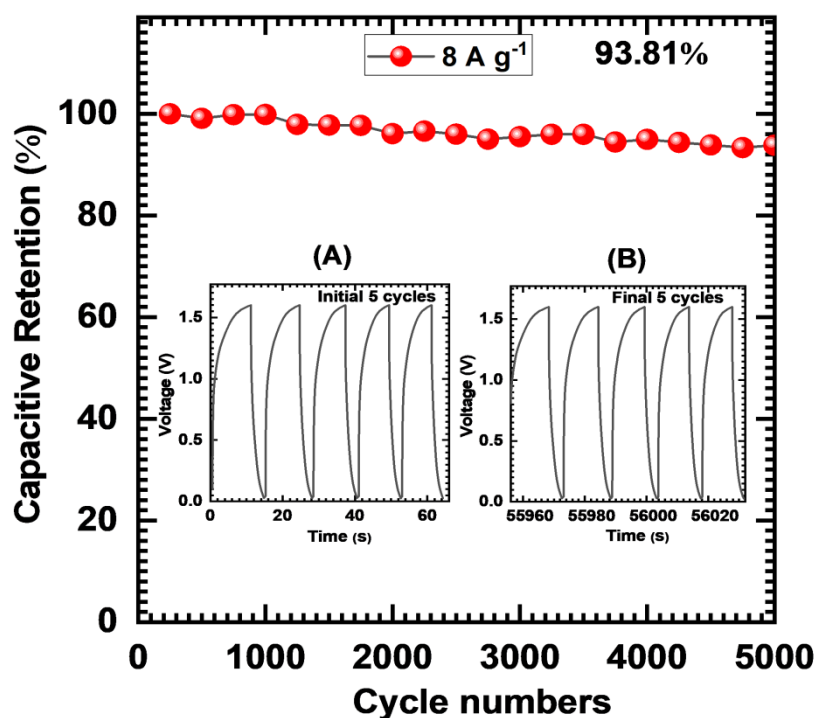


Figure 5.18: The plot of capacitive retention of S-NCP-3//PVA-KOH//rGO ASD at the current density of 8 A g^{-1} with respect to cycle numbers (5000) (inset: initial (A) and last (B) 5 GCD cycles).

The electrochemical cyclic stability of S-NCP-3//PVA-KOH//rGO asymmetric SSD is examined by taking the GCD over 5000 cycles at a fixed current density of 8 A g^{-1} (**Figure 5.18**). The S-NCP-3//PVA-KOH//rGO asymmetric SSD delivers 93.81%

capacitance retention over 5000 cycles. The initial (A) and final (B) 5 GCD cycles are depicted as inset of **Figure 5.18**.

5.2.C.2.2.6 Demonstration of S-NCP-3//PVA-KOH//rGO asymmetric solid-state device:

The practical applicability of S-NCP-3//PVA-KOH//rGO asymmetric solid-state is tested by charging two serially connected devices for 30 s by employing constant potential of +3.2 V and discharged through 201 red light emitting diodes (LEDs) designed in text of “DYPU CDL GROUP”. The text contains “DYPU” relate to D. Y. Patil University, “CDL GROUP” related to Prof. C. D. Lokhande research group. The 201 LED panel lights up for 125 s (**Figure 5.19**). This demonstration highlights the potential of the SSD as a most promising ESD in various portable electronic areas.

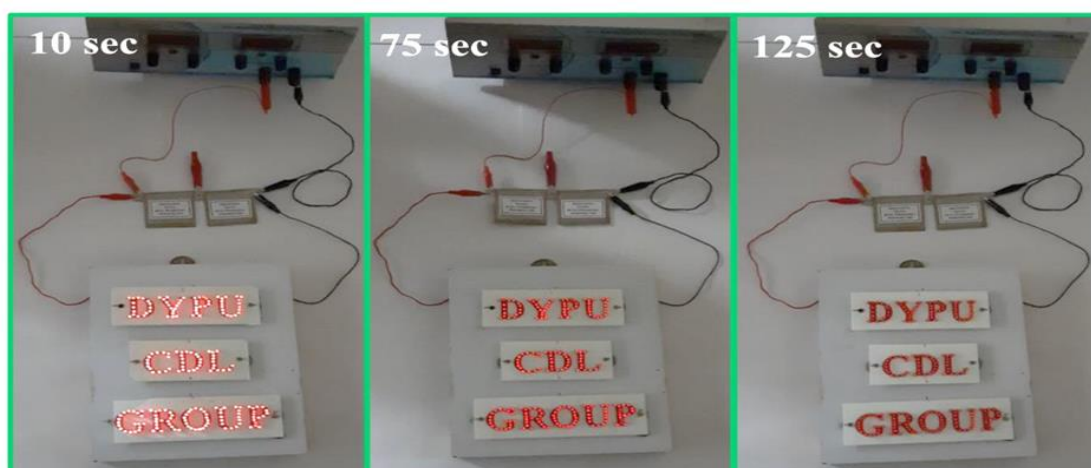


Figure 5.19: Digital photographs of device demonstration of S-NCP-3//PVA-KOH//rGO asymmetric SSD glowing panel of 201 red LEDs panel at different time periods.

Table 5.1: Supercapacitive performance evaluation of S-NCP-3//PVA-KOH//rGO ASD with an aqueous and solid-state electrolytes.

Sr. No.	Name of device	Specific capacitance (F g^{-1}) at current density (A g^{-1})	Energy density (Wh kg^{-1})	Power density (kW kg^{-1})	Cycles No.	Stability (%)
1.	S-NCP-3//KOH//rGO	95.62 at 3	34	2.40	5000	94.11
2.	S-NCP-3//PVA-KOH//rGO	37.62 at 0.7	13.51	0.55	5000	93.81

5.2.C.3 Conclusions:

The aqueous and solid state asymmetric SC devices were successfully fabricated by combining nickel copper phosphate (prepared by SILAR method) and rGO electrodes as cathode and anode, respectively. The asymmetric aqueous device demonstrated superior electrochemical capacitive performance with maximum C_s of 95.62 F g^{-1} with ED of 34 Wh kg^{-1} at PD of 2.40 kW kg^{-1} and asymmetric SSD showed highest maximum C_s of 37.62 F g^{-1} with ED of 13.51 Wh kg^{-1} at PD of 0.55 kW kg^{-1} . In addition, S-NCP-3//rGO asymmetric aqueous device exhibits capacitance retention of 94.11% and SSD displays 93.81% over 5000 cycles, which confirmed excellent cyclic stability of devices. The cost efficient nickel copper phosphate based SCs can be beneficial for various commercial applications in portable electronic devices.

5.3 References:

1. D. Dubal, J. Kim, Y. Kim, R. Holze, C. Lokhande, W. Kim, *Energy. Technol.*, 2, (2014), 325-341.
2. S. Shi, C. Xu, C. Yang, J. Li, H. Du, B. Li, F. Kang, *Particuology*, 11, (2013), 371-377.
3. B. Deka, A. Hazarika, O. Kwon, D. Kim, Y. Park, H. Park, *Chem. Eng.*, 325, (2017), 672-680.
4. L. Deng, Y. Gu, Y. Gao, Z. Ma, G. Fan, *J. Colloid Interf. Sci.*, 494, (2017), 355-362.
5. N. Li, T. Lv, Y. Yao, H. Li, K. Liu, T. Chen, *J. Mater. Chem. A*, 5, (2017), 3267-3273.
6. H. Zhang, H. Su, L. Zhang, B. Zhang, F. Chun, X. Chu, W. He, W. Yang, *J. Power Sources*, 331, (2016), 332-339.
7. Z. Tang, C. Jia, Z. Wan, Q. Zhou, X. Ye, Y. Zhu, *RSC Adv.*, 6, (2016), 112307-112316.
8. N. Choudhary, C. Li, J. Moore, N. Nagaiah, L. Zhai, Y. Jung, J. Thomas, *Adv. Mater.*, 29, (2017), 1605336.
9. P. Wen, M. Fan, D. Yang, Y. Wang, H. Cheng, J. Wang, *J. Power Sources*, 320, (2016), 28-36.
10. H. Cheng, Z. Dong, C. Hu, Y. Hu, L. Qu, Y. Zhao, N. Chen, L. Dai, *Nanoscale*, 5, (2013), 3428-3434.
11. B. Choi, S. Chang, C. Park, H. Kang, H. Kim, W. Hong, S. Lee, Y. Huh, *Nanoscale*, 4, (2012), 4983-4988.
12. A. Sumboja, C. Foo, X. Wang, P. Lee, *Adv. Mater.*, 25, (2013), 2809-2815.
13. F. Luan, G. Wang, Y. Ling, X. Lu, H. Wang, Y. Tong, X. Liu, Y. Li, *Nanoscale*, 5, (2013), 7984-7990.
14. H. Gao, F. Xiao, C. Ching, H. Duan, *ACS Appl. Mater. Interfaces*, 4, (2012), 7020-7026.
15. X. Li, B. Wei, *Nano Energy*, 2, (2013), 159-173.
16. Q. Wang, J. Yan, Z. Fan, *Energy Environ. Sci.*, 9, (2016), 729-762.
17. L. Liu, Z. Niu, J. Chen, *Chem. Soc. Rev.*, 45, (2016), 4340-4363.
18. A. Davies, A. Yu, *Can. J. Chem. Eng.*, 89, (2011), 1342-1357.
19. H. Bashid, H. Lim, S. Hafiz, Y. Andou, M. Altarawneh, Z. Jiang, N. Huang, *Carbon-Based Polymer Nanocomposites for Environmental and Energy Applications*; Elsevier: Amsterdam, The Netherlands, 2018; pp. 393-413.
20. J. Chen, Y. Li, L. Huang, C. Li, G. Shi, *Carbon*, 81, (2015), 826-834.
21. W. Hummers, R. Offeman, *J. Am. Chem. Soc.*, 80, (1958), 1339-1339.
22. M. Mohamed, D. Bhat, *AIMS Mater. Sci.*, 4, (2017), 158-171.
23. B. Ahmeda, A. Ojha, F. Hirsch, I. Fischer, D. Patrice, A. Materny, *RSC Adv.*, 7, (2017), 13985-13996.
24. G. Shen, S. H. Yu, Y. Xia, X. W. D. Lou, *J. Mater. Chem. A*, 2, (2014), 10710-10711.
25. N. Chodankar, D. Dubal, G. Gund, C. Lokhande, *Energy Technol.*, 3, (2015), 625-631.
26. J. Cheng, M. Sprik, *Phys. Chem. Chem. Phys.*, 14, (2012), 11245-11267.
27. H. Gerischer, W. Ekardt, *Appl. Phys. Lett.*, 43, (1983), 393-395.
28. P. Katkar, S. Marje, S. Pujari, S. Khalate, A. Lokhande, U. Patil, *ACS Sustain. Chem. Eng.*, 7, (2019), 11205-11218.
29. S. Marje, P. Katkar, S. Pujari, S. Khalate, A. Lokhande, U. Patil, *Synth. Met.*, 259, (2020), 116224.

30. L. Fan, F. Pan, Q. Tu, Y. Gu, J. Huang, Y. Huang, J. Wu, *Int. J. Hydrog. Energy*, 43, (2018), 23372-23381.
31. Y. Gua, L. Fana, J. Huanga, C. Genga, J. Lina, M. Huanga, Y. Huang, J. Wua, J. *Power Sources*, 425, (2019), 60-68.
32. X. Fan, H. Zhou, X. Guo, *RSC Adv.*, 5, (2015), 45484-45491.
33. F. Omar, A. Numan, S. Bashir, N. Duraisamy, R. Vikneswaran, Y. Loo, K. Ramesh, S. Ramesh, *Electrochim. Acta*, 273, (2018), 216-228.
34. S. Kandalkar, H. Lee, S. Seo, K. Lee, C. Kim, *J. Mater. Sci.*, 46, (2011), 2977-2981.

CHAPTER-6

SUMMARY AND CONCLUSIONS

Summary and conclusions:

Rising global energy crisis and the environmental issues have prompted the investigation and development of clean and efficient ESDs for a sustainable community. To date, three varieties of ESDs are available in the market such as capacitors, SCs and batteries. However, the battery has low power, safety problems and a short cycle lifetime, which restricts their application in electronic devices that demand high power. Among the various ESDs, SC represent one of the key factor in energy storage systems having the potential to replace batteries or even complement in a variety of applications. The SC market is driven by its exclusive electrochemical characteristics like as extremely short charging time, high PD and superior low-temperature performance. Therefore, SCs are performed to fulfill the gap between batteries and conventional capacitors. Presently, SCs are being utilized in various applications such as power back up system, automotive engine starting devices, telecommunications, hybrid electric vehicles, automotive auxiliary devices, etc.

Till today, the various types of electrode materials have been examined for SCs including carbon based materials (AC, CNTs, graphene, etc.), conducting polymers (polypyrrole, polyaniline, etc.) and transition metal oxides/hydroxide. Out of these electrode materials, TMPs are the promising electrode material for SCs application due to high electrical conductivity, high reversible redox reactions and high stability. Nowadays, nickel copper phosphates are gaining attention as cathode material for SCs because of their cost-effectiveness, good electrical conductivity, multiple oxidation states, non-toxic nature and electrochemical stability. By utilizing such metal phosphates, the electrochemical performance of SC can be enhanced. The synergistic effect of bimetal phosphates can increase electrochemical capacitive performance.

The aim of the research work was a synthesis of nickel copper phosphate thin films using chemical methods and fabricates asymmetric SC devices using the same. So, the nickel copper phosphate thin films with Ni-Cu composition variation were synthesized on SS substrate via hydrothermal and SILAR methods. The composition of nickel and copper ratio varied to achieve better results by using synergy among them. Binder-free and adherent thin films of nickel copper phosphate were characterized by various physico-chemical methods. The best performing nickel copper phosphate electrodes were used for the fabrication of asymmetric (Ni-Cu Phosphate//rGO) aqueous (1 M KOH electrolyte) and SSD (PVA-KOH gel electrolyte). The present thesis work is described into six chapters.

Chapter 1 starts general introduction which talks about the requirement of SC in the present world, recent developments, background and evolution of SCs. Several types of SC with examples are described and comparison of ESDs is demonstrated via Ragone plot. A basic principles for charge storage mechanism in electrochemical SC is discussed using charge storing schematic. The higher electrochemical performance of SC can be obtained by employing active material with desired properties. So, the required properties of electrode material are described in detail with the variety of available active materials for SCs in the literature. So, the literature review on nickel phosphate, copper phosphate, and nickel copper phosphate materials is summarized. Lastly, the orientation and purpose of the dissertation are described at the end of chapter 1.

Chapter 2 discusses introduction of thin films, different deposition techniques, and their classifications. Theoretical background of hydrothermal and SILAR methods with various preparative parameters and advantages are given in detail. Thereafter, the various thin film characterization techniques employed for prepared thin film investigation such as, XRD for structural analysis, FT-IR spectroscopy for chemical bonding, BET for specific surface area, XPS for elemental analysis, FE-SEM and EDS for surface morphology and elemental mapping, respectively are described in this chapter. Finally, theoretical background of electrochemical supercapacitive techniques as CV, GCD and EIS are explained in detail.

Chapter 3 consists of synthesis of nickel copper phosphate thin films using hydrothermal method, characterization and supercapacitive performance evaluation. This chapter is divided into two sections i.e. section 'A' and 'B'. Section A consists of the preparation of nickel copper phosphate thin films on conducting SS substrate with Ni-Cu ratio variation using a simple binder-free hydrothermal method. The deposited nickel copper phosphate thin films are characterized by different physico-chemical techniques. The effect of nickel and copper molar ratio variation on structure and surface morphology of nickel copper phosphate thin film is studied. The successful preparation of nickel copper phosphate is confirmed from the XRD, FT-IR, BET, XPS, FE-SEM and EDS analysis. The XRD study confirms successful synthesis of nickel copper phosphate material in thin film form. Also, FT-IR spectroscopy utilized to analyze the molecular chemical bonds and confirms the formation of hydrous nickel copper phosphate material. The N₂ adsorption-desorption experiments were executed for the analysis of specific surface area and pore size distribution of prepared thin

films. Moreover, XPS analysis exhibits the presence of nickel, copper, oxygen and phosphorous elements in the prepared thin films. Further, the change in the nano/microstructures of nickel copper phosphate thin films as an impact of the different content of nickel and copper is observed from FE-SEM images and EDS study confirms achievement of expected molar ratio (nickel and copper) in the samples.

Section ‘B’ deals with the supercapacitive performance evaluation of hydrothermally deposited nickel copper phosphate thin films. The influence of molar ratio of nickel and copper on electrochemical performance of H-NCP series electrodes is studied. The electrochemical capacitive measurements displays that, the maximum C_s of 711 F g^{-1} is obtained for H-NCP-3 ($\text{Ni}_{1.62}\text{Cu}_{1.35}(\text{PO}_4)_2 \cdot \text{H}_2\text{O}$) electrode at 1.5 A g^{-1} current density as shown in **Figure 6.1**. Moreover, it reveals excellent capacitive retention of 88.5% over 4000 cycles. The good electrochemical capacitive performance concluded that, strong adhesion among nickel copper phosphate ($\text{Ni}_{1.62}\text{Cu}_{1.35}(\text{PO}_4)_2 \cdot \text{H}_2\text{O}$) and SS substrate with unique morphology, which delivers easy charge transportation and ion penetration.

Chapter 4 emphasizes the synthesis, characterization and electrochemical performance evaluation of SILAR deposited nickel copper phosphate thin film electrodes. As like chapter 3, chapter 4 is also divided into two different sections ‘A’ and ‘B’. Section ‘A’ deals with synthesis of nickel copper phosphate thin films by SILAR method. Moreover, the preparative factors include precursor concentration, number of cycles, rinsing and reaction time were optimized. The SILAR deposited nickel copper phosphate thin films are used as working electrode for electrochemical study. The impact on structure as well as surface morphology with the variation in molar ratio of nickel and copper is studied. The amorphous nature of nickel copper phosphate has been confirmed by the XRD analysis. The surface areas of nickel copper phosphate thin films measured from BET analysis. The nickel, copper, oxygen and phosphorous elements with expected composition are found in XPS and EDS study. Further, the FE-SEM images for nickel copper phosphate material confirm the formation of porous material consisting of a nanoparticle-like morphology. Section ‘B’ describes the supercapacitive performance of SILAR deposited nickel copper phosphate thin film electrodes and change in effect is observed at different compositions of nickel and copper. The high C_s demonstrated by nanoparticle like morphology of nickel copper phosphate ($\text{Ni}_{1.56}\text{Cu}_{1.44}(\text{PO}_4)_2 \cdot \text{H}_2\text{O}$) thin film electrode of

750 F g⁻¹ at 1 A g⁻¹ current density (as shown in **Figure 6.1**) with good cyclic stability up to 89.34% after 4000 GCD cycles. The good performance of SILAR deposited nickel copper phosphate (Ni_{1.56}Cu_{1.44}(PO₄)₂·H₂O) material is detected due to good contact among deposited material and SS substrate (binder-free synthesis) and porous consisting nanoparticles like morphology.

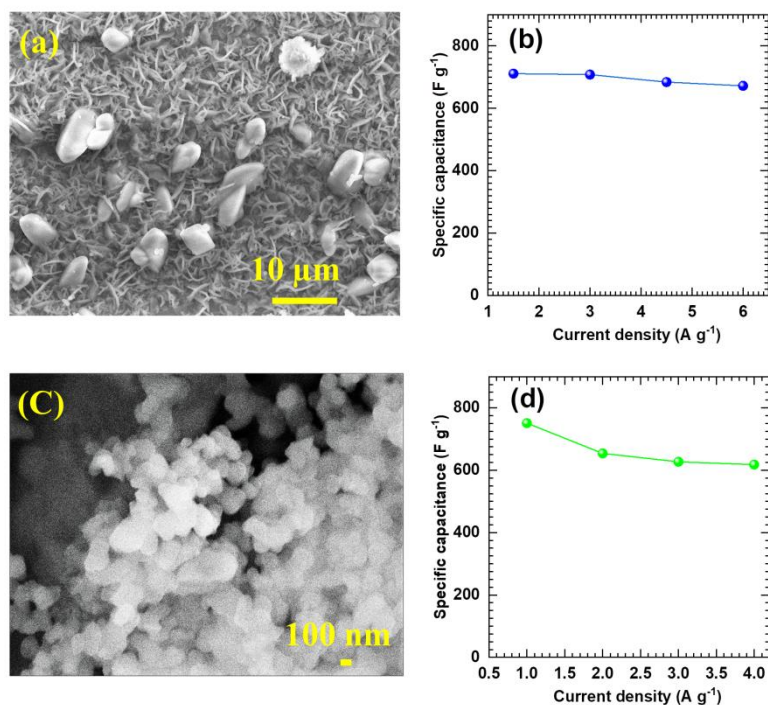


Figure 6.1: The FE-SEM images of (a) Ni_{1.62}Cu_{1.35}(PO₄)₂·H₂O (X2000) and (c) Ni_{1.56}Cu_{1.44}(PO₄)₂·H₂O (X100000) thin films. The plots of specific capacitance versus current densities for (b) Ni_{1.62}Cu_{1.35}(PO₄)₂·H₂O and (d) Ni_{1.56}Cu_{1.44}(PO₄)₂·H₂O thin film electrodes.

Chapter 5 covers the fabrication and supercapacitive performance evaluation of asymmetric aqueous and SSDs. The SILAR deposited nickel copper phosphate (S-NCP-3) [Ni_{1.56}Cu_{1.44}(PO₄)₂·H₂O] as a cathode and rGO as an anode was utilized to fabricate asymmetric aqueous and SSDs with aqueous (KOH) and polymer (PVA-KOH) gel electrolytes, respectively. This chapter distributed into three different sections (A, B and C). Section A describes synthesis, characterization and electrochemical performance evaluation of the rGO electrode. The well-known modified Hummer's method is employed for GO synthesis and then it reduced hydrothermally. The successfully reduction of GO to rGO is affirmed by XRD study. For electrochemical analysis, the anode is prepared by coating rGO material on conducting SS substrate by casting method. Also, the supercapacitive performance

evaluation of rGO was studied in three electrode system with 1 M KOH electrolyte. It demonstrates maximum C_s of 159 F g^{-1} at 1.5 A g^{-1} current density. Also, it exhibits 77.42% capacitive retention over 3000 GCD cycles. So, the rGO electrode is employed as negative (anode) electrode for device fabrication. Section B gives entire information about electrode preparation, PVA-KOH gel electrolyte preparation as well as the aqueous and solid-state device fabrication process. Section C contains the supercapacitive performance evaluation of S-NCP-3 (SILAR synthesized)//rGO asymmetric aqueous and SSDs. The asymmetric aqueous (S-NCP-3//KOH//rGO) and solid-state (S-NCP-3//PVA-KOH//rGO) SC devices are prepared. The S-NCP-3//rGO asymmetric aqueous (95.62 F g^{-1} at 3 A g^{-1}) and solid-state (37.62 F g^{-1} at 0.7 A g^{-1}) device revealed excellent electrochemical performance with maximum C_s . Moreover, the high ED and PD of asymmetric aqueous (34 Wh kg^{-1} , 2.40 kW kg^{-1}) and solid-state (13.51 Wh kg^{-1} , 0.55 kW kg^{-1}) device are obtained. Additionally, S-NCP-3//rGO asymmetric aqueous (94.11%) and solid-state (93.81%) device exhibited excellent cyclic stability over 5000 cycles. The practical applicability of S-NCP-3//PVA-KOH//rGO asymmetric solid-state is tested by charging two serially connected devices for 30 s and discharged through 201 red LEDs are lightened up to 125 s.

Lastly, **chapter 6** provides the extract of all the chapters i.e. summary and conclusions. In this work, nickel copper phosphate thin films are successfully prepared by hydrothermal and SILAR methods. The characterization techniques are used for analyses and confirmation of prepared nickel copper phosphate thin films. The result achieved from chapter 3 and 4 proposes that, the ~0.50:0.50 ratio of nickel and copper content in nickel copper phosphate thin film reveals higher electrochemical performance than other compositions. The hydrothermally deposited microstructures of nickel copper phosphate ($\text{Ni}_{1.62}\text{Cu}_{1.35}(\text{PO}_4)_2 \cdot \text{H}_2\text{O}$) electrode shows less performance (711 F g^{-1} at 1.5 A g^{-1}) than the SILAR deposited (750 F g^{-1} at 1 A g^{-1}) nanoparticle like morphology of nickel copper phosphate ($\text{Ni}_{1.56}\text{Cu}_{1.44}(\text{PO}_4)_2 \cdot \text{H}_2\text{O}$) electrode are displays in **Figure 6.1**. The best performed SILAR deposited (S-NCP-3) nickel copper phosphate electrodes are used for the asymmetric aqueous and SSDs and studied their supercapacitive performance. The comparative ED and PD (Ragone plot) of fabricated asymmetric (aqueous and solid state) devices are portrayed in **Figure 6.2**. The available SCs are incapable to perform higher PD than capacitors as well as high ED than batteries. However, the asymmetric aqueous device based on nickel copper phosphate electrode obtains higher values than the available SC devices they reveal

ED almost equal to fuel cells/batteries and lower PD than a capacitor. The SILAR deposited nickel copper phosphate ($\text{Ni}_{1.56}\text{Cu}_{1.44}(\text{PO}_4)_2 \cdot \text{H}_2\text{O}$) based aqueous ASD exhibits greater ED and PD than the SSD. The aqueous devices have constraint in their commercial level and that can be reduced by preparing SSD. So, the SILAR deposited nickel copper phosphate ($\text{Ni}_{1.56}\text{Cu}_{1.44}(\text{PO}_4)_2 \cdot \text{H}_2\text{O}$) thin film electrode based solid state SC device along with comparable ED (13.51 Wh kg^{-1}) and PD (0.55 kW kg^{-1}) can be applicable at commercial level in lightweight electronic devices.

The supercapacitive performance of aqueous and SSDs is summarized in **Table 6.1**.

Table 6.1 Electrochemical performance of asymmetric aqueous and solid-state SC devices

Sr. No.	Name of Device	Specific capacitance (F g^{-1}) at current density (A g^{-1})	Energy density (Wh kg^{-1})	Power density (kW kg^{-1})	Cycles No.	Stability (%)
1.	S-NCP-3//KOH//rGO	95.62 at 3	34	2.40	5000	94.11
2.	S-NCP-3//PVA-KOH//rGO	37.62 at 0.7	13.51	0.55	5000	93.81

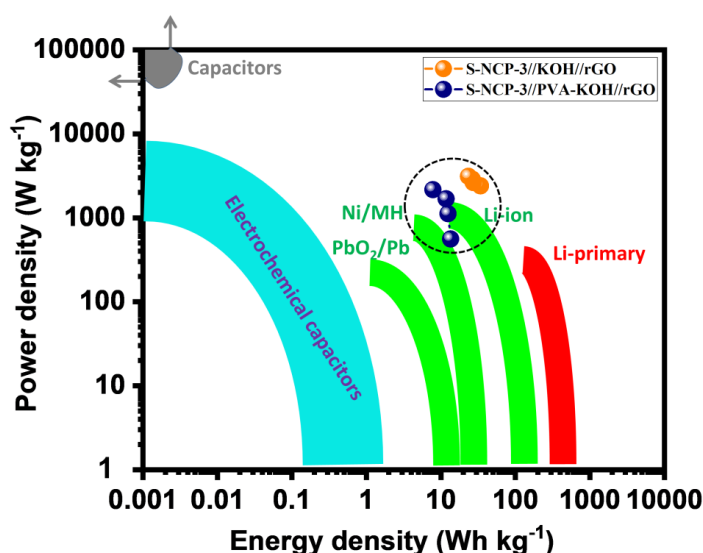
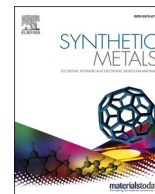


Figure 6.2: The comparative Ragone plots of prepared asymmetric (aqueous and solid state) device based on nickel copper phosphate as positive and rGO as negative electrodes.

PUBLICATIONS



Amorphous, hydrous nickel phosphate thin film electrode prepared by SILAR method as a highly stable cathode for hybrid asymmetric supercapacitor

Sachin S. Pujari^a, Vinod V. Patil^a, Akash S. Patil^a, Vinayak G. Parale^b, Hyung-Ho Park^b, Jayavant L. Gunjekar^a, Chandrakant D. Lokhande^a, Umakant M. Patil^{a,*}

^a Centre for Interdisciplinary Research, D. Y. Patil Education Society, Kasaba Bawada, Kolhapur 416 006, India

^b Department of Materials Science and Engineering, Yonsei University, 50 Yonsei-ro, Seodaemun-gu, Seoul 03722, South Korea

ARTICLE INFO

Keywords:

Amorphous materials
Particles cluster
Nickel phosphate
SILAR method
Hybrid Supercapacitor
Thin film electrode

ABSTRACT

To achieve higher supercapacitive performance of active material, several materials with precise structures and properties have been prepared using different chemical synthesis methods. Recently, amorphous materials are gaining much attention as an electrode in supercapacitor application as it provides superior electrochemical properties due to disorder in structure. So, in this investigation, a facile, binder free successive ionic layer adsorption and reaction (SILAR) method is adopted for the preparation and deposition of amorphous, hydrous nickel phosphate thin films on stainless steel substrates. The amorphous nickel phosphate shows mesoporous, clusters of particles like morphology. In the electrochemical study, the amorphous, hydrous nickel phosphate electrode demonstrates a superior specific capacitance of 1700 F g^{-1} (specific capacity- 814 C g^{-1}) at 0.5 mA cm^{-2} current density along with excellent capacitive retention (96.55%) and coulombic efficiency (98.62%) over 5000 cycles. Furthermore, fabricated hybrid supercapacitor device using the nickel phosphate as cathode and reduced graphene oxide as anode exhibits specific capacitance of 113.5 F g^{-1} at 3 mA cm^{-2} current density with a high 40.37 Wh kg^{-1} energy density at 1.689 kW kg^{-1} power density alongwith excellent cyclic stability (95.09% retention after 5000 cycles). The obtained results illustrate that the amorphous, hydrous nature of nickel phosphate is a beneficial and superior choice as a cathode material in high-performing hybrid asymmetric supercapacitor devices.

1. Introduction

Electrochemical supercapacitors have recently gained much attention as superior electrochemical energy storage devices due to their high power density and exceptional stability. Generally, stored electrical energy in supercapacitors is based on two primary electrochemical double-layer capacitance and pseudocapacitance mechanisms. EDLC based supercapacitor exhibits excellent stability and high power, since charge storing proceeds physically via ions adsorption/desorption inside carbon-based materials; however, these materials suffer from low energy density [1]. The pseudocapacitive capacitance originates electrochemically either via redox reactions (e.g., metal oxides/hydroxides/phosphate) or through ion intercalation (e.g., conducting polymers) [2–5]. Further, pseudocapacitor is divided into three types such as intrinsic, intercalation, and extrinsic pseudocapacitor. In

intrinsic pseudocapacitor, charges are stored by double layer and surface redox mechanism on the surface of a material or near the material surface. In intercalation type, pseudocapacitor charge stores through intercalation of electrolytic ion in interplanar space or tunnels. However, in extrinsic pseudocapacitors, battery-type materials exhibit pseudocapacitive behavior with a reduction in their crystallinity or morphology (nanomaterials) [6]. Besides the excellent energy density of pseudocapacitive materials, they suffer from poor stability and less power density.

Transition metal sulfides/oxide/hydroxide and phosphates have been comprehensively explored as pseudocapacitive material for energy storage devices because of their abundant resources and electrochemical activity [7,8]. Among various pseudocapacitive materials, the excellent electrical conductivity of metal phosphate executes a rapid charge transfer, and it is beneficial for supercapacitor [9,10]. Also, the

* Corresponding author.

E-mail address: umakant.physics84@gmail.com (U.M. Patil).

<https://doi.org/10.1016/j.synthmet.2021.116876>

Received 11 June 2021; Received in revised form 19 July 2021; Accepted 3 August 2021

Available online 12 August 2021

0379-6779/© 2021 Elsevier B.V. All rights reserved.



Highly sensitive hydrothermally prepared nickel phosphate electrocatalyst as non-enzymatic glucose sensing electrode

Sachin S. Pujari¹ · Sujit A. Kadam² · Yuan-Ron Ma² · Suraj A. Khalate¹ · Pranav K. Katkar¹ · Supriya J. Marje¹ · Umakant M. Patil¹

© Springer Science+Business Media, LLC, part of Springer Nature 2020

Abstract

Present investigation describes a successful preparation of nickel phosphate ($\text{Ni}_3(\text{PO}_4)_2 \cdot 8\text{H}_2\text{O}$) thin film electrodes by facile one pot hydrothermal method. As developed $\text{Ni}_3(\text{PO}_4)_2 \cdot 8\text{H}_2\text{O}$ thin film electrodes with the variation of thickness are examined for morphological change and glucose sensing. The $\text{Ni}_3(\text{PO}_4)_2 \cdot 8\text{H}_2\text{O}$ thin film electrodes exhibit linear response with respect to the variation in glucose concentration from 2.5 to 30 mM and acquire the sensitivity of $8312 \mu\text{A mM}^{-1} \text{cm}^{-2}$ with 437 μM LOD. Selectivity performance of $\text{Ni}_3(\text{PO}_4)_2 \cdot 8\text{H}_2\text{O}$ thin film electrode towards glucose in presence of dopamine, fructose and lactose is studied. The results suggest that $\text{Ni}_3(\text{PO}_4)_2 \cdot 8\text{H}_2\text{O}$ thin film electrode is beneficial for glucose sensing application due to enormous active sites with the high specific surface area of the active material.

Keywords Nickel phosphate · Hydrothermal method · Microplates · Non-enzymatic glucose sensor · Thin film electrode

1 Introduction

Nowadays, biosensors are mostly investigated in the area of biomedical analysis, food industry, and clinic diagnosis [1, 2]. Glucose sensors are widely used in clinical diagnostics because of their fast examination and reliability [3]. Therefore, a lot of efforts are underway for the construction of rapid, reliable and reproducible glucose sensing devices [4]. Electrochemical sensors are known as a good scientific device due to their fast and low-cost glucose recognition [5, 6]. Biosensors prepared by various methods have been studied from past few years. Based on the multiple characteristics and phenomena of the techniques as well as detector, applied biosensors would be classified into electrical biosensors, vibrational biosensors, electrochemical

biosensors, optical biosensors and mechanical biosensors. Chronoamperometric or electrochemical glucose sensors are classified into two types an enzymatic and non-enzymatic glucose sensor. In the type first, enzymatic oxidase on the surface of electrode is immobilized and dioxygen quantitatively reduced to the hydrogen peroxide and monitored by chronoamperometric method [7]. The traditional enzymatic glucose sensor offers high selectivity, better time response but some drawbacks are associated such as, limited stability and difference in response with the changing pH as well as temperature [8]. On the other hand, non-enzymatic glucose sensors offer many advantages such as stability, reproducibility and their mechanism for detecting glucose molecules is based on redox reaction of active material [5, 9]. Among different biosensors, electrochemical biosensors involve easy mechanism and fabrication processes, simple operation and quick response time. It is familiar that, transition metal based electrodes are extremely cost-effective, facile to synthesize, highly electroactive and exhibit good glucose sensing [10, 11].

In recent times, there are lots of efforts undergoing for glucose detection using nickel based catalysts. Almost all of them shown improved performance of glucose sensor by developing nickel catalyst on the conductive materials like as carbon nanofiber [12], Mxene [13] and graphene [14]. Yet few works were prepared to simultaneously modify

Electronic supplementary material The online version of this article (<https://doi.org/10.1007/s10934-020-01000-0>) contains supplementary material, which is available to authorized users.

✉ Umakant M. Patil
umakant.physics84@gmail.com

¹ Centre for Interdisciplinary Research, D. Y. Patil Education Society, Kasaba Bawada, Kolhapur 416 006, India

² Department of Physics, National Dong Hwa University, Hualien 97401, Taiwan

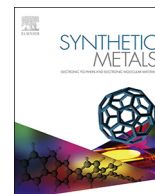


Facile Synthesis of Microstrip-Like Copper Phosphate Hydroxide Thin Films for Supercapacitor Applications

SACHIN S. PUJARI,¹ SUJIT A. KADAM,² YUAN-RON MA,²
PRANAV K. KATKAR,¹ SUPRIYA J. MARJE,¹ SURAJ A. KHALATE,¹
ABHISHEK C. LOKHANDE,³ and UMAKANT M. PATIL^{1,4}

1.—Centre for Interdisciplinary Research, D. Y. Patil Education Society, Kasaba Bawada, Kolhapur 416 006, India. 2.—Department of Physics, National Dong Hwa University, Hualien 97401, Taiwan. 3.—Department of Physics, Khalifa University of Science and Technology (KUST), Abu Dhabi, United Arab Emirates. 4.—e-mail: umakant.physics84@gmail.com

Binder-free copper phosphate hydroxide $[\text{Cu}_2(\text{PO}_4)(\text{OH})]$ thin films have been prepared on stainless-steel (SS) substrates at 393 K via a facile hydrothermal method. X-ray diffraction analysis confirmed the formation of orthorhombic-structured copper phosphate hydroxide $[\text{Cu}_2(\text{PO}_4)(\text{OH})]$ thin films with uniform microstrip-like morphology and Brunauer–Emmett–Teller (BET) surface area of $5.26 \text{ m}^2 \text{ g}^{-1}$. The electrochemical performance of the films depended on their thickness, with a maximum specific capacitance of 280 F g^{-1} at a scan rate 5 mV s^{-1} in 1 M KOH electrolyte. The $[\text{Cu}_2(\text{PO}_4)(\text{OH})]$ electrode delivered an energy density of 3.85 Wh kg^{-1} and a power density of 264.70 W kg^{-1} with excellent (91%) capacitive retention after 2000 cycles. This excellent electrochemical performance shows that such microstrip-like $\text{Cu}_2(\text{PO}_4)(\text{OH})$ thin films are promising electrodes for high-performance supercapacitors.



Single-pot hydrothermal synthesis of manganese phosphate microrods as a cathode material for highly stable flexible solid-state symmetric supercapacitors

Pranav K. Katkar^a, Supriya J. Marje^a, Sachin S. Pujari^a, Suraj A. Khalate^a, Prashant R. Deshmukh^b, Umakant M. Patil^{a,*}

^a Centre for Interdisciplinary Research, D. Y. Patil Education Society (Deemed to Be University), Kasaba Bawada, Kolhapur, 416 006, M.S, India

^b Department of Mechanical Engineering, Chungnam National University (CNU), Daejeon, 34137, Republic of Korea



ARTICLE INFO

Keywords:

Hydrothermal method
Manganese phosphate
Microrods
Flexible symmetric solid-state device
Supercapacitor
Thin film

ABSTRACT

Here, we report a binder-free synthesis of microrods-like manganese phosphate thin film over stainless steel substrate by a facile, single-pot hydrothermal method. The XRD analysis reveals that, the formation of manganese phosphate [$\text{Mn}_3(\text{PO}_4)_2$] material of a monoclinic crystal structure. From SEM images observed microrods like morphology of manganese phosphate with an average width of $\sim 25 \mu\text{m}$. The manganese phosphate electrode shows a better electrochemical performance with a specific capacitance of 145 F g^{-1} at 0.2 mA cm^{-2} current density in $1.0 \text{ M Na}_2\text{SO}_4$ electrolyte. Moreover, the flexible solid-state symmetric electrochemical energy storage device was assembled with PVA- Na_2SO_4 solid gel-electrolyte consists of manganese phosphate as anode and cathode electrode. The corresponding symmetric supercapacitor achieves a high energy density of 11.7 Wh kg^{-1} at a high power density of 1.41 kW kg^{-1} with an excellent specific capacitance of 37 F g^{-1} at 0.1 mA cm^{-2} current density. Manganese phosphate shows long-term electrochemical cyclic stability at a current density of 0.8 mA cm^{-2} for 9000 galvanostatic charge-discharge cycles with excellent capacitance retention (99 %). This excellent capacitive performance confirms that the manganese phosphate is promising material and fabricated flexible solid-state symmetric supercapacitor has high potential in the field of portable and bendable energy storage devices.

1. Introduction

Global extensions have stimulated the rate of energy consumption to very high levels, and the utilization of highly efficient, clean and sustainable energy conversion technologies and renewable energy resources are getting much attention. Among the existing energy generation and storage devices, supercapacitors (SCs) are considerably well attractive to solve the increasing concern about the energy crisis. [1]. Supercapacitor provides high power density, moderate energy density, longer durability and fast charging capability than batteries or fuel cells. Remarkably, flexible device with long cycle life has attracted significant attention in the field of power-source applications such as portable electronics, rollup/wearable displays, energy back-up device, sensor networks, electric vehicles, and mobile phones [2–4]. On the basis of energy storage mechanism, electrochemical capacitors are categorized into mainly two types, pseudocapacitors and electric double-layer capacitors (EDLCs). The EDLCs based materials with large specific

surface area, like carbonaceous materials, are storing the energies through electrical double layers. However, pseudocapacitor materials display quite a lot of oxidation states and store energy in electric double layers, as well as redox reaction at the electrode surfaces as like the transition metal oxides/hydroxides, sulfides, and conductive polymers [5–7]. Therefore, comparing pseudocapacitors with the EDLCs, pseudocapacitor shows good capacitive behavior with excellent specific capacitance [8].

Significantly more effort for fabricating high-performance supercapacitors has been done using various materials, such as $\text{Co}(\text{OH})_2$ [9], MnCo_2O_4 [10], rGO-MnO_2 [11], $\alpha\text{-MnO}_2$ [12], and $\text{Mn}(\text{OH})_2$ [13]. Mn-based oxide/hydroxides are hard to reach the theoretical capacitance, power and energy density values because of poor electrical conductivity and the less specific capacitance due to the lower ion transfer rate [10,14]. The cobalt-based materials are more concentrated because of their attractive capacitance values, but they shows less cyclic stability compared to manganese based materials [15].

* Corresponding author.

E-mail address: umakant.physics84@gmail.com (U.M. Patil).

<https://doi.org/10.1016/j.synthmet.2020.116446>

Received 7 February 2020; Received in revised form 26 May 2020; Accepted 29 May 2020

0379-6779/ © 2020 Elsevier B.V. All rights reserved.

Enhanced Energy Density of All-Solid-State Asymmetric Supercapacitors Based on Morphologically Tuned Hydrous Cobalt Phosphate Electrode as Cathode Material

Pranav K. Katkar,[†] Supriya J. Marje,[†] Sachin S. Pujari,[†] Suraj A. Khalate,[†] Abhishek C. Lokhande,[‡] and Umakant M. Patil^{*,†}

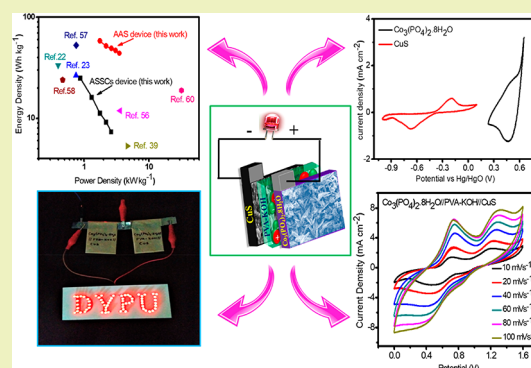
[†]Centre for Interdisciplinary Research, D. Y. Patil Education Society (Deemed to be University), Kasaba Bawada, Kolhapur, 416 006 Maharashtra, India

[‡]Department of Material Science and Engineering, Chonnam National University, Yongbong-dong, Puk-Gu, Gwangju 500 757, Republic of Korea

Supporting Information

ABSTRACT: In the present investigation, microflowers-like hydrous cobalt phosphate is prepared via a facile single-step hydrothermal method on stainless steel substrate. The microflowers-like morphology of hydrous cobalt phosphate thin film consists of microplates and further microplates converted to flakes by means of a change in length, width, and thickness with urea variation. Hydrous cobalt phosphate thin film electrode demonstrates a high specific capacitance of 800 F g^{-1} at 2 mA cm^{-2} with 33.62 Wh kg^{-1} energy density and 3.12 kW kg^{-1} power density. By taking advantage of hydrous cobalt phosphate thin film (as a cathode electrode) and copper sulfide thin film (as an anode electrode), the asymmetric devices (aqueous/all-solid-state) are fabricated. Aqueous asymmetric device shows a high specific capacitance of 163 F g^{-1} at 2 mA cm^{-2} with an energy density of 58.12 Wh kg^{-1} and power density of 3.52 kW kg^{-1} . Moreover, the all-solid-state asymmetric supercapacitor device delivers a high specific capacitance of 70 F g^{-1} at 2 mA cm^{-2} with 24.91 Wh kg^{-1} energy density and 2.63 kW kg^{-1} power density in PVA–KOH gel electrolyte. The long-term cyclic stability (94% after 3000 cycles) and actual practical demonstration (lightning 65 red LEDs) suggest an industrial application of the all-solid-state asymmetric device.

KEYWORDS: Cobalt phosphate, Hydrothermal method, Microflowers, Solid-state asymmetric supercapacitor, Thin film



INTRODUCTION

Increasing demand for portable electronics (like mobile phones, e-papers, laptops, etc.) has significantly encouraged the research community to fabricate high-performing electric energy storage devices.^{1–3} Among the various types of energy storage devices, a supercapacitor (SC) is the supreme choice for clean and green energy, which offers excellent characteristics such as good cycle stability, high power density, and environmental benignity and is presently employed in hybrid vehicles, consumer electronics, and renewable energy storage devices,^{2–5} though the major challenges of a supercapacitor are less stability at high-rate conditions and low energy density (as compared to batteries), which significantly constrains its application.⁵ As per the energy density equation (0.5 CV^2), to increase the energy density development of new electrode materials with a high capacitance (C) is one way and another is to build a supercapacitor device with a wide operating potential window (V). Thus, new superior electrode materials having high specific capacitances, long cycling lives, and rational assemblies of anode and cathode materials in a supercapacitor device are required to be investigated. Therefore, extensive

research has been devoted to fabricating asymmetric supercapacitor devices using different cost-effective electrode materials with high specific capacitance.^{6,7}

Generally, carbon-based materials, e.g., carbon nanotubes (CNTs), graphene and activated carbon (AC), conducting polymers (e.g., polythiophene, polypyrrole, and polyanilines), transition metal oxides/hydroxides/sulfides, and their composites, are employed as active materials for supercapacitors. The transition-metal oxides, metal hydroxides, and metal sulfides such as Co_3O_4 ,⁸ MnCoO_4 ,⁹ RuO_4 ,¹⁰ $\beta\text{-Co}(\text{OH})_2$,¹¹ CoS ,¹² CoS_2 ,¹³ etc., have attracted significant attention as pseudocapacitive electrode material, but they suffer from low specific capacitance and energy density due to poor conductivity.^{14,15} Thus, there is a need to develop low-cost alternative electrode materials to improve the performance of supercapacitors. Recently, for supercapacitor as well as catalysis application, various transition-metal phosphates have been studied and

Received: January 25, 2019

Revised: June 7, 2019

Published: June 7, 2019



Hydrothermally synthesized Iron Phosphate Hydroxide thin film electrocatalyst for electrochemical water splitting

Suraj A. Khalate ^a, Sujit A. Kadam ^b, Yuan-Ron Ma ^b, Sachin S. Pujari ^a, Supriya J. Marje ^a,
Pranav K. Katkar ^a, Abhishek C. Lokhande ^c, Umakant M. Patil ^{a,*}

^a Centre for Interdisciplinary Research (CIR), D. Y. Patil Education Society (Deemed to Be University), Kolhapur, 416 006, India

^b Department of Physics, National Dong Hwa University, Hualien, 97401, Taiwan

^c Department of Physics, Khalifa University of Science and Technology (KUST), Abu Dhabi, United Arab Emirates (UAE)



ARTICLE INFO

Article history:

Received 6 March 2019

Received in revised form

31 May 2019

Accepted 27 June 2019

Available online 28 June 2019

Keywords:

Electrochemistry

Hydrothermal synthesis

Heterogeneous catalysis

Ligand effects

Transition metals

Voltammetry

ABSTRACT

Hydrogen production is an immediate need to replace the fossil fuels to keep environmental balance, and water splitting is an effective solution in presence of catalyst through oxygen evolution reaction (OER) and hydrogen evolution reaction (HER). Herein, for the first time, we have synthesized Iron Phosphate Hydroxide ($\text{Fe}_{2.95}(\text{PO}_4)_2(\text{OH})_2$) thin film electrode as a superior electrocatalyst by facile hydrothermal method using binder free approach. The crystallographic properties are studied from X-ray diffraction pattern, and Reitveld refinement analysis shows best fit with the tetragonal Lipscombite structure of Iron Phosphate Hydroxide ($\text{Fe}_{2.95}(\text{PO}_4)_2(\text{OH})_2$). Flower like structure consist of agglomerated nanorods on micro and sub-micrometric spheres of $\text{Fe}_{2.95}(\text{PO}_4)_2(\text{OH})_2$ exhibits lower overpotential of 281 mV at 10 mA/cm² current density towards OER in alkaline (1 M KOH) medium and maintains its activity after 12 h catalytic stability test. Moreover, prepared electrode shows HER with overpotential 165.7 mV at current density 10 mA/cm² in acidic (1 M H_3PO_4) medium and demonstrates enhanced performance (126.4 mV overpotential) after 12 h catalytic stability. The $\text{Fe}_{2.95}(\text{PO}_4)_2(\text{OH})_2$ thin film electrodes show superior performance in OER and HER, compared with its oxide counterpart (Fe_2O_3).

© 2019 Elsevier Ltd. All rights reserved.

1. Introduction

Now days, a very intense work focused on the renewable energy generation by different sources such as wind [1], solar [2], hydrodynamical [3], tidal [4] and geothermal [5], and utilization in terms of electrical energy to control the global energy crisis and reduce environmental issues. Hydrogen is one of the most clean and potential renewable energy sources and the electrolysis of water to generate Oxygen and Hydrogen molecules is the cost-effective and efficient approach to get renewable energy [6–9]. The hydrogen evolution reaction (HER) and oxygen evolution reaction (OER) are the fundamentals of typical water splitting reaction and HER is comparatively easy which takes place at low overpotential. On the other hand, water splitting efficiency is largely constrained by the rate determining sluggish oxygen evolution reaction (OER), which involves four proton-coupled electron transfer causes high overpotential for O_2 assembly. In

electrochemical energy sources, appropriate electrocatalysts are crucial components of an energy efficient hydrogen generation. To minimize the overpotential for OER and energy losses, a good electrocatalyst must have high catalytic activity, superior conductivity and adequate electrocatalytic stability. The state-of-the-art electrocatalysts considered to the noble metal-based valuable materials such as Platinum (Pt), Ruthenium (Ru) and Iridium Oxides (IrO_2) have an identity as best OER catalysts due to low overpotential [10–12]. However, these metals are very rare in the Earth's crust, thus it is difficult to commercialize them. To create the significant development in the field of electrocatalysis and there is need to replace the conventional electrocatalysts. Amongst various non-noble metal catalysts, transition metals are the promising alternative for these rare metal electrocatalysts due to their smaller d orbitals, lower crystal-field activation energies and competent bifunctional catalytic properties for water splitting. The materials of transition metals as Hydroxides, Sulphides, Selenides, Phosphates, Phosphides, Nitrides, have great interest due to their Earth abundance, high-efficiency and stability for large-scale energy production [13–20].

* Corresponding author.

E-mail address: umakant.physics84@gmail.com (U.M. Patil).



Effect of phosphate (anion) precursor on structural and morphology behavior of nickel phosphate thin films and its supercapacitive performance

Supriya J. Marje^a, Pranav K. Katkar^a, Sachin S. Pujari^a, Suraj A. Khalate^a, Prashant R. Deshmukh^b, Umakant M. Patil^{a,*}

^a Centre for Interdisciplinary Research, D. Y. Patil Education Society (Deemed to be University), Kasaba Bawada, Kolhapur 416 006, M.S., India

^b Department of Mechanical Engineering, Chungnam National University, Daejeon, South Korea

ARTICLE INFO

Keywords:

Anion precursor effect
Asymmetric supercapacitor
Binder-free synthesis
Chemical bath deposition method
Nickel phosphate
Thin film electrode

ABSTRACT

In present work, reproducible and economic chemical bath deposition method is used to deposit nickel phosphate thin films on stainless steel substrate for supercapacitor application and effect of anion precursors on structure and morphology of prepared thin film is studied. Change in structure from crystalline to amorphous is observed in prepared thin films due to precursor variation. Also, microplate to microsphere like morphological alteration is observed with the same. The microsphere like morphology of amorphous nickel phosphate thin film electrode exhibits the highest specific capacitance of $\sim 1031 \text{ F g}^{-1}$ (specific capacity 114.6 mAh g^{-1}) at 0.5 mA cm^{-2} current density. Its practical application is tested by preparing asymmetric supercapacitor device comprising amorphous nickel phosphate thin film as positive electrode and reduced graphene oxide as negative electrode. Asymmetric device delivers highest specific capacitance of $\sim 100 \text{ F g}^{-1}$ at 6 mA cm^{-2} current density with energy density of 45.33 Wh kg^{-1} at a high power density of 1.5 kW kg^{-1} and offers 80% capacitance retention over 3000 cycles.

1. Introduction

Today's increasing requirement of energy storage devices for high power applications catches researcher's attention. Main requirements of energy storage device are reversible and fast release of electrical energy and that can be fulfilled by supercapacitor devices [1,2]. Numerous materials has been developed and studied by researcher for supercapacitor application such as, transition metal oxides [3], hydroxides [4], sulfides [5] and phosphides [6]. To develop economical stabled material with high energy and power density for supercapacitor application needs to explore new materials. In the search of inexpensive electrochemically active material, many researchers attracted towards metal phosphate materials for supercapacitor application [7].

Among metal phosphates, nickel and cobalt phosphate were widely studied for different application due to its earth abundancy and high conductivity. Moreover, several chemical methods were used to prepare nickel phosphate materials for supercapacitor application such as hydrothermal [8–12], microwave assisted [13], calcination [14,15], co-precipitation [16,17] and sonochemical [18,19] etc. Different chemical method offers different microstructure of nickel phosphate such as nano-microrod, microflower, nanosphere etc. that ultimately exhibits

different electrochemical capacitive performances.

However, very few reports explored the effect of precursor source on the microstructure and ultimately supercapacitive performance of the material. Li et. al achieved different morphologies of Ag_3PO_4 material using simple way phosphate precursor variation from H_3PO_4 to Na_2HPO_4 in hydrothermal synthesis process. This experiment resulted tremendous change in morphologies in prepared material with respect to precursor variation. Analogous effects are studied in terms of supercapacitive performance, 3D tetrapod like microcrystals of Ag_3PO_4 sample shows 1.6 times higher capacitance than a sample composed with irregular particles and some polyhedrons [20]. Selective shapes/morphology of material can be prepared by changing precursors and these results are observed by Bi. et. al. only changing silver precursor from acetate to nitrate in the preparation of silver phosphate using precipitation process. Without using capping agent selective shapes from rhombic dodecahedrons to perfect cubes of silver phosphate were prepared. Photocatalytic activity of controlled but different morphologies were studied and reported that, the rhombic dodecahedrons are more catalytically active than perfect cubic structured material [21]. Similar type of results obtained by Gunjekar et. al. in the simple chemical bath preparation of silver phosphate thin films. Authors obtained

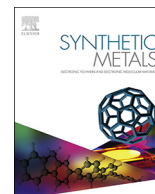
* Corresponding author.

E-mail address: umakant.physics84@gmail.com (U.M. Patil).

<https://doi.org/10.1016/j.mseb.2020.114641>

Received 30 January 2020; Received in revised form 8 June 2020; Accepted 16 July 2020

0921-5107/ © 2020 Elsevier B.V. All rights reserved.



Regulated micro-leaf like nickel pyrophosphate as a cathode electrode for asymmetric supercapacitor

Supriya J. Marje^a, Pranav K. Katkar^a, Sachin S. Pujari^a, Suraj A. Khalate^a, Abhishek C. Lokhande^b, Umakant M. Patil^{a,*}

^a Centre for Interdisciplinary Research, D.Y. Patil Education Society (Deemed to be University), Kasaba Bawada, Kolhapur, 416 006, Maharashtra, India

^b Department of Physics, Khalifa University of Science and Technology (KUST), Abu Dhabi, United Arab Emirates

ARTICLE INFO

Keywords:

Asymmetric supercapacitor
Chemical bath deposition method
Composition variation
Nickel pyrophosphate
Thin film electrode

ABSTRACT

In present work, nickel pyrophosphate ($\text{Ni}_2\text{P}_2\text{O}_7 \cdot 8\text{H}_2\text{O}$) thin film on stainless steel substrate synthesized using facile chemical bath deposition method and used as cathode electrode for asymmetric supercapacitor. Three compositions of nickel phosphate with varying of nickel:phosphate (2:1, 1:1 and 1:2) molar ratio are prepared to study composition effect on microstructure and subsequently on supercapacitive performance. Morphology changes with composition from microflower to leaf like, consequently supercapacitive performance influences with increasing phosphate content in material. The well dispersed leaf like microstructure (nickel:phosphate;1:2) of nickel pyrophosphate offers more active sites and it shows maximum specific capacitance of 482 F g^{-1} at current density of 3 mA cm^{-2} along with 99.73% capacitive retention over 2500 cycles. Moreover, an asymmetric device fabricated using nickel pyrophosphate and reduced graphene oxide as a positive and negative electrode, respectively. Prepared asymmetric supercapacitor offers specific capacitance of 74.81 F g^{-1} at 0.9 mA cm^{-2} current density with 26.6 Wh kg^{-1} energy density at a moderately high power density of 870.6 W kg^{-1} . Also, exhibits 87.35% of capacitive retention over 5500 cycles at 4 mA cm^{-2} current density.

1. Introduction

To reduce global warming, promote green and clean energy, and fight with energy crisis, usage of sustainable energy sources increased [1]. Fulfil increasing demand in global power supply for different application, have to store electricity efficiently produced from sustainable energy sources [2]. So, attention shifted towards cost effective, easy to use and maintenance free energy storage devices with high stability [3]. Supercapacitor come in focus because it offers high energy and power density as compare to conventional capacitors and batteries, respectively [4,5]. These amazing properties of supercapacitor encourage to use it either individually or in combination with batteries/fuel cell for different application [6,7].

Supercapacitors are divided into three categories on the basis of charge storage mechanism such as EDLC, pseudocapacitor and hybrid supercapacitor [8]. There are numerous materials were investigated as an supercapacitor electrode material such as, metal oxides [9,10], hydroxides [11] and sulfides [12] but they suffers from some limitations such as, poor stability, poor conductivity and lower specific capacitance [13,14]. To reach high energy and economical demands, need to

develop electrode material has low-cost, high specific capacitance and favourable cycling ability [15].

Transition metal phosphates widely studies for decades and used in various applications as, catalysis/photocatalysis [16,17], energy storage devices [18] and sensors [19]. Recently, they fascinated for energy storage application owing to their excellent conductivity, abundant active sites, wide structural channels for electrolyte ions percolation and most importantly offer stable structure due to P–O covalent bond [20]. Among metal phosphates, nickel and cobalt aided in energy storage due to excellent redox action and also, they are earth abundant and widely distributed. Various structures of nickel phosphates such as pyrophosphate and orthophosphate, can facilitates different ionic conductivity and consequently rate capability [21].

So, different microstructure and polymorphs of nickel phosphate were prepared using various methods for supercapacitor application and reported in literature. Sankar et al. grown one dimensional nanorods of nickel pyrophosphate on nickel foam by simple hydrothermal method [22]. Similarly, Pang et al. [23] synthesized nickel pyrophosphate microrods by calcination of ammonium nickel phosphate material and Senthilkumar et al. [24] prepared nano grains of nickel

* Corresponding author.

E-mail address: umakant.physics84@gmail.com (U.M. Patil).



Cobalt doped iron phosphate thin film: An effective catalyst for electrochemical water splitting

Suraj A. Khalate^a, Sujit A. Kadam^b, Yuan-Ron Ma^b, Sachin S. Pujari^a, Umakant M. Patil^{a,*}

^a Centre for Interdisciplinary Research (CIR), D.Y. Patil Education Society, Kolhapur 416006, India

^b Department of Physics, National Dong Hwa University, Hualien 97401, Taiwan

ARTICLE INFO

Article history:

Received 26 March 2021

Received in revised form 9 June 2021

Accepted 19 June 2021

Available online 24 June 2021

Keywords:

Catalytic stability

Doping

Electrochemistry

Heterogeneous catalysis

Water splitting

ABSTRACT

For practically feasible water splitting to fulfill the need of energy, the development of efficient, robust and long lasting catalyst is necessary. Transition metal compounds facilitates the good catalytic properties due to facile transition of their oxidation states. We here reported a novel process for the synthesis of novel material as cobalt doped iron phosphate thin films. The pristine iron phosphate thin films have synthesized by regular facile hydrothermal method and to achieve doping of the cobalt into iron phosphate, second step hydrothermal ion-exchange process was used. The as synthesized cobalt doped iron phosphate thin film electrode exhibits excellent electrochemical OER and HER catalytic water splitting performance. The prepared material was demonstrated by two electrodes overall water splitting electrolyzer in alkaline medium at lowest potential of 1.72 V to deliver 10 mA/cm² current density after 4 days' continuous water splitting test. The outstanding catalytic stability proved 0.4 Co:FePi thin film electrodes are robust water splitting electrocatalyst.

© 2021 Elsevier B.V. All rights reserved.

1. Introduction

Upon looking at the present scenario of the energy generation and consumption, an eye capturing fact can be realized that we need greater energy than what we have today. It is the necessity to produce energy from green and sustainable energy resources to maintain our benign environment and future from the energy crisis, global warming and environmental pollution. Hydrogen is one of the best energy sources from clean and green energy sources, and is expected to play a major role in a future sustainable energy sector [1,2]. Hydrogen from energy sources such as solar or wind electricity is the clean production of energy, also the storage of energy in the clean form as a standby during the ups and downs of solar and wind power. Electrochemical water splitting is an effective technique to convert electrical energy into chemical energy in the form of hydrogen by using proper catalyst electrode. Electrochemical water splitting is the combined reaction of two half reactions as oxygen evolution reaction (OER) and complimentary hydrogen evolution reaction (HER). These reactions of water splitting (OER and HER) are constrained by the rate determining sluggish four electron coupled proton transfer process and hence have low conversion efficiency

[3–5]. At present, the best electrocatalysts with high efficiency are the state-of-the-art materials as platinum, ruthenium/iridium based oxides which are widely used. The best electrocatalyst for HER is platinum, which only requires onset overpotential of nearly zero. But the commercial use of these state-of-the-art catalyst materials is limited by their scarcity, high cost, large overpotentials at high current densities and poor stability [6]. Many researchers are interested and engage in the development of alternative cost-effective, non-noble metal and highly stable electrocatalysts for efficient overall water splitting. Variety of new non-noble metal based catalysts are under research and development process. First row (3d) transition metal based materials have good catalytic properties due to facile transition of their oxidation states. Transition metal based materials such as, transition metal-transition metal alloys (TMAs), transition metal oxides (TMOs), transition metal nitrides (TMNs), transition metal dichalcogenides (TMDs), transition metal phosphides (TMPs), transition metal carbides (TMCs), transition metal borides (TMBs), etc. are playing leading role in water splitting [7]. Few reports are available on transition metal phosphate electrode materials for electrochemical water splitting. Transition metal phosphates play an important role by facilitating adsorption and stabilizing active centers, also phosphate ligands give the favorable conditions for electrolyte ion adsorption and oxidation by distorting local atomic geometry and facilitating the oxidation of metal atoms during proton coupled electron transfer [8].

* Corresponding author.

E-mail address: umakant.physics84@gmail.com (U.M. Patil).